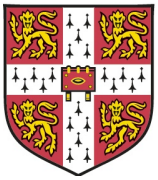

University of Cambridge
Department of Materials Science & Metallurgy

Defect-induced magnetism and transport phenomena in epitaxial oxides

Frank Schoofs

Wolfson College

A dissertation submitted for the degree
of Doctor of Philosophy

March 2012

Abstract

This work focuses on the impact of defects, intrinsic or artificially introduced, on the functional properties of thin, epitaxial oxide films. In the first part, the origin of the ferromagnetic properties of Mn-doped and undoped zinc oxide is studied. The deposition conditions are found to have a significant impact on the structural, transport and magnetic properties of the thin films. Combining x-ray magnetic circular dichroism and magnetometry experiments, it is established that the transition metal dopants (i.e. Mn) have no influence on the ferromagnetic nature of the zinc oxide, but that localised magnetic moments on intrinsic defects are in fact responsible for the ferromagnetic behaviour. A relation between strain (related to defect concentration) and magnetisation is established.

In the second part of this dissertation, artificially introduced defects are employed in order to discover the fundamental conduction mechanism behind the two-dimensionally conductive $LaAlO_3/SrTiO_3$ interface. All experiments, from varying deposition temperature, to oxygen pressure, to laser fluence or to the insertion of (doped) perovskite layers, point towards a structurally governed conduction mechanism, although the exact details are still unclear. Distinct transitions in the resistance versus temperature curves are observed at different values than the bulk phase transformation temperature. These transitions form the boundaries of different conduction modes, with tendencies towards non-Fermi-liquid behaviour observed in certain two-dimensionally conducting samples in limited temperature regimes. By optimising the (defect) structure at the interface, i.e. by introducing a single unit cell of $(La_{0.5},Sr_{0.5})TiO_3$ or $SnTiO_3$, it is shown that the sheet carrier density can be dramatically enhanced, up to an order of magnitude higher than unmodified $LaAlO_3/SrTiO_3$ interfaces with a value of 10^{14} cm^{-2} at 200 K. Finally, attempts at functionalising the conductive heterointerface by doping and inserting (anti)ferromagnetic layers are made.

List of publications

F. Schoofs, M. Egilmez, T. Fix, J. L. MacManus-Driscoll and M. G. Blamire. Enhanced two-dimensional electron transport in $(La_{0.5},Sr_{0.5})TiO_3$-modified $LaAlO_3/SrTiO_3$ heterointerfaces. *submitted*.

F. Schoofs, M. Egilmez, T. Fix, J. L. MacManus-Driscoll and M. G. Blamire. Structural and magnetic properties of $CoTiO_3$ thin films on $SrTiO_3$(0 0 1). *submitted*.

F. Schoofs, M. Egilmez, T. Fix, J. L. MacManus-Driscoll and M. G. Blamire. Impact of structural transitions on electron transport at $LaAlO_3/SrTiO_3$ heterointerfaces. *Applied Physics Letters*, 100:081601, 2012.

F. Schoofs, T. Fix, A. S. Kalabukhov, D. Winkler, Y. Boikov, I. Serenkov, V. Sakharov, T. Claeson, J. L. MacManus-Driscoll and M. G. Blamire. Optimized transport properties of $LaAlO_3/SrTiO_3$ heterointerfaces by variation of pulsed laser fluence. *Journal of Physics: Condensed Matter*, 23:305002, 2011.

F. Schoofs, T. Fix, A. M. H. R. Hakimi, S. S. Dhesi, G. van der Laan, S. Cavill, S. Langridge, J. L. MacManus-Driscoll and M. G. Blamire. Strain dependent defect mediated ferromagnetism in Mn-doped and undoped ZnO thin films. *Journal of Applied Physics*, 108:053911, 2010.

Acknowledgments

In the first place I would like to thank my supervisor, Prof. Mark Blamire, to have given me the opportunity and support to work in the Device Materials Group. Throughout the years, Prof. Judith MacManus-Driscoll, Thomas Fix, Mehmet Egilmez and Mary Vickers have helped me on a very practical level, for which I am grateful. Of course my amazing Cambridge PhD experience was only possible thanks to my parents, Sian and the wonderful, diverse bunch of friends that I met through DMG & Wolfson College.

Frank (March 2012)

Declaration of originality

This dissertation is submitted for the degree of Doctor of Philosophy at the University of Cambridge, United Kingdom. It describes work carried out from October 2008 to March 2012 in the Department of Materials Science and Metallurgy, University of Cambridge, under the supervision of prof. Blamire.

Except where specific reference is made to the work of others, this is the result of my own work. No part of this work has been submitted for any other qualification at this or any other institution.

This dissertation is less than 60,000 words in length.

Frank Schoofs March 2012

List of abbreviations

2DEG	two-dimensional electron gas
AFM	atomic force microscope/microscopy
BMP	bound magnetic polaron
CTO	cobalt titanate, $CoTiO_3$
DMO	dilute magnetic oxide
DMS	dilute magnetic semiconductor
EDX	energy dispersive x-ray spectroscopy
EELS	electron energy loss spectroscopy
FWHM	full width at half maximum
FY	fluorescence yield
HAXPES	high angle x-ray photoemission spectroscopy
LAO	lanthanum aluminate, $LaAlO_3$
LSAT	$(LaAlO_3)_{0.3}(Sr_2AlTaO_3)_{0.7}$
LSTO	lanthanum-doped strontium titanate, $(La_x,Sr_{1-x})TiO_3$
MBE	molecular beam epitaxy
MEIS	medium energy ion spectroscopy
MIT	metal-insulator transition
NGO	neodymium gallate, $NdGaO_3$
PL	photoluminescence
PLD	pulsed laser deposition
RBS	Rutherford backscattering spectroscopy
RE	rare earth (element)
RHEED	reflection high-energy electron diffraction
RSM	reciprocal space map
SEM	scanning electron microscope/microscopy
SIMS	secondary ion mass spectroscopy
SQUID	superconducting quantum interference device
STO	strontium titanate, $SrTiO_3$
SXRD	surface x-ray diffraction
TEM	transmission electron microscope/microscopy
TEY	total electron yield
TM	transition metal
VSM	vibrating sample magnetometer/magnetometry
XAS	x-ray absorption spectroscopy
XMCD	x-ray magnetic circular dichroism
XPS	x-ray photoelectron spectroscopy
XRD	x-ray diffraction

Contents

Chapter 1

Introduction

Thin films of oxide materials, commonly complex oxides including transitions metals and/or rare earth elements, are generating an ever increasing interest from the scientific community and from industry. It is their versatility, but especially their unique combination of functional properties that grants these materials a promising future in electronic or spintronic device applications [1–3]. Superconductivity, (anti)ferromagnetism, (anti)ferroelectricity (or a combination of these) can occur with various degrees of conduction, ranging from (half-)metal-like to insulating [4, 5]. Another advantage of oxide materials is their similar crystal lattice sizes, which eases the incorporation of these materials into epitaxial heterostructures, opening the path to, for example, two-dimensionally confined properties [5–8].

Control over the functional behaviour of oxide materials can be obtained through modulation of two aspects. The strain or lattice distortion has a significant impact on the functional phase stability with respect to temperature – this stress can be applied horizontally (e.g. [9, 10]) or vertically (e.g. [11]). The second significant aspect of oxides is defect management [2, 12]: the careful balance of lattice defects is crucial in understanding and manipulating the functional properties of oxide materials. Lattice defects can come in many forms: intrinsic (cation or anion vacancies or interstitials) or extrinsic (dopants or impurity atoms).

In this work two different oxide materials systems are investigated, with an emphasis on the interplay between functional properties and structural defects. The latter can occur as a result from the preparation of the oxides or can be artificially and controllably introduced (dopants or layers) to reveal the fundamental underlying principle behind the functional behaviour of the oxide system under scrutiny. The goal of this work is to provide an insight into this intimate interplay and to provide a handle to tune the functional properties.

After an introduction of the experimental methods (chapter 2), part I (chapters 3–6) explores the ferromagnetic properties of ZnO films and the crucial impact of lattice defects on its electronic and magnetic properties. Part II (chapters 7–15) focuses on the intriguing two-dimensional conductive properties at the interface of two insulators, namely $LaAlO_3$ and $SrTiO_3$. By controlling the introduction of (artificial) defects into the heterostructure, a better understanding of this remarkable and much-discussed phenomenon is provided.

Bibliography

[1] Manuel Bibes and Agnès Barthélémy. Oxide spintronics. *IEEE Transactions on Electron Devices*, 54(5):1003, 2007.

[2] Mark G. Blamire, J. L. MacManus-Driscoll, Neil D. Mathur, and Zoe H. Barber. The materials science of functional oxide thin films. *Advanced Materials*, 21(38-39): 3827–3839, 2009.

[3] Manuel Bibes, Javier E. Villegas, and Agnes Barthelemy. Ultrathin oxide films and interfaces for electronics and spintronics. *Advances in Physics*, 60(1):5–84, 2011.

[4] L. W. Martin, Y.-H. Chu, and R. Ramesh. Advances in the growth and characterization of magnetic, ferroelectric and multiferroic oxide thin films. *Materials Science and Engineering R*, 68:89–133, 2010.

[5] Matthias Opel, Stephan Geprägs, Edwin P. Menzel, Andrea Nielsen, Daniel Reisinger, Karl-Wilhelm Nielsen, Andreas Brandlmaier, Franz D. Czeschka, Matthias Althammer, Mathias Weiler, Sebastian T. B. Goennewein, Jürgen Simon, Matthias Svete, Wentao Yu, Sven-Martin Hühne, Werner Mader, and Rudolf Gross. Novel multifunctional materials based on oxide thin films and artificial heteroepitaxial multilayers. *Physica Status Solidi A*, 208(2):232–251, 2011.

[6] J. Mannhart and D. G. Schlom. Oxide interfaces an opportunity for electronics. *Science*, 327:1607, 2010.

[7] Pavlo Zubko, Stefano Gariglio, Marc Gabay, Philippe Ghosez, and Jean-Marc Triscone. Interface physics in complex oxide heterostructures. *Annual Review of Condensed Matter Physics*, 2:141–165, 2011.

[8] H. Y. Hwang, Y. Iwasa, M. Kawasaki, B. Keimer, N. Nagaosa, and Y. Tokura. Emergent phenomena at oxide interfaces. *Nature Materials*, 11:103–113, 2012.

[9] K. J. Choi, M. Biegalski, Y. L. Li, A. Sharan, J. Schubert, R. Uecker, P. Reiche, Y. B. Chen, X. Q. Pan, V. Gopalan, L.-Q. Chen, D. G. Schlom, and C. B. Eom. Enhancement of ferroelectricity in strained $BaTiO_3$ thin films. *Science*, 306:1005, 2004.

[10] Craig J. Fennie and Karin M. Rabe. Magnetic and electric phase control in epitaxial $EuTiO_3$ from first principles. *Physical Review Letters*, 97:267602, 2006.

[11] Judith L. MacManus-Driscoll. Self-assembled heteroepitaxial oxide nanocomposite thin film structures: designing interface-induced functionality in electronic materials. *Advanced Functional Materials*, 20:2035–2045, 2010.

[12] Lukas Schmidt-Mende and Judith L. MacManus-Driscoll. ZnO – nanostructures, defects and devices. *Materials Today*, 10(5):40, 2007.

Chapter 2

Experimental methods

This chapter introduces the deposition and characterisation techniques used in the projects which will be described in later chapters.

2.1 Pulsed laser deposition (PLD)

2.1.1 Background information

Chrisey and Hubler [1] describe pulsed laser deposition (PLD) for thin films to be 'based on the physical processes arising from the impact of high-power pulsed laser radiation on solid targets and leading to the removal of partially ionised material (as a plasma) from the impact zone'. This material is condenses on a (heated) substrate of choice, positioned opposite of the target in the vacuum chamber. Figure 2.1 shows a schematic PLD process with all essential system components.

In essence three major process steps can be identified in PLD [2]: (1) ablation of target material, (2) expansion of the plasma plume and (3) condensation and nucleation at the substrate surface. These three steps will be discussed in more detail below.

The impact of a high-energy laser on the target material causes so-called photon induced sputtering. The nature of this process is complex, not very well understood and therefore difficult to exactly reproduce. Chrisey and Hubler [1] identify three main types of energy absorption: volume absorption by electrons and phonons in the lattice, free carrier absorption at the surface and absorption from the plasma plume. The relative weight of these processes depends on the laser characteristics and the material properties, e.g. for metals the free carrier mechanism will dominate, whereas dielectrics will mostly have lattice absorption. Ellmer and Klein [2] add a few more 'secondary' ablation mechanisms to this list, such as thermal shockwave induced cracking, photoablation (photon-induced breaking of chemical bonds) and indirect collisional sputtering (by photon generated secondary ions and electrons from laser plasma). Figure 2.2 shows a micrograph of the track on a PLD target after it was ablated by a laser.

The choice of laser depends on the material to deposit: it should absorb the energy at the laser wavelength. Usually lasers are in the 200–400 nm range, where most materials exhibit strong absorption [1]. Popular lasers are KrF (248 nm), XeCl (308 nm) and frequency tripled (sometimes doubled) Nd:YAG (355 nm or 532 nm respectively) lasers, although the former two seem to give the best results in terms of film quality. The lasers are operated in (tens of) nanosecond pulses to minimise dissipation of the laser energy beyond the volume of the ablated surface layer of the target [2, 3]. This avoids thermal destruction and phase segregation in the target. Femtosecond lasers decrease the thermal effect even

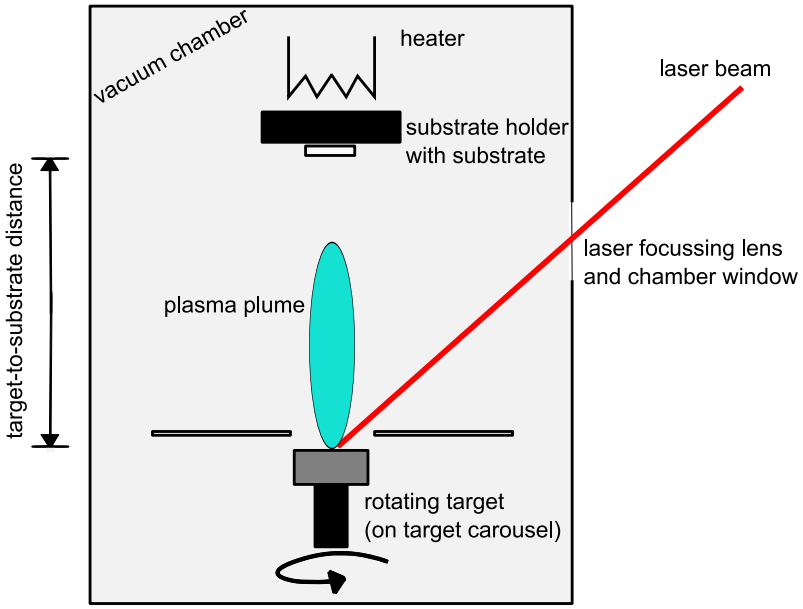

Figure 2.1: Schematic representation of a pulsed laser deposition (PLD) process.

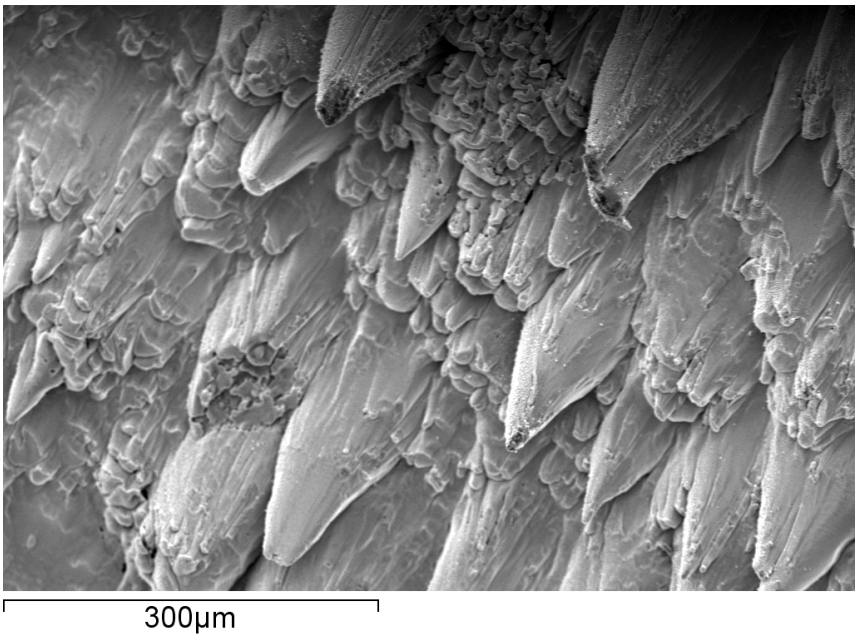

Figure 2.2: SEM micrograph of the surface of a (5.4 at% Mn, 0.54 at% Al):ZnO target in an area where it was ablated by a KrF laser.

more, but the resulting film quality is poor, due to the difference in kinetic energy of the ejected species [4]. Whereas femtosecond lasers eject species with energies around 1 keV, this is only a few hundreds of eV for nanosecond lasers, which are therefore more advisable. The importance of impact energy is also reflected in the optimum laser energy density (sometimes indicated as laser fluence), which is preferably between 1–2.5 J/cm^2 [4]. Lower energies will result in low kinetic energy of sputtered material, promoting island growth. The energy could even be below the ablation threshold if set too low. Excessive kinetic energy will degrade film properties due to physical bombardment of the surface.

An issue in PLD is the so-called splashing of material particles, up to 1 μm in diameter, which are essentially droplets of condensed sputtered material [1, 3]. This phenomenon is mostly an issue for deposition of metals and less for oxides. Splashing can be reduced by rotating the target, as the centrifugal force removes the heavier particles from their trajectory towards the substrate. Also the choice of an appropriate laser (and laser energy) can diminish the effect, e.g. KrF lasers seem to be favourable over YAG lasers to avoid splashing [4]. Other, more complicated options include double beam illumination and off-axis deposition [1].

The second major step after the ablation is the expansion of the plasma plume, which involves the transfer of material through the vacuum chamber towards the substrate. A photograph of a plasma plume during ZnO deposition is shown in Figure 2.3. The plume axis is always oriented perpendicular to the target surface, even for non-normal laser incidence. If the plume tilts at all, it would be towards the laser beam direction [1]. The angular material distribution of the plasma plume is related to the background pressure: in vacuum it is determined only by collisions between particles of the plume itself, whereas in a gas also gas collisions have to be taken in account. Increasing gas pressure from vacuum level will sharpen the plume boundary (creating a shock front), spatially confining the plume and slowing down its propagation rate, which can be visualised *in situ* by photoemission spectroscopy e.g. [5]. The process will thus shift away from being a purely line-of-sight deposition as the background gas pressure increases.

The models applied to describe the material transfer depend on the pressure range (as intuitively indicated above) and the target-to-substrate distance [2]. This distance is an important system characteristic, the optimum of which is determined by the laser energy delivered to the target (distance can be increased if energy is high) and the desired deposition rate [1]. A bigger distance should reduce incorporation of particles from splashing (see above), as these will not reach the substrate surface.

The background gas during deposition serves several purposes [1]: it attenuates and thermalises the plume and changes the spatial distribution of all elements. The gas also influences the deposition rate and the kinetic energy distribution of the sputtered material. The balance between differently charged species in the plume can be changed by the background gas [6]. When oxides are deposited in an oxygen plasma starting from metallic targets, so-called 'reactive scattering' will occur. For the growth of oxide films it is usually necessary to maintain an oxidising environment during deposition, in order to help form and stabilise the desired crystal phase at the deposition temperature. Only extremely stable oxides can be deposited in vacuum, as can be derived from the so-called Ellingham diagram [7]. This means that a high oxygen background pressure becomes necessary to maintain an equilibrium composition in target and film. For doped targets, the composition transfer to the deposited film depends on the oxygen pressure and probably on the element's vapour pressure (and hence deposition temperature) [2]. Off-stoichiometric targets might be necessary if preferential loss of cation species occurs, e.g. due to excessive

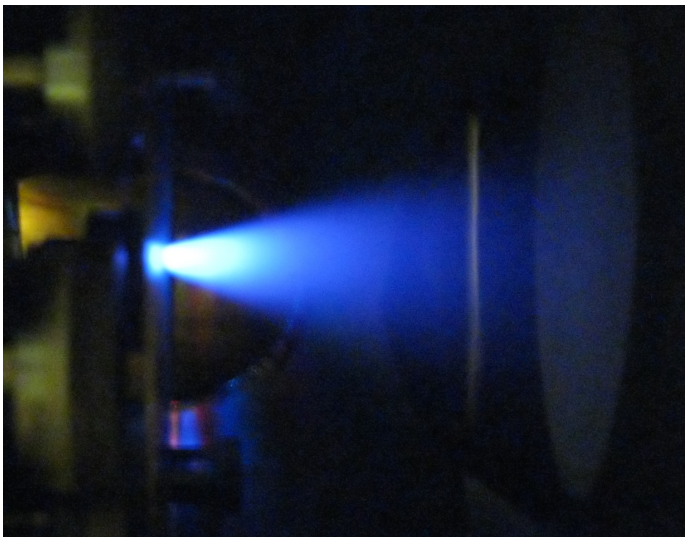

Figure 2.3: Plasma plume during pulsed laser deposition of ZnO.

gas phase scattering or volatilisation from the film surface at higher temperatures [1]. This is for example the case for the deposition of $LaTiO_3$ ($La_2Ti_2O_7$ target) [8–10] and $BiFeO_3$ (target with Bi-excess) [11].

After the ablation and the plume expansion, the last step of the PLD process is the condensation of evaporated material on the substrate surface, involving the thin film nucleation and growth processes as known for MBE and sputtering. These are the so-called 2D (layer-by-layer or Frank-van der Merwe), 3D (island or Volmer-Weber), combined (Stranski-Krastanov) or step-flow (on vicinal surfaces, i.e. substrate with a deliberate miscut angle) growth modes. The details of their thermodynamics are described in e.g. [1]. Important parameters that determine the type and speed of growth are energy of the arriving species, background pressure, target-to-substrate distance, laser pulse frequency and substrate temperature. A change in these conditions (common variables are frequency and temperature) could result in a change of growth mode, e.g. a thermodynamical 2D growth can be kinetically limited to 3D.

The substrate temperature should be chosen to be sufficiently high to ensure good film crystallinity (i.e. texture) and to preserve stoichiometry: a too low temperature will result in a low adatom diffusion mobility. The main diffusion occurs during and immediately after the arrival of the species at the surface, after crystallisation little mobility has been observed [12]. It is desirable to heat the substrate by a heater that is located at the backside to avoid deposition of heater material on the film.

Pulsed laser deposition is a flexible and versatile thin film deposition for all sorts of materials, from metals [13], to complex oxides [1], borides [14], nitrides [13, 15], even to polymers [16, 17] and amorphous materials [18]. By spatially separating the energy source (the laser) from the actual deposition, any reactive gas (e.g. O_2, N_2, N_2O) can be controllably added to the chamber, maintaining a very clean process (no filament or plasma gas required). The interaction between the beam and the target is relatively independent of other parameters, except maybe the ablation state of the target (pristine surface as opposed to a trenched track). PLD is capable of transferring multi-element compounds from a single target to a substrate due to its (fluence dependent) congruent ablation,

making it very attractive for deposition of (co)doped semiconductors. Thickness control can be very accurate by limiting the amount of pulses; monolayer accurate multilayers are possible by simply rotating to the desired target in a target carousel. By playing with temperature and pressure, it is even possible to deposit nanorods and nanowires with diameter control through variation of the target-to-substrate distance. This has been shown for ZnO, with [2] and without [19] the aid of Au colloids as nucleation sites.

On the other hand there are several disadvantages to PLD, which are mostly related to the limited industrial applicability [2]. The volume deposition rate is rather low as well as the covered substrate area, similar to MBE. Without lateral scanning of the substrate, thickness and homogeneity of PLD films (assuming a constant target surface condition) is limited to about 1 cm^2. The overall (energy) efficiency is low as well, mostly due to the low energetical efficiency of the laser.

2.1.2 Experimental procedure

Thin film fabrication for this work has been carried out in the system shown in Figure 2.4. The laser is a Lambda Physik KrF excimer laser (248 nm). Film deposition is carried out at an approximate laser energy density of 1 J/cm^2, unless otherwise specified. The target-to-substrate distance is roughly 80 mm in this setup. The vacuum chamber is pumped down to high vacuum (10^{-6}–10^{-7} mbar), but during deposition oxygen can be controllably introduced into the system through a needle valve. Growth can be monitored by RHEED, as explained in section 2.2.1.

Targets are synthesised from the powders in the desired stoichiometry. The powders are mixed and ground in a mortar, then pressed into a 'green shape' pellet and subsequently sintered for 8 hours at 900℃ in air for ZnO-based targets. For perovskite targets, an extra step is introduced between milling and pressing to allow for a solid state reaction between the $SrCO_3$ (or other carbonates as required, e.g. $BaCO_3$, $CaCO_3$) and TiO_2. Powders are mixed and ground in a mortar, placed in the furnace for 6 hours at 900℃ in air, then milled again, pressed into a pellet and sintered for 8 hours at 1100℃. The sintered target is glued on the target stub with silver glue (SPI Silver Paste Plus) and placed in the chamber.

The substrate of choice is mounted with silver paint on a heater with adaptable tilt and rotation. Prior to deposition, the substrates are cleaned with isopropanol and glued on the holder with silver paint.

2.2 Structural characterisation

2.2.1 Reflection High-Energy Electron Diffraction (RHEED)

A high vacuum column with W-filament electron emitter is incorporated in the deposition chamber, allowing in-situ and real time monitoring of film properties by reflection electron diffraction. A collimated electron beam of about 20 keV is directed towards the film and the resulting diffraction pattern (in reflection) is visualised on a fluorescent screen. The equipment and its working principle are schematically shown in Figure 2.5. The diffracted electrons that reach the screen have undergone only little interaction with the sample, i.e. their penetration depth was very low, making this a very surface sensitive technique, probing only the first few monolayers of material.

Several different types of information can be extracted from studying these electron diffraction patterns [20, 21]. A (static) diffraction pattern can give morphological information about a deposited film. Single crystals are characterised by well-defined spots, according to their crystal structure and orientation. Smooth films (roughness <1–2 nm)

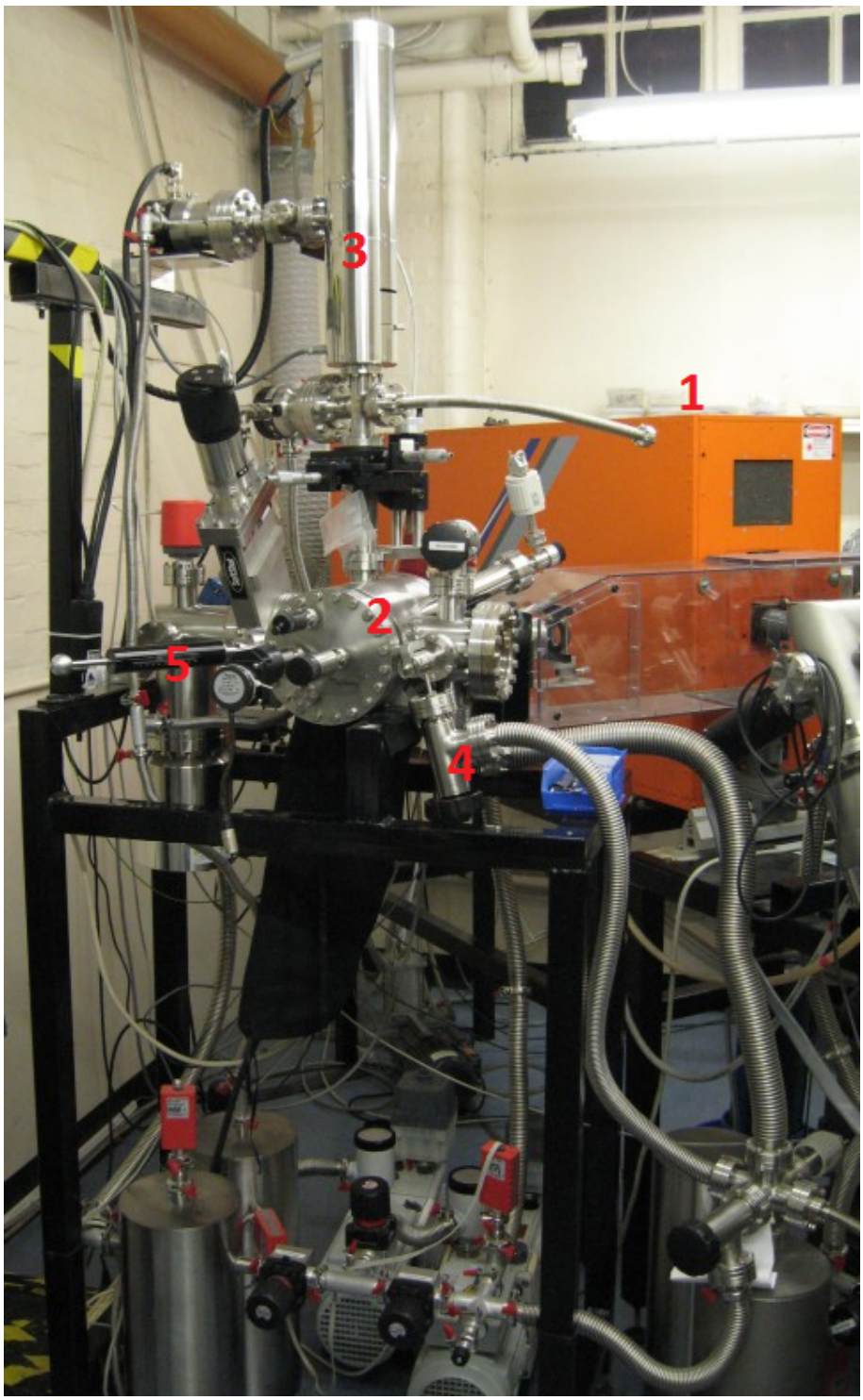

Figure 2.4: The PLD setup used in this work. **(1)** KrF laser **(2)** main vacuum chamber with target carousel **(3)** RHEED column **(4)** oxygen supply line **(5)** linear drive shutter for RHEED screen

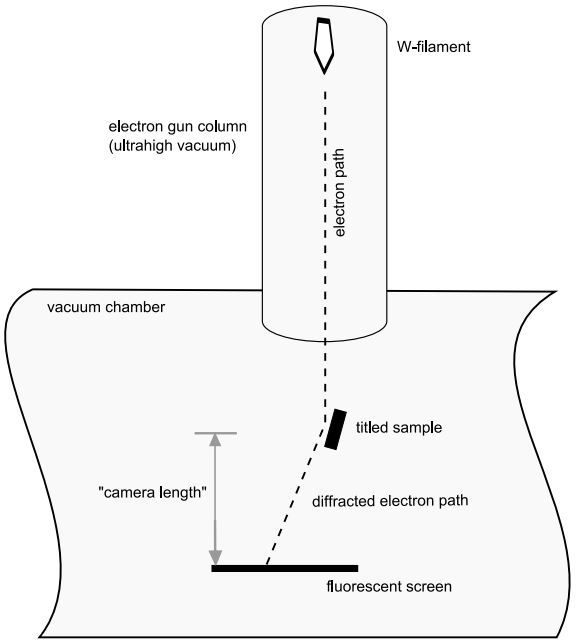

Figure 2.5: Schematic representation of the reflection high-energy electron diffraction system and its incorporation in the deposition chamber. The magnitude of the incident beam angle is exaggerated for clarity.

appear as a streaky diffraction pattern, typical of surface reconstructions (so-called 2D lattices), their spacing being a direct measure of the surface lattice constant [20]. Island growth is clearly characterised as a spotty diffraction pattern, due to multiple diffraction of the electrons through the islands.

In principle the in-plane lattice parameter can be calculated from these diffraction images, provided that the camera length, i.e. the distance between sample and diffraction patter, is known [21]. This means the in-plane strain (as well as in-plane orientation [22]) can be calculated or its evolution even monitored during film growth.

An interesting tool for film growers are the so-called intensity oscillations, sometimes just termed RHEED oscillations: changes in intensity of the specular spot over time during crystal growth. This allows to determine growth rates and accurately control thickness to the monolayer level. In an intuitive picture these intensity fluctuations arise from a variation in the surface morphology during 2D (layer-by-layer) growth [20, 21, 23–25]. Initially the intensity drops as the roughness increases due to the formation of small nucleation centres on the perfectly flat substrate. With each completely formed monolayer the intensity increases again (flat surface), decreasing afterwards upon formation of a new layer (rough surface). This is schematically shown in Figure 2.6. The drawback to this extremely accurate and sensitive phenomenon is that it is only active under deposition conditions of layer-by-layer growth, which have to be discovered first. On $SrTiO_3$ substrates, it appears that a substrate temperature of roughly half the melting temperature of the oxide in Kelvin results in 2D growth.

A more advanced and 'hidden' information is in the so-called RIPS effect, the reconstruction induced phase shift [20]. Essentially this refers to a phase shift of the intensity signal depending on the previous layer (homo- or hetero-epitaxy). From the position of this phase shift, it is possible to deduce the number of monolayers required for interface accommodation.

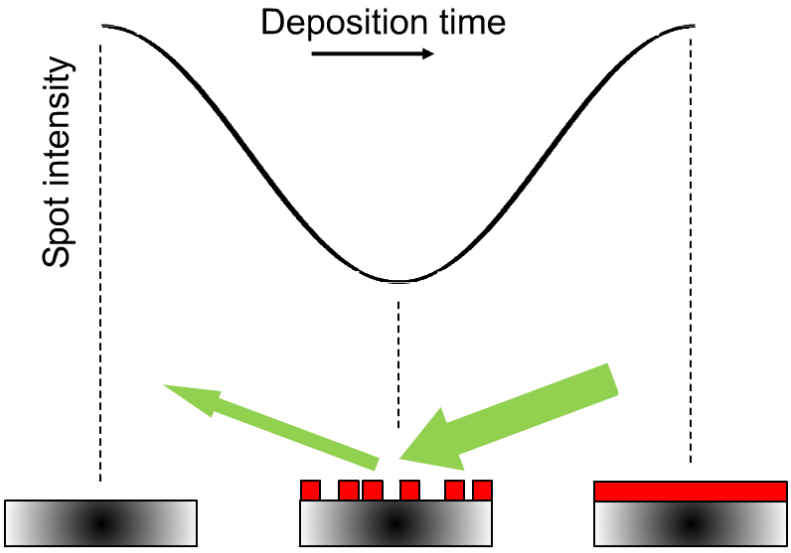

Figure 2.6: Schematic representation of the evolution of the RHEED specular spot intensity during 2D film growth. The magnitude of the incident beam angle is exaggerated for clarity.

2.2.2 X-ray diffraction (XRD)

Since the oxide films grown and studied here are (in theory) all epitaxial with respect to the single crystal substrate and therefore exhibit a single out-of-plane orientation, specific x-ray diffraction techniques can be employed to characterise these materials.

A Bruker D8 θ/θ (fixed sample) diffractometer with position sensitive detector (abbreviated as B1) is used to make general sample $2\theta/\theta$ ('goniometric') scans and determine thin film rocking curves. Aside from the crystallographic orientation of the film and presence of secondary phases (if any), the out-of-plane lattice parameter can be determined from goniometric scans. The substrate peaks as well as the film peaks are fitted with the TOPAS software to determine their exact positions, taking into account the multi-wavelength properties of the incoming x-ray beam. To correct for the sample height displacement error, the experimental 2θ displacement error of the substrate peaks (e.g. $SrTiO_3$) is determined and fitted by linear regression, with the displacement $\Delta 2\theta$ as a function of the experimental 2θ angle. Using this relation as an internal standard, the measured 2θ values for the film peaks are corrected. The experimental out-of-plane lattice parameter can be calculated from Bragg's law and compared to the theoretical value.

A rocking curve measurement probes the width in θ at constant 2θ, i.e. the angular distribution of the out-of-plane axis of the crystallites, providing an indication of the degree of orientation of the crystal. A wide rocking curve (expressed in terms of its full width at half maximum or FWHM) means that at fairly large misorientations from the perpendicular axis, diffraction from the lattice still occurs. Single crystal substrates will (and should) have very narrow rocking curves[1], whereas polycrystalline samples will have completely flat rocking curves (no preferred out of plane orientation).

Reflectometry is carried out on a Bruker D8 θ/θ diffractometer with 4 circles (ω, 2θ, ψ, ϕ) and graded mirror to give a nearly parallel beam (abbreviated as B2), in combination

[1] $SrTiO_3$ substrates typically have a rocking curve FWHM of about 0.05°, whereas $NdGaO_3$ substrates have a FWHM below the machine's resolution, i.e. $\leq 0.006°$.

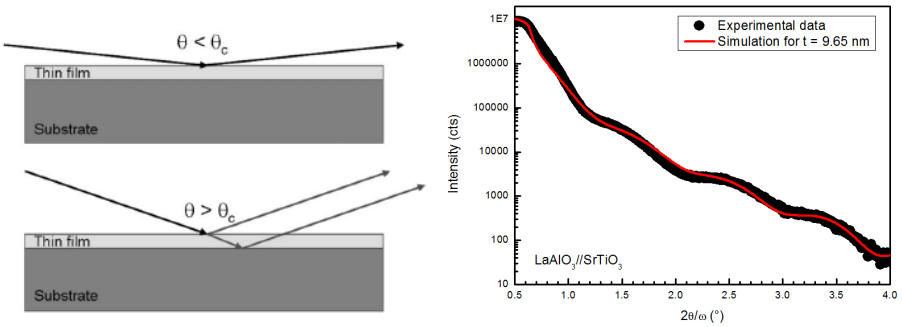

(a) (b)

Figure 2.7: **(a)** Schematic view of x-ray reflectometry with θ below and above the critical angle θ_c [from 26]
(b) Experimental reflectometry curve with fitted simulation of a 9.65 nm LAO//STO sample.

with a scintillator detector. The technique probes differences in electron density with an incident beam under small angles (typically 0.5°–3° 2θ), resulting in thickness information of multilayered structures, independent of crystalline quality [26]. At angles above a certain critical angle, x-rays are reflected at all interfaces and the interference from different layers results in so-called Kiessig fringes in the intensity versus 2θ. Whereas the amplitude of the fringes depends on the surface or interface roughness[2] and the difference in (electron) densities, the fringe spacing is related to the layer thickness. Assuming one layer on top of a flat substrate (as in Figure 2.7a), the relation considering successive experimental fringe maxima at angle θ_i is:

$$\frac{(2m_i + 1)\lambda^2}{4t_{film}^2} = \sin^2\theta_{i+1} - \sin^2\theta_i \tag{2.1}$$

with m_i being the fringe order (1, 2, 3...), λ the x-ray wavelength and t_{film} the layer thickness. A plot of the right hand side of the above equation versus m_i has a gradient of $\lambda/(2t_{film}^2)$, resulting in an accurate measurement of the thickness. The X'Pert Reflectivity software provides more complex simulations and fitting algorithms to analyse multilayer samples in order to obtain all relevant thickness and roughness data. Figure 2.7b shows an experimental curve for an LAO//STO sample, exhibiting the characteristic fringes superposed with a simulation to fit the experimental data.

In order to determine the relative orientation of the epitaxial film crystal with respect to the substrate, so called ϕ-scans are performed on diffractometer B2. A reference scan on the substrate indicates the orientation of the crystal axes, which form a reference frame for the epitaxial film. Such ϕ-scans are performed on crystallographic reflections at known offsets from the out-of-plane orientation, e.g. on the $SrTiO_3$ (011) or (111) reflection for a (001) oriented $SrTiO_3$ substrate.

A further step in the full XRD analysis of an epitaxial film is the measurement of a reciprocal space map (RSM). These are also collected on the B2 diffractometer. This procedure consists of the collection of data in a range around an asymmetric crystal reflection. Such a reflection has a partial out-of-plane and in-plane direction component. For example for (001) STO substrates, the area around the (103) or (113) reflections is typically studied. The selection of the appropriate substrate reflection depends on the

[2]Roughness should generally be below 2 nm, otherwise reflected x-rays are strongly damped and intensity drops off quickly above the critical angle.

crystal symmetry of the deposited film: the film's asymmetric reflection should not be too far away from the substrate reflection. This method is commonly used to quickly (visually) check whether the in-plane lattice parameter of a film is the same as that of the substrate. It also allows to extract the exact position of the asymmetric reflection and therefore another means to calculate to in-plane or out-of-plane lattice parameter.

2.2.3 Other techniques

Photoluminescence (PL)

Photoluminescence experiments are carried out at room temperature in an Accent RPM 2000. A 266 nm laser excites electrons in the material, while the wavelength dependent emitted photon intensity is recorded. This technique gives only the energy difference between a high and low energy electronic level, it does not specify where these levels are located in the band diagram [27]. Certain specific emission bands can sometimes be related to specific defects or impurities by comparison to literature data.

Atomic Force Microscopy (AFM)

An AFM Multimode Nanoscope III is operated in tapping mode at room temperature to investigate sample topography and to calculate the root mean square (rms) surface roughness. Images are produced with the WSxM software [28].

Energy dispersive x-ray spectroscopy (EDX)

Film compositions are determined by energy dispersive x-ray spectroscopy on a Jeol 5800 scanning electron microscope with a beam acceleration voltage of 15 keV. The atomic ratios are recalculated to exclude the elements from the substrate. For the case of ZnO films, dopant concentrations are noted in at% with respect to the Zn concentration. For example (1 at% Mn, 1 at% Al):ZnO stands for $Zn_{0.98}Mn_{0.01}Al_{0.01}O$. For doped STO films, concentrations are with respect to the Sr (for e.g. La) or Ti (for e.g. Mn, Co).

2.3 Characterisation of electrical properties

Measurements are carried out in a cryogen-free high-field measurement system by Cryogenic Ltd, which has a temperature range of 2–300 K and can apply magnetic fields up to 9 T. Carrier densities and mobilities are measured in the van der Pauw configuration [29]. Al-connections are wire bonded to the sample: 4 contacts in a rectangle at the edges of the sample (see Figure 2.8), with an optional fifth contact to apply a gate voltage through the substrate. Horizontal and vertical resistances can be defined as follows:

$$R_{34,12} = \frac{V_{34}}{I_{12}} \tag{2.2}$$

$$R_{12,34} = \frac{V_{12}}{I_{34}} \tag{2.3}$$

$$R_{23,14} = \frac{V_{23}}{I_{14}} \tag{2.4}$$

$$R_{14,23} = \frac{V_{14}}{I_{23}} \tag{2.5}$$

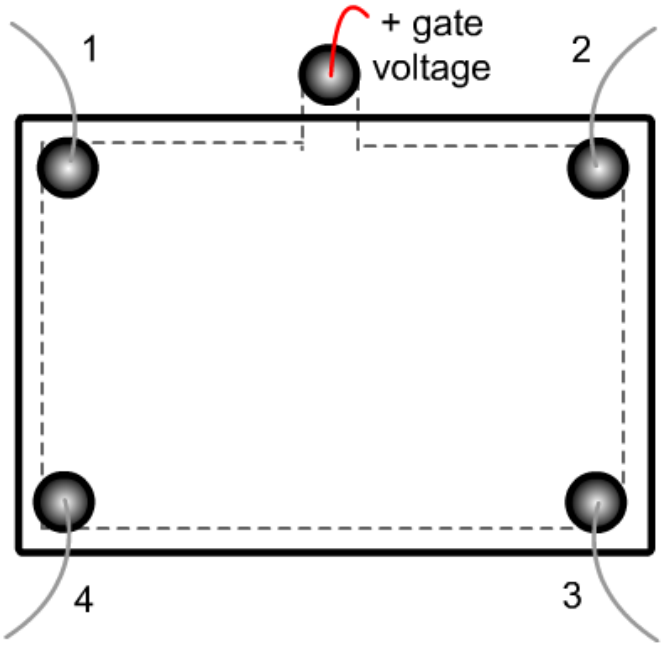

Figure 2.8: Schematic drawing of the contacts for a Hall effect measurement.

The pairs of horizontal (2.2)-(2.3) and vertical (2.4)-(2.5) resistances should not differ more than a few percent if an accurate measurement is to be obtained. The Hall voltage across contacts 4 and 2 (V_{42}) is measured at a constant current between contacts 1 and 3 (I_{13}) while sweeping the magnetic field. The Hall voltage is related to the carrier density n_c by the formula:

$$n_c = \frac{B}{V_{42}} \cdot \frac{I_{13}}{t_{\text{film}} \cdot q_e} \tag{2.6}$$

where the ratio of voltage versus magnetic field (V_{42}/B) is obtained by linear regression in the measurement range, t_{film} is the thickness of the conductive sheet and q_e is the elementary electron charge.

Solving the van der Pauw equation (2.7) for the sheet resistance R_s for each averaged value of the horizontal (R_{hor}) and vertical (R_{ver}) resistance, the Hall mobility can be calculated from (2.8).

$$1 = \exp\left(-\pi R_{\text{hor}}/R_s\right) + \exp\left(-\pi R_{\text{ver}}/R_s\right) \tag{2.7}$$

$$\mu_{\text{Hall}} = \left[q_e n_s R_s\right]^{-1} \tag{2.8}$$

where n_s is the sheet carrier density, equal to $(n_c \cdot t_{\text{film}})$.

Similarly the magnetoresistance (MR) of the sheet resistance can be obtained, by solving the Van der Pauw equation (2.7) for all resistance values versus magnetic field and normalising by the zero field value.

2.4 Characterisation of magnetic properties

Magnetic properties of films are investigated using a vibrating sample magnetometer (VSM) at room temperature. The sample is vibrated at constant frequency in a variable

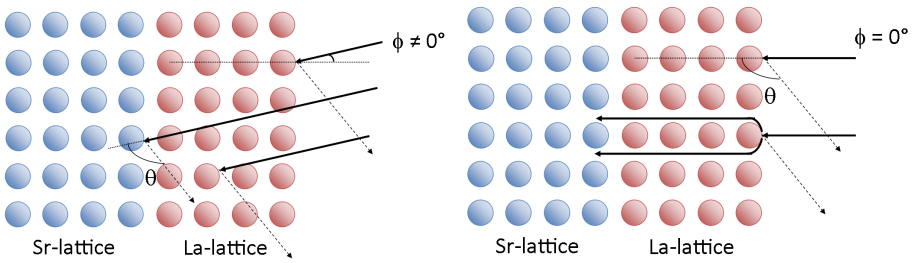

(a) (b)

Figure 2.9: Schematic drawing of the two measurements modes of MEIS applied to an LAO/STO heterostructure: **(a)** random and **(b)** aligned.

(in-plane[3]) magnetic field in between measuring coils; the magnetisation of the sample induces a current in these pick-up coils. This current is measured and converted to a magnetisation value. Prior to each measurement the VSM is calibrated to ensure a correct measurement of the low signal magnetic oxide.

The magnetisation measurement of a thin magnetic film is dominated by a large diamagnetic (e.g. STO) or paramagnetic (e.g. NGO) signal from substrate and (diamagnetic) sample holder. This is corrected for in the experimental data. A least squares line is fitted in the saturation region of the sample since this is purely due to the diamagnetic contribution – the ferromagnetic signal is constant in this magnetic field range. The gradient of this line (averaged between the positive and negative field value) is multiplied by the field and subtracted from the data to give the purely ferromagnetic signal.

Some (ZnO) samples were also tested in a superconducting quantum-interference device (SQUID), which adds an extra order of sensitivity and a wider temperature range (2–300 K). These experiments were carried out by Sean Langridge (Science and Technology Facilities Council, Rutherford Appleton Laboratory, Didcot, UK).

2.5 Medium energy ion spectroscopy (MEIS)

During medium energy ion spectroscopy (MEIS), He-ions are accelerated towards the sample and the yield of the backscattered beam in a certain energy range is monitored, similar to Rutherford Backscattering Spectroscopy (RBS) [30]. The difference between RBS and MEIS is the lower ion acceleration energy in MEIS: 50–250 keV compared to 1–4 MeV in RBS. This implies that inelastic scattering effects can no longer be ignored. As a result, it provides a higher depth resolution (1 nm) while the chemical selectivity is kept even for light scatterers. The technique comes in two modes: one which gives information on scatterers from deep layers ('random' mode) and one which is mainly sensitive to the outmost layer of atoms ('aligned' mode). This technique has been applied to a set of $LaAlO_3$ (LAO)/$SrTiO_3$ (STO) heterostructures. A schematic drawing of the two modes as applied to such an LAO/STO stack is shown in Figure 2.9.

The information obtained from random mode spectra is very similar to RBS: composition, depth and spread of all (heavy) elements in the sample (Figure 2.9a). The penetration depth is in the range of 100-200 nm. Therefore the obtained signal contains information from all elements in the film (e.g. La, Al for $LaAlO_3$) and the substrate (e.g. Sr, Ti for

[3]Due to the thin film geometry, the magnetic properties will be easily accessible in-plane, while the out-of-plane coercivity can exceed several Tesla.

$SrTiO_3$). However, the sensitivity to lighter elements is rather poor. Within the penetration depth, the area of each random peak corresponds to the amount of material in the sample. The slope of the peaks can give indications of the surface (interface) roughness of the films.

In the crystallographically aligned mode the He^+ ions can channel between the lattice (Figure 2.9b). The surface atoms in the sample effectively screen deeper lying atoms, meaning that peaks from the substrate elements (Sr, Ti) are not visible. Due to the effect of screening, aligned peaks are often called surface peaks. This screening depends on various parameters, the crystalline quality of the material being the most important factor. For an ideal crystal lattice, the screening is limited by thermal vibrations. The presence of crystal defects (e.g. vacancies, interstitials) would strongly affect the behaviour of the surface peak. In an intuitive picture, in a perfect lattice, the ions will channel through all the way down and only the top atoms will backscatter, resulting in a lower aligned peak intensity. If the structure becomes more disordered, the peak intensity increases as more He^+ ions are scattered.

Details of the experimental setup for medium energy ion spectroscopy (MEIS) used in this work are described elsewhere [30]. MEIS spectra recordings were performed in two different regimes where incident beam angle was either aligned around 8^o from the crystallographic [001] $LaAlO_3$ direction (random spectra) or parallel to this [001] $LaAlO_3$ direction (aligned spectra). The exact beam angle in the aligned regime was optimised by minimising the bulk signal from the $SrTiO_3$ substrate.

During the MEIS experiments, the sample was mechanically attached to a holder in a vacuum chamber and pumped for several hours to achieve ultra-high vacuum conditions (below 10^{-8} mbar). A highly collimated beam of $^4He^+$ ions with energy of 100 keV and diameter of 1 mm^2 was projected on the surface of the sample. The ion beam has an energy spread of less than 10^{-4} of the ion energy, and the energy instability during the measurement cycle is also about 10^{-4}. The beam angular divergence at the sample surface dropping point is less than 0.05^o. A high-resolution electrostatic semispherical analyser with relative energy resolution of 0.002 was fixed at the backscattering angle of 120^o. The backscattering signal at the detector was calibrated to the bulk signal from the $SrTiO_3$ substrate in random spectra. The accuracy of this calibration procedure is about 5% and allows for quantitative comparison of the experimental data obtained in different measurements, independent of the geometry of the experiment.

MEIS experiments were carried out by Y. Boikov, I. Serenkov and V. Sakharov at the Ioffe Physico-Technical Institute, Russian Academy of Sciences (Saint-Petersburg, Russia), in collaboration with A. S. Kalabukhov, D. Winkler and T. Claeson at the Department of Microtechnology and Nanoscience, Chalmers University of Technology (Göteborg, Sweden).

2.6 X-ray absorption spectroscopy (XAS)

Valence electron states vary strongly between atoms and are strongly affected by the atomic arrangement in solids [31]. The characteristic features of these valence states determine the physical as well as functional properties of solids. The deep lying core electron states of atoms are hardly affected by the bonding with neighbouring species. Therefore spectroscopic analysis with respect to these (reference) core levels can be used to study the valence electron states of a material. The general idea is that a beam of x-rays (or electrons) excites a core electron, after which the valence states are detected using the core electron (or hole) as a probe. Figure 2.10 gives a schematic representation of the

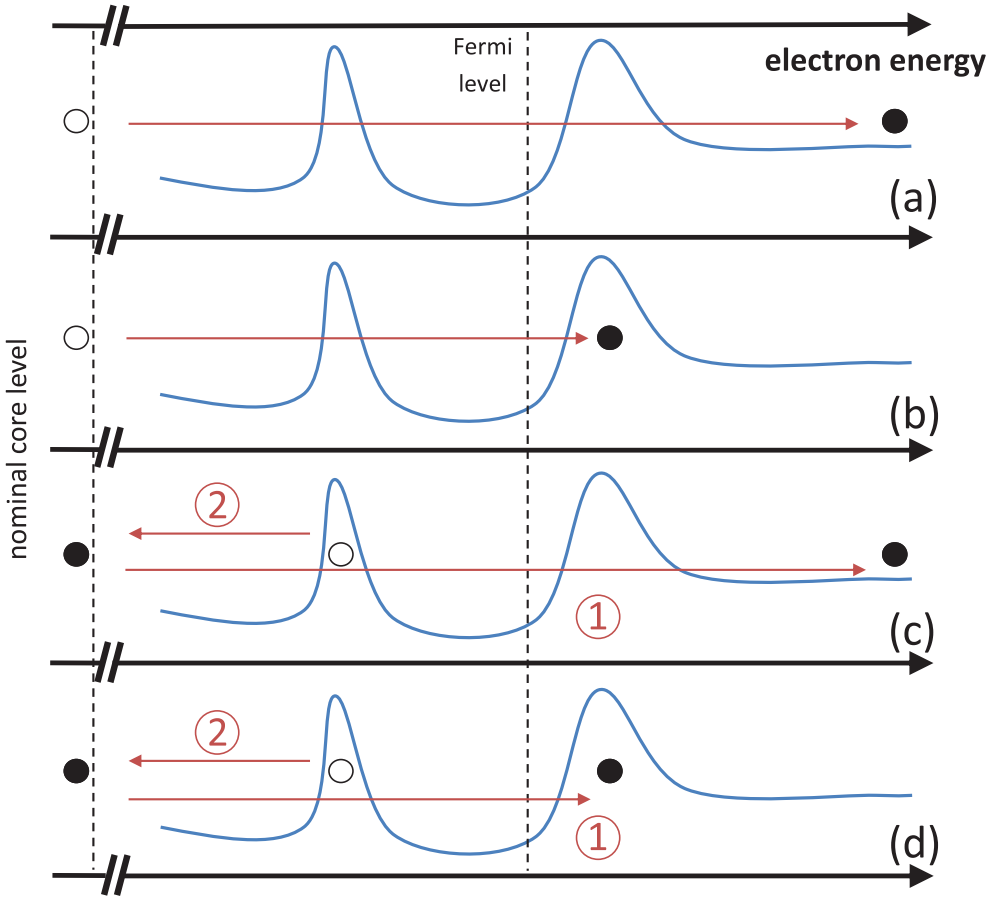

Figure 2.10: Schematic overview of different core level spectroscopy techniques, whereby a core electron is excited to different states and different states are used to detect the transition. The techniques are **(a)**, XPS **(b)**, XAS **(c)** and NXES **(d)** RXES (after [31]).

most important types of core level spectroscopy: x-ray photoelectron spectroscopy (XPS), x-ray absorption spectroscopy (XAS) and x-ray emission spectroscopy (XES) [31]. In all three techniques an x-ray beam excites the core electron, but the final state of the electron and the information obtained vary. Whereas a core electron is excited to the high energy continuum and detected as a photoelectron in XPS, in XAS it is excited to the excitation threshold, i.e. the conduction band of the material. XES involves a second order optical process where the excited state decays radiatively by emitting x-rays. Depending on the final state of the electron, there are two possibilities: an XPS-like ('normal XES', NXES) or XAS-like ('resonant XES', RXES) process. The focus here is on XAS, as it provides a direct measure of the projected partial density of states of the excited states.

The x-ray energy of the incoming beam is varied in a certain range around the known band transition energies of the elements, in order to observe the position and shape of any occurring 'resonances'. In general there are three modes to detect the XAS signal: direct observation of the x-ray beam in transmission, by measuring all current flowing from the sample ('total electron yield', TEY) and by monitoring the fluorescence ('fluorescence yield', FY) [31]. Transmission detection requires a very thin sample (100-200 nm) and is therefore difficult to achieve in general. Since the electrons are excited by the incoming x-rays into the conduction band, the TEY detection allows a measurement proportional to

the empty valence states. This is not an energy selective measurement: electrons generated by the Auger process during the decay of core holes are also included. The probing depth of this measurement is related to the electron escape depth due to solid/electron interactions and is between 3 and 10 nm, making this a surface sensitive measurement. When a (shallow) core electron or valence electron fills the (deep) core hole, the energy difference can be released as photons, i.e. by radiative decay. This gives rise to the FY, whereby the generated photons have a mean free path of the same order of magnitude as the incoming x-rays. The implication is that FY detection is much more bulk sensitive (100-200 nm). In general the shape of TEY and FY XAS spectra will be (slightly) different, because essentially a different set of excited states are probed.

The most important application of XAS is to probe magnetic materials or the behaviour of specific elements inside a material in a magnetic field. In the electric dipole transitions governing XAS, spin flip transitions are forbidden, meaning that spin-up (-down) photoelectrons from the p core shell can only be excited into spin-up (-down) d hole states [32]. So if spin-up (-down) photoelectrons can be preferentially generated in a measurement, the difference in transition intensity between up and down would reflect the difference in up and down holes in the d shell. This can be achieved by using circularly polarised x-rays with positive or negative helicity. This technique is called x-ray magnetic circular dichroism (XMCD) and is an x-ray, element specific equivalent of the optical Kerr-effect.

The so-called XMCD sum rules allow the calculation of the element specific orbital and spin magnetic moment [33, 34]. After their theoretical postulation, they have been experimentally confirmed for Fe and Co [35]. An exemplary analysis of a Co foil is shown in Figure 2.11. The formulas relating the integrated spectra (values p, q and r) with the magnetic moments are:

$$\mu_{\mathrm{L}} = -\frac{4n_h}{3r}q \tag{2.9}$$

$$\mu_{\mathrm{S}} = -\frac{n_h}{r}(6p - 4q) \tag{2.10}$$

where μ_{L} and μ_{S} are the orbital and spin magnetic moment respectively (in μ_{B}/atom) and n_h is the number of holes in the d shell. The values for p, q and r are indicated in Figure 2.11 and are the values of the integral of the XMCD spectrum before (p) and after (q) the L_2-edge and of the integral of the average XAS spectrum after the L_2-edge respectively. The XMCD intensity needs to corrected for the angle of incidence and the degree of circular polarisation, which practically means it needs to be divided by $\cos(\phi)$ and by the polarised fraction.

In order to integrate the average XAS spectrum, a background needs to be fitted and subtracted, which takes the following general form:

$$I = \frac{2A}{\pi}\arctan(x - x_{L3}) + \frac{A}{\pi}\arctan(x - x_{L2}) + C \tag{2.11}$$

where A and C are constants to fit the curve and x_{L3} and x_{L2} indicate the energies at which the L_3 and L_2 peaks occur in the spectrum.

This sum rule analysis has of course its limitations [32, 33]. It is only valid for $2p$ to $3d$ transitions in transition metals, assuming that the magnetisation and x-ray polarisation are known and constant over time and energy range. Detection should be by TEY, where the detection effectiveness should be the same for spin-up and -down. FY detection creates angular and energy dependent distortions, complicating the analysis. Furthermore the

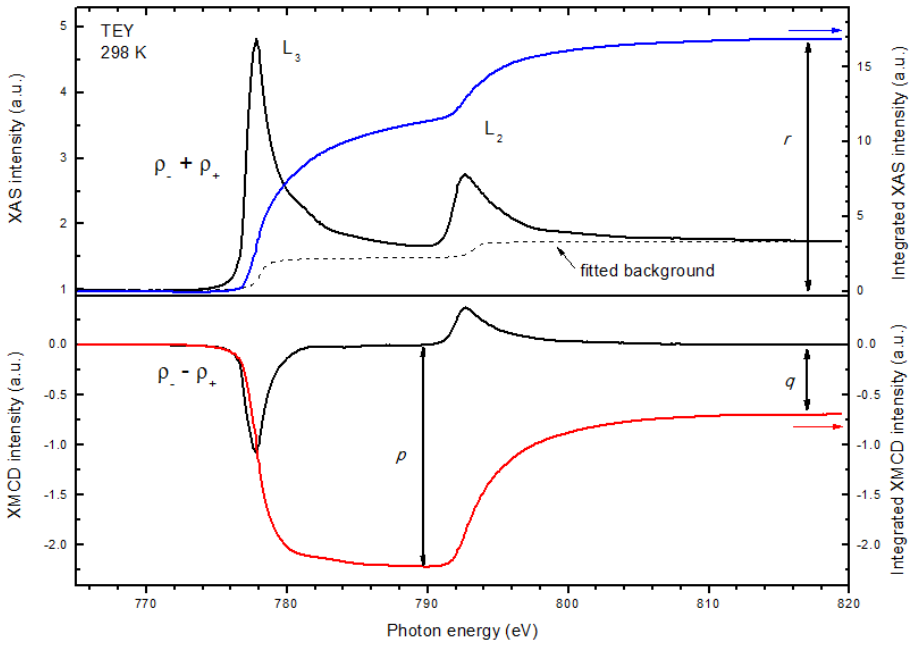

Figure 2.11: Average XAS intensity and the XMCD signal with their respective integrations for a Co calibration sample at room temperature and perpendicular photon incidence. Data were recorded in TEY. The values p, q and r required for sum rule analysis are indicated.

number of holes in the $3d$ band is not always known and is usually obtained from theoretical fits.

XAS and XMCD measurements were performed on beamline I06 at Diamond Light Source using the UHV compatible three-dimensional-vector superconducting high-field magnet (Scientific Magnetics) with fields up to 6 T and a temperature range between 2 and 370 K. Data were collected in TEY and FY mode at various temperatures and in-plane magnetic fields. Element specific hysteresis loops are obtained by normalising the signal at the L_3 peak maximum with the background signal at the pre-edge region. This work was done in collaboration with S. S. Dhesi and G. van der Laan from Diamond Light Source (Didcot, UK).

Bibliography

[1] Douglas B. Chrisey and Graham K. Hubler, editors. *Pulsed laser deposition of thin films*. John Wiley & Sons, 1994.

[2] Klaus Ellmer and Andreas Klein, editors. *Transparent conductive zinx oxide*. Springer, 2008.

[3] T. J. Jackson and S. B. Palmer. Oxide superconductor and magnetic metal thin film deposition by pulsed laser ablation: a review. *Journal of Physics D: Applied Physics*, 27:1581–1594, 1994.

[4] Jagadisch Chennupati and Stephen J. Pearton, editors. *Zinc oxide: bulk, thin films and nanostructures*. Elsevier, 2006.

[5] C. Aruta, S. Amoruso, R. Bruzzese, X. Wang, D. Maccariello, F. Miletto Granozio, and U. Scotti di Uccio. Pulsed laser deposition of $SrTiO_3/LaGaO_3$ and $SrTiO_3/LaAlO_3$: plasma plume effects. *Applied Physics Letters*, 97:252105, 2010.

[6] M. Esposito, M. Bator, M. Döbeli, T. Lippert, C. W. Schneider, and A. Wokaun. Negative ions: the overlooked species in thin film growth by pulsed laser deposition. *Applied Physics Letters*, 99:191501, 2011.

[7] H. J. T. Ellingham. Reducibility of oxides and sulphides in metallurgical processes. *Journal of the Society of the Chemical Industry*, 63:125–133, 1944.

[8] Franklin J. Wong, Seung-Hyub Baek, Rajesh V. Chopdekar, Virat V. Mehta, Ho-Won Jang, Chang-Beom Eom, and Yuri Suzuki. Metallicity in $LaTiO_3$ thin films induced by lattice deformation. *Physical Review B*, 81:161101, 2010.

[9] R. Ohtsuka, M. Matvejeff, K. Nishio, R. Takahashi, and M. Lippmaa. Transport properties of $LaTiO_3/SrTiO_3$ heterostructures. *Applied Physics Letters*, 96:192111, 2010.

[10] M. D. Biegalski, K. Dörr, D. H. Kim, and H. M. Christen. Applying uniform reversible strain to epitaxial oxide films. *Applied Physics Letters*, 96:151905, 2010.

[11] E. Weal, S. Patnaik, Z. Bi, H. Wang, T. Fix, A. Kursumovic, and J. L. MacManus-Driscoll. Coexistence of strong ferromagnetism and polar switching at room temperature in Fe_3O_4-$BiFeO_3$ nanocomposite thin films. *Applied Physics Letters*, 97:153121, 2010.

[12] Gyula Eres, J. Z. Tischler, C. M. Rouleau, P. Zschack, H. M. Christen, and B. C. Larson. Quantitative determination of energy enhanced interlayer transport in pulsed laser deposition of $SrTiO_3$. *Physical Review B*, 84:195467, 2011.

[13] R. E. Treece, J. S. Horwitz, D. B. Chrisey, E. P. Donovan, and S. B. Qadri. Pulsed laser ablation synthesis of NbN_x ($0 \leq x \leq 1.3$ thin films. *Chemistry of Materials*, 6(12): 2205–2207, 1994.

[14] A. Heinrich, C. Leirer, and B. Stritzker. Pulsed laser deposition of MgB_2-films with high critical temperatures. *Superconductor Science and Technology*, 18:1215–1217, 2005.

[15] Vijay Rawat and Timothy Sands. Growth of TiN/GaN metal/semiconductor multilayers by reactive pulsed laser deposition. *Journal of Applied Physics*, 100:064901, 2006.

[16] Yong-Tae Shin, Seung-Woo Shin, Jeongmi Shin, Kwanghee Lee, and Myoungsik Cha. Pulsed laser deposition of a thin conjugated-polymer film. *Thin Solid Films*, 360(1-2): 13–16, 2000.

[17] G. Keckskemeti, T. Smausz, N. Kresz, Zs. Toth, B. Hopp, D. Chrisey, and O. Berkesi. Pulsed laser deposition of polyhydroxybutyrate biodegradable polymer thin films using arf excimer laser. *Applied Surface Science*, 253:1185–1189, 2006.

[18] M. Dussauze, A. Giannoudakos, L. Velli, C. P. E. Varsamis, M. Kompitsas, and E. I. Kamitsos. Structure and optical properties of amorphous lead-germanate films developed by pulsed-laser deposition. *Journal of Chemical Physics*, 127:034704, 2007.

[19] Z. W. Liu and C. K. Ong. Synthesis and size control of ZnO nanorods by convenctional pulsed laser deposition without catalyst. *Materials Letters*, 61(16):3329–3333, 2007.

[20] Wolfgang Braun. *Applied RHEED: reflection high-energy electron diffraction during crystal growth.* Springer, 1999.

[21] Ayahiko Ichimiya and Philip I. Cohen. *Reflection High Energy Electron Diffraction.* Cambridge University Press, 2004.

[22] J. W. Hartman, R. T. Brewer, and Harry A. Atwater. Reflection high-energy electron diffraction analysis of polycrystalline films with grain size and orientation distributions. *Journal of Applied Physics*, 92(9):5133–5139, 2002.

[23] J. M. Van Hove, C. S. Lent, P. R. Pukite, and P. I. Cohen. Damped oscillations in reflection high energy electron diffraction during GaAs MBE. *Journal of Vacuum Science & Technology*, 1:741–746, 1983.

[24] M. D. Johnson, J. Sudijono, A. W. Hunt, and B. G. Orr. The dynamical transition to step-flow growth during molecular beam epitaxy of GaAs (001). *Surface Science*, 298:392–398, 1993.

[25] Andrzej Daniluk. Kinematical calculations of RHEED intensity oscillations during the growth of thin epitaxial films. *Computer Physics Communications*, 170:265–286, 2005.

[26] P. Colombi, D. K. Agnihotri, E. Asadchikov, E. Bontempi, D. K. Bowen, C. H. Chang, L. E. Depero, M. Farnworth, T. Fujimoto, A. Gibaud, M. Jergel, M. Krumrey, T. A. Lafford, A. Lamperti, T. Ma, R. J. Matyi, M. Meduna, S. Milita, K. Sakurai, L. Shabel'nikov, A. Ulyanenkov, A. Van der Lee, and C. Wiemer. Reproducibility in X-ray reflectometry: results from the first world-wide round-robin experiment. *Journal of Applied Crystallography*, 41:143–152, 2008.

[27] Richard H. Bube. *Photoelectronic properties of semiconductors*. Cambridge University Press, 1992.

[28] I. Horcas, R. Fernandez, J. M. Gomez-Rodriguez, J. Colchero, J. Gomez-Herrero, and A. M. Baro. WSXM: A software for scanning probe microscopy and a tool for nanotechnology. *Review of Scientific Instruments*, 78:013705, 2007.

[29] L. J. van der Pauw. A method of measuring specific resistivity and Hall effect of discs of arbitrary shape. *Philips Research Reports*, 13(1):1–9, 1958.

[30] V. V. Afrosimov, R. N. Il'in, V. I. Sakharov, and I. T. Serenkov. Diagnostics of films and layers of nanometer thickness using middle energy ion scattering technique. *Semiconductors*, 41(4):487–490, 2007.

[31] Frank de Groot and Akio Kotani. *Core level spectroscopy of solids*. CRC Press, 2008.

[32] J. Stöhr and R. Nakajima. Magnetic properties of transition-metal multilayers with x-ray magnetic circular dichroism spectroscopy. *IBM Journal of Research and Development*, 42(1):73–88, 1998.

[33] Gert van der Laan and B. T. Thole. Strong magnetic x-ray dichroism in $2p$ absorption spectra of $3d$ transition-metal ions. *Physical Review B*, 43(6):13401, 1991.

[34] B. T. Thole, Paolo Carra, F. Sette, and Gerrit van der Laan. X-ray circular dichroism as a probe for obital magnetization. *Physical Review Letters*, 68(12):1943–1946, 1992.

[35] C. T. Chen, Y. U. Idzerda, H.-J. Lin, N. V. Smith, G. Meigs, E. Chaban, G. H. Ho, E. Pellegrin, and F. Sette. Experimental confirmation of the x-ray magnetic circular dichroism sum rules for iron and cobalt. *Physical Review Letters*, 75(1):152–155, 1995.

Part I

Intrinsic defects & magnetism in ZnO

Chapter 3

A brief history of dilute magnetic ZnO

This chapter provides some background on the on-going quest for a room temperature dilute magnetic semiconducting oxide and ZnO in particular, including early attempts and recent realisations, which immediately highlight the importance of intrinsic defects on the properties of ZnO.

3.1 Why zinc oxide?

Zinc oxide (ZnO) is commonly considered a promising semiconductor, owing to its unique combination of properties. The review of Ozgür et al. [1] and the books by Chennupati and Pearton [2] and Ellmer and Klein [3] provide an excellent overview of the established and cutting edge technology. The most prominent electronic property is a direct bandgap of 3.37 eV, making ZnO a transparent material that can be used to obtain optical devices in the blue and UV wavelength range.

ZnO is comparable to another promising and broadly studied semiconductor, gallium nitride (GaN), but has several advantages over this material [2]. Processing wise, ZnO can be grown in single crystal substrates (just like Si) and flexibly etched by many wet chemical solutions. Improved radiation hardness and biocompatibility open a broad range of applications for zinc oxide, from devices for outer space to implantable electronics.

The crystal structure of ZnO is normally a hexagonal wurtzite structure ($a = 0.32495$ nm; $c = 0.50269$ nm; $\rho = 5.605$ g/cm^3), but can also transform into a zinc blende type (on cubic substrates) or rocksalt (NaCl) type (high pressure metastable phase) [2]. In the hexagonal structure, each Zn ion is surrounded by a tetrahedron of oxygen ions (and vice versa). Even though the zinc-oxygen bond is on the borderline between an ionic and covalent bond, the polarity created along the c-axis by the lack of inversion symmetry in the hexagon is sufficient to create spontaneous polarisation and piezoelectricity in the material. This makes ZnO a transparent piezoelectric semiconductor.

Typical applications for ZnO include pigments (as white powder), transparent electrodes in combination with organic solar cells, polycrystalline varistors (voltage dependent resistors, [e.g. 4]), piezoelectric devices [e.g. 5], phosphors and transparent oxide thin film transistors (TFT).

3.2 Conductivity in ZnO

Single crystalline zinc oxide is intrinsically an n-type semiconductor, with carrier concentrations in the range of 10^{16}–10^{18} cm^{-3} and electron mobilities[1] at room temperature around 100–200 cm^2 V^{-1} s^{-1} [1–3]. These properties (and others) can be greatly varied by doping with various elements. The intrinsic n-type conductivity of ZnO is due to the presence of electron-donating oxygen vacancies and zinc interstitials [6]. According to Zhang et al. [7] oxygen interstitials and zinc vacancies would result in intrinsic p-type doping. This however does not occur since the compensating n-type defects form easily. Work by McCluskey and Jokela [8] argues however that the aforementioned defects can not explain the n-type conductivity, which should be ascribed largely to the presence of H-donors instead.

In addition to the intrinsic defects, extrinsic electron doping in ZnO can be achieved in 3 different ways, by adding either group I, III (on Zn positions) or VII (on O positions) elements [2, 3]. Gallium but especially aluminium, both on the Zn-site, are applied for this purpose. The halogenides (on an O-site) are not popular due to the difficulty of implanting them into ZnO and the risk of evaporation during annealing treatments. Alkali metals such as Li, Na and K would be suitable, but difficult to force into a substitutional Zn position. If interstitial, these elements form mid-gap states rendering the doped ZnO insulating by compensating (intrinsic) n-type dopants . Hydrogen is frequently unintendedly present, forming shallow donor states, especially in the near-surface region. Carrier densities of intentionally doped ZnO can be as high as 10^{20} cm^{-3}.

Addition of group V elements (N, P, As and Sb) theoretically results in hole doping of ZnO. The most popular element to implant is N, followed by As [e.g. 9, 10]. Practically it is very difficult to obtain stable and true p-type ZnO. Authors report on decaying [3] or even completely absent [11] p-type conductivity under standard conditions. Several hypotheses have been formulated to explain this unusual behaviour. The commonly accepted theory is that the elements assume undesired (non-substitutional) positions or form complexes, resulting in self-compensation of the p-type conductivity [12]. Other theories include lattice relaxation effects or low solubility of the target dopant in the matrix, as mentioned by Claflin et al. [11].

Recently several authors have successfully obtained stable p-type ZnO by codoping, i.e. adding an n- and p-type dopant to the ZnO. For example Tang et al. [13] adds 0.4 at% Al as well as N, creating p-type material, whereas adding 1 at% Al would make it n-type. It is believed that the addition of Al stabilises or at least eases the formation of ionised N acceptor levels.

3.3 Magnetism & ZnO

In 2000, Dietl et al. [14] published a paper in which they propose a theoretical model that predicts room temperature ferromagnetism in transition metal doped ZnO. This started a whole new trend in the scientific community, with numerous papers published on the subject e.g. [15, and references therein]. The interest for such a 'ferromagnetic semiconductor' is in the combination of those two interesting properties (which might be interrelated, see e.g. [16]), as well as allowing a new range of devices on the same substrate [2]. Potential devices include spin-FETS [17, 18], which theoretically allow switching operations with a lower power consumption.

[1]The carrier mobility is a measure of the efficiency at which charge carriers are transferred from one contact to another through a channel of material [2].

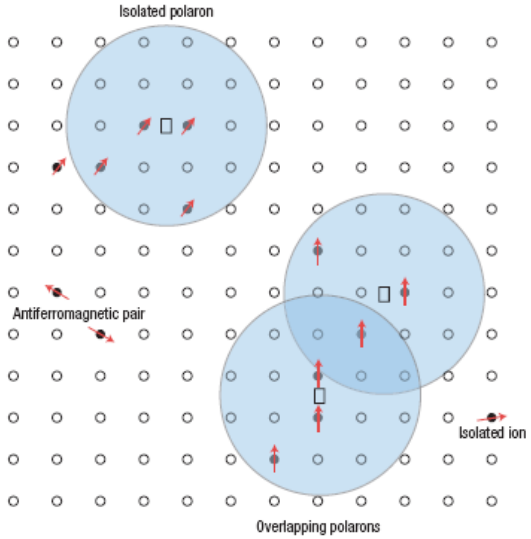

Figure 3.1: Schematic representation of bound magnetic polarons. Cation sites are represented by small circles. Oxygen is not shown; the unoccupied oxygen sites are represented by squares. [from 24]

Dilute magnetic semiconductors with spin polarised carriers, abbreviated DMS, have been around for longer: Mn:GaAs is a 'true' and well-studied system, which however has a Curie temperature of only 160–170 K, making it useless for practical devices. Hence the great interest in the predicted room temperature ferromagnetism of doped ZnO.

Intuitively it can be understood that introducing transition metal or rare earth ions in a host lattice will result in partially filled d or f electron shells with unpaired electrons, which may couple (anti)ferromagnetically. To date there is no conclusive theory to explain all behaviour, but most authors agree that the initial model by Dietl et al. [14] is far too simplified [19–21]. Essentially Dietl's model is an extrapolation from the Mn:GaAs system, where magnetism is induced and mediated by carriers (electron) that are abundantly present. This implies that ZnO doped with 5 at% Mn is only ferromagnetic above room temperature in case of heavy p-type doping (i.e. $3.5 \cdot 10^{20}$ holes/cm^3), which is practically impossible to achieve experimentally.

Yet ferromagnetism is observed in certain systems. This led Kaminski and Das Sarma [22] to formulate a theory based on a different mechanism, namely that of a 'bound magnetic polaron' (BMP), inspired by the antiferromagnetic polaron of Kasuya [23]. In this model the magnetic dopant is assumed to be coupled with defects (such as oxygen vacancies) in the ZnO matrix, mediating ferromagnetism by overlapping of these polarons. This is schematically shown in figure 3.1. The BMP theory can be further refined with a spin-split donor impurity band [24]. Coey and Chambers [20] even proposed a purely defect related mechanism, which was expanded later to provide an explanation for what is now called 'd^0 ferromagnetism' [25]. As a further refinement, Coey et al. [25] propose a model, based on measurements of Fe:TiO_2, in which the transition metal dopants act as a charge reservoir for a spin split impurity band, which is related to intrinsic defects in the oxide.

Hite et al. [26] study similar DMS, namely Gd:GaN and Cr:GaN under proton irradiation. Such irradiation creates more (structural) defects in the structure, but in this case they seem to degrade rather than enhance ferromagnetism. This indicates that a certain type of defect is important for magnetism, not just 'crystal defects' in general. Referring

back to ZnO, different defects have been identified by different authors: oxygen vacancies [27–30], zinc interstitials [31, 32] as well as zinc vacancies [32–41]. Usually these results have been obtained by controlled atmosphere annealing.

Xu et al. [42] even claim ferromagnetism in undoped ZnO, i.e. purely based on the presence of defects, something that has been shown in HfO_2 as well [43]. Coey [44] emphasises that the magnetism is most likely related to the dominance of interfaces (and related defects) in thin films, implying that it is not a bulk effect. Hence measurements on bulk single crystal yield extremely low ferromagnetic signals [45]. The work by Straumal et al. [46] marks the importance of the interfaces, more specifically the grain boundaries. They have discovered that there is a critical grain boundary to volume ratio beyond which ferromagnetism occurs, both in doped (Co or Mn) as well as undoped ZnO [46–48]. These intergrain regions are known to be defect-tolerant, so this does not conflict with the purely defect-based model by Coey and Chambers [20], although in terms of the model in [25] it is unclear where the charge reservoirs are in the absence of dopants. Other defect states might perhaps act as such for the spin split impurity band-causing defects.

Although many papers on ZnO-based DMS have been published, results greatly vary and reproducibility is generally below 10% [2]. Transition metal (TM) dopants investigated include Sc, Ti, V, Cr, Mn, Fe, Co, Ni and Cu [2, 15], but also rare earths such as Nd and Gd [49]. The latter elements in concentrations of 1 at% seem to result in ferromagnetism, although only up to 150 K. From the group of $3d$ elements, most authors have experimented with Mn (since this was originally described by Dietl et al. [14]), but a great deal of work has been performed on Co-doped ZnO. Most authors report no magnetism for Sc, Ti, V, Cr and Fe doped samples, although once again results vary among authors [2, 3, 15]. Nickel and copper doping seem to result in ferromagnetism [2, 50], although Snure et al. [51] are noticing a low solid solubility of Ni in the ZnO matrix, producing Ni clusters. These Ni clusters result in a ferromagnetic signal, but from an extrinsic source rather than the desired intrinsic one. In any case the ferromagnetic signal is low and usually expressed in Bohr magnetons (μ_B) per dopant atom; typical values are on the order of 0.5 μ_B/TM, but generally much lower, although highs of 3–5 μ_B/TM are reported [15]. Of course if the magnetic moment is originating from defects rather than dopant atoms, describing the moment per dopant atom is meaningless.

In the previous paragraph the issue of phase purity was brought up: since most thin films are probed for their (bulk) magnetical properties by VSM or SQUID measurements to prove their DMS behaviour, any phase that creates such a signal will bias the measurement and possibly lead to false conclusions. Great care must therefore be taken when handling these samples to avoid any ferromagnetic contamination [52]. Characterisation of the thin films by various methods is therefore of utmost importance to eliminate the possibility of a second phase [15]. A good mixture would consist of: x-ray diffraction (XRD), transmission electron microscopy (TEM) and x-ray magnetic circular dichroism (XMCD). X-ray photoelectron spectroscopy (XPS) is a good addition to confirm that the transition metals are substitutionally positioned in the ZnO, although no guarantee if they have the same oxidation state in the magnetic secondary phase. The anomalous Hall effect (AHE), a magnetisation loop-like feature in the Hall voltage, is sometimes claimed to be proof of intrinsic ferromagnetism, although Snure et al. [51] obtain such AHE effect in their extrinsic films.

If the ferromagnetism is to be ascribed to the transition metal dopants, sound evidence for this hypothesis is required. Farley et al. [53] suggest the following criteria: (i) high saturation magnetization close to the expected spin moment, (ii) detailed structural characterization confirming that the dopants are uniformly incorporated; (iii) clear

demonstration of a relationship between the dopant concentration and Curie temperature; (iv) use of an element specific magnetometry technique (such as XMCD) to probe specifically the magnetic polarization of the dopant atoms. Except perhaps for Mn:GaAs, the combination of these criteria has not yet been proven for any DMS (ZnO-based or otherwise).

The possible presence of a secondary phase complicates the interpretation of results, especially for Co:ZnO samples where phases such as metallic Co as well as some Co-oxides are ferromagnetic (or structurally induced ferromagnetic). Probably most of the reported magnetism in Co:ZnO and certainly in early reports and/or with high Co concentrations ([e.g. 54]) is due to Co clusters in the sample, even if they claim it is not: only limited characterisation was carried out and seldomly XMCD. Park et al. [55] clearly demonstrate the presence of Co clusters as the source of magnetism in their films. Also Ivill et al. [28] notice precipitation of Co and CoO in their films under certain growth conditions. Recent reports indicate Co clusters (usually in the region near the substrate) as the source of most magnetic signals observed, as evidenced by XPS [56] and cathodeluminescence [57] or a combination of techniques [58].

Even though no known Mn-based metal or oxide phases (that can form in the ZnO host) are ferromagnetic, Kundaliya et al. [59] claim that ferromagnetism in Mn:ZnO occurs because of a metastable phase, namely an oxygen vacancy stabilised Zn-substituted Mn-oxide with the formula $Mn_{(2-x)}Zn_xO_{(3-\delta)}$. So far these authors were the only ones to report on this secondary phase. Other authors find either quite well reproducible ferromagnetism [60–63] or no traces of it at all [64–66].

Behan et al. [67] report on carrier density dependent magnetism in their Co:ZnO and Mn:ZnO films, namely that these are only magnetic in the insulating and conducting (by Al codoping) regime. This effect of codoping Co:ZnO with Al is confirmed by Liu et al. [68]. However Kaspar et al. [69] are unable to reproduce such carrier density dependent results as they find negligible room temperature ferromagnetism in all their Co:ZnO films. Codoping of Co:ZnO and Mn:ZnO films with similar co-dopants seems to result in opposing magnetic effects in these materials [70]: whereas n-type dopants tend to increase ferromagnetism in Co:ZnO films, they decrease it in Mn:ZnO. The opposite effect happens for p-type dopants. This might point towards different mechanisms in these two, at first sight similar, DMS. However on a closer look at the original paper, Kittilstved et al. [70] claim that surface N-doped ZnO films are p-type (which might be the case, see section 3.2) and 'surface O-doped' films n-type by changing the outer layer capping agent in their sol-gel procedure. It is however known that adsorbed oxygen on ZnO films tends to decrease conductivity by trapping electrons, therefore acting as acceptor states [71, 72]. The observed effect is probably related to an intrinsic defect balance and the (de)stabilisation of them, rather than n or p type conductivity (all films are probably n-type conductive due to compensating defects).

Codoping of Co- or Mn-doped ZnO has attracted attention in the light of stabilising oxygen vacancies (or other defects), similar to the effect for p-type doping (section 3.2). Common codoping is performed with Al [61] or Ga [73] as mentioned before, but theoretical calculations for non-transition metal dopants show promising results. Yadav et al. [74] predict that in Mn:ZnO co-doped with C atoms at O sites (hole dopant), the ferromagnetic state becomes stabilised via a hole mediated double exchange mechanism. According to calculations [40, 75, 76] only carbon doping should even be sufficient to create ferromagnetic ZnO, which was experimentally proven by Zhou et al. [77].

Bibliography

[1] U. Ozgür, Ya. I. Alivov, C. Liu, A. Teke, M. A. Reshchikov, S. Dogan, V. Avrutin, S.-J. Cho, and H. Morkoc. A comprehensive review of ZnO materials and devices. *Applied Physics Reviews*, 98:041301, 2005.

[2] Jagadisch Chennupati and Stephen J. Pearton, editors. *Zinc oxide: bulk, thin films and nanostructures*. Elsevier, 2006.

[3] Klaus Ellmer and Andreas Klein, editors. *Transparent conductive zinx oxide*. Springer, 2008.

[4] G. D. Mahan. Intrinsic defects in ZnO varistors. *Journal of Applied Physics*, 54(7): 3825–3832, 1983.

[5] Zhong Lin Wang and Jinhui Song. Piezoelectric nanogenerators based on zinc oxide nanowire arrays. *Science*, 14:242–246, 2006.

[6] Yong-Sung Kim and C. H. Park. Rich variety of defects in ZnO via an attractive interaction between O vacancies and Zn interstitials: origin of *n*-type doping. *Physical Review Letters*, 102:086403, 2009.

[7] S. B. Zhang, S.-H. Wei, and Alex Zunger. Intrinsic n-type versus p-type doping asymmetry and the defect physics of ZnO. *Physical Review B*, 63:075205, 2001.

[8] M. D. McCluskey and S. J. Jokela. Defects in ZnO. *Journal of Applied Physics*, 106: 071101, 2009.

[9] Y. R. Ryu, T. S. Lee, J. A. Lubguban, H. W. White, Y. S. Park, and C. J. Youn. ZnO devices: photodiodes and p-type field-effect transistors. *Applied Physics Letters*, 87:153504, 2005.

[10] Sejoon Lee, Yoon Shon, and Deuk Young Kim. Temperature-dependent photoluminescence study of As-doped p-type $(Zn_{0.93}Mn_{0.07})O$ layer. *Thin Solid Films*, 516: 4889–4893, 2008.

[11] B. Claflin, Look D. C., S. J. Park, and G. Cantwell. Persistent n-type photoconductivity in p-type ZnO. *Journal of Crystal Growth*, 287:16–22, 2006.

[12] C. H. Park, S. B. Zhang, and Su-Huai Wei. Origin of p-type doping difficulty in ZnO: the impurity perspective. *Physical Review B*, 66:073202, 2002.

[13] Haiping Tang, Zhizhen Ye, and Haiping He. Comparative photoluminescence study on p-type and n-type ZnO films codoped by nitrogen and aluminium. *Optical Materials*, 30:1422–1426, 2008.

[14] T. Dietl, H. Ohno, F. Matsukura, J. Cibert, and D. Ferrand. Zener model description of ferromagnetism in zinc-blende magnetic semiconductors. *Science*, 287:1019, 2000.

[15] F. Pan, C. Song, X. J. Liu, Y. C. Yang, and F. Zeng. Ferromagnetism and possible application in spintronics of transition-metal-doped ZnO films. *Materials Science and Engineering R*, 62:1–35, 2008.

[16] Hideo Ohno. A window on the future of spintronics. *Nature Materials*, 9:952–954, 2010.

[17] Supriyo Datta and Biswajit Das. Electronic analog of the electrooptic modulator. *Applied Physics Letters*, 56:665, 1990.

[18] Hyun Cheol Koo, Jae Hyun Kwon, Jonghwa Eom, Joonyeon Chang, Suk Hee Han, and Mark Johnson. Control of spin precession in a spin-injected field effect transistor. *Science*, 325:1515–1518, 2009.

[19] Rebecca Janisch, Priya Gopal, and Nicola A. Spaldin. Transition metal-doped TiO_2 and ZnO – present status of the field. *Journal of Physics: Condensed Matter*, 17: R657–R689, 2005.

[20] J. M. D. Coey and S. A. Chambers. Oxide dilute magnetic semiconductors – fact or fiction? *MRS Bulletin*, 33:1053–1058, 2008.

[21] B. W. Wessels. Ferromagnetic semiconductors and the role of disorder. *New Journal of Physics*, 10:055008, 2008.

[22] A. Kaminski and S. Das Sarma. Polaron percolation in diluted magnetic semiconductors. *Physical Review Letters*, 88:247202, 2002.

[23] T. Kasuya. Mobility of the antiferromagnetic large polaron. *Solid State Communications*, 8:1635–1638, 1970.

[24] J. M. D. Coey, M. Venkatesan, and C. B. Fitzgerald. Donor impurity band exchange in dilute ferromagnetic oxides. *Nature Materials*, 4:173–179, 2005.

[25] J. M. D. Coey, P. Stamenov, R. D. Gunning, M. Venkatesan, and K. Paul. Ferromagnetism in defect-ridden oxides and related materials. *New Journal of Physics*, 12: 053025, 2010.

[26] J. K. Hite, K. K. Allums, G. T. Thaler, C. R. Abernathy, S. J. Pearton, R. M. Frazier, R. Dwivedi, R. Wilkins, and J. M. Zavada. Effects of proton irradiation on the magnetic properties of GaGdN and GaCrN. *New Journal of Physics*, 10:055005, 2008.

[27] H. S. Hsu, J. C. A. Huang, Y. H. Huang, Y. F. Liao, M. Z. Lin, C. H. Lee, J. F. Lee, L. Y. Chen, S. F.and Lai, and C. P. Liu. Evidence of oxygen vacancy enhanced room-temperature ferromagnetism in Co-doped ZnO. *Applied Physics Letters*, 88: 242507, 2006.

[28] M. Ivill, S. J. Pearton, S. Rawal, L. Leu, P. Sadik, R. Das, A. F. Hebard, M. Chisholm, J. D. Budai, and D. P. Norton. Structure and magnetism of cobalt-doped ZnO thin films. *New Journal of Physics*, 10:065002, 2008.

[29] Wensheng Yan, Qinghua Jiang, Zhihu Sun, Tao Yao, Fengchun Hu, and Shiqiang Wei. Determination of the role of O vacancy in Co:ZnO magnetic film. *Journal of Applied Physics*, 108:013901, 2010.

[30] Peng Zhan, Weipeng Wang, Can Liu, Yang Hu, Zhengcao Li, Zhengjun Zhang, Peng Zhang, Baoyi Wang, and Xingzhong Cao. Oxygen vacancy-induced ferromagnetism in un-doped ZnO thin films. *Journal of Applied Physics*, 111:033501, 2012.

[31] Judith L. MacManus-Driscoll, Neeraj Khare, Yinglin Liu, and Mary E. Vickers. Structural evidence for Zn interstitials in ferromagnetic $Zn_{1-x}Co_xO$ films. *Advanced Materials*, 19:2925–2929, 2007.

[32] X. Zhang, Y. H. Cheng, Y. Li, Hui Liu, X. Zuo, G. H. Wen, L. Li, R. K. Zheng, and S. P. Ringer. Evidence for high-T_c ferromagnetism in $Zn_x(ZnO)_{1-x}$ granular films mediated by native point defects. *Physical Review B*, 80:174427, 2009.

[33] M. Khalid, M. Ziese, A. Setzer, P. Esquinazi, M. Lorenz, H. Hochmuth, M. Grundmann, D. Spemann, T. Butz, G. Brauer, W. Anwand, G. Fischer, W. Adaegbo, W. Hergert, and A. Ernst. Defect-induced magnetic order in pure ZnO films. *Physical Review B*, 80:035331, 2009.

[34] Yong Jiang, Wensheng Yan, Zhihu Sun, Qinghua Liu, Zhiyun Pan, Tao Yao, Yuanyuan Li, Zemin Qi, Guobin Zhang, Pengshou Xu, Ziyu Wu, and Shiqiang Wei. Experimental and theoretical investigations on ferromagnetic nature of Mn-doped dilute magnetic semiconductors. *Journal of Physics: Conference Series*, 190:012100, 2009. 14th International Conference on X-Ray Absorption Fine Structure (XAFS14).

[35] Yongfeng Li, Rui Deng, Bin Yao, Guozhong Xing, Dandan Wang, and Tom Wu. Tuning ferromagnetism in $Mg_xZn_{1-x}O$ thin films by band gap and defect engineering. *Applied Physics Letters*, 97:102506, 2010.

[36] J. B. Yi, C. C. Lim, G. Z. Xing, H. M. Fan, L. H. Van, S. L. Huang, K. S. Yang, X. L. Huang, X. B. Qin, B. Y. Wang, T. Wu, L. Wang, H. T. Zhang, X. Y. Gao, T. Liu, A. T. S. Wee, Y. P. Feng, and J. Ding. Ferromagnetism in dilute magnetic semiconductors through defect engineering: Li-doped ZnO. *Physical Review Letters*, 104:137201, 2010.

[37] Aurab Chakrabarty and Charles H. Patterson. Defect-trapped electrons and ferromagnetic exchange in ZnO. *Physical Review B*, 84:054441, 2011.

[38] J. Haug, A. Chassé, M. Dubiel, Ch. Eisenschmidt, M. Khalid, and P. Esquinazi. Characterization of lattice defects by x-ray absorption spectroscopy at the Zn K-edge in ferromagnetic, pure ZnO films. *Journal of Applied Physics*, 110:063507, 2011.

[39] B. Y. Zhang, B. Yao, Y. F. Li, A. M. Liu, and Z. Z. Zhang. Evidence of cation vacancy induced room temperature ferromagnetism in Li-N codoped ZnO thin films. *Applied Physics Letters*, 99:182503, 2011.

[40] W. Q. Li, J. X. Cao, J. W. Ding, and Xuedong Hu. Modulating magnetism of ZnO:C with vacancy and substitution. *Journal of Applied Physics*, 110:123908, 2011.

[41] Usman Ilyas, R. S. Rawat, T. L. Tan, P. Lee, R. Chen, H. D. Sun, Li Fengji, and Sam Zhang. Enhanced indirect ferromagnetic p-d exchange coupling of Mn in oxygen rich ZnO:Mn nanoparticles synthesizeed by wet chemical method. *Journal of Applied Physics*, 111:033503, 2012.

[42] Qingyu Xu, Heidemarie Schmidt, Shenqiang Zhou, Kay Potzger, Manfred Helm, Holger Hochmuth, Michael Lorenz, Annette Setzer, and Pablo Esquinazi. Room temperature ferromagnetism in ZnO films due to defects. *Appled Physics Letters*, 92:082508, 2008.

[43] Nguyen Hoa Hong. Magnetism due to defects/oxygen vacancies in HfO_2 thin films. *Physica Status Solidi (c)*, 4(3):1270–1275, 2007.

[44] J. M. D. Coey. Dilute magnetic oxides. *Current Opinion in Solid State and Materials Science*, 10:83–92, 2006.

[45] M. Khalid, A. Setzer, M. Ziese, P. Esquinazi, D. Spemann, A. Pöppl, and E. Goering. Ubiquity of ferromagnetic signals in common diamagnetic oxide crystals. *Physical Review B*, 81:214414, 2010.

[46] Boris B. Straumal, Andrei A. Mazilkin, Svetlana G. Protasova, Ata A. Myatiev, Petr B. Straumal, Gisela Schütz, Peter A. van Aken, Eberhard Goering, and Brigitte Baretzky. Magnetization study of nanograined pure and Mn-doped ZnO films: formation of a ferromagnetic grain-boundary-foam. *Physical Review B*, 79:205206, 2009.

[47] B. B. Straumal, S. G. Protasova, A. A. Mazilkin, A. A. Myatiev, P. B. Straumal, G. Schütz, E. Goering, and B. Baretzky. Ferromagnetic properties of the Mn-doped nanograined ZnO films. *Journal of Applied Physics*, 108:073923, 2010.

[48] B. B. Straumal, A. A. Mazilkin, S. G. Protasova, A. A. Myatiev, P. B. Straumal, E. Goering, and B. Baretzky. Amorphous grain boundary layers in the ferromagnetic nanograined ZnO films. *Thin Solid Films*, 520(4):1192–1194, 2011.

[49] Mariana Ungureanu, Heidemarie Schmidt, Holger von Wenckstern, Holger Hochmuth, Michael Lorenz, Marius Grundmann, Marian Fecioru-Morariu, and Gernot Güntherodt. A comparison between ZnO films doped with 3d and 4f magnetic ions. *Thin Solid Films*, 515:8761–8763, 2007.

[50] Deepayan Chakraborti. *Novel diluted magnetic semiconductor materials based on zinc oxide*. PhD thesis, North Carolina State University, 2007.

[51] Michael Snure, Dhananjay Kumar, and Ashutosh Tiwari. Ferromagnetism in Ni-doped ZnO films: extrinsic or intrinsic? *Applied Physics Letters*, 94:012510, 2009.

[52] Y. Belghazi, G. Schmerber, J. L. Rehspringer, and A. Dinia. Extrinsic origin of ferromagnetism in ZnO and $Zn_{0.9}Co_{0.1}O$ magnetic semiconductor films prepared by sol-gel technique. *Appled Physics Letters*, 89:122504, 2006.

[53] N. R. S. Farley, K. W. Edmonds, A. A. Freeman, G. van der Laan, C. R. Staddon, D. H. Gregory, and B. L. Gallagher. Magnetic properties of sol-gel-derived doped ZnO as a potential ferromagnetic semiconductor: a synchrotron-based study. *New Journal of Physics*, 10:055012, 2008.

[54] S. Ramachandran, Ashutosh Tiwari, and J. Narayan. $Zn_{0.9}Co_{0.1}O$-based diluted magnetic semiconducting thin films. *Applied Physics Letters*, 84(25):5255–5257, 2004.

[55] Jung H. Park, Min G. Kim, Hyun M. Jang, and Sangwoo Ryu. Co-metal clustering as the origin of ferromagnetism in Co-doped ZnO thin films. *Applied Physics Letters*, 84(8):1338–1340, 2004.

[56] Xueqion Su, Li Wang, Jiangbo Chen, Xiaojing Wan, XinPing Zhang, and R. P. Wang. Role of cobalt in ZnO:Co thin films. *Journal of Physics D: Applied Physics*, 44:265002, 2011.

[57] M. Godlewski, E. Guziewicz, M.I . Lukasiewicz, I. A. Kowalik, M. Sawicki, B. S. Witkowski, R. Jakiela, W. Lisowski, J. W. Sobczak, and M. Krawczyk. Role of interface in ferromagnetisom of (Zn,Co)O films. *Physica Status Solidi B*, 248:1596–1600, 2011.

[58] A. Ney, A. Kovacs, V. Ney, S. Ye, K. Ollefs, T. Kammermeier, F. Wilhelm, A. Rogalev, and R. E. Dunin-Borkowski. Structural, chemical and magnetic properties of secondary phases in Co-doped ZnO. *New Journal of Physics*, 13:103001, 2011.

[59] Darshan C. Kundaliya, S. B. Ogale, S. E. Lofland, S. Dhar, C. J. Metting, S. R. Shinde, Z. Ma, B. Varughese, K. V. Ramanujachary, L. Salamanca-Riba, and T. Venkatesan. On the origin of high-temperature ferromagnetism in the low-temperature-processed Mn–Zn–O system. *Nature Materials*, 3:709–714, 2004.

[60] Parmanand Sharma, Amita Gupta, K. V. Rao, Frank J. Owens, Renu Sharma, Rajeev Ahuja, J. M. Osorio Guillen, Börje Johansson, and G. A. Gehring. Ferromagnetism above room temperature in bulk and transparent thin films of Mn-doped ZnO. *Nature Materials*, 2:673–677, 2003.

[61] X. H. Xu, H. J. Blythe, M. Ziese, A. J. Behan, J. R. Neal, A. Mokhtari, R. M. Ibrahim, A. M. Fox, and G. A. Gehring. Carrier-induced ferromagnetism in n-type ZnMnAlO and ZnCoAlO thin films at room temperature. *New Journal of Physics*, 8:135, 2006.

[62] Nikoleta Theodoropoulou, Vinith Misra, John Philip, Patrick LeClair, Geetha P. Berera, Jagadeesh S. Moodera, Biswarup Satpati, and Tapobrata Som. High-temperature ferromagnetism in $Zn_{1-x}Mn_xO$ semiconductor thin films. *Journal of Magnetism and Magnetic Materials*, 300:407–411, 2006.

[63] M. Ivill, S. J. Pearton, Y. W. Heo, J. Kelly, A. F. Hebard, and D. P. Norton. Magnetization dependence on carrier doping in epitaxial ZnO thin films co-doped with Mn and P. *Journal of Applied Physics*, 101:123909, 2007.

[64] J. Alaria, M. Bouloudenine, G. Schmerber, S. Colis, A. Dinia, P. Turek, and M. Bernard. Pure paramagnetic behaviour in Mn-doped ZnO semiconductors. *Journal of Applied Physics*, 99:08M118, 2006.

[65] E. Przezdziecka, E. Kaminska, M. Kiecana, M. Sawicki, W. Klopotowski, L.and Pacuski, and J. Kossut. Magneto-optical properties of the diluted magnetic semiconductor p-type ZnMnO. *Solid State Communications*, 139:541–544, 2006.

[66] K. Masuko, A. Ashida, T. Yoshimura, and N. Fujimura. Influence of antiferromagnetic exchange interaction on magnetic properties of ZnMnO thin films grown pseudomorphically on ZnO $(000\bar{1})$ single-crystal substrates. *Journal of Applied Physics*, 103: 043714, 2008.

[67] A. J. Behan, A. Mokhtari, H. J. Blythe, D. Score, X.-H. Xu, J. R. Neal, A. M. Fox, and G. A. Gehring. Two magnetic regimes in doped ZnO corresponding to a dilute magnetic semiconductor and a dilute magnetic insulator. *Physical Review Letters*, 100:047206, 2008.

[68] Xue-Chao Liu, Er-Wei Shi, Zhi-Zhan Chen, Hua-Wei Zhang, Bo-Yuan Chen, Li-Xin Song, Shi-Qiang Wei, Bo He, and Zhi Xie. Effect of donor doping on the magnetic properties of Co-doped ZnO films. *Journal of Crystal Growth*, 307:14–18, 2007.

[69] T. C. Kaspar, T. Droubay, S. M. Heald, P. Nachimuthu, C. M. Wang, V. Shutthanandan, C. A. Johnson, D. R. Gamelin, and S. A. Chambers. Lack of ferromagnetism in n-type cobalt-doped ZnO epitaxial thin films. *New Journal of Physics*, 10:055010, 2008.

[70] Kevin R. Kittilstved, Nick S. Norberg, and Daniel R. Gamelin. Chemical manipulation of high-T_C ferromagnetism in ZnO diluted magnetic semiconductors. *Physical Review Letters*, 94:147209, 2005.

[71] I. V. Tudose, P. Horvath, M. Suchea, S. Christoulakis, T. Kitsopoulos, and G. Kiriakidis. Correlation of ZnO thin film surface properties with conductivity. *Applied Physics A*, 89:57–61, 2007.

[72] Volodymyr Khranovskyy, Jens Eriksson, Anita Lloyd-Spetz, Rositza Yakimova, and Lars Hultman. Effect of oxygen exposure on the electrical conductivity and gas sensitivity of nanostructured ZnO films. *Thin Solid Films*, 517(6):2073–2078, 2009.

[73] Zhonglin Lu, Hua-Shu Hsu, Yonhua Tzeng, and Jung-Chun-Andrew Huang. Carrier-mediated ferromagnetism in single crystalline (Co,Ga)-codoped ZnO films. *Applied Physics Letters*, 94:152507, 2009.

[74] Manoj K. Yadav, Biplab Sanyal, and Abhijit Mookerjee. Stabilization of ferromagnetism in Mn doped ZnO with C co-doping. *Journal of Magnetism and Magnetic Materials*, 321:273–276, 2009.

[75] Xiangyang Peng and Rajeev Ahuja. Non-transition-metal doped diluted magnetic semiconductors. *Applied Physics Letters*, 94:102504, 2009.

[76] Anh Pham, M. H. N. Assadi, Y. B. Zhang, A. B. Yu, and S. Li. Weak d^0 magnetism in C and N doped ZnO. *Journal of Applied Physics*, 110:123917, 2011.

[77] Shengqiang Zhou, Qingyu Xu, Kay Potzger, Georg Talut, Rainer Grötzschel, Jürgen Fassbender, Mykola Vinnichenko, Jörg Grenzer, Manfred Helm, Holger Hochmuth, Michael Lorenz, Marius Grundmann, and Heidemarie Schmidt. Room temperature ferromagnetism in carbon-implanted ZnO. *Applied Physics Letters*, 93:232507, 2008.

Chapter 4

Fabrication of doped & undoped ZnO films

This chapter provides an overview of the deposition of ZnO thin films, as well as their structural and electronic properties and how they are influenced by defects and dopants. The magnetic properties will be discussed separately and in more detail in the next chapter.

4.1 Procedure

Samples are prepared in the PLD system presented in section 2.1. The substrates are 5x10x0.3 mm^3 $SrTiO_3$ single crystals, oriented in the (011) direction, supplied by Crystal GmbH. This crystal orientation is known to result in excellent quality epitaxy of *c*-axis oriented ZnO [1]. The choice for STO also allows the potential combination or integration with other perovskites, as well as beneficial field-effect properties [2, 3]. Other substrates included fused quartz (2 samples) and *c*-plane Al_2O_3 (2 samples). Targets are custom made following the procedure outlined in section 2.1.2. The starting powders are: ZnO (99.999%, Sigma-Aldrich), MnO_2 (99.999%, Alfa Aesar) and Al_2O_3 (99.998%, Sigma-Aldrich). These are all high purity to reduce possible ferromagnetic contamination of the deposited films.

4.2 Interplay between deposition parameters and thin film properties

One of the advantages of PLD is the ease of stoichiometry transfer from the target to the deposited film [4]. However, it has been demonstrated for the case $SrTiO_3$ that the laser fluence plays an important role in this transfer [5, 6]. Figure 4.1 shows another dependency, namely on oxygen pressure. This can be understood intuitively, as the vapour pressure of the element or preferential sputtering might vary depending on the vacuum level. Another aspect is that the gas (oxygen) molecules increase the scattering in the plume as the species are transferred from the target to the substrate. This effect is expected to become more pronounced for longer target-to-substrate distances. From Figure 4.1 the trend is clear for doped ZnO: heavier atoms are more affected by the scattering, implying roughly a doubling of the Mn-content in the film compared to the target, whereas the Al content is always higher than in the target. Similar oxygen pressure dependent results were reported for $LaGaO_3$ and $LaAlO_3$ perovskites [7].

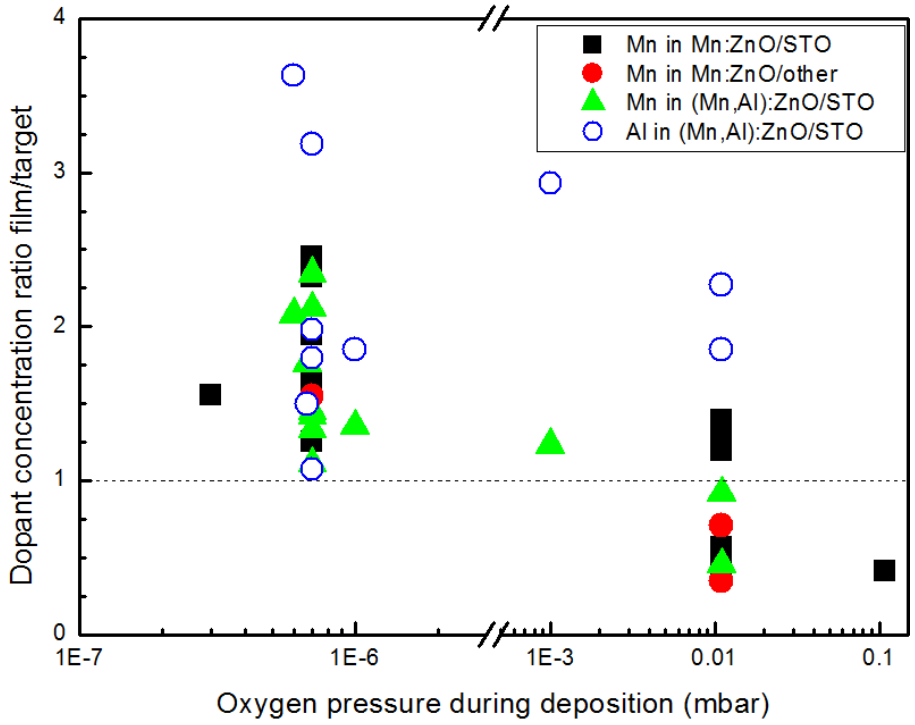

Figure 4.1: Variation of the dopant ratio in film and target versus partial oxygen pressure during PLD of doped ZnO films.

In order to optimise the quality of the deposited ZnO films, several combinations of buffer layers, oxygen pressure and substrate temperature were attempted, resulting in various morphologies (roughnesses) and structural qualities. Buffer layers, especially low temperature ones, cause a large increase in surface roughness (measured by AFM) and decrease the degree of orientation, as characterised by the full width at half maximum (FWHM) of the ZnO (002) XRD rocking curves. Both properties are also strongly affected by temperature as evidenced by Figure 4.2, whereas oxygen pressure only has a limited influence. The presence of low temperature buffer layers significantly decreased the strain in the film, but at the expense of roughness which increased as the temperature of the buffer layer decreased. The large variation in structural parameters with slight changes in deposition conditions clearly demonstrates the sensitivity of ZnO (and dilute magnetic oxides) to these influences, perhaps providing an explanation for the general low reproducibility of ferromagnetism in DMS [8].

The optimum parameter combination for ZnO and especially 1 at% Mn:ZnO films as determined from the experiments is a partial oxygen pressure of 10^{-2} mbar and a substrate temperature of 700 °C. This is for a laser fluence of 1 J/cm^2 and repetition rate of 10 Hz, values which were not varied in this study. This parameter combination results in smooth films with single unit cell steps and hexagonal growth spirals around a screw dislocation (Figure 4.3); rocking curve FWHM is typically around 0.3° for these films.

Photoluminescence spectra of doped & undoped ZnO films with a STO substrate for comparison are presented in Figure 4.4. The bandgap-related peak around 375 nm (≈3.31 eV) is clearly visible in all ZnO samples. The position of this 'near-band-edge' is similar to that reported in literature and is related to thermal smearing of the bandgap [9–12]. The intensity is decreased by the introduction of dopants, as other carrier recombination mechanisms (which might be non-radiative) with mid-gap defect states become possible.

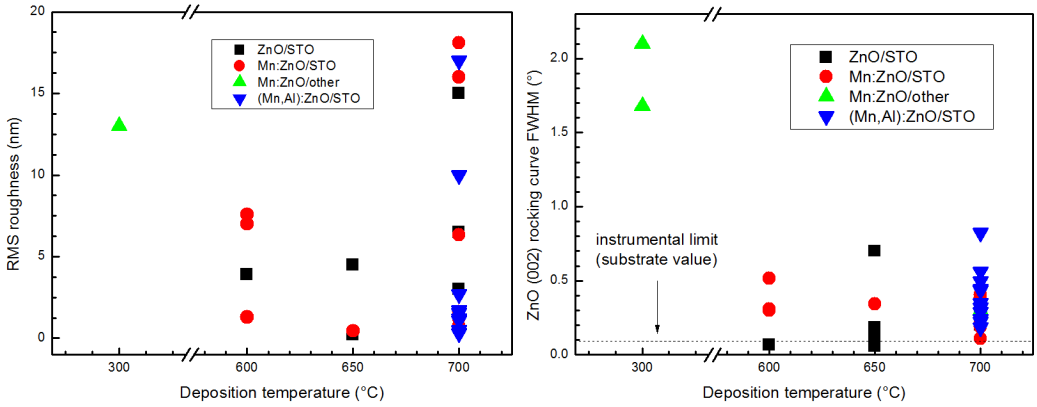

(a) (b)

Figure 4.2: Effect of temperature on **(a)** RMS roughness and **(b)** full width at half maximum of ZnO (002) rocking curves.

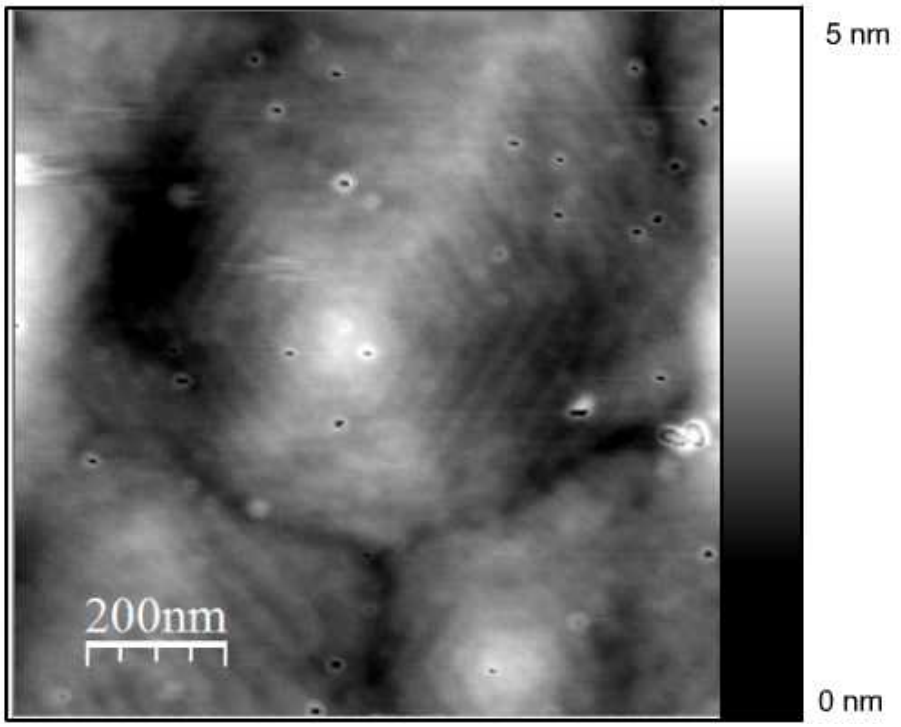

Figure 4.3: AFM topography image of a 0.88 at% Mn:ZnO film deposited at 700 °C and 10^{-2} mbar O_2, showing hexagonal growth spirals with single unit cell height steps.

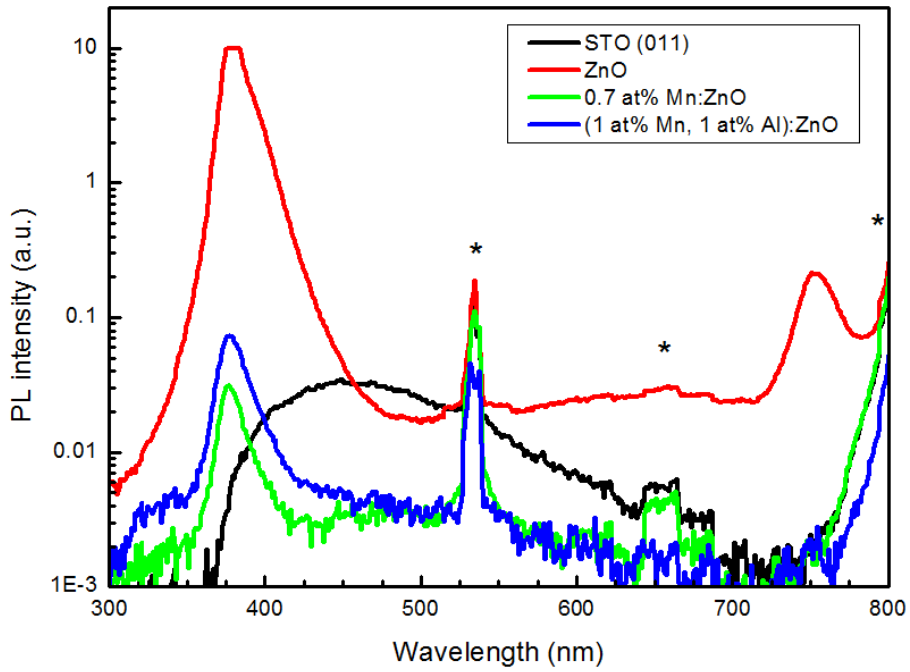

Figure 4.4: Photoluminescence spectra of a bare STO (011) substrate and a ZnO, Mn:ZnO and (Mn,Al):ZnO film. Artefacts due to the measurement apparatus are indicated by a star (*).

The extra peak at 750 nm (≈1.65 eV) in the ZnO spectrum is related to a certain type of intrinsic defect in the ZnO. Unfortunately there is no consensus in literature on the nature of this defect, although zinc vacancies [13, 14] have been most frequently proposed as the origin.

4.3 Strain state of deposited films

Figure 4.5 shows the detail of a goniometric scan on a STO (011) substrate and a ZnO, Mn:ZnO and (Mn,Al):ZnO film (all deposited at 650 °C in 10^{-2} mbar O_2). All films are epitaxial and *c*-axis oriented, as expected from literature [1–3] and none of them show any hints of secondary phases (neither MnO_x nor more complex $ZnMn_xO_y$ compounds [15]). The ZnO (00*l*) peak is clearly shifting depending on the doping level, suggesting substitutional incorporation of the Mn atoms. None of the films are however fully strained to the substrate, as the reciprocal space map in Figure 4.6 clearly shows.

The evolution of the relative change in the out-of-plane lattice parameter is shown in Figure 4.7. There is a variation in the lattice parameter of undoped ZnO, mostly caused by the use of strain alleviating buffer layers. The dotted line indicates the expected change according to Vegard's law, an approximation for a mixture of MnO and (strained) ZnO. The expected decreasing slope in lattice parameter occurs for samples with up to 1 at% Mn, but higher concentrations deviate from this trend. This would suggest that some phase segregation of the Mn occurs. The samples on quartz and sapphire however seem to follow the downward trend up to 3 at% – these films are usually less perfectly oriented (or just textured in the case of quartz) and might therefore be more defect-tolerant and more able to accommodate the Mn substitutionally.

Keeping this potential phase segregation in mind, the study of the magnetic properties will be limited to undoped ZnO films and Mn:ZnO films with ≈1 at% Mn.

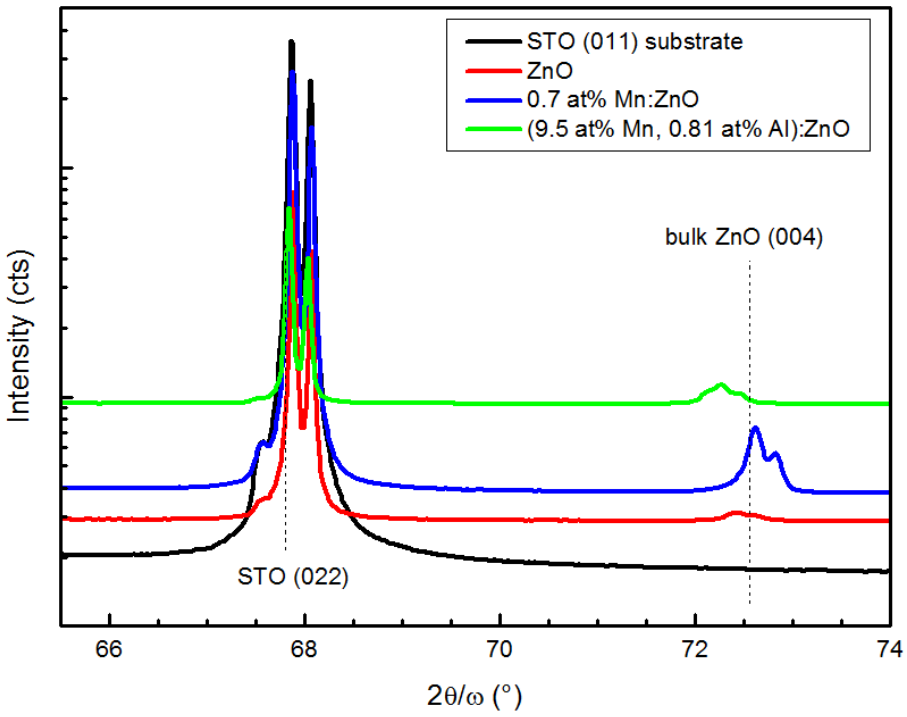

Figure 4.5: Detail of a goniometric XRD scan of a STO (011) substrate and ZnO thin films at different doping levels.

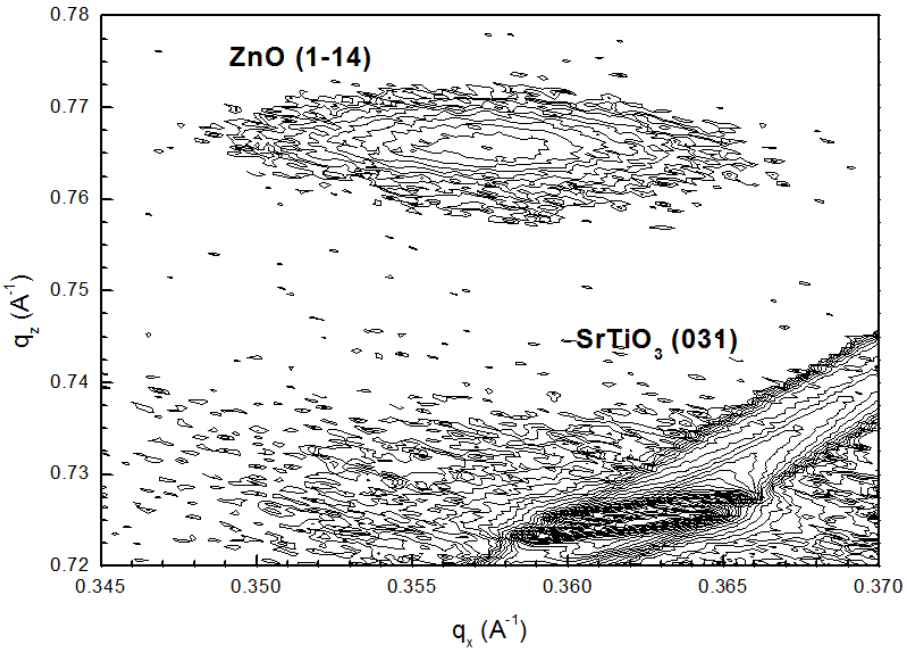

Figure 4.6: Reciprocal space map showing the partially relaxed ZnO ($1\bar{1}4$) peak with respect to the STO (031) for a 100 nm ZnO sample without any buffer layers (deposited at 700 °C in 10^{-2} mbar O_2.

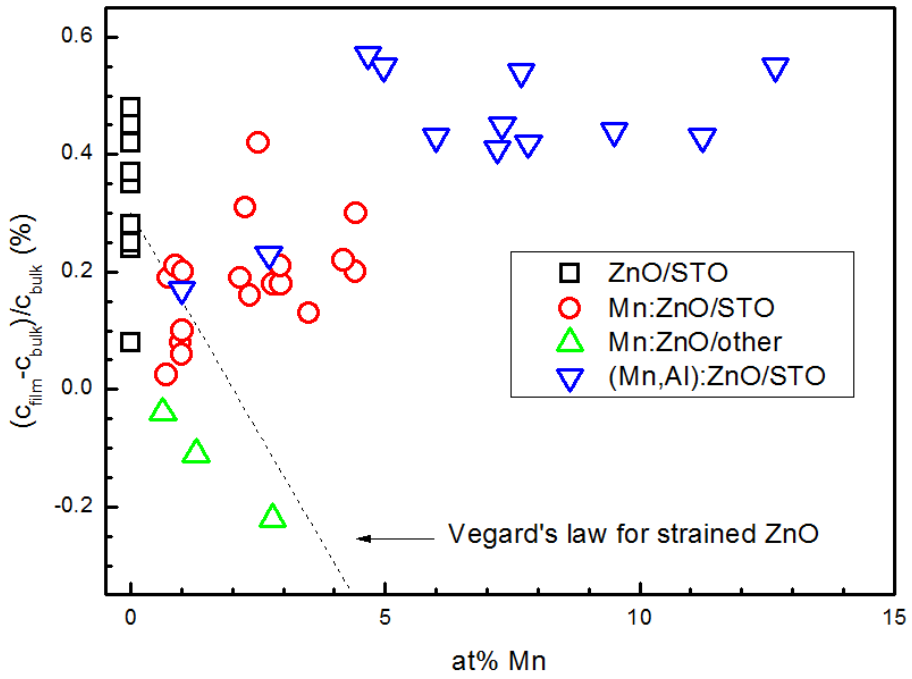

Figure 4.7: Relative change in out-of-plane ZnO lattice parameter as a function of Mn-doping level. The dotted line indicates the evolution of Vegard's law for (nominally strained) ZnO.

4.4 Electrical properties

The deposited, epitaxial, *c*-axis oriented ZnO films are fairly conductive at room temperature and exhibit characteristic semiconducting behaviour with respect to temperature (Figure 4.8a). The substrate can be used as a gate dielectric to create a pseudo-transistor structure in a 4-point measurement. The 10 K I-V characteristics, with applied gate voltage, are shown in Figure 4.8b, highlighting the presence of *n*-type carriers: a negative voltage causes a depletion or trapping of the electrons, whereas a positive gate enhances the conductivity.

Several direct bandgap semiconductors are well known to exhibit a photo-induced enhancement of the conductivity, so-called 'photoconductivity' [16]. In the case of ZnO, this has been applied in UV sensors [17, 18] as well as photodetectors [19], since the sensitivity extends to visible light (sub-bandgap). Illumination of (single crystalline) ZnO with UV light causes two processes to occur simultaneously [20–22]: an increase in carrier density by photon generated electron/hole pairs and oxygen photodesorption from the surface. The oxygen is adsorbed as a negatively charged ion, thereby capturing and/or depleting electrons from the conduction band of the underlying ZnO. This phenomenon is more important in thin films [20] due to the high relative importance of the surface. Experimental results are presented as photoconductivity gain, which is the relative increase in conductivity with respect to the dark reference.

Figure 4.9a shows an example of a photoconductivity measurement on a ZnO film, that is being irradiated by a 400 nm UV LED. There is a fairly slow rise and fast decay as the light is being turned on or off respectively. These time constants are determined by defects and impurities in the films which hinder the creation or cause the recombination of photon-generated electron/hole pairs. The overall constant increase in gain is to be attributed to persistent photoconductivity, i.e. photon-generated carriers that have a lifetime exceeding

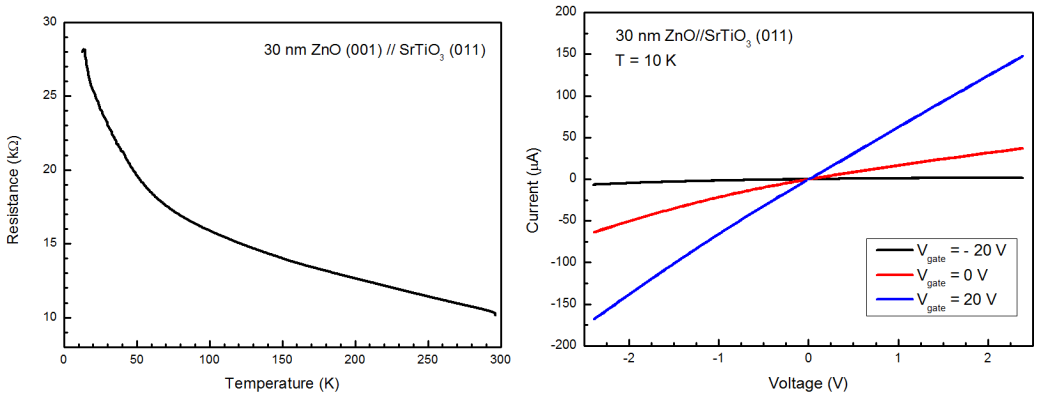

(a) (b)

Figure 4.8: Electrical behaviour of semiconducting ZnO
(a) evolution of resistance versus temperature
(b) I-V curves when applying a gate voltage through STO substrate at 10 K

the illumination time [23]. A comparison between different samples and wavelengths is shown in Figure 4.9b – note that all wavelengths are essentially below the bandgap, as evidenced by the PL spectra (Figure 4.4). The relative magnitude of the gains varies from sample to sample, because their dark conductivity changes: the Mn:ZnO sample is the most resistive, while the (Mn,Al):ZnO co-doped sample has the lowest resistance. More important is however the relative difference between the wavelengths. All samples show the highest increase under UV (400 nm) illumination, probably related to intrinsic donor levels close to the bandgap. In accordance to the peak in the PL spectrum (Figure 4.4), the ZnO sample shows an increase under red (640 nm) illumination, which is not as pronounced in the Mn-doped samples. In these doped samples, the green light (525 nm) produces a significant increase in conductivity, close to the gain from the UV. It has been observed by Li et al. [24] that Mn^{2+} doping results in an enhancement of the 'green band' states in photoluminescence spectra of ZnO. Prosanov [25] suggested a model that explains the green luminescence as a result from a recombination of an electron from the conduction band with a hole trapped by a luminescence centre. Looking from a photoconductivity perspective at this model, the green light generates an electron/hole pair at the acceptor-like (see [26]) Mn^{2+} defect level, exciting the electron to the conduction band, causing the observed enhancement in conductivity.

Hall measurements (at room temperature) confirm the dominance of n-type carriers and reveal interesting trends with Mn- and Al-doping (Figure 4.10). Addition of a small amount of Mn ($<$ 1 at%) seems to decrease the carrier density slightly, but above that value, little impact is observed. This initial decrease at room temperature is in accordance with Han et al. [26] for bulk Mn-doped ZnO. They predict however an increase in conductivity at higher temperatures, when the Mn-donor levels become thermally activated. The observation that a higher Mn-content has no significant influence on the carrier density, could be related to the phase segregation suggested by the deviation from Vegard's law for these concentrations (section 4.3). Addition of $\approx$1 at% of Al causes an increase in carrier density by 2 orders of magnitude, as expected for this n-type dopant [27–31].

The electron mobility however is consistently enhanced, i.e. more than doubled, by the introduction of Mn and irrespective of the presence of Al. This is a rather surprising result, which has not been reported in literature before. In Mn-doped LAO//STO interfaces (discussed in the second part), this mobility enhancement also occurs [32]. It seems

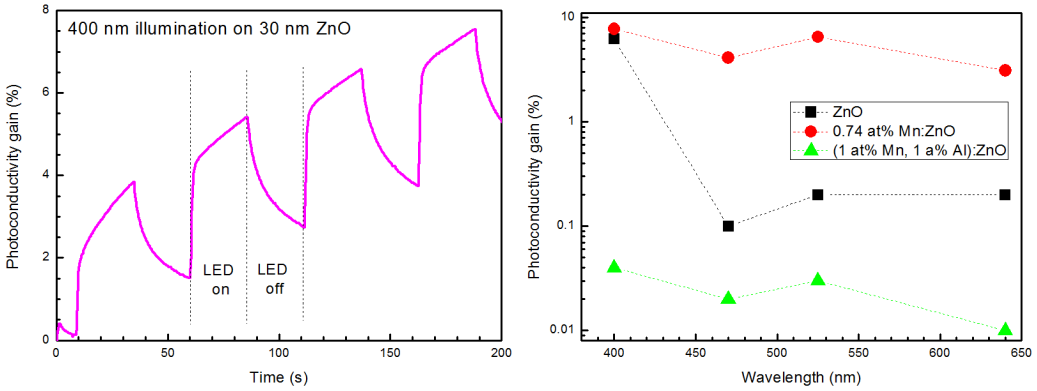

Figure 4.9: **(a)** Photoconductivity gain versus time of a 30 nm ZnO film under 400 nm LED illumination
(b) Photoconductivity gain versus illumination wavelength for doped and undoped ZnO films.

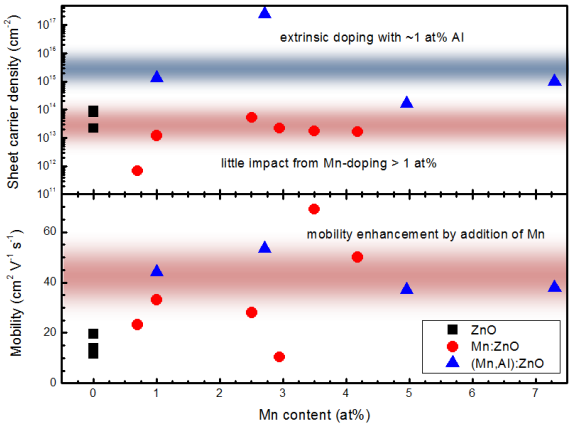

Figure 4.10: Evolution at room temperature of sheet carrier density and electron mobility of epitaxial ZnO films with Mn- and Al-doping.

that the screening from the Mn-levels is, in both cases, efficiently reducing scatter in the conductive path.

Figure 4.11 shows a possible dependence of the room temperature carrier density on the out-of-plane lattice parameter variation for Mn-doped and undoped ZnO films (no extrinsic carriers from Al-doping). Disregarding the possible phase separation and its influence on strain, there seems to be an interplay between the two quantities: a higher degree of strain seems to imply a higher carrier density. Since the carriers are introduced only intrinsically by oxygen vacancies or zinc interstitials [26–28, 33], one could assume from this graph that the variation in out-of-plane lattice parameter is an indication for a change in concentration of native defects in the ZnO.

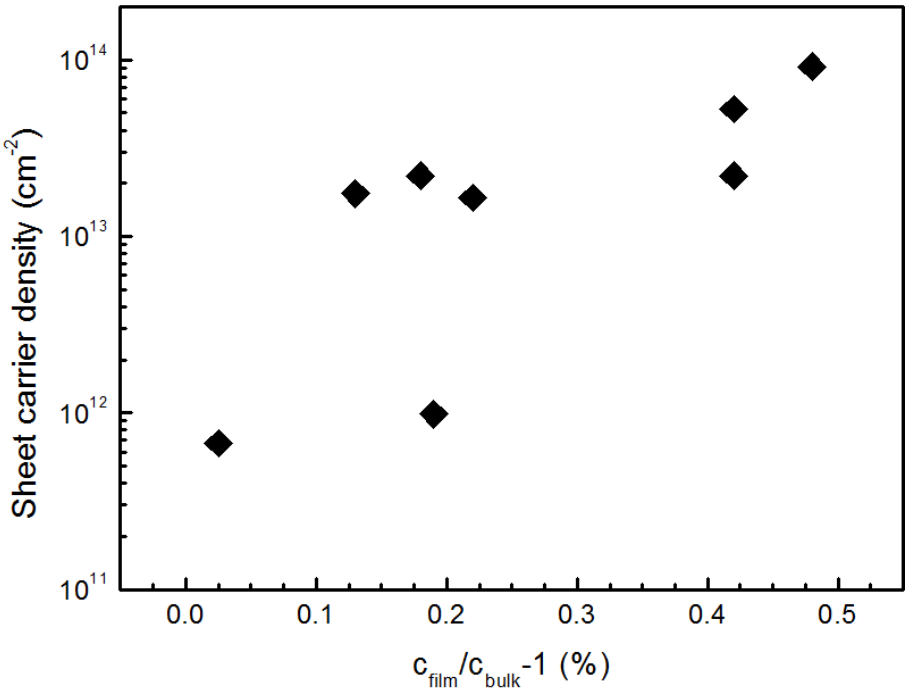

Figure 4.11: Sheet carrier density (at room temperature) versus variation in the out-of-plane lattice parameter for epitaxial ZnO and Mn:ZnO films.

Bibliography

[1] X. H. Wei, Y. R. Li, J. Zhu, W. Huang, Y. Zhang, W. B. Luo, and H. Ji. Epitaxial properties of ZnO thin films on $SrTiO_3$ substrates grown by laser molecular beam epitaxy. *Applied Physics Letters*, 90:151918, 2007.

[2] E. Bellingeri, D. Marré, I. Pallecchi, L. Pellegrino, and A. S. Siri. High mobility in ZnO thin films deposited on perovskite substrates with a low temperature nucleation layer. *Applied Physics Letters*, 86:012109, 2005.

[3] E. Bellingeri, I. Pallecchi, L. Pellegrino, G. Canu, M. Biasotti, M. Vignolo, A. S. Siri, and D. Marré. Crystalline $ZnO/SrTiO_3$ transparent field effect transistor. *Physica Status Solidi (a)*, 205(8):1934–1937, 2008.

[4] Douglas B. Chrisey and Graham K. Hubler, editors. *Pulsed laser deposition of thin films*. John Wiley & Sons, 1994.

[5] Tsuyoshi Ohnishi, Keisuke Shibuya, Takahisa Yamamoto, and Mikk Lippmaa. Defects and transport in complex oxide thin films. *Journal of Applied Physics*, 103:103703, 2008.

[6] D. J. Keeble, S. Wicklein, R. Dittmann, L. Ravelli, R. A. Mackie, and W. Egger. Identification of *A*- and *B*-site cation vacancy defects in perovskite oxide thin films. *Physical Review Letters*, 105:226102, 2010.

[7] S. Amoruso, C. Aruta, R. Bruzzese, X. Wang, and U. Scotti di Uccio. Substrate heating influence on the deposition rate of oxides during pulsd laser deposition in ambient gas. *Applied Physics Letters*, 98:101501, 2011.

[8] F. Pan, C. Song, X. J. Liu, Y. C. Yang, and F. Zeng. Ferromagnetism and possible application in spintronics of transition-metal-doped ZnO films. *Materials Science and Engineering R*, 62:1–35, 2008.

[9] Xiangyang Ma, Chen Peiliang, Dongsheng Li, Yuanyuan Zhang, and Deren Yang. Electrophotoluminescence of ZnO film. *Applied Physics Letters*, 91:021105, 2007.

[10] Sejoon Lee, Yoon Shon, and Deuk Young Kim. Temperature-dependent photoluminescence study of As-doped p-type $(Zn_{0.93}Mn_{0.07})O$ layer. *Thin Solid Films*, 516: 4889–4893, 2008.

[11] Haiping Tang, Zhizhen Ye, and Haiping He. Comparative photoluminescence study on p-type and n-type ZnO films codoped by nitrogen and aluminium. *Optical Materials*, 30:1422–1426, 2008.

[12] P. Misra, T. K. Sharma, and L. M. Kukreja. Temperature dependent photoluminescence processes in ZnO thin films grown on sapphire by pulsed laser deposition. *Current Applied Physics*, 9:179–183, 2009.

[13] R. B. M. Cross, M. M. De Souza, and E. M. Sankara Narayanan. A low temperature combination method for the production of ZnO nanowires. *Nanotechnology*, 16:2188–2192, 2005.

[14] A. Bera and D. Basak. Role of defects in the anomalous photoconductivity in ZnO nanowires. *Applied Physics Letters*, 94:163119, 2009.

[15] Darshan C. Kundaliya, S. B. Ogale, S. E. Lofland, S. Dhar, C. J. Metting, S. R. Shinde, Z. Ma, B. Varughese, K. V. Ramanujachary, L. Salamanca-Riba, and T. Venkatesan. On the origin of high-temperature ferromagnetism in the low-temperature-processed Mn–Zn–O system. *Nature Materials*, 3:709–714, 2004.

[16] Richard H. Bube. *Photoelectronic properties of semiconductors*. Cambridge University Press, 1992.

[17] C. Y. Liu, B. P. Zhang, Z. W. Lu, N. T. Binh, K. Wakatsuki, Y. Segawa, and R. Mu. Fabrication and characterization of ZnO film based UV photodetector. *Journal of Materials Science: Materials in Electronics*, 20:197–201, 2009.

[18] Y. R. Ryu, T. S. Lee, J. A. Lubguban, H. W. White, Y. S. Park, and C. J. Youn. ZnO devices: photodiodes and p-type field-effect transistors. *Applied Physics Letters*, 87:153504, 2005.

[19] H. S. Bae, M. H. Yoon, J. H. Kim, and Seongil Im. Photodetecting properties of ZnO-based thin-film transistors. *Applied Physics Letters*, 83(25):5313–5315, 2003.

[20] Yasutaka Takahashi, Masaaki Kanamori, Akiko Kondoh, Hideki Minoura, and Yutaka Ohya. Photoconductivity of ultrathin zinc oxide films. *Japanese Journal of Applied Physics*, 33:6611–6615, 1994.

[21] D. H. Zhang and D. E. Brodie. Photoresponse of polycrystalline ZnO films deposited by rf bias sputtering. *Thin Solid Films*, 261:334–339, 1995.

[22] I. V. Tudose, P. Horvath, M. Suchea, S. Christoulakis, T. Kitsopoulos, and G. Kiriakidis. Correlation of ZnO thin film surface properties with conductivity. *Applied Physics A*, 89:57–61, 2007.

[23] B. Claflin, Look D. C., S. J. Park, and G. Cantwell. Persistent n-type photoconductivity in p-type ZnO. *Journal of Crystal Growth*, 287:16–22, 2006.

[24] J. H. Li, Shen D. Z., J. Y. Zhang, D. X. Zhao, B. S. Li, Y. M. Lu, Y. C. Liu, and X. W. Fan. The effect of Mn^{2+} doping on structure and photoluminescence of ZnO nanofilms synthesized by sol-gel method. *Journal of Luminescence*, 122-123:352–354, 2007.

[25] I. Yu. Prosanov. Investigation of the recombination proceses in zinc oxide under pulsed excitation. *Russian Physics Journal*, 46(7):721–725, 2003.

[26] Jiaping Han, P. Q. Mantas, and A. M. R. Senos. Defect chemistry and electrical characteristics of undoped and Mn-doped ZnO. *Journal of the European Ceramic Society*, 22:49–59, 2002.

[27] Jagadisch Chennupati and Stephen J. Pearton, editors. *Zinc oxide: bulk, thin films and nanostructures*. Elsevier, 2006.

[28] Klaus Ellmer and Andreas Klein, editors. *Transparent conductive zinx oxide*. Springer, 2008.

[29] A. J. Behan, A. Mokhtari, H. J. Blythe, D. Score, X.-H. Xu, J. R. Neal, A. M. Fox, and G. A. Gehring. Two magnetic regimes in doped ZnO corresponding to a dilute magnetic semiconductor and a dilute magnetic insulator. *Physical Review Letters*, 100:047206, 2008.

[30] T. C. Kaspar, T. Droubay, S. M. Heald, P. Nachimuthu, C. M. Wang, V. Shutthanandan, C. A. Johnson, D. R. Gamelin, and S. A. Chambers. Lack of ferromagnetism in n-type cobalt-doped ZnO epitaxial thin films. *New Journal of Physics*, 10:055010, 2008.

[31] M. D. McCluskey and S. J. Jokela. Defects in ZnO. *Journal of Applied Physics*, 106: 071101, 2009.

[32] T. Fix, J. L. MacManus-Driscoll, and M. G. Blamire. Delta-doped $LaAlO_3/SrTiO_3$ interfaces. *Applied Physics Letters*, 94:172101, 2009.

[33] S. B. Zhang, S.-H. Wei, and Alex Zunger. Intrinsic n-type versus p-type doping asymmetry and the defect physics of ZnO. *Physical Review B*, 63:075205, 2001.

Chapter 5

Defect mediated magnetism in doped & undoped ZnO films

This chapter focuses exclusively on the (ferro)magnetic properties of ZnO and 1 at% Mn:ZnO thin films. The initial analysis by magnetometry is presented, followed by an in-depth study of the x-ray magnetic circular dichroism properties. Finally conclusive evidence is provided for a strain tunable, purely defect mediated mechanism as the source for ferromagnetism.

5.1 Magnetometry on ZnO & Mn:ZnO

Room temperature ferromagnetism is observed in both undoped and 1 at% Mn-doped ZnO films, as verified by SQUID and/or VSM measurements. An exemplary room temperature hysteresis loop measured by SQUID on a 115 nm 1 at% Mn:ZnO film is shown in Figure 5.1. The magnetisation is rather low and seems to be unrelated to the oxygen pressure during deposition (which was varied over several orders of magnitude, see section 4.2), suggesting no influence of oxygen vacancy concentration. Saturation is achieved at fairly low magnetic fields (0.2–0.3 T) with a coercive field of about 0.03–0.04 T. The saturation magnetisation ranges between 0.5–3 emu/cm^3. This falls within the wide range of values (0.1–10 emu/cm^3) from other work on undoped ferromagnetic ZnO [1–4]. At 2 K the hysteresis loop looks markedly different from other temperatures (inset of Figure 1), with a significantly higher saturation magnetisation ($\approx$ 2.3 emu/cm^3) and coercive field ($\approx$ 0.05 T) for the same 1 at% Mn:ZnO sample.

Figure 5.2 displays the measured ferromagnetic moment (after linear diamagnetic background subtraction) versus temperature for a 115 nm 1 at% Mn:ZnO film (as in Figure 5.1) and an undoped 60 nm ZnO film. As expected for a ferromagnet below its critical temperature, only minimal changes in the saturation magnetisation are observed as a function of the temperature. There is a slight decrease at room temperature, indicating a Curie temperature above room temperature, in agreement with other reports on doped magnetic ZnO [5, 6]. The strongly increased magnetisation at 2 K in both films indicates the appearance of another contribution, which also causes a larger coercive field and a higher saturating field (see inset of Figure 5.1). This could possibly be due to Mn_3O_4 clusters, an oxide which is normally ferrimagnetic below 45 K, with the critical temperature lowered depending on the cluster size, similar to the case for metallic Co clusters [7]. However Mn_3O_4 clustering can be excluded since the undoped ZnO exhibits the same increase in saturation magnetisation at low temperatures. Another possibility is the formation of a spin glass, which has been described before in Mn-doped ZnO [8]. Yet

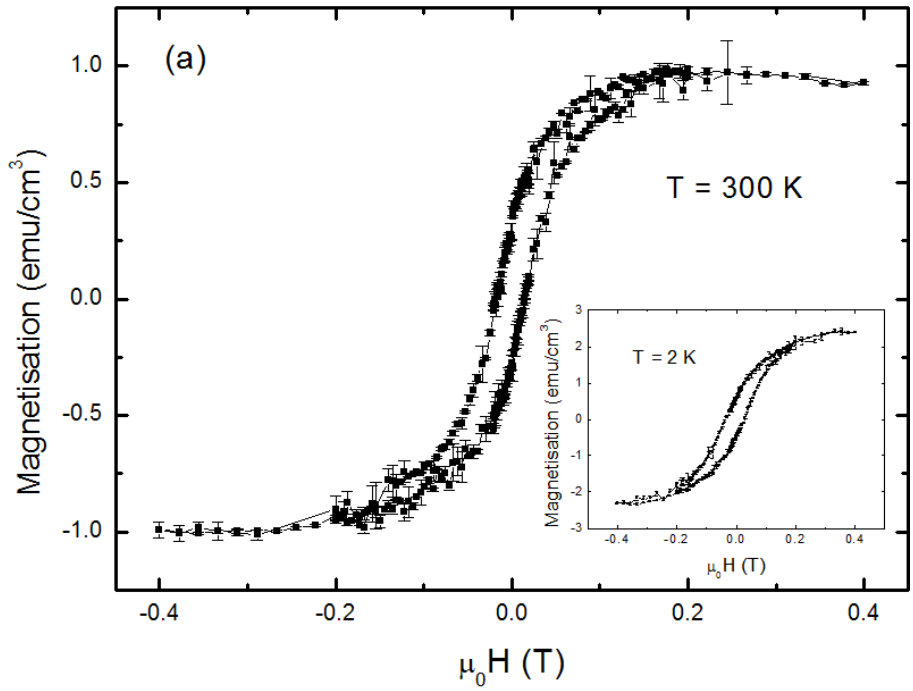

Figure 5.1: Room temperature hysteresis loop of a 115 nm 1 at% Mn:ZnO film. The linear diamagnetic background was subtracted from the SQUID data. Inset: background-corrected loop at a temperature of 2 K.

another option could be a contamination related to the experimental setup of the SQUID (e.g. Kapton tape [9]). In any case, none of these phenomena explain or contribute to the ferromagnetism at higher temperatures.

Additional experiments were carried out to verify the influence of carrier density on the magnetisation. Behan et al. [10] reported a distinct carrier density dependence in their (Mn,Al):ZnO films, namely the occurrence a highly conductive (metal-like) ferromagnetic phase. No significant influence of Al-doping was observed in the films studied here. A field-effect (created by back-gating through the STO substrate) could also induce more carriers, but room temperature VSM measurements in this configuration did not result in any significant difference in the magnetisation, despite the clear increase in conductivity observed (see section 4.4). A third method to introduce additional carriers into the ZnO films was by UV illumination (section 4.4). Samples were kept in the dark for at least 15 hours, with VSM measurements before and after the dark treatment, followed by UV illumination (400 nm) for several hours. This also did not produce a significant difference in the magnetisation characteristics of samples. Therefore it is concluded that there is no carrier density dependence of the magnetisation of the ZnO or Mn:ZnO films, pointing towards a purely defect-based model [11–13].

5.2 X-ray magnetic circular dichroism of 1 at% Mn:ZnO

Details of the technique and experimental setup for XAS and XMCD are discussed in section 2.6. The sample studied is the 115 nm 1 at% Mn:ZnO thin film of which the ferromagnetic hysteresis is shown in Figure 5.1. Measurements are performed in TEY-mode only, due to the fluorescence self-absorption phenomena between the Mn- and O-edges. A scan recorded at a temperature of 2 K and an applied magnetic field of 5 T

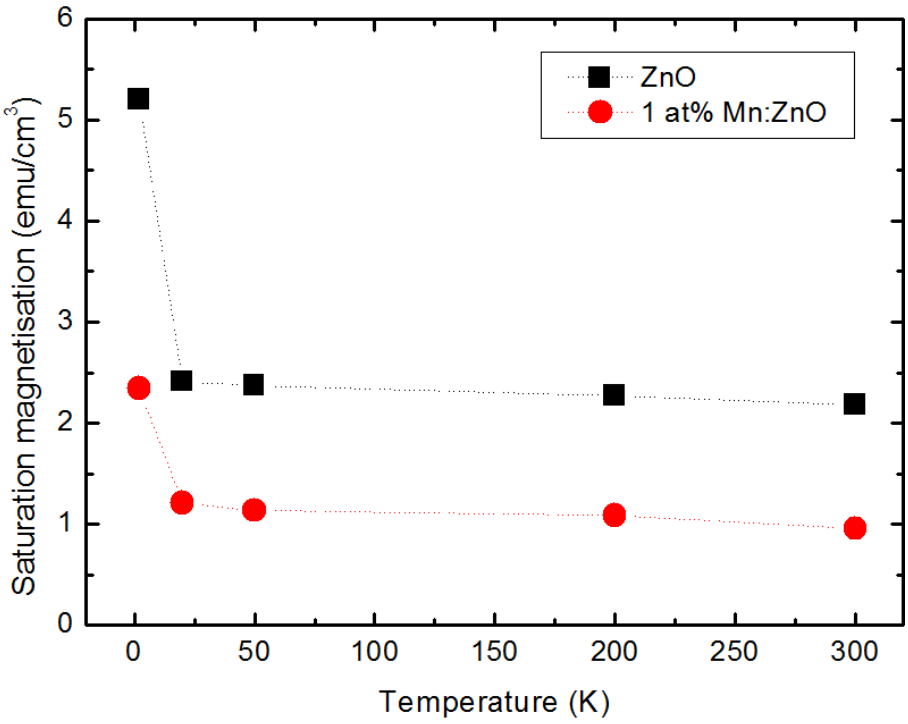

Figure 5.2: Saturation magnetization at a magnetic field of 0.4 T as a function of temperature as derived from background-corrected SQUID data for pure ZnO (60 nm) and 1 at% Mn:ZnO (115 nm). The dotted line is a guide to the eye.

over the O K edge, yielded no measureable XMCD-signal. The XAS profile (collected in TEY mode) is shown in Figure 5.3 for completion, as it differs from other oxygen (in ZnO) profiles in the literature [14–17]. This is related to different fabrication methods, dopants and doping levels, causing a different local defect chemistry that influences the crystal field around the atoms probed. The same is true for the Mn-spectra (see e.g. [18]). Tietze et al. [15] estimated the possible magnitude of the oxygen magnetic moment, yielding a value of $\approx 0.07\ \mu_B$ per O atom, which is significantly above the resolution limit of the measurement. This implies that there is no magnetic moment at the oxygen sites, corresponding to the findings of Tietze et al. [15].

The XAS and XMCD recorded over the Mn $L_{2,3}$ edges are displayed in Figure 5.4. The experimental spectra clearly exhibit a multiplet structure, indicating that the Mn is not in a metallic state. For comparison, theoretically calculated spectra[1] are also shown in Figure 5.4. The atomic multiplet calculation is for the Mn d^5 configuration in tetrahedral crystal field symmetry ($10Dq$ = -0.7 eV) and with Slater parameters scaled to 80% of the atomic Hartree-Fock values [19]. The fit with the experimental data is exceptionally good, indicating that Mn is indeed substituting for Zn^{2+} ions in the wurtzite structure and with the same valence .

The magnetisation curve at the Mn edge (in TEY mode) down to 2 K, at an applied field of 5 T, is shown in Figure 5.5. The low temperature data are fitted with a Brillouin function which describes paramagnetic behaviour. From the fit at 2 K, an effective magnetic moment of 2.833 μ_B/Mn^{2+} can be calculated – this is well below the maximum theoretical limit of 5.9 μ_B/Mn [20]. The inset of Figure 5.5 shows the temperature dependency of the XMCD signal in a magnetic field of 5 T, fitted with a modified CurieWeiss

[1]Simulations performed by S. S. Dhesi and G. van der Laan, Diamond Light Source

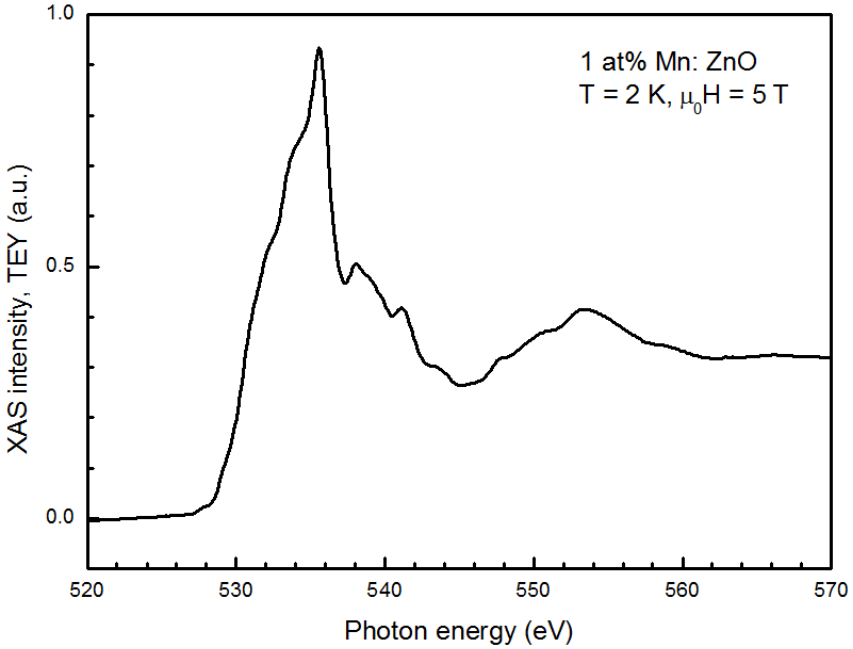

Figure 5.3: X-ray absorption spectrum (in TEY mode) over the O K edge of a 1 at% Mn:ZnO sample at a temperature of 2 K and an applied magnetic field of 5 T.

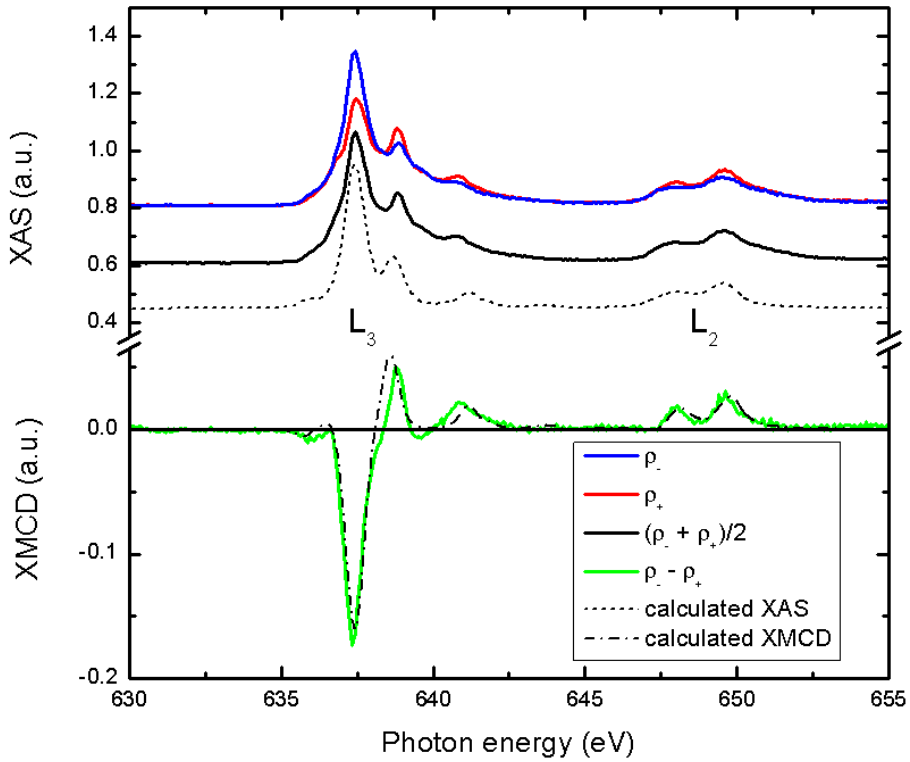

Figure 5.4: Experimental (solid lines) XAS and XMCD spectra (in TEY mode) at 5 T and 2 K at the Mn $L_{2,3}$ edge for a 115 nm 1 at% Mn:ZnO thin film. Calculated XAS (dashed line) and XMCD (dashed dotted line) for a Mn d^5 configuration in tetrahedral symmetry ($10Dq$= - 0.7 eV).

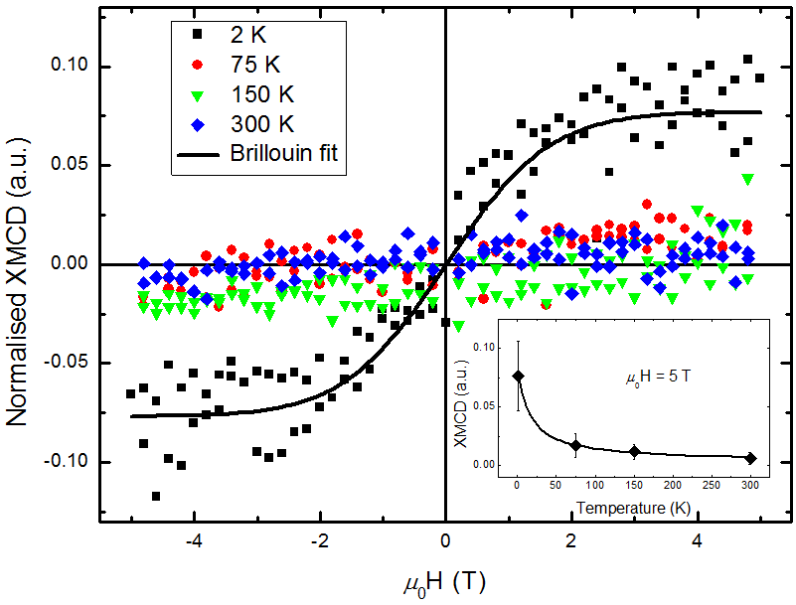

Figure 5.5: Normalized Mn L_3 edge XMCD (in TEY mode) versus applied magnetic field for various temperatures (115 nm 1 at% Mn:ZnO film). The 2 K data are fitted with a Brillouin function, indicating purely paramagnetic behaviour of the Mn dopant. The inset shows the normalized XMCD at the Mn L_3 edge at 5 T versus temperature fitted with a modified CurieWeiss law, also indicating paramagnetic behaviour.

law, which is also characteristic of paramagnetism. The Curie-Weiss temperature of ≈17 K is slightly higher, but comparable to that for Co^{2+} in Co:ITO, another defect-mediated DMS [21].

5.3 Discussion

Comparing the low temperature SQUID measurement (inset of Figure 5.1) and the XMCD at 2 K (Figure 5.4), it is clear that different phenomena are being observed: the magnetometry measurement clearly shows saturation at 0.3–0.4 T and a coercive field. Saturation of the Mn^{2+} paramagnetism occurs only around 3–4 T, much higher than the saturation field of the ferromagnetic hysteresis loop, without displaying any hysteresis. The consequence of this is that the Mn^{2+} moment as such does not contribute to the ferromagnetic moment at any temperature[2]. Other authors have found similar paramagnetic behaviour of transition metal dopants in ferromagnetic zinc oxide [7, 15, 18, 22]. Di Trolio et al. [16] did not measure any XMCD at all in their Co:ZnO or Mn:ZnO samples, but they only measured at room temperature and an applied field of 0.4 T – assuming the paramagnetic behaviour of the dopants observed here, these parameters are indeed insufficient to observe any significant change in the XMCD signal. Kataoka et al. [22] however did observe a small ferromagnetic signal on Mn^{2+} in (Mn,N):ZnO films, indicating a small (but localised) magnetic moment in this case, within the background of a large paramagnetic contribution of the majority of Mn^{2+} ions.

The XMCD results from Figure 5.4 also corroborate the ferromagnetism observed in the undoped ZnO films in that the ferromagnetic moment is not related to the Mn atoms. These results indicate that the ferromagnetism in pure and Mn-doped ZnO thin films

[2]Perhaps the unusual shape of the hysteresis loop at 2 K could be due to the defect-induced ferromagnetic and a Mn-dominated paramagnetic contribution.

is related to a native defect in the material. The possible defects are oxygen vacancies and zinc interstitials as intrinsic donors and zinc vacancies as intrinsic acceptors (see section 3.2). There is no consensus as to precisely which defect is the significant one for room temperature ferromagnetism: oxygen vacancies [23–26], zinc interstitials [6, 27] or zinc vacancies [2, 6, 28–35], although the latter type gains an increasing support from several authors. Zunger et al. [36] mentions that the zinc vacancy defect can support a (localised) magnetic moment, which is further refined by the theoretical calculations of Chakrabarty and Patterson [31] who require this defect to trap an electron in order to support ferromagnetism.

It is therefore reasonable to assign the variation in ferromagnetism in the (Mn:)ZnO films to a change in the concentration of the determining intrinsic defect (or defects). Doping as well as lattice parameter variations can all influence the defect concentration and hence result in a different magnetisation. The interplay between a change in c-axis lattice parameter and the conductivity was already indicated in section 4.4 - it can therefore be assumed that there actually is a link between the variation in c and the (relative) defect concentrations. A correlation between magnetisation and the c-axis lattice parameter was previously shown by MacManus-Driscoll et al. [27], which they assigned to a variation in zinc interstitial concentration, as obtained from annealing experiments. Also Khalid et al. [2] simulated the effect of different zinc vacancy concentrations on the in-plane lattice constant in undoped ZnO, which the authors link to their obtained variation in ferromagnetism. From these calculations it appears that an increase in zinc vacancy concentration from 0 to 9% would imply an increase of about 0.6% in the c-axis parameter.

The dependence of the room temperature saturation magnetization of the films on the relative change of the out of plane c-axis lattice parameter reveals an interesting trend, shown in Figure 5.6. The results generally demonstrate that at particular c-axis lattice parameters the ferromagnetism almost or even completely disappears. At extremes the magnetization strongly increases, resulting in a parabola-like shape, although an outlier appears at 0.37% for the undoped films, which have higher uncertainties in general. This behaviour means that a lower or a higher lattice parameter in the film, with respect to the minimum of the curve, promotes ferromagnetism, whereas intermediate values are less favourable. Doping with Mn seems to shift the position of this minimum to a lower film lattice parameter, but roughly retaining the shape of the dependency. This shift toward lower values is in accordance with Vegard's law. It is possible that two different intrinsic defects cause the ferromagnetism in a different range of lattice parameters, resulting in the parabola-like behaviour as observed.

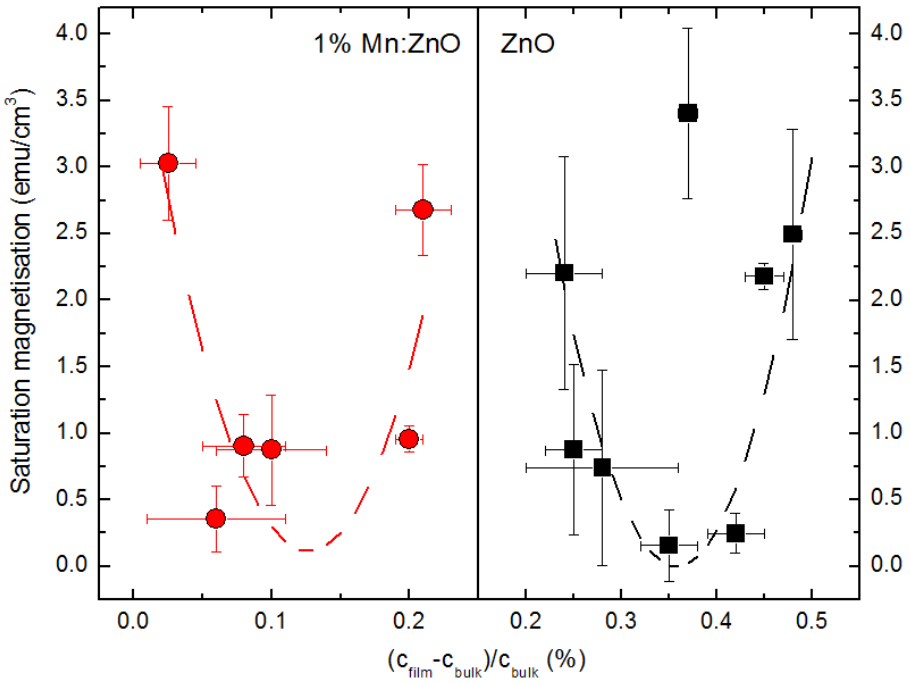

Figure 5.6: Room temperature ferromagnetic saturation magnetisation plotted versus the relative change in the out of plane (c-axis) lattice parameter for thin films of 1 at% Mn:ZnO (left) and ZnO (right) on STO (011) substrates. The dashed lines are guides to the eye.

Bibliography

[1] Qingyu Xu, Heidemarie Schmidt, Shenqiang Zhou, Kay Potzger, Manfred Helm, Holger Hochmuth, Michael Lorenz, Annette Setzer, and Pablo Esquinazi. Room temperature ferromagnetism in ZnO films due to defects. *Appled Physics Letters*, 92:082508, 2008.

[2] M. Khalid, M. Ziese, A. Setzer, P. Esquinazi, M. Lorenz, H. Hochmuth, M. Grundmann, D. Spemann, T. Butz, G. Brauer, W. Anwand, G. Fischer, W. Adaegbo, W. Hergert, and A. Ernst. Defect-induced magnetic order in pure ZnO films. *Physical Review B*, 80:035331, 2009.

[3] Boris B. Straumal, Andrei A. Mazilkin, Svetlana G. Protasova, Ata A. Myatiev, Petr B. Straumal, Gisela Schütz, Peter A. van Aken, Eberhard Goering, and Brigitte Baretzky. Magnetization study of nanograined pure and Mn-doped ZnO films: formation of a ferromagnetic grain-boundary-foam. *Physical Review B*, 79:205206, 2009.

[4] B. B. Straumal, S. G. Protasova, A. A. Mazilkin, A. A. Myatiev, P. B. Straumal, G. Schütz, E. Goering, and B. Baretzky. Ferromagnetic properties of the Mn-doped nanograined ZnO films. *Journal of Applied Physics*, 108:073923, 2010.

[5] F. Pan, C. Song, X. J. Liu, Y. C. Yang, and F. Zeng. Ferromagnetism and possible application in spintronics of transition-metal-doped ZnO films. *Materials Science and Engineering R*, 62:1–35, 2008.

[6] X. Zhang, Y. H. Cheng, Y. Li, Hui Liu, X. Zuo, G. H. Wen, L. Li, R. K. Zheng, and S. P. Ringer. Evidence for high-T_c ferromagnetism in $Zn_x(ZnO)_{1-x}$ granular films mediated by native point defects. *Physical Review B*, 80:174427, 2009.

[7] Jung H. Park, Min G. Kim, Hyun M. Jang, and Sangwoo Ryu. Co-metal clustering as the origin of ferromagnetism in Co-doped ZnO thin films. *Applied Physics Letters*, 84(8):1338–1340, 2004.

[8] T. Fukumura, Jin Zhengwu, M. Kawasaki, T. Shono, T. Hasegawa, S. Koshihara, and H. Koinuma. Magnetic properties of Mn-doped ZnO. *Applied Physics Letters*, 78(7): 958–960, 2001.

[9] M. A. Garcia, E. Fernandez Pinel, J. de la Venta, A. Quesada, V. Bouzas, J. F. Fernandez, J. J. Romero, M. S. Martin Gonzalez, and J. L. Costa-Krämer. Sources of experimental errors in the observation of nanoscale magnetism. *Journal of Applied Physics*, 105:013925, 2009.

[10] A. J. Behan, A. Mokhtari, H. J. Blythe, D. Score, X.-H. Xu, J. R. Neal, A. M. Fox, and G. A. Gehring. Two magnetic regimes in doped ZnO corresponding to a dilute magnetic semiconductor and a dilute magnetic insulator. *Physical Review Letters*, 100:047206, 2008.

[11] J. M. D. Coey. Dilute magnetic oxides. *Current Opinion in Solid State and Materials Science*, 10:83–92, 2006.

[12] J. M. D. Coey and S. A. Chambers. Oxide dilute magnetic semiconductors – fact or fiction? *MRS Bulletin*, 33:1053–1058, 2008.

[13] J. M. D. Coey, P. Stamenov, R. D. Gunning, M. Venkatesan, and K. Paul. Ferromagnetism in defect-ridden oxides and related materials. *New Journal of Physics*, 12: 053025, 2010.

[14] P. Thakur, K. H. Chae, J.-Y. Kim, M. Subramanian, R. Jayavel, and K. Asokan. X-ray absorption and magnetic circular dichroism characterizations of Mn doped ZnO. *Applied Physics Letters*, 91:162503, 2007.

[15] Thomas Tietze, Milan Gacic, Gisela Schütz, Gerhard Jakob, Sebastian Brück, and Eberhard Goering. XMCD studies on Co and Li doped ZnO magnetic semiconductors. *New Journal of Physics*, 10:055009, 2008.

[16] A. Di Trolio, R. Larciprete, S. Turchini, and N. Zema. Bulk sensitive x-ray absorption and magnetic circular dichroism investigation of Mn- and Co-doped ZnO thin films. *Applied Physics Letters*, 97:052505, 2010.

[17] T. S. Herng, D.-C. Qi, T. Berlijn, J. B. Yi, K. S. Yang, Y. Dai, Y. P. Feng, I. Santoso, C. Sanchez-Hanke, X. Y. Gao, Andrew T. S. Wee, W. Ku, J. Ding, and A. Rusydi. Room-temperature ferromagnetism of Cu-doped ZnO films probed by soft x-ray magnetic circular dichroism. *Physical Review Letters*, 105:207201, 2010.

[18] N. R. S. Farley, K. W. Edmonds, A. A. Freeman, G. van der Laan, C. R. Staddon, D. H. Gregory, and B. L. Gallagher. Magnetic properties of sol-gel-derived doped ZnO as a potential ferromagnetic semiconductor: a synchrotron-based study. *New Journal of Physics*, 10:055012, 2008.

[19] Gert van der Laan and B. T. Thole. Strong magnetic x-ray dichroism in $2p$ absorption spectra of $3d$ transition-metal ions. *Physical Review B*, 43(6):13401, 1991.

[20] E. du Tremolet de Lacheisserie, D. Gignoux, and M. Schlenker. *Magnetism I – Fundamentals*. Kluwer, 2002.

[21] A. M. H. R. Hakimi, F. Schoofs, R. Bali, N. A. Stelmashenko, and M. G. Blamire. Origin of magnetism in cobalt-doped indium tin oxide thin films. *Physical Review B*, 82:144429, 2010.

[22] T. Kataoka, Y. Yamazaki, V. R. Singh, Y. Sakamoto, A. Fujimori, Y. Takeda, T. Ohkochi, S.-I. Fujimori, T. Okane, Y. Saitoh, H. Yamagami, A. Tanaka, M. Kapilashrami, L. Belova, and K. V. Rao. Ferromagnetism in ZnO co-doped with Mn and N studied by soft x-ray magnetic circular dichroism. *Applied Physics Letters*, 99: 132508, 2011.

[23] H. S. Hsu, J. C. A. Huang, Y. H. Huang, Y. F. Liao, M. Z. Lin, C. H. Lee, J. F. Lee, L. Y. Chen, S. F.and Lai, and C. P. Liu. Evidence of oxygen vacancy enhanced room-temperature ferromagnetism in Co-doped ZnO. *Applied Physics Letters*, 88: 242507, 2006.

[24] M. Ivill, S. J. Pearton, S. Rawal, L. Leu, P. Sadik, R. Das, A. F. Hebard, M. Chisholm, J. D. Budai, and D. P. Norton. Structure and magnetism of cobalt-doped ZnO thin films. *New Journal of Physics*, 10:065002, 2008.

[25] Wensheng Yan, Qinghua Jiang, Zhihu Sun, Tao Yao, Fengchun Hu, and Shiqiang Wei. Determination of the role of O vacancy in Co:ZnO magnetic film. *Journal of Applied Physics*, 108:013901, 2010.

[26] Peng Zhan, Weipeng Wang, Can Liu, Yang Hu, Zhengcao Li, Zhengjun Zhang, Peng Zhang, Baoyi Wang, and Xingzhong Cao. Oxygen vacancy-induced ferromagnetism in un-doped ZnO thin films. *Journal of Applied Physics*, 111:033501, 2012.

[27] Judith L. MacManus-Driscoll, Neeraj Khare, Yinglin Liu, and Mary E. Vickers. Structural evidence for Zn interstitials in ferromagnetic $Zn_{1-x}Co_xO$ films. *Advanced Materials*, 19:2925–2929, 2007.

[28] Yong Jiang, Wensheng Yan, Zhihu Sun, Qinghua Liu, Zhiyun Pan, Tao Yao, Yuanyuan Li, Zemin Qi, Guobin Zhang, Pengshou Xu, Ziyu Wu, and Shiqiang Wei. Experimental and theoretical investigations on ferromagnetic nature of Mn-doped dilute magnetic semiconductors. *Journal of Physics: Conference Series*, 190:012100, 2009. 14th International Conference on X-Ray Absorption Fine Structure (XAFS14).

[29] Yongfeng Li, Rui Deng, Bin Yao, Guozhong Xing, Dandan Wang, and Tom Wu. Tuning ferromagnetism in $Mg_xZn_{1-x}O$ thin films by band gap and defect engineering. *Applied Physics Letters*, 97:102506, 2010.

[30] J. B. Yi, C. C. Lim, G. Z. Xing, H. M. Fan, L. H. Van, S. L. Huang, K. S. Yang, X. L. Huang, X. B. Qin, B. Y. Wang, T. Wu, L. Wang, H. T. Zhang, X. Y. Gao, T. Liu, A. T. S. Wee, Y. P. Feng, and J. Ding. Ferromagnetism in dilute magnetic semiconductors through defect engineering: Li-doped ZnO. *Physical Review Letters*, 104:137201, 2010.

[31] Aurab Chakrabarty and Charles H. Patterson. Defect-trapped electrons and ferromagnetic exchange in ZnO. *Physical Review B*, 84:054441, 2011.

[32] J. Haug, A. Chassé, M. Dubiel, Ch. Eisenschmidt, M. Khalid, and P. Esquinazi. Characterization of lattice defects by x-ray absorption spectroscopy at the Zn K-edge in ferromagnetic, pure ZnO films. *Journal of Applied Physics*, 110:063507, 2011.

[33] B. Y. Zhang, B. Yao, Y. F. Li, A. M. Liu, and Z. Z. Zhang. Evidence of cation vacancy induced room temperature ferromagnetism in Li-N codoped ZnO thin films. *Applied Physics Letters*, 99:182503, 2011.

[34] W. Q. Li, J. X. Cao, J. W. Ding, and Xuedong Hu. Modulating magnetism of ZnO:C with vacancy and substitution. *Journal of Applied Physics*, 110:123908, 2011.

[35] Usman Ilyas, R. S. Rawat, T. L. Tan, P. Lee, R. Chen, H. D. Sun, Li Fengji, and Sam Zhang. Enhanced indirect ferromagnetic p-d exchange coupling of Mn in oxygen rich ZnO:Mn nanoparticles synthesizeed by wet chemical method. *Journal of Applied Physics*, 111:033503, 2012.

[36] Alex Zunger, Stephan Lany, and Hannes Raebinger. The quest for dilute ferromagnetism in seminconductors: guides and misguides by theory. *Physics*, 3:53, 2010.

Chapter 6

Conclusions & outlook for ferromagnetic ZnO

Ferromagnetism was observed in both undoped as well as Mn-doped thin films of ZnO. XAS and XMCD results confirm that the ferromagnetic moment is not related to the Mn, as this dopant exhibits a purely paramagnetic behaviour. The carrier density does not have any influence on the magnetic properties. There is however a clear relationship and interplay between the lattice strain in the ZnO films and the magnitude of the observed ferromagnetism. Therefore the ferromagnetic signature of these materials is to be attributed to intrinsic defects in the ZnO matrix, the concentrations of which are altered with film lattice constant and dopant concentration. It is unclear from the measurements which defect or defects are responsible for the observed (parabolic) behaviour. In any case, the analysis presented here emphasises the importance of defect management in oxide films in order to tune the desired functional properties.

In order to investigate which lattice defect (or defects) determines the amount of ferromagnetism in ZnO thin films, XAS is most suited. This characterisation technique is extremely sensitive to the local structure of the material. The lineshape of the XAS spectrum is influenced by the local coordination of the site under investigation, i.e. the presence of vacancies or interstitials. Additionally, the XMCD signal can also yield more subtle information about the local coordination, providing another measure of the defect concentration. However, the Zn spectrum will be hardly influenced by tiny local fluctuations, since the signal is averaged over a large number of atoms. Therefore, a so-called tracer atom with a known concentration can be introduced, which results in a more sensitive measurement. Andreasson et al. [1] and Levin et al. [2] performed comparable experiments with transition metals in $SrTiO_3$ single crystals to look at variations in oxygen vacancy concentration. Even though these experiments were performed on transition metal K edges, similar behaviour at the Mn L edges is expected.

Introducing 1 at% Mn-atoms in ZnO does not change the ferromagnetism, as shown in chapter 5, so these are excellent candidates for the purpose. By changing deposition conditions, samples with different lattice parameter values can be obtained, which can be expected to have different defect concentrations and therefore different ferromagnetic strength. This procedure eliminates the need for controlled atmosphere annealing experiments to modify relative defect concentrations. The absorption spectrum at the Mn $L_{2,3}$ edges in electron yield mode, as well as the XMCD spectrum at these edges, should be studied in detail. Fitting with appropriate theoretical calculations for the XAS lineshape, will help to determine relative defect concentrations and identify the interplay between the relevant interstitials and/or vacancies.

Bibliography

[1] B. P. Andreasson, M. Janousch, U. Staub, T. Todorova, B. Delley, G. I. Meijer and E. Pomjakushina. Detecting oxygen vacancies in $SrTiO_3$ by $3d$ transition-metal tracer ions. *Physical Review B*, 80:212103, 2009.

[2] I. Levin, V. Krayzman, J. C. Woicik, A. Tkach and P. M. Vilarinho. X-ray absorption fine structure studies of Mn coordination in doped perovskite $SrTiO_3$. *Applied Physics Letters*, 96:052904, 2010.

Part II

Induced interface conduction in $LaAlO_3/SrTiO_3$

Chapter 7

$LaAlO_3/SrTiO_3$: a literature review

This chapter provides an overview of the literature on $LaAlO_3/STO_3$ heterostructures, highlighting different important aspects with respect to both fundamental understanding as well as observed functional properties, while keeping the significant influences of crystal defects in mind.

7.1 Introduction

In their seminal paper, Ohtomo and Hwang [1] presented transport measurements on a heterostructure, composed of $LaAlO_3$ (LAO) overlayers on an $SrTiO_3$ (001) substrate with different surface terminations. A perovskite ABO_3 material in the crystallographic (001) direction can be either terminated by a (BO_2) or an (AO) type plane, although commonly a mixture of the two is found. There are recipes known in literature to obtain a specific surface termination, usually a combination of selective etching and annealing [2–4]. In the case of STO, only a TiO_2-termination is easy to achieve. A heterostructure of LAO on TiO_2-terminated STO appears to be conductive, while on an SrO-terminated substrate (by deposition of an SrO monolayer on TiO_2-terminated STO) it is not.

The occurrence of conduction between these two insulators (with bandgaps of 3.25 and 5.6 eV for STO and LAO respectively) is very surprising and Ohtomo and Hwang [1] immediately proposed an explanation, namely a so-called electronic reconstruction at the interface between the LAO and the STO, which will be discussed in detail in section 7.2. Later however, other explanations emerged, based on oxygen vacancies (section 7.3) and cation intermixing (section 7.4). Recently a better understanding of the transport properties has led to a more complex picture with the suggestion of the presence of two types of carriers at the interface (section 7.5). In any case, interesting functional properties have been observed and confirmed to be confined to the interface, which will be elaborated in section 7.6.

Finally, it should be noted that there is a fundamental difference between the occurrence of a conductive interface (or two-dimensional electron gas, 2DEG) in the LAO/STO system and those in the MgZnO/ZnO and AlGaAs/GaAs structures [5–7]. The latter occur between semiconductors as a result of band bending, whereas in the case of LAO/STO both materials involved are insulators by nature.

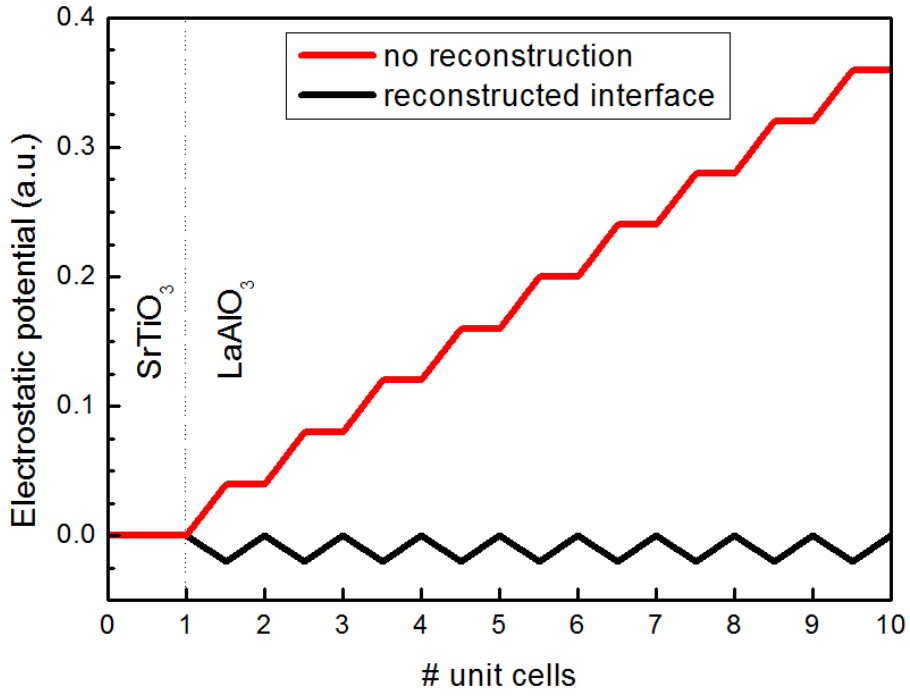

Figure 7.1: Electrostatic simulation for LAO overlayers on STO using the nominal charges of the perovskite planes without and with electronic reconstruction.

7.2 A possible explanation: electronic reconstruction

The model for conduction at the LAO/STO interface initially proposed by Ohtomo and Hwang [1] is the so-called 'electronic reconstruction', which originates from the fact that the perovskite (001) planes in STO are uncharged, i.e. $(SrO)^0/(TiO_2)^0$, whereas those in LAO carry a nominal charge, i.e. $(LaO)^+/(AlO_2)^-$, due to the valence of the cations. The conductive n-type interface is based on a (TiO_2)-termination of the STO, which implies that the next layer is $(LaO)^+$. Stacking LAO on top of STO would create a so-called 'polar discontinuity' [8], which results in a diverging electrostatic potential in the LAO layer. This can be visualised by a simple, layer-by-layer electrostatic calculation (Figure 7.1), based on the nominal charges of each layer of atoms and the finite differential form of Poisson's equation for the electrostatic potential U and charge density ρ:

$$-\nabla^2 U = \rho/\epsilon_0 \tag{7.1}$$

To avoid this unstable divergence, an electronic reconstruction can occur, that is, 0.5 electron per unit cell is transferred from the top surface, resulting in Ti^{3+} ions at the reconstructed interface. The reaction at the LAO surface is unclear, although will probably involve some oxygen vacancies or adsorption for charge compensation [9]. In any case, the result of this electron transfer is an oscillating, not a diverging potential (Figure 7.1). This effect can be demonstrated by simple electrostatics or can be simulated by DFT, which also predicts its two-dimensional confinement [10–13].

Experimentally it has been observed that at least 4–5 unit cells (uc) of LAO are required before the conductivity at the interface occurs, both in PLD [14–17] as well as MBE grown samples [18]. Intuitively, this can be explained by a threshold of electrostatic potential driving force above which it is more favourable for the system to transfer the electrons to the interface. This conductivity onset is also correctly predicted by theory and

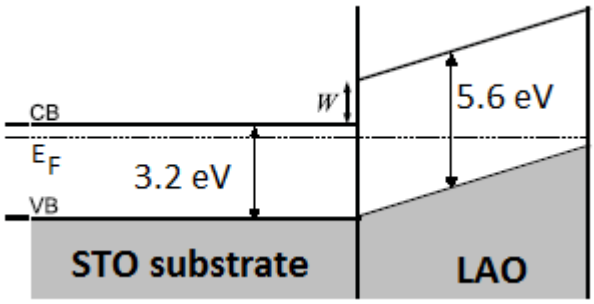

Figure 7.2: Schematic figure of the electric field induced shift in (rigid) band edges in LAO/STO. After ≈ 4 uc of LAO, its valence band level reaches the Fermi level and electron transfer occurs. (Adapted from [9].)

can be explained by a rigid band model [10, 12, 19, 20]. Figure 7.2 shows the schematic of such a model: each additional unit cell of LAO adds 0.9 eV to the electrostatic potential and when the conduction band of the STO is reached, electronic reconstruction occurs.

Following the hypothesis of 0.5 electron per unit cell, this would result in a sheet carrier density of $\approx 3{\cdot}10^{14}$ cm^{-2}, a value which is never attained in 'pure' 2D samples with little influence of oxygen vacancies, as discussed below (section 7.3). It is still not fully clear why this value is not reached. Simulations taking into account layer buckling and defects in the LAO produce a lower expected carrier density as a result of the electrostatic screening [20, 21].

The discussion so far focused on the conductive *n*-type interface, but in the electronic reconstruction model, the equivalent *p*-type interface – with SrO-terminated STO – should support a two-dimensional *hole* gas. However all experimental attempts at the *p*-type interface result in insulating heterostructures [1, 18, 22]. Nakagawa et al. [8] suggested that oxygen vacancies compensate for the electrostatic build-up at the *p*-type interface, since they appear to form more readily under these conditions.

A different explanation for the *n*/*p*-difference could be based on simple ion valence considerations. For the *n*-type interface, Ti^{4+} ions are reduced to Ti^{3+}, both of which are stable Ti-ion configurations. In the case of the 'two-dimensional hole gas', some of the Sr^{2+} ions should be oxidised to Sr^{3+} in order to support hole conduction. However the only stable valence configuration for Sr is Sr^{2+}, since this results in a noble gas electron configuration. As a result, the hole-doping of the interface does not occur and other mechanisms (defects, buckling etc.) compensate for the electrostatic potential.

In summary, the electronic reconstruction model proposes a purely electrostatically governed carrier activation due to an internal electric field in the LAO, with the conductive sheet perfectly confined to the interface. To verify this hypothesis, several authors have employed different techniques with variable success. The presence of Ti^{3+} at the interface between the two perovskites should indicate that an electronic reconstruction occurred, although these ions might also arise from oxygen vacancy compensation (see [23] and section 7.3). TEM studies carried out by Verbeeck et al. [24] show only Ti^{4+} ions at the interface and the authors therefore conclude an absence of the electronic reconstruction in the LAO/STO system. Care should however be taken in this situation, since TEM sample preparation involves the creation of another interface, namely with air, where Ti^{3+} is an unstable oxidation state. In-situ probing techniques, without disturbing the interface, are therefore more advisable. Several authors [17, 25–28] observed the presence of Ti^{3+} by (soft or hard) x-ray photoelectron spectroscopy (XPS) techniques (Figure 7.3a) for samples

with an LAO thickness above the threshold. However there might be an influence from oxygen vacancies in some samples (see further in section 7.3), which would also cause the presence of Ti^{3+}.

Since the signal from obtained from XPS is sensitive to the electrostatic potential of the material that it travels through (i.e. LAO), careful calibration and analysis of such measurements should allow to determine the magnitude of the electric field in the LAO. Boschker [29] and Segal et al. [18] however report an absence of such field (Figure 7.3b). On the other hand, there does appear to be an electrostrictive effect in the thin limit(< 6 uc LAO), as evidenced from x-ray diffraction [30]. Another indication that the electrostatic potential plays an important role in the conductive properties of the LAO/STO system is the response to partial substitution of the interface Ti ions by other atoms [31–33]. When transition metals (Sc, V, Cr, Mn, Fe, Co, Nb, In) with different valence and ionisation energies are introduced, from very low (0.001 at%) to light doping levels (2 at%), the impact on both carrier density and electron mobility is significant. Especially Sc-doping appears very 'effective' at removing carriers from the conductive sheet.

A third possible manifestation of electronic reconstruction would be the effective thickness of the conductive layer, which is predicted to be a single sheet of atoms. Some authors claim no influence of possible two-dimensionality on their measurements [34], which might indicate that they are studying a 3D conductor indeed (see section 7.3). Clear Shubnikov-de Haas oscillations have been observed in LAO/STO at low temperatures, with an angular magnetic field dependence characteristic of two-dimensional transport [35]. Also Rubano et al. [16] report a strong interface confinement of the electrons, as observed by optical second harmonic generation spectroscopy. From their angle resolved hard XPS, Sing et al. [26] and Chu et al. [28] derive that the thickness of the conductive layer must be smaller than 4–5 nm, which implies roughly thinner than 10 uc. This value was further narrowed down by Fix et al. [32] by offset-doping: using a transition metal doped layer (with profound impact on transport properties) as 'marker', they showed that the properties of a 'standard' LAO/STO interface were obtained when a single uc of undoped STO separated the δ-doped marker layer from the interface.

All the results reported above identify the electrostatic influence as a significant factor for conduction at the LAO/STO interface, although the lack of full evidence implies a more complicated picture. Finally however, if the $LaAlO_3/SrTiO_3$ system exhibits such an electronic reconstruction-based 2DEG, similar systems with generalised formulas $A^{3+}B^{3+}O_3/C^{2+}D^{3+/4+}O_3$ should be conductive too. Indeed such conductive properties were observed for $LaVO_3/SrTiO_3$ [36], $LaVO_3/SrVO_3$ [37], $DyScO_3/SrTiO_3$ [38], $NdGaO_3/SrTiO_3$, $LaGaO_3/SrTiO3$ [39] and $GdTiO_3/SrTiO_3$ [40] interfaces. However the $LaCrO_3/SrTiO_3$ interface is found to be insulating [41].

7.3 The role of oxygen vacancies

Important intrinsic electron donors in STO are oxygen vacancies, which can be deliberately introduced by hydrogen or vacuum annealing (see e.g. [42]). Shortly after the discovery of the impressively high sheet carrier density and mobility values, it became clear that oxygen vacancies in the bulk of the STO accounted for a significant proportion of the conductive properties of LAO/STO samples. This causes for example heterostructures with a number of LAO uc below the electronic reconstruction threshold (see section 7.2) to be conductive as well (see e.g. [43]). Depending on the oxygen pressure during LAO deposition by PLD, a certain concentration of oxygen vacancies is introduced into the STO, which renders the substrate (rather than just the interface) conductive [44–47]. The conductive tip-AFM

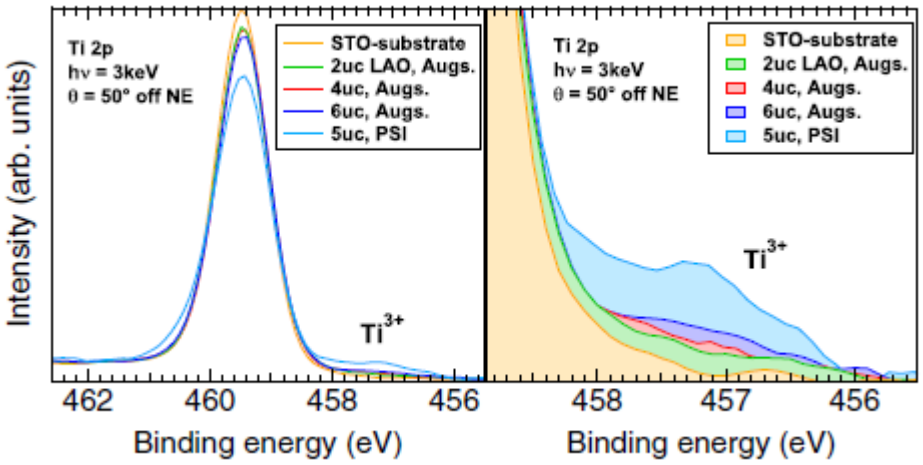

(a)

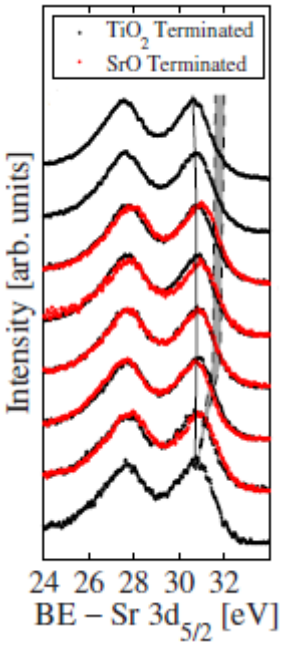

(b)

Figure 7.3: **(a)** Ti 2*p* HAXPES spectra of LAO/STO samples plus an STO substrate reference at a fixed emission angle, with a clear Ti^{3+} manifestation in the samples above the threshold thickness [26].
(b) La 4*d* photoemissions in annealed LAO/STO samples, the x axis being the binding energy relative to the Sr $3d^{5/2}$ peak in the same sample. The thin solid line tracks the observed peak centre, while the grey band follows the range of calculated and predicted shifts of the peak, according to the electronic reconstruction model (adapted from [18]).

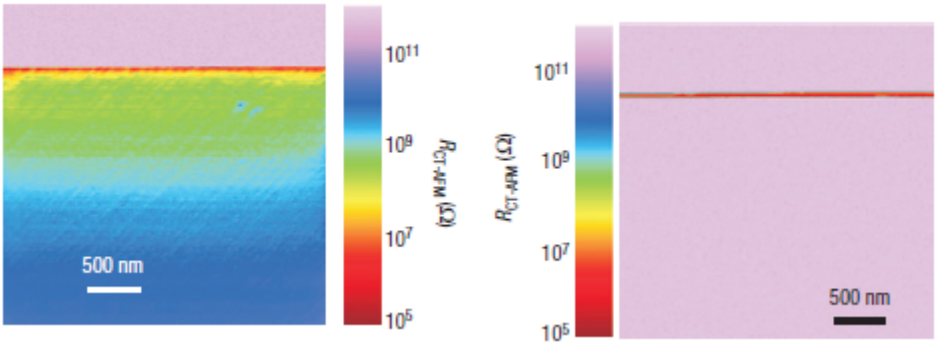

(a) (b)

Figure 7.4: Conductive tip AFM of a LAO/STO cross-section.
(a) as deposited (in 10^{-6} mbar O_2) with the conductive region extending well into the STO substrate due to oxygen vacancy formation
(b) post-deposition oxygen annealed (in 300 mbar O_2) sample with the conductive region confined to the interface [48].

experiments on cross sections of LAO/STO samples by Basletic et al. [48] clearly show this difference (Figure 7.4). The conductive region extends several micrometers into the substrate when the LAO film is grown in an oxygen deficient atmosphere.

The creation of these oxygen defects under the influence of PLD can be caused by two effects: first of all there is the oxygen sputtering due to the impacting species [49], but also the oxygen affinity (or oxygen vacancy formation energy) of the deposited material plays a role. For example, for the case of LAO/STO, the LAO has a higher oxygen affinity than the STO, resulting in a diffusion of STO-oxygen into the LAO film [50]. Both mechanisms contribute to a reduction of the STO substrate, rendering it semiconducting or even metallic. A similar case has been observed for the insulator $CaHfO_3$ on STO, a heterostructure which becomes conductive only under oxygen deficient deposition conditions [51], i.e. due to the reduced STO. To further highlight the intrinsic properties, Ar^+-ion bombarded STO (and thus locally reduced in the bombarded interface region) has been demonstrated to exhibit the same characteristics [52, 53].

It is generally agreed, certainly after the work of Brinkman et al. [45] and Herranz et al. [44], that an oxygen pressure (during deposition) lower than 10^{-3} mbar will cause the transport properties to be dominated by the reduced STO substrate. Different groups solve this issue through different methods: some use a post-deposition anneal to remove oxygen vacancies (e.g. [7, 18, 28, 30, 54, 55]), while others consistently deposit in high pressure environments (e.g. [31–33, 56, 57]). The problem with the former method is that such an anneal might not remove all defects in the structure, especially if the stoichiometry is not correct. Additionally this procedure could induce Sr vacancies at the interface [58]. It should be emphasised that the presence of oxygen vacancies at the interface can not be excluded, even not at higher deposition pressures – they are just not dominating the transport properties in this case.

Density functional theory calculations suggest that oxygen vacancies are easily formed at the LAO surface and can cause interface conductivity or can act as a compensation mechanism [9, 59]. It is however hard to experimentally verify this hypothesis, although the LAO surface appears to have a significant influence on the conductivity indeed [60, 61].

7.4 An alternative explanation: cation intermixing

Aside from an electronic reconstruction (section 7.2) or the introduction of compensating defects (section 7.3), the build-up of an electrostatic potential can also be circumvented by a chemical reconstruction, i.e. the creation of an interdiffused interface. Such intermixing has been observed for the case of GaAs (polar in certain directions) on Ge (non-polar) [62], in $LaNiO_3/LaAlO_3$ superlattices [63] and suggested in $LaCrO_3/SrTiO_3$ [41]. The tendency for interface washing can also be appreciated from a thermodynamic point of view: elements that are present on one side but not on the other, have a high driving force (chemical potential difference) for diffusion. Theoretical work by Chen et al. [64] suggests that La/Sr interdiffusion is favourable for the n-type interface, whereas for the p-type it is not, which could possibly account for the difference in conductive properties between these interfaces.

La is a notable electron donor in STO, with $La_xSr_{1-x}TiO_3$ being conductive for a wide range of x, but closely related to the oxygen stoichiometry [65–71]. Sceptics of the electronic reconstruction picture claim that all transport properties of LAO/STO interfaces can and should be explained in terms of an intermixed, i.e. La-doped STO, interface. Indeed, the properties of the 2DEG are remarkably similar to those of electron-doped STO, but one should keep in mind that in the electronic reconstruction picture, the electrons are effectively being donated to the STO, although only at the interface.

Just as for the electronic reconstruction model, several authors have attempted to prove the existence of an intermixed interface. This is not an evident task, especially not with the spectroscopic techniques commonly applied. The probing resolution of these techniques typically comprises several unit cells, which implies that proper statistical analysis and/or calibration are required before conclusions can be drawn.

A first technique is by transmission electron microscopy (TEM) and complimentary electron energy loss spectroscopy (EELS) [8, 72]. There appears to be some degree of interface intermixing, although this depends on the beam spot size and interaction volume in the sample. Qiao et al. [73] and Chambers et al. [72] provide an extensive overview of other spectroscopic techniques, all of which appear to indicate a certain amount of interdiffusion. The characterisation methods include angle resolved x-ray photoelectron spectroscopy (XPS), secondary ion mass spectroscopy (SIMS) and Rutherford backscattering spectroscopy (RBS). It should be noted that the resolution of these techniques is normally around 1 nm (i.e. 2-3 uc of LAO or STO). Another technique is a low-energy form of RBS, called medium energy ion spectroscopy (MEIS), which was already introduced in section 2.5. This technique has a better resolution for very thin films (1-2 uc LAO on STO), allowing for careful analysis (with appropriate simulations) of interdiffusion in the thin limit. A good fit to the experimental data (Figure 7.5) is observed for a decreasing La-content throughout the first few monolayers of STO, even for a single deposited uc of LAO [74, 75].

A similar, fully spread picture is obtained from surface x-ray diffraction (SXRD) techniques [20, 76–78]. The refinement of Pauli et al. [20] clearly shows a full range of cation intermixing, with Ti, Sr diffusing into the LAO overlayer and La, Al into the STO substrate (Figure 7.6). From the structural refinement of the SXRD data, a buckling of the LAO layers is observed, which acts to depolarise the built-in electric field [20]. Taking this into account, the authors were able to correctly predict the threshold of 4 uc for the onset of conduction, as predicted from the electronic reconstruction model (section 7.2).

A completely different approach analyses the high temperature LAO/STO transport properties in terms of (oxygen) defect chemistry and compares with pure STO [58, 79].

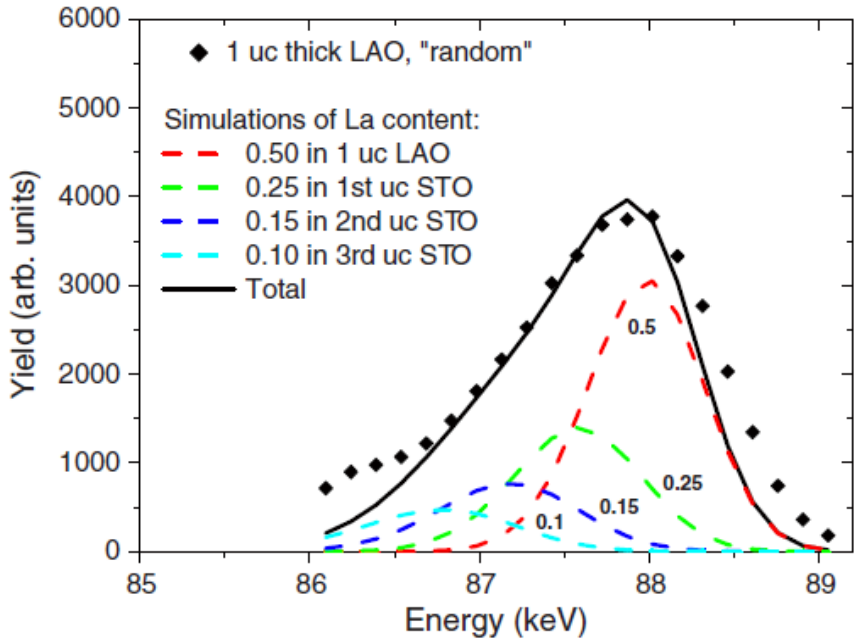

Figure 7.5: Experimental data and model fitting of random MEIS spectra for 1 uc LAO on STO [74].

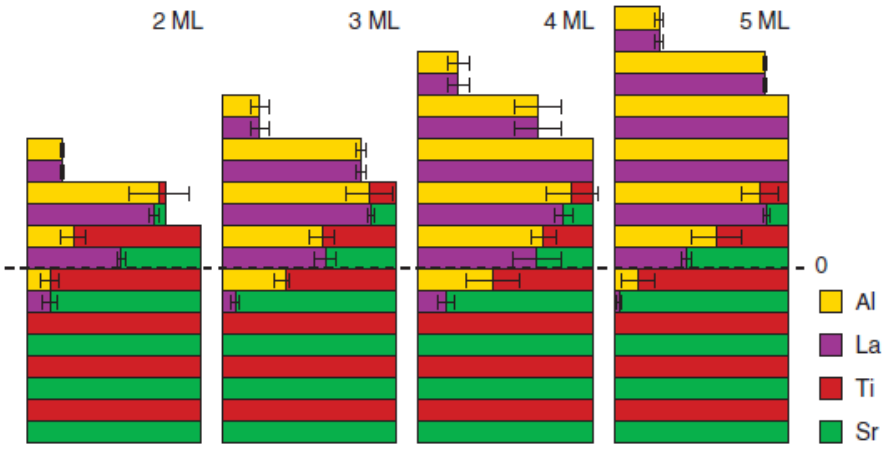

Figure 7.6: Refined cation occupation from SXRD for four LAO film thicknesses depicted as blocks. The horizontal line at 0 marks the nominal interface.[20].

From the calculations, an interface La concentration of 2-5 at% appears plausible. Furthermore, Sr vacancies appear to play a significant role as trapping centres, especially during post-annealing in high oxygen pressures [58].

All the above measurements indicate that the LAO/STO interface is likely to be interdiffused, as could be intuitively expected, although a fully quantitative picture in terms of concentrations and number of layers affected is difficult to obtain. Furthermore it remains unclear to what extent this interdiffusion affects the transport properties of LAO/STO heterostructures.

7.5 A more complicated picture

The actual conduction at the LAO/STO interface appears to be much more complicated than any of the above explanations are able to describe. A first phenomenon is that of carrier localisation. Comparisons between spectroscopy techniques (infrared ellipsometry, second harmonic generation, SHG and resonant inelastic x-ray scattering, RIXS) and transport measurements reveal that a significant number of carriers are present, but localised, which could be one of the reasons why the theoretical 'electronic reconstruction'-carrier density is not observed [15–17, 28, 54, 80]. In any case these studies also confirm that the carriers are confined to a region near the interface. The electrons in the LAO/STO system also appear to have an effective mass of ≈3 times the electron mass [54, 81], although at temperatures below the superconducting transition it appears to be ≈1.45 times the electron mass [35].

Aside from the localised carriers, there is increasing evidence of the presence of two types of carriers with different transport characteristics. The dual-carrier model was initially proposed through band calculations by Popovic et al. [11], where such two bands with different curvature appeared. One set of carriers is highly surface-confined, abundantly present but with a relatively low mobility ('type I'), whereas another kind ('type II') normally has a lower (sheet) carrier density, but a high mobility and lie deeper in the substrate. It is suggested that the type I is a result of the LAO/STO reconstruction and the type II finds its origin in oxygen vacancies in the STO near-surface region with their abundance depending on the oxygen pressure conditions during deposition (see section 7.3). Several groups have also reported experimental evidence for this, obtained through different probing methods. By soft x-ray scattering, Wadati et al. [82] observed a difference in oxygen binding state between interface and bulk, suggesting indeed the presence of two carrier types. As indicated above, type I & II differ in their surface sensitivity: type I carriers are more easily localised or trapped by interface defects, such as transition metals [32], dislocation cores in bicrystals [83] or (single crystal) surface steps [56, 84]. Upon careful analysis, low temperature transport and magnetoresistance measurements also reveal a dual band structure [85–88].

From a different perspective, several authors have observed structural anomalies in LAO/STO heterostructures. It appears that oxygen octahedra rotations occur in the LAO layer due straining of the rhombohedral structure into a perovskite cube on STO and that these rotations decay into the STO substrate. This has been observed by TEM on cross-sections [89] and by HRXRD [90]. Calculations indicate that such rotations could induce or affect a 2DEG at the interface [91, 92]. Salluzzo et al. [93] suggest that the 2DEG is (partially) structural in origin, based on their XAS measurements. Strain also appears to have a strong influence on the transport properties of the 2DEG, which once again points towards a structural factor [94].

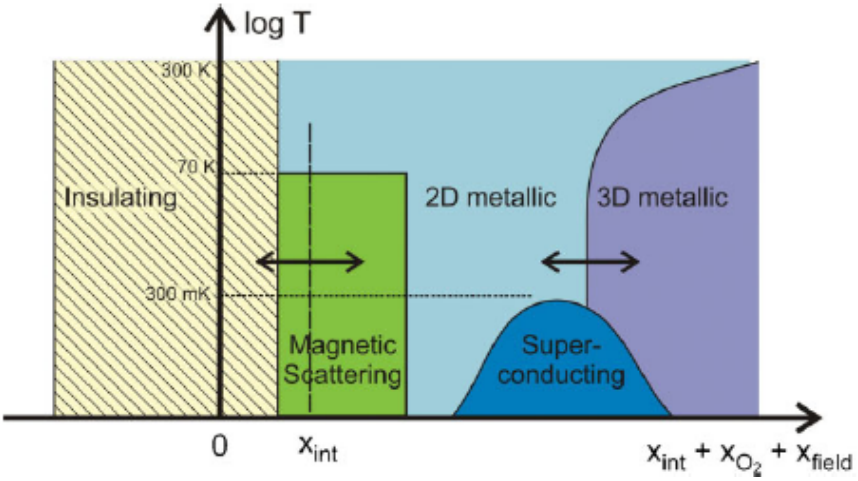

Figure 7.7: Schematic phase diagram of doping versus temperature for LAO/STO interfaces. Three possibilities exist for carrier doping: 'electronic reconstruction' (x_{int}), oxygen vacancies (x_{O_2}) and field effect (x_{field}) [22].

7.6 Functional behaviour

A number of functional properties have been discovered in the LAO/STO 2DEG. The most notable one is that of superconductivity below a temperature of 0.2-0.3 K [95, 96]. The properties of the superconductor are readily tunable (e.g. by back-gating) and exhibit a distinct two-dimensional signature [86, 96–98]. The appearance of this transition is however not so surprising. The electrons, both from the field effect and from the LAO/STO reconstruction (whatever their true origin), are doped into the STO, which is known to become a superconductor at $T_c \approx 0.25$ K [99]. So the superconducting state is not specific to the 2DEG, but rather a property of the STO (substrate). Nevertheless, this superconducting phase shows distinct Shubnikov-de Haas oscillations with a clear two-dimensional signature [35, 86].

Several authors have proposed the presence of ferromagnetism at the LAO/STO interface, based on magnetoresistance measurements [45, 87, 100, 101]. Although this is much more difficult to verify, it is clear that there is a strong spin-orbit coupling in the oxide system, causing an influence of a magnetic field on the transport properties. The superconductivity and magnetism occur for a range of carrier density (introduced through different methods), which leads to the schematic phase diagram presented in Figure 7.7.

Later on, several groups have independently reported the coexistence of superconductivity and ferromagnetism at the LAO/STO interface, observed through different experimental techniques [87, 102, 103]. This can possibly be interpreted in terms of the dual carrier model (section 7.5), whereby the oxygen vacancy-originating STO-like 'type II' electrons are responsible for the superconducting phase and the interface confined 'type I' are subjected to magnetic ordering due to strong spin-orbit coupling. This hypothesis is supported by theoretical simulations [104]. Fitzsimmons et al. [105] measured a very small effective magnetisation of LAO/STO superlattices by polarised neutron reflectometry with a large background signal due to impurities (possibly in the STO substrate). The authors suggest that the much higher effective magnetisations found in [102, 103] are therefore overestimations.

Another interesting phenomenon is the so-called 'memory effect' of the LAO/STO:

when a gate voltage is applied and removed, the 2DEG remains in the lower resistance state [14, 83, 106]. It has been suggested to be the result of electric field-induced motion of defects (e.g. oxygen vacancies), an explanation similar to that advanced for the presence of resistive switching in ion bombarded (and thus reduced) $SrTiO_3$ [107]. This memory effect has been taken a step further by a versatile conductive tip-AFM based write/erase process [108–110]. This mechanism only appears to work on 3 uc LAO/STO structures, not on bare STO, 2 or 4 uc LAO overlayers [108]. Some authors proposed the hypothesis that locally oxygen is removed during the writing process, and adsorption is facilitated during the erase-step. Bi et al. [60] reported that this write/erase-cycle is only possible in water-containing environments, suggesting that oxygen, hydroxyl-ions or hydrogen are essential. The influence of adsorbed hydrogen has been modelled theoretically and was confirmed to donate carriers to the interface [111].

Several groups have attempted to fabricate electronic device structures with the LAO/STO 2DEG [110, 112, 113] or try to employ its unique two-dimensional properties in other uses, such as for the thermoelectric Seebeck effect [34]. Certain polar adsorbates have been demonstrated to modulate the conduction at the LAO/STO interface, indicating an electrostatic effect (section 7.2) but also opening up the possibilities of sensor applications [61].

7.7 Conclusion

Despite the several years of studying a deceptively simple perovskite heterostructure as LAO/STO, a fundamental explanation for its conductive properties is still lacking. A number of defect-related issues need to be resolved for this: the role of oxygen vacancies, the impact of interface interdiffusion and possibly a structural influence. Nevertheless the transport properties of the LAO/STO 2DEG are promising and allow for tailoring of the functional properties and possible applications.

Bibliography

[1] A. Ohtomo and H. Y. Hwang. A high-mobility electron gas at the $LaAlO_3/SrTiO_3$ heterointerface. *Nature*, 427:423–426, 2004.

[2] G. Koster, B. L. Kropman, G. J. H. M. Rijnders, D. H. A. Blank, and H. Rogalla. Quasi-ideal strontium titanate crystal surfaces through formation of strontium hydroxide. *Applied Physics Letters*, 73(20):2920–2922, 1998.

[3] R. Gunnarsson, A. S. Kalabukhov, and D. Winkler. Evaluation of recipes for obtaining single terminated perovskite oxide substrates. *Surface Science*, 603(1):151–157, 2009.

[4] Josée Kleibeuker, Gertjan Koster, Wolter Siemons, David Dubbink, Bouwe Kuiper, Jeroen L. Blok, Chan-Ho Yang, Jayakanth Ravichandran, Ramamoorthy Ramesh, Johan E. ten Elshof, Dave H. A. Blank, and Guus Rijnders. Atomically defined rare-earth scandate crystal surfaces. *Advanced Functional Materials*, 20(20):3490–3496, 2010.

[5] M. Breitschaft, V. Tinkl, N. Pavlenko, S. Paetel, C. Richter, J. R. Kirtley, Y. C. Liao, G. Hammerl, V. Eyert, T. Kopp, and J. Mannhart. Two-dimensional electron liquid state at $LaAlO_3/SrTiO_3$ interfaces. *Physical Review B*, 81:153414, 2010.

[6] J. Mannhart and D. G. Schlom. Oxide interfaces an opportunity for electronics. *Science*, 327:1607, 2010.

[7] Y. C. Liao, T. Kopp, C. Richter, A. Rosch, and J. Mannhart. Metal-insulator transition of the $LaAlO_3$–$SrTiO_3$ interface electron system. *Physical Review B*, 83: 075402, 2011.

[8] Naoyuki Nakagawa, Harold Y. Hwang, and David A. Muller. Why some interfaces cannot be sharp. *Nature Materials*, 5:204–209, 2006.

[9] N. C. Bristowe, P. B. Littlewood, and E. Artacho. Surface defects and conduction in polar oxide heterostructures. *Physical Review B*, 83:205405, 2011.

[10] N. C. Bristowe, Emilio Artacho, and P. B. Littlewood. Oxide superlattices with alternating p and n interfaces. *Physical Review B*, 80:045425, 2009.

[11] Zoran S. Popovic, Sashi Satpathy, and Richard M. Martin. Origin of the two-dimensional electron gas carrier density at the $LaAlO_3$ on $SrTiO_3$ interface. *Physical Review Letters*, 101:256801, 2008.

[12] Rossitza Pentcheva and Warren E. Pickett. Electronic phenomena at complex oxide interfaces: insights from first principles. *Journal of Physics: Condensed Matter*, 22: 043001, 2010.

[13] Pietro Delugas, Alessio Filippetti, Vincenzo Fiorentini, Daniel I. Bilc, Denis Fontaine, and Philippe Ghosez. Spontaneous 2-dimensional carrier confinement at the n-type $SrTiO_3/LaAlO_3$ interface. *Physical Review Letters*, 106:166807, 2011.

[14] S. Thiel, G. Hammerl, A. Schmehl, C. W. Schneider, and J. Mannhart. Tunable quasi-two-dimensional electron gases in oxide heterostructures. *Science*, 313:1942–1945, 2006.

[15] A. Savoia, D. Paparo, P. Perna, Z. Ristic, M. Salluzzo, F. Miletto Granozio, U. Scotti di Uccio, C. Richter, S. Thiel, J. Mannhart, and L. Marrucci. Polar catastrophe and electronic reconstructions at the $LaAlO_3/SrTiO_3$ interface: evidence from optical second harmonic generation. *Physical Review B*, 80:075110, 2009.

[16] A. Rubano, M. Fiebig, D. Paparo, A. Marino, D. Maccariello, U. Scotti di Uccio, F. Miletto Granozio, L. Marrucci, C. Richter, S. Paetel, and J. Mannhart. Spectral and spatial distribution of polarization at the $LaAlO_3/SrTiO_3$ interface. *Physical Review B*, 83:155405, 2011.

[17] M. Takizawa, S. Tsuda, T. Susaki, H. Y. Hwang, and A. Fujimori. Electronic charges and electric potential at $LaAlO_3/SrTiO_3$ interfaces studied by core-level photoemission spectroscopy. *Physical Review B*, 84:245124, 2011.

[18] Y. Segal, J. H. Ngai, J. W. Reiner, F. J. Walker, and C. H. Ahn. X-ray photoemission studies of the metal-insulator transition in $LaAlO_3/SrTiO_3$ structures grown by molecular beam epitaxy. *Physical Review B*, 80:241107, 2009.

[19] Jaekwang Lee and Alexander A. Demkov. Charge origin and localization at the n-type $SrTiO_3/LaAlO_3$ interface. *Physical Review B*, 78:193104, 2008.

[20] S. A. Pauli, S. J. Leake, B. Delley, M. Bjorck, C. W. Schneider, C. M. Schleputz, D. Martoccia, S. Paetel, J. Mannhart, and P. R. Willmott. Evolution of the interfacial structure of $LaAlO_3$ on $SrTiO_3$. *Physical Review Letters*, 106:036101, 2011.

[21] Yun Li and Jaejun Yu. Polarization screening and induced carrier density at the interface of $LaAlO_3$ overlayer on $SrTiO_3$ (001). *Journal of Applied Physics*, 108: 013701, 2010.

[22] Mark Huijben, Alexander Brinkman, Gertjan Koster, Guus Rijnders, Hans Hilgenkamp, and Dave H. A. Blank. Structure-property relation of $SrTiO_3/LaAlO_3$ interfaces. *Advanced Materials*, 21(17):1665–1677, 2009.

[23] Ke-Jin Zhou, Milan Radovic, Justine Schlappa, Vladimir Strocov, Ruggero Frison, Joel Mesot, Luc Patthey, and Thorsten Schmitt. Localized and delocalized Ti 3d carriers in $LaAlO_3/SrTiO_3$ superlattices revealed by resonant inelastic x-ray scattering. *Physical Review B*, 83:201402(R), 2011.

[24] J. Verbeeck, S. Bals, A. N. Kravtsova, D. Lamoen, M. Luysberg, M. Huijben, G. Rijnders, A. Brinkman, H. Hilgenkamp, D. H. A. Blank, and G. Van Tendeloo. Electronic reconstruction at n-type $SrTiO_3/LaAlO_3$ interfaces. *Physical Review B*, 81: 085113, 2010.

[25] M. El Kazzi, C. Merckling, G. Delhaye, L. Arzel, G. Grenet, E. Bergignat, and G. Hollinger. Photoemission (XPS and XPD) study of epitaxial $LaAlO_3$ film grown on $SrTiO_3$ (001). *Materials Science in Semiconductor Processing*, 9:954–958, 2006.

[26] M. Sing, G. Berner, K. Goss, A. Müller, A. Ruff, A. Wetscherek, S. Thiel, J. Mannhart, S. A. Pauli, C. W. Schneider, P. R. Willmott, M. Gorgoi, F. Schäfers, and R. Claessen. Profiling the interface electron gas of $LaAlO_3/SrTiO_3$ heterostructures with hard x-ray photoelectron spectroscopy. *Physical Review Letters*, 102: 176805, 2009.

[27] G. Drera, F. Banfi, F. Federici Canova, P. Borghetti, L. Sangaletti, F. Bondino, E. Magnano, J. Huijben, M. Huijben, G. Rijnders, D. H. A. Blank, H. Hilgenkamp, and A. Brinkman. Spectroscopic evidence of in-gap states at the $SrTiO_3/LaAlO_3$ ultrathin interfaces. *Applied Physics Letters*, 98:052907, 2011.

[28] Y. F. Chu, Y. Y. an Liao, V. T. Tra, J. C. Yang, W. Z. Liu, Y. H. Chu, J. Y. Lin, J. H. Huang, J. Weinen, S. Agrestini, K.-D. Tsuei, and D. J. Huang. Distribution of electronic reconstruction at the *n*-type $LaAlO_3/SrTiO_3$ interface revealed by hard x-ray photemission spectroscopy. *Applied Physics Letters*, 99:262101, 2011.

[29] Hans Boschker. *Perovskite oxide heteroepitaxy – strain and interface engineering.* PhD thesis, Universiteit Twente, 2011.

[30] C. Cancellieri, D. Fontaine, S. Gariglio, N. Reyren, A. D. Caviglia, A. Fete, S. J. Leake, S. A. Pauli, P. R. Willmott, M. Stengel, Ph. Ghosez, and J.-M. Triscone. Electrostriction at the $LaAlO_3/SrTiO_3$ interface. *Physical Review Letters*, 107:056102, 2011.

[31] T. Fix, J. L. MacManus-Driscoll, and M. G. Blamire. Delta-doped $LaAlO_3/SrTiO_3$ interfaces. *Applied Physics Letters*, 94:172101, 2009.

[32] T. Fix, F. Schoofs, J. L. MacManus-Driscoll, and M. G. Blamire. Charge confinement and doping at $LaAlO_3/SrTiO_3$ interfaces. *Physical Review Letters*, 103:166802, 2009.

[33] T. Fix, F. Schoofs, J. L. MacManus-Driscoll, and M. G. Blamire. Influence of doping at the nanoscale at $LaAlO_3/SrTiO_3$ interfaces. *Applied Physics Letters*, 97:072110, 2010.

[34] I. Pallecchi, M. Codda, E. Galleani d'Agliano, D. Marré, A. D. Caviglia, N. Reyren, S. Gariglio, and J.-M. Triscone. Seebeck effect in the conducting $LaAlO_3/SrTiO_3$ interface. *Physical Review B*, 81:085414, 2010.

[35] A. D. Caviglia, S. Gariglio, C. Cancellieri, B. Sacepe, A. Fete, N. Reyren, M. Gabay, A. F. Morpurgo, and J.-M. Triscone. Two-dimensional quantum oscillations of the conductance at $LaAlO_3/SrTiO_3$ interfaces. *Physical Review Letters*, 105:236802, 2010.

[36] Y. Hotta, T. Susaki, and H. Y. Hwang. Polar discontinuity doping of the $LaVO_3/SrTiO_3$ interface. *Physical Review Letters*, 99:236805, 2007.

[37] A. David, R. Frésard, Ph. Boullay, W. Prellier, U. Lüders, and P.-E. Janolin. Structural transition in $LaVO_3/SrVO_3$ superlattices and its influence on transport properties. *Applied Physics Letters*, 98:212106, 2011.

[38] D. F. Li, Yan Wang, and J. Y. Dai. Tunable electronic transport properties of $DyScO_3/SrTiO_3$ polar heterointerface. *Applied Physics Letters*, 98:122108, 2011.

[39] C. Aruta, S. Amoruso, R. Bruzzese, X. Wang, D. Maccariello, F. Miletto Granozio, and U. Scotti di Uccio. Pulsed laser deposition of $SrTiO_3/LaGaO_3$ and $SrTiO_3/LaAlO_3$: plasma plume effects. *Applied Physics Letters*, 97:252105, 2010.

[40] Pouya Moetakef, Tyler A. Cain, Daniel G. Ouellette, Jack Y. Zhang, Dmitri O. Klenov, Anderson Janotti, Chris G. Van de Walle, Siddharth Rajan, S. James Allen, and Susanne Stemmer. Electrostatic carrier doping of $GdTiO_3/SrTiO_3$ interfaces. *Applied Physics Letters*, 99:232116, 2011.

[41] S. A. Chambers, L. Qiao, T. C. Droubay, T. C. Kaspar, B. W. Arey, and P. V. Sushko. Band alignment, built-in potential and the absence of conductivity at the $LaCrO_3/SrTiO_3$ heterojunction. *Physical Review Letters*, 107:206802, 2011.

[42] D. Bäuerle and W. Rehwald. Structural phase transitions in semiconducting $SrTiO_3$. *Solid State Communications*, 27:1343–1346, 1978.

[43] Wolter Siemons, Gertjan Koster, Hideki Yamamoto, Theodore H. Geballe, Dave H. A. Blank, and Malcolm R. Beasley. Experimental investigation of electronic properties of buried heterointerfaces of $LaAlO_3$ on $SrTiO_3$. *Physical Review B*, 76: 155111, 2007.

[44] G. Herranz, M. Basletic, M. Bibes, C. Carretero, E. Tafra, E. Jacquet, K. Bouzehouane, C. Deranlot, A. Hamzic, J.-M. Broto, A. Barthelemy, and A. Fert. High mobility in $LaAlO_3/SrTiO_3$ heterostructures: origin, dimensionality and perspectives. *Physical Review B*, 98:216803, 2007.

[45] A. Brinkman, M. Huijben, M. Van Zalk, J. Huijben, U. Zeitler, J. C. Maan, W. G. Van Der Wiel, G. Rijnders, D. H. A. Blank, and H. Hilgenkamp. Magnetic effects at the interface between non-magnetic oxides. *Nature Materials*, 6:493–496, 2007.

[46] Alexey S. Kalabukhov, Robert Gunnarsson, Johan Börjesson, Eva Olsson, Tord Claeson, and Dag Winkler. Effect of oxygen vacancies in the $SrTiO_3$ substrate on the electrical properties of the $LaAlO_3/SrTiO_3$ interface. *Physical Review B*, 75: 121404, 2007.

[47] A. Koitzsch, J. Ocker, M. Knupfer, M. C. Dekker, K. Dörr, B. Büchner, and P. Hoffmann. In-gap electronic structure of $LaAlO_3$-$SrTiO_3$ heterointerfaces investigaged by soft x-ray spectroscopy. *Physical Review B*, 84:245121, 2011.

[48] M. Basletic, J.-L. Maurice, C. Carrétéro, G. Herranz, O. Copie, M. Bibes, E. Jacquet, K. Bouzehouane, S. Fusil, and A. Barthélémy. Mapping the spatial distribution of charge carriers in $LaAlO_3/SrTiO_3$ heterostructures. *Nature Materials*, 7:621–625, 2008.

[49] G. Herranz, M. Basletic, O. Copie, M. Bibes, A. N. Khodan, C. Carrétéro, E. Tafra, E. Jacquet, K. Bouzehouane, A. Hamzic, and A. Barthélémy. Controlling high-mobility conduction in $SrTiO_3$ by oxide thin film deposition. *Applied Physics Letters*, 94:012113, 2009.

[50] C. W. Schneider, M. Esposito, I. Marozau, K. Conder, M. Doebeli, Yi Hu, M. Mallepell, A. Wokaun, and T. Lippert. The origin of oxygen in oxide thin films: role of the substrate. *Applied Physics Letters*, 97:192107, 2010.

[51] Keisuke Shibuya, Tsuyoshi Ohnishi, Mikk Lippmaa, and Masaharu Oshima. Metallitc conductivity at the $CaHfO_3/SrTiO_3$ interface. *Applied Physics Letters*, 91: 232106, 2007.

[52] A. F. Santander-Syro, O. Copie, T. Kondo, F. Fortuna, S. Pailhes, R. Weht, X. G. Qiu, F. Bertran, A. Nicolaou, A. Taleb-Ibrahimi, P. Le Fevre, G. Herranz, M. Bibes, N. Reyren, Y. Apertet, P. Lecoeur, A. Barthelemy, and M. J. Rozenberg. Two-dimensional electron gas with universal subbands at the surface of $SrTiO_3$. *Nature*, 469:189–194, 2011.

[53] Heiko Gross, Namrata Bansal, Yong-Seung Kim, and Seongshik Oh. In situ study of emerging metallicity of ion-bombarded $SrTiO_3$ surface. *Journal of Applied Physics*, 110:073704, 2011.

[54] A. Dubroka, M. Rössle, K. W. Kim, V. K. Malik, L. Schultz, S. Thiel, C. W. Schneider, J. Mannhart, G. Herranz, O. Copie, M. Bibes, A. Barthélémy, and C. Bernhard. Dynamical response and confinement of the electrons at the $LaAlO_3/SrTiO_3$ interface. *Physical Review Letters*, 104:156807, 2010.

[55] Wei Wei and Alp Sehirlioglu. Strain relaxation analysis of $LaAlO_3/SrTiO_3$ heterostructure using reciprocal lattice mapping. *Applied Physics Letters*, 100:071901, 2012.

[56] T. Fix, F. Schoofs, Z. Bi, A. Chen, H. Wang, J. L. MacManus-Driscoll, and M. G. Blamire. Influence of $SrTiO_3$ substrate miscut angle on the transport properties of $LaAlO_3/SrTiO_3$ interfaces. *Applied Physics Letters*, 99:022103, 2011.

[57] W. M. Lü, X. Wang, Z. Q. Liu, S. Dhar, A. Annadi, K. Gopinadhan, A. Roy Barman, H. B. Su, T. Venkatesan, and Ariando. Metal-insulator transition at a depleted $LaAlO_3/SrTiO_3$ interface: evidence for charge transfer induced by $SrTiO_3$ phase transitions. *Applied Physics Letters*, 99:172103, 2011.

[58] F. Gunkel, P. Brinks, S. Hoffmann-Eifert, R. Dittmann, M. Huijben, J. E. Kleibeuker, G. Koster, G. Rijnders, and R. Waser. Influence of charge compensation mechanisms on the sheet electron density at conducting $LaAlO_3/SrTiO_3$-interfaces. *Applied Physics Letters*, 100:052103, 2012.

[59] Yun Li, Sutassana Na Phattalung, Sukit Limpijumnong, Jiyeon Kim, and Jaejun Yu. Formation of oxygen vacancies and charge carriers induced in the n-type interface of a $LaAlO_3$ overlayer on $SrTiO_3$ (001). *Physical Review B*, 84:245307, 2011.

[60] Feng Bi, Daniela F. Bogorin, Cheng Cen, Chung Wung Bark, Jae-Wan Park, Chang-Beom Eom, and Jeremy Levy. 'water-cycle' mechanism for writing and erasing nanostructures at the $LaAlO_3/SrTiO_3$ interface. *Applied Physics Letters*, 97:173110, 2010.

[61] Yanwu Xie, Yasuyuki Hikita, Christopher Bell, and Harold Y. Hwang. Control of electronic conduction at an oxide heterointerface using surface polar adsorbates. *Nature Communications*, 2:494, 2011.

[62] W. A. Harrison, E. A. Kraut, J. R. Waldrop, and R. W. Grant. Polar heterojunction interfaces. *Physical Review B*, 18(8):4402–4410, 1978.

[63] Jian Liu, M. Kareev, S. Prosandeev, B. Gray, P. Ryan, J. W. Freeland, and J. Chakhalian. Effect of polar discontinuity on the growth of $LaNiO_3/LaAlO_3$ superlattices. *Applied Physics Letters*, 96:133111, 2010.

[64] Hanghui Chen, Alexie M. Kolpak, and Sohrab Ismail-Beigi. Electronic and magnetic properties of $SrTiO_3/LaAlO_3$ interfaces from first principles. *Advanced Materials*, 22(26-27):2881–2899, 2010.

[65] N. G. Eror and U. Balachandran. Self-compensation in lanthanum-doped strontium titanate. *Journal of Solid State Chemistry*, 40:85–91, 1981.

[66] Joseph E. Sunstrom, Susan M. Kauzlarich, and Peter Klavins. Synthesis, structure and properties of $La_{1-x}Sr_xTiO_3$ ($0 \leq x \leq 1$). *Chemistry of Materials*, 4:346–353, 1992.

[67] Y. Tokura, Y. Taguchi, Y. Okada, Y. Fujishima, T. Arima, K Kumagai, and Y. Iye. Filling dependence of electronic properties on the verge of the metal–Mott-insulator transitions in $Sr_{1-x}La_xTiO_3$. *Physical Review Letters*, 70(14):2126–2129, 1993.

[68] A. Ohtomo, J. Nishimura, Y. Murakami, and M. Kawasaki. Electronic transport properties in $SrTiO_3$–$LaAlO_3$ solid-solution films. *Applied Physics Letters*, 88: 232107, 2006.

[69] Bharat Jalan, Susanne Stemmer, Shawn Mack, and S. James Allen. Two-dimensional electron gas in δ-doped $SrTiO_3$. *Physical Review B*, 82:081103, 2010.

[70] Junwoo Son, Pouya Moetakef, Bharat Jalan, Oliver Bierwagen, Nicholas J. Wright, Roman Engel-Herbert, and Susanne Stemmer. Epitaxial $SrTiO_3$ films with electron mobilities exceeding 30,000 $cm^2\ V^{-1}\ s^{-1}$. *Nature Materials*, 9:482–484, 2010.

[71] Meng Gu, Craig R. Dearden, Chengyu Song, Nigel D. Browning, and Yayoi Takamura. Structural variability in $La_{0.5}Sr_{0.5}TiO_{3\pm\delta}$ thin films. *Applied Physics Letters*, 99:261907, 2011.

[72] S. A. Chambers, M. H. Engelhard, V. Shutthanandan, Z. Zhu, T. C. Droubay, L. Qiao, P. V. Sushko, T. Feng, H. D. Lee, T. Gustafsson, E. Garfunkel, A. B. Shah, J.-M. Zuo, and Q. M. Ramasse. Instability, intermixing and electronic structure at the epitaxial $LaAlO_3/SrTiO_3$ (001) heterojunction. *Surface Science Reports*, 65: 317–352, 2010.

[73] L. Qiao, T. C. Droubay, V. Shutthanandan, Z. Zhu, P. V. Sushko, and S. A. Chambers. Thermodynamic instability at the stoichiometric $LaAlO_3/SrTiO_3$ (001) interface. *Journal of Physics: Condensed Matter*, 22:312201, 2010.

[74] A. S. Kalabukhov, Yu. A. Boikov, I. T. Serenkov, V. I. Sakharov, V. N. Popok, R. Gunnarsson, J. Börjesson, N. Ljustina, E. Olsson, D. Winkler, and T. Claeson. Cationic disorder and phase segregation in $LaAlO_3/SrTiO_3$ heterointerfaces evidenced by medium-energy ion spectroscopy. *Physical Review Letters*, 103:146101, 2009.

[75] A. Kalabukhov, Yu. A. Boikov, I. T. Serenkov, V. I. Sakharov, J. Börjesson, N. Ljustina, E. Olsson, D. Winkler, and T. Claeson. Improved cationic stoichiometry and insulating behavior at the interface of $LaAlO_3/SrTiO_3$ formed at high oxygen pressure during pulsed laser deposition. *Europhysics Letters*, 93(3):37001, 2011.

[76] P. R. Willmott, S. A. Pauli, R. Herger, C. M. Schlepütz, D. Martoccia, B. D. Patterson, B. Delley, R. Clarke, D. Kumah, C. Cionca, and Y. Yacoby. Structural basis for the conducting interface between $LaAlO_3$ and $SrTiO_3$. *Physical Review Letters*, 99:155502, 2007.

[77] Ryosuke Yamamoto, Christopher Bell, Yasuyuki Hikita, Harold Y. Hwang, Hiroyuki Nakamura, Tsuyoshi Kimura, and Yusuke Wakabayashi. Structural comparison of n-type and p-type $LaAlO_3/SrTiO_3$ interfaces. *Physical Review Letters*, 107:036104, 2011.

[78] V. Vonk, J. Huijben, D. Kukuruznyak, A. Stierle, H. Hilgenkamp, A. Brinkman, and S. Harkema. Polar-discontinuity-retaining a-site intermixing and vacancies at $SrTiO_3/LaAlO_3$ interfaces. *Physical Review B*, 85:045401, 2012.

[79] F. Gunkel, S. Hoffman-Eifert, R. Dittmann, S. B. Mi, C. L. Jia, P. Meuffels, and R. Waser. High temperature conductance characteristics of $LaAlO_3/SrTiO_3$-heterostructures under equilibrium oxygen atmospheres. *Applied Physics Letters*, 97:012103, 2010.

[80] G. Berner, S. Glawion, J. Walde, F. Pfaff, H. Hollmark, L.-C. Duda, S. Paetel, C. Richter, J. Mannhart, M. Sing, and R. Claessen. $LaAlO_3/SrTiO_3$ oxide heterostructures studied by resonant inelastic x-ray scattering. *Physical Review B*, 82: 241405(R), 2010.

[81] D. Rakhmilevitch, M. Ben Shalom, M. Eshkol, A. Tsukernik, A. Palevski, and Y. Dagan. Phase coherent transport in $SrTiO_3/LaAlO_3$ interfaces. *Physical Review B*, 82: 235119, 2010.

[82] H. Wadati, J. Geck, D. G. Hawthorn, T. Higuchi, M. Hosoda, C. Bell, Y. Hikita, H. Y. Hwang, C. Schussler-Langeheine, E. Schierle, E. Weschke, and G. A. Sawatzky. Electronic structure of the $SrTiO_3/LaAlO_3$ interface revealed by resonant soft x-ray scattering. *IOP Conference Series: Materials Science and Engineering*, 24:012012, 2011.

[83] S. Thiel, C. W. Schneider, L. Fitting Kourkoutis, D. A. Muller, N. Reyren, A. D. Caviglia, S. Gariglio, J.-M. Triscone, and J. Mannhart. Electron scattering at dislocations in $LaAlO_3/SrTiO_3$ interfaces. *Physical Review Letters*, 102:046809, 2009.

[84] P. Brinks, W. Siemons, J. E. Kleibeuker, G. Koster, G. Rijnders, and M. Huijben. Anisotropic electrical transport properties of a two-dimensional electron gas at $SrTiO_3$–$LaAlO_3$ interfaces. *Applied Physics Letters*, 98:242904, 2011.

[85] Franklin J. Wong, Seung-Hyub Baek, Rajesh V. Chopdekar, Virat V. Mehta, Ho-Won Jang, Chang-Beom Eom, and Yuri Suzuki. Metallicity in $LaTiO_3$ thin films induced by lattice deformation. *Physical Review B*, 81:161101, 2010.

[86] M. Ben Shalom, A. Ron, A. Palevski, and Y. Dagan. Shubnikov–De Haas oscillations in $SrTiO_3/LaAlO_3$ interface. *Physical Review Letters*, 105:206401, 2010.

[87] D. A. Dikin, M. Mehta, C. W. Bark, C. M. Folkman, C. B. Eom, and V. Chandrasekhar. Coexistence of superconductivity and ferromagnetism in two dimensions. *Physical Review Letters*, 107:056802, 2011.

[88] S. Lerer, M. Ben Shalom, G. Deutscher, and Y. Dagan. Low-temperature dependence of the thermomagnetic transport properties of the $SrTiO_3/LaAlO_3$ interface. *Physical Review B*, 84:075423, 2011.

[89] C. L. Jia, S. B. Mi, M. Faley, U. Poppe, J. Schubert, and K. Urban. Oxygen octahedron reconstruction in the $SrTiO_3/LaAlO_3$ heterointerfaces investigated using aberration-corrected ultrahigh-resolution transmission electron microscopy. *Physical Review B*, 79:081405(R), 2009.

[90] J. E. Boschker, C. Folkman, C. W. Bark, A. F. Monsen, E. Folven, J. K. Grepstad, E. Wahlström, C. B. Eom, and T. Tybell. Structural coupling across the $LaAlO_3/SrTiO_3$ interface: high-resolution x-ray diffraction study. *Physical Review B*, 84:205418, 2011.

[91] Satoshi Okamoto, Andrew J. Millis, and Nicola A. Spaldin. Lattice relaxation in oxide heterostructures: $LaTiO_3/SrTiO_3$ superlattices. *Physical Review Letters*, 97: 056802, 2006.

[92] N. Lazarides, V. Paltoglou, P. Maniadis, G. P. Tsironis, and C. Panagopoulos. Strain-induced interface reconstruction in epitaxial heterostructures. *Physical Review B*, 84:245428, 2011.

[93] M. Salluzzo, J. C. Cezar, N. B. Brookes, V. Bisogni, G. M. De Luca, C. Richter, S. Thiel, J. Mannhart, M. Huijben, A. Brinkman, G. Rijnders, and G. Ghiringhelli. Orbital reconstruction and the two-dimensional electron gas at the $LaAlO_3/SrTiO_3$ interface. *Physical Review Letters*, 102:166804, 2009.

[94] C. W. Bark, D. A. Felker, Y. Wang, Y. Zhang, H. W. Jang, C. M. Folkman, J. W. Park, S. H. Baek, H. Zhou, D. D. Fong, X. Q. Pan, E. Y. Tsymbal, M. S. Rzchowski, and C. B. Eom. Tailoring a two-dimensional electron gas at the $LaAlO_3/SrTiO_3$ (001) interface by epitaxial strain. *Proceedings of the National Academy of Sciences of the United States of America*, 108(12):4720–4724, 2011.

[95] N. Reyren, S. Thiel, A. D. Caviglia, L. Fitting Kourkoutis, G. Hammerl, C. Richter, C. W. Schneider, T. Kopp, A.-S. Rüetschi, D. Jaccard, M. Gabay, D. A. Muller, J.-M. Triscone, and J. Mannhart. Superconducting interfaces between insulating oxides. *Science*, 317:1196, 2007.

[96] A. D. Caviglia, S. Gariglio, N. Reyren, D. Jaccard, T. Schneider, M. Gabay, S. Thiel, G. Hammerl, J. Mannhart, and J.-M. Triscone. Electric field control of the $LaAlO_3/SrTiO_3$ interface ground state. *Nature*, 456:624–627, 2008.

[97] A. D. Caviglia, M. Gabay, S. Gariglio, N. Reyren, C. Cancellieri, and Triscone J.-M. Tunable Rashba spin-orbit interaction at oxide interfaces. *Physical Review Letters*, 104:126803, 2010.

[98] M. Ben Shalom, M. Sachs, D. Rakhmilevitch, A. Palevski, and Y. Dagan. Tuning spin-orbit coupling and superconductivity at the $SrTiO_3/LaAlO_3$ interface: a magnetotransport study. *Physical Review Letters*, 104:126802, 2010.

[99] J. F. Schooley, W. R. Hosler, and Marvin L. Cohen. Superconductivity in semiconducting $SrTiO_3$. *Physical Review Letters*, 12(17):474–475, 1964.

[100] M. Sachs, D. Rakhmilevitch, M. Ben Shalom, S. Shefler, A. Palevski, and Y. Dagan. Anomalous magneto-transport at the superconducting interface between $LaAlO_3$ and $SrTiO_3$. *Physica C: Superconductivity*, 470:S746, 2010.

[101] X. Wang, W. M. Lü, A. Annadi, Z. Q. Liu, K. Gopinadhan, S. Dhar, T. Venkatesan, and Ariando. Magnetoresistance of two-dimensional and three-dimensional electron gas in $LaAlO_3/SrTiO_3$ heterostructures: influence of magnetic ordering, interface scattering and dimensionality. *Physical Review B*, 84:075312, 2011.

[102] Lu Li, C. Richter, J. Mannhart, and R. C. Ashoori. Coexistence of magnetic order and two-dimensional superconductivity at $LaAlO_3/SrTiO_3$ interfaces. *Nature Physics*, 7:762–766, 2011.

[103] Julia A. Bert, Beena Kalisky, Christopher Bell, Minu Kim, Yasuyuki Hikita, Harold Y. Hwang, and Kathryn A. Moler. Direct imaging of the coexistence of ferromagnetism and superconductivity at the $LaAlO_3/SrTiO_3$ interface. *Nature Physics*, 7:767–771, 2011.

[104] N. Pavlenko, T. Kopp, E. Y. Tsymbal, G. A. Sawatzky, and J. Mannhart. Magnetic and superconducting phases at the $LaAlO_3/SrTiO_3$ interface: the role of interfacial Ti $3d$ electrons. *Physical Review B*, 85:020407(R), 2012.

[105] M. R. Fitzsimmons, N. W. Hengartner, S. Singh, M. Zhernenkov, F. Y. Bruno, J. Santamaria, A. Brinkman, M. Huijben, H. J. A. Molegraaf, J. de la Venta, and Ivan K. Schuller. Upper limit to magnetism in $LaAlO_3/SrTiO_3$ heterostructures. *Physical Review Letters*, 107:217201, 2011.

[106] Y. Z. Chen, J. L. Zhao, J. R. Sun, N. Pryds, and B. G. Shen. Resistance switching at the interface of $LaAlO_3/SrTiO_3$. *Applied Physics Letters*, 97:123102, 2010.

[107] Heiko Gross and Seongshik Oh. Efficient resistive memory effect on $SrTiO_3$ by ionic-bombardment. *Applied Physics Letters*, 99:092105, 2011.

[108] C. Cen, S. Thiel, G. Hammerl, C. W. Schneider, K. E. Andersen, C. S. Hellberg, J. Mannhart, and J. Levy. Nanoscale control of an interfacial metal-insulator transition at room temperature. *Nature Materials*, 7:298–302, 2008.

[109] Cheng Cen, Stefan Thiel, Jochen Mannhart, and Jeremy Levy. Oxide nanoelectronics on demand. *Science*, 323:1026–1030, 2009.

[110] Daniela F. Bogorin, Chung Wung Bark, Ho Won Jang, Cheng Cen, Chad M. Folkman, Chang-Beom Eom, and Jeremy Levy. Nanoscale rectification at the $LaAlO_3/SrTiO_3$ interface. *Applied Physics Letters*, 97:013102, 2010.

[111] Won-koon Son, Eunae Cho, Jaichan Lee, and Seungwu Han. Hydrogen adsorption and carrier generation in $LaAlO_3$–$SrTiO_3$ heterointerfaces: a first-principles study. *Journal of Physics: Condensed Matter*, 22:315501, 2010.

[112] R. Jany, M. Breitschaft, G. Hammerl, A. Horsche, C. Richter, S. Paetel, J. Mannhart, N. Stucki, N. Reyren, S. Gariglio, P. Zubko, A. D. Caviglia, and J.-M. Triscone. Diodes with breakdown voltages enhanced by the metal-insulator transition of $LaAlO_3$-$SrTiO_3$ interfaces. *Applied Physics Letters*, 96:183504, 2010.

[113] B. Förg, C. Richter, and J. Mannhart. Field-effect devices utilizing $LaAlO_3$–$SrTiO_3$ interfaces. *Applied Physics Letters*, 100:053506, 2012.

Chapter 8

Fabrication of LAO/STO heterostructures

This chapter gives an overview of the deposition procedure of LAO/STO heterostructure and provides some general structural characteristics.

8.1 PLD of LAO/STO

Samples are prepared in the PLD system presented in section 2.1. The substrates are TiO_2-terminated 5x10x1 mm^3 $SrTiO_3$ single crystals, oriented in the (001) direction, supplied by Crystal GmbH. The single unit height termination is verified by AFM (Figure 8.1). The targets are either commercially sintered ones ($SrTiO_3$, a = 3.905 Å; $LaAlO_3$, pseudo-cubic a = 3.790 Å) or custom made following the procedure outlined in section 2.1.2. The starting powders are: $SrCO_3$ (Alfa Aesar, 99.99%), TiO_2 (Alfa Aesar, 99.99%), Co_3O_4 (Alfa Aesar, 99.9985%), $CaCO_3$ (Sigma Aldrich, 99.995+%), $BaCO_3$ (Alfa Aesar, 99.99%), SnO_2 (Alfa Aesar, 99.9%) La_2O_3 (Alfa Aesar, 99.99%), Nd_2O_3 (Alfa Aesar, 99.99%), Sm_2O_3 (Alfa Aesar, 99.99%), Dy_2O_3 (Alfa Aesar, 99.99%).

Before deposition, the STO substrates are annealed for approximately 10 minutes in 10^{-2} mbar O_2 at 850 ℃, irrespective of the deposition pressure or temperature afterwards. The repetition rate is set to 10 Hz. The substrate heater temperature is 850 ℃ and the oxygen pressure during depositing and cooling down was around 10^{-2} mbar, unless otherwise specified. The laser fluence is 1 J/cm^2 for the deposition of all films, except for $CoTiO_3$ (1.5 J/cm^2; see chapter 14). However in chapter 10, the laser fluence is varied during deposition of LAO to study the impact of that parameter.

8.2 RHEED on LAO/STO

The growth of the perovskites is monitored by RHEED to determine the number of unit cells (uc) deposited. At a laser fluence of $\approx$ 1 J/cm^2 around 150 pulses are required per LAO uc and around 100 pulses for one STO (or doped STO) uc. The intensity oscillations of the specular spot during the growth of LAO on STO are shown in Figure 8.2. The RHEED diffraction patterns corresponding to 0 uc (STO substrate), 5 uc LAO and 15 uc LAO are presented in Figure 8.3 – their streaky character indicating 2D growth is clearly visible.

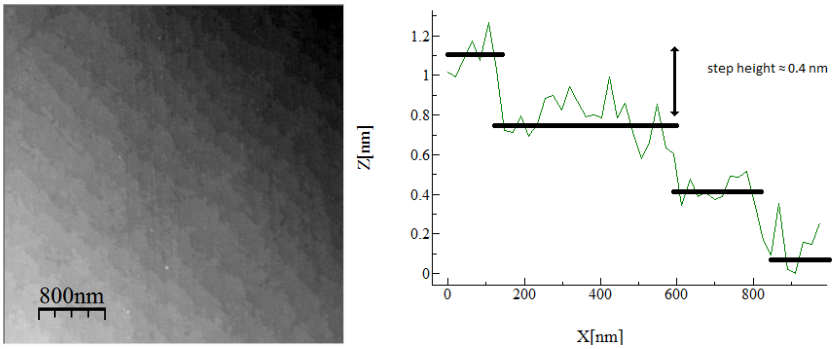

(a) (b)

Figure 8.1: **(a)** AFM topography image of a TiO_2-terminated $SrTiO_3$ (001) substrate exhibiting steps **(b)** Single unit cell step height visible on a line scan across the surface steps.

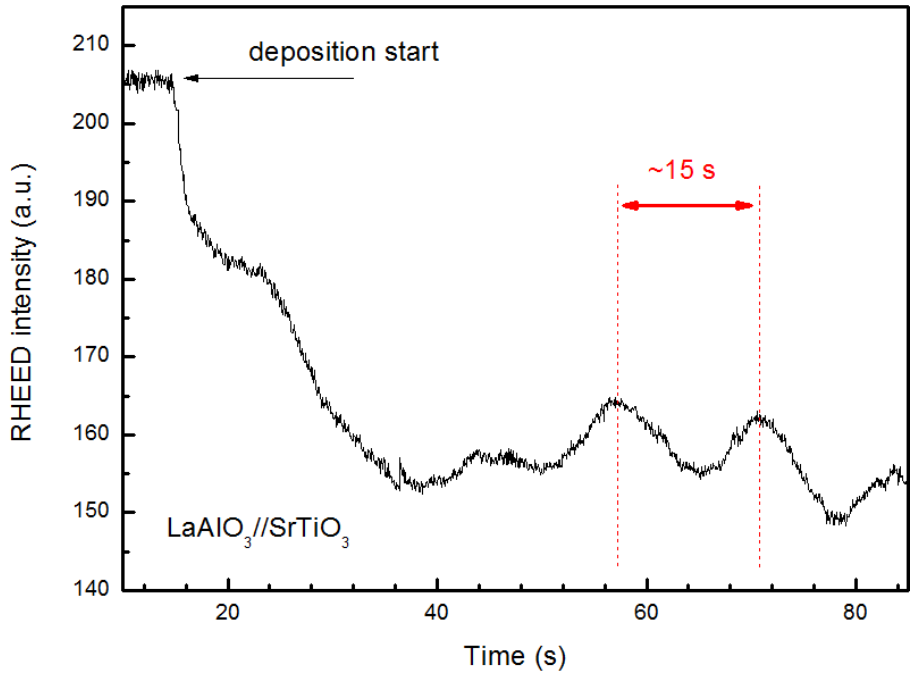

Figure 8.2: RHEED intensity oscillations for heteroepitaxial growth of LAO on STO, at a laser fluence of 1 J/cm^2 and a repetition rate of 10 Hz.

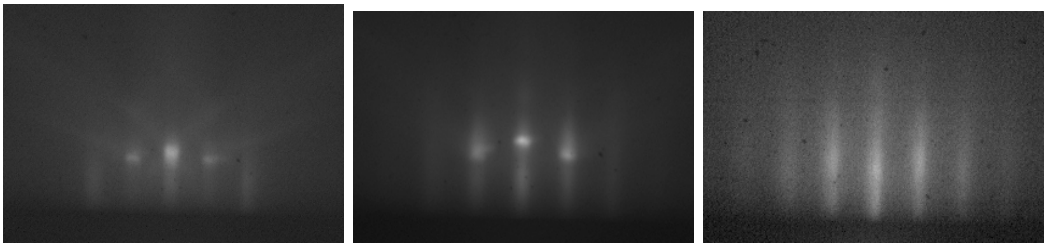

(a) (b) (c)

Figure 8.3: RHEED diffraction patterns of **(a)** a bare STO substrate **(b)** 5 uc LAO//STO and **(c)** 15 uc LAO//STO.

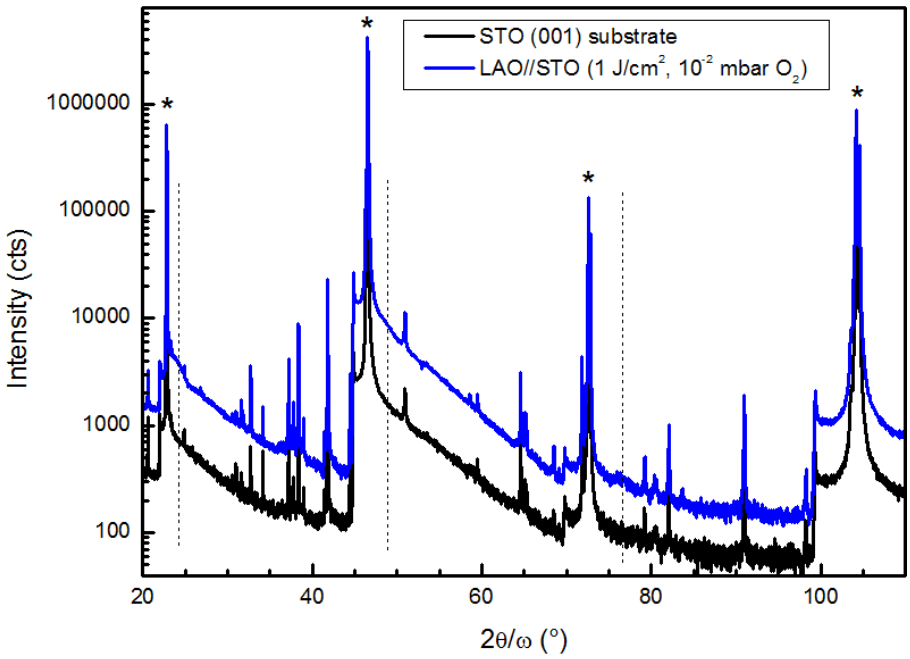

Figure 8.4: XRD $2\theta/\omega$ measurement (diffractometer B1) on a regular LAO//STO sample. The STO (0 0 l) substrate peaks are indicated by a star (*), the positions of the LAO (0 0 l) film peaks are indicated by dashed lines. The sharp lines between the substrate peaks are impurity lines related to the instrument as they also occur in the pure substrate reference sample (shown in black).

8.3 XRD of LAO/STO

It is possible to obtain an XRD diffraction pattern of 15 uc LAO samples on diffractometer B1, although the LAO peaks are fairly weak compared to the high background (Figure 8.4). Diffractometer B2 should have better resolution, but here the peaks are not well resolved compared to the background of the STO peak. It is however possible to obtain good quality reciprocal space maps of the $(\bar{1}\ 0\ 3)$ reflections, indicating (usually) fully in-plane strained LAO on STO (see section 10.3).

8.4 Influence of substrate temperature during deposition

As a quick optimisation, 15 uc LAO//STO samples were grown under the same oxygen (10^{-2} mbar), repetition rate (10 Hz) and laser fluence (1 J/cm^2) conditions, but with different substrate heater temperatures (600–700–850 °C). The resistance versus temperature of these samples is shown in Figure 8.5. There appears to be a significant difference, with a higher deposition temperature causing a decrease in the resistivity and corresponding metal-insulator transition temperature. The reason for this is most likely structural in origin (inset of Figure 8.5). The rocking curve full width at half maximum (FWHM) of these samples (normalised by the substrate's FWHM) appears to increase with decreasing deposition temperature. This indicates a deterioration of the structural and epitaxial quality of the LAO film, as can be expected based on an exponentially decreasing surface diffusivity of the deposited species. The implication is that a pure intermixing effect (section 7.4) can not explain this dependency. Instead, the structural defect management of the LAO seems to play a key role, as will be further elaborated in the following chapters.

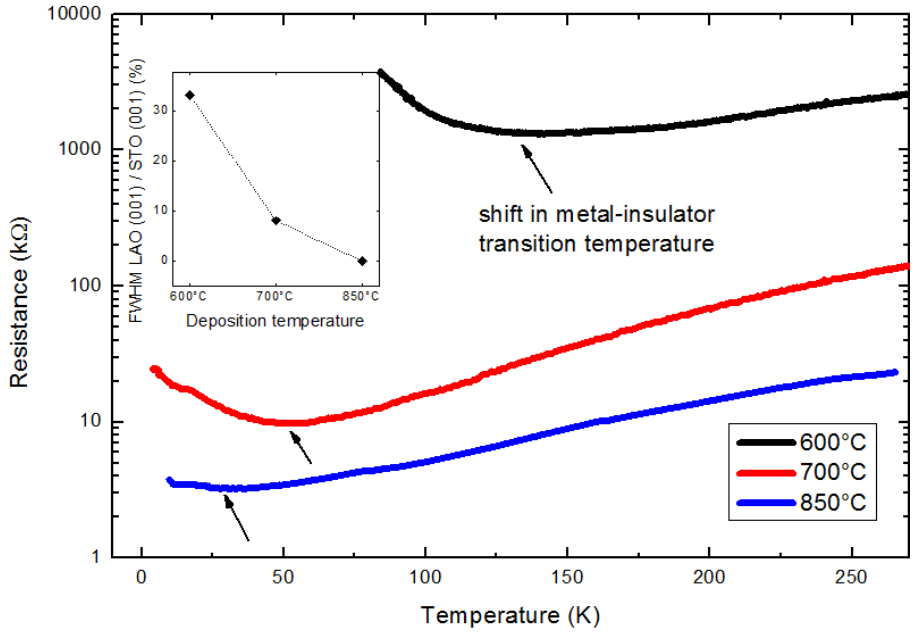

Figure 8.5: Resistance versus temperature for 15 uc LAO//STO heterostructures grown at different substrate temperatures. The inset shows the rocking curve full width at half maximum of the LAO (0 0 1) reflection with respect to the substrate's STO (0 0 1).

Chapter 9

Oxygen vacancies in LAO/STO heterostructures

In this first chapter on the conductive properties of LAO/STO, the influence of oxygen pressure during the deposition of LAO/STO heterostructures is investigated. This results in a clear and distinctly different picture, exhibiting fundamentally different conduction mechanisms, based on the relative abundance of oxygen vacancies in the substrate.

9.1 Introduction

As mentioned in section 7.3, the oxygen pressure during deposition of LAO on STO has a significant impact on the conduction of the LAO/STO 2DEG – if it still can be called a 2DEG in this case. This chapter intends to independently prove the distinct difference between samples deposited in low (10^{-4} mbar) and high (10^{-2} mbar) oxygen pressure. The next step is to identify the key differences in the conductive behaviour, i.e. the dominant scattering mechanism as derived from resistance versus temperature plots.

9.2 Proving the presence of oxygen vacancies

When the oxygen partial pressure during deposition is higher than 10^{-3} mbar, it is commonly accepted that the majority of the conduction is via an interfacial 2DEG, whereas samples produced at lower oxygen partial pressure exhibit properties dominated by the bulk of the oxygen deficient STO substrate (see section 7.3). Photoluminescence spectra can reveal the relative abundance of these oxygen vacancies. Due to the low thickness (≈ 6 nm) and the large bandgap (5.6 eV) of the LAO, the PL measurement in Figure 9.1 is expected to show only transitions related to the STO substrate. The only significant feature on the PL spectra appears as a bandgap-related peak – the bandgap of STO lies around 388 nm (3.2 eV). The broadness of the peak is related to thermal smearing, as observed for ZnO in section 4.2. The peak in the LAO/STO spectra occurs at a higher wavelength, indicating that the transition is not from the conduction band to the valence band, but rather originating from a defect level close to the conduction band. Since oxygen vacancies act as donor states in the STO (see e.g. [1]), this transition (and the corresponding peak area) is most likely related to their concentration.

Even in the as-received substrate some PL intensity is observed, indicating the presence of oxygen vacancy defect states. Their concentration increases slightly after deposition of LAO at 10^{-2} mbar oxygen. However for the samples deposited in 10^{-4} and 10^{-5} mbar

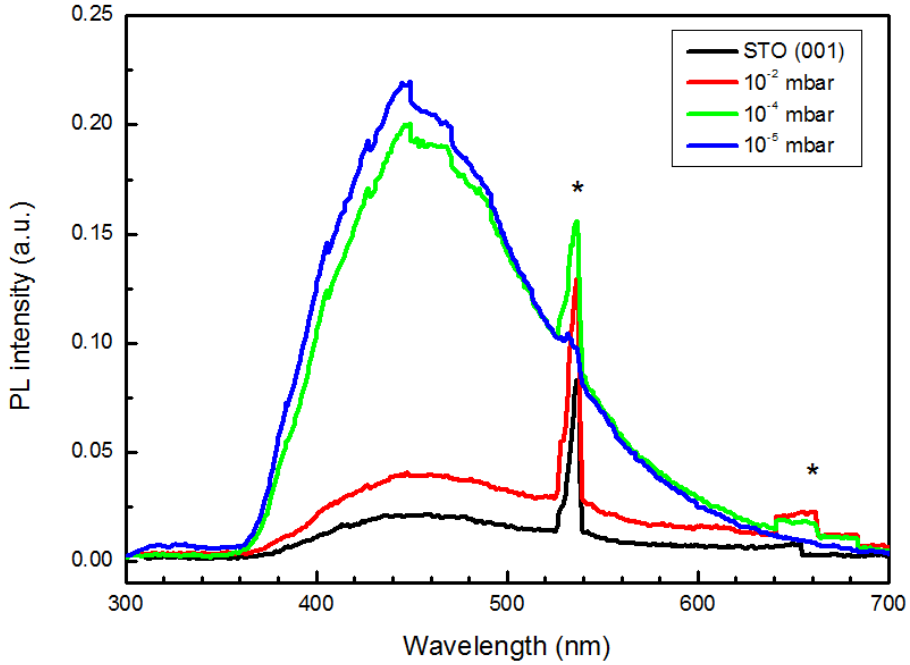

Figure 9.1: Photoluminescence spectra of a STO (0 0 1) substrate (as received) and LAO/STO samples deposited at different oxygen pressures. Measurement artefacts from the equipment are marked by a star (*).

oxygen, a tenfold increase in the peak intensity is observed. This clearly indicates a significant rise in the oxygen vacancy concentration in the STO substrate, confirming the reports on the true origins of the conductivity in low pO_2 LAO/STO samples, i.e. oxygen vacancy mediated conduction [2–6]. These results also confirm the optical dynamics studies on LAO/STO heterostructures published by Wang et al. [7]. The difference in oxygen vacancy abundance should be reflected in the transport properties of both samples and it should therefore allow to clearly distinguish between two- or three-dimensional electron transport.

Magnetoresistance measurements on a two-dimensional system can reveal Shubnikov-de Haas oscillations, if the magnetic field is oriented perpendicular to the plane and the electron mobility is sufficiently high. This has been observed in confined donor-doped STO structures [8, 9]. Out-of-plane measurements on LAO/STO have been performed in relation to the superconducting transition and the spin-orbit coupling of the system in that conduction mode [10–13]. In-plane magnetoresistance measurements however, can reveal the thickness of the conductive layer: the electron orbit (related to the cyclotron frequency) at any given magnetic field is related to the width of the material in which it can move freely [14]. Wong et al. [15] have performed both in-plane as well as out-of-plane MR measurements on LAO/STO and due to the difference between the two, i.e. ruling out orbital effects in the in-plane configuration, they conclude that the carriers are lying within one mean free path length. Unfortunately their samples were deposited at 10^{-5} mbar O_2, which biases the results strongly. Wang et al. [16] have performed in-plane and perpendicular MR measurements to look for anisotropy and distinguish between quasi-2D and 3D conductive behaviour. The samples studied are however both deposited at 'low' pO_2, i.e. 10^{-4} and 10^{-6} mbar; their results obtained for the 10^{-4} mbar sample are comparable to the measurements below and will be proven in section 9.3 to be distinctively 3D as well.

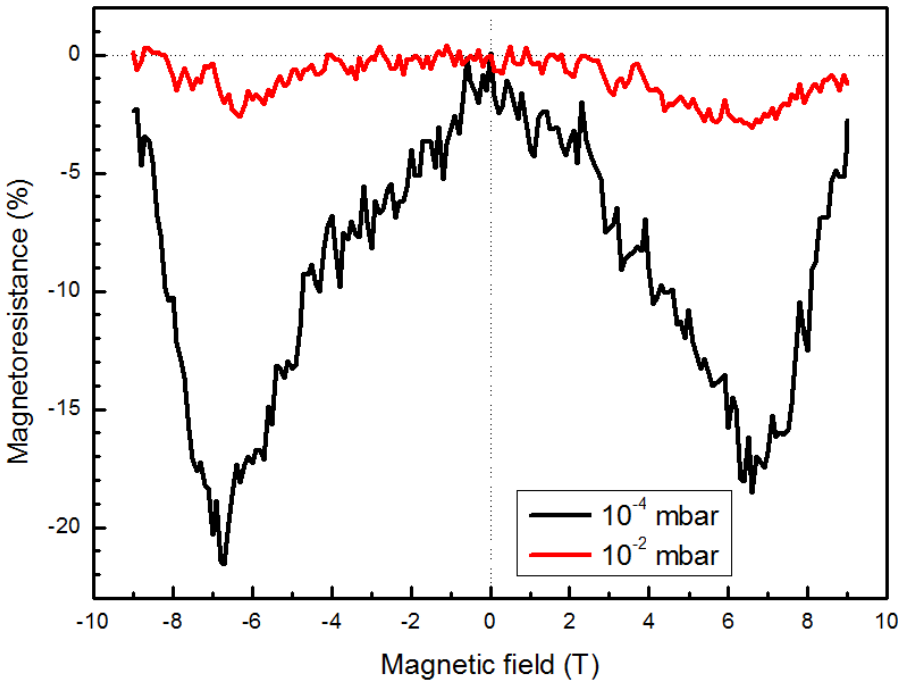

Figure 9.2: Relative magnetoresistance of the sheet resistance versus in-plane magnetic field at a temperature of 10 K for LAO/STO samples deposited at 10^{-2} mbar and 10^{-4} mbar oxygen pressure.

Figure 9.2 shows the magnetoresistance (at 10 K) as a function of in-plane magnetic field for LAO/STO samples deposited at a high (10^{-2} mbar) and a low (10^{-4} mbar) oxygen pressure. The MR was calculated from a measurement of the sheet resistance at different magnetic field values, which causes large fluctuations in the data, possibly due to local temperature variations. No hysteresis in the MR could be observed – reports of such hysteresis were at much lower temperatures [17]. In any case, the difference between the two measurements is obvious: the 10^{-4} mbar sample shows a maximum negative MR of about -20%, whereas the 10^{-2} mbar sample only has a minimum of $\approx$ -2.5%. Both curves follow the general trend outlined in [14], for electrons in a quantum well, where spin-split levels exist and some degree of spin-flipping occurs. It is however impossible to apply that model to the data, as many theoretical parameters are unknown and several combinations will fit the same curve. The thickness (width) of the quantum well and degree of spin splitting can therefore not be calculated. On the other hand, it is clear that there is a distinct difference in the MR behaviour of samples deposited in a different oxygen pressure, which is probably related to the amount of material (i.e. depth within the STO substrate) that contributes to the conductivity.

9.3 Fundamental resistance versus temperature behaviour

The resistance versus temperature behaviour of these LAO/STO samples reveals information on the underlying electron scattering mechanism in the heterostructures. The temperature dependence of the resistance can be described by the following power law [18]:

$$R = R_0 + A \cdot T^{\alpha} \tag{9.1}$$

where R_0 is the residual resistivity due to elastic scattering, A is a temperature-independent coefficient related to a quasi-particle effective mass and the exponent α provides more information on the nature of the metallic state.

A temperature coefficient of resistance (TCR) can be defined as:

$$TCR = -\frac{1}{R}\frac{\partial R}{\partial T} \tag{9.2}$$

This coefficient highlights changes in the resistance versus temperature profiles as peaks imposed on a flat background [19].

For the 10^{-4} mbar sample (Figure 9.3b), a resistance anomaly occurs at T* $\approx$ 150 K, which is clearly visible from the TCR graph (Figure 9.3c). The temperature dependence of the resistance yields $\alpha' \approx \alpha'' \approx 2$, where the two α values relate to the behaviour below and above T*. According to the so-called Fermi-liquid theory, electrons (at low energies) in bulk metals behave as a collection of weakly interacting particles, resulting in a T^2 evolution of the resistance [20, 21]. This result is consistent with previous detailed studies of electron transport in doped bulk STO [22, 23]. The slight increase in α'' compared to α' could be due to a phonon contribution ($\alpha \to 3$), which might have an effect in the higher temperature range. The temperature T* is significantly higher than the 105 K STO bulk phase transition temperature and corresponds to a surface phase transition temperature of STO [24, 25], implying that the conduction is associated with a certain thickness ($\approx 1\mu$m) below the STO substrate surface, as demonstrated previously by conductive AFM experiments [3].

In contrast, the temperature dependence of the resistance of 10^{-2} mbar samples yields two distinct transition temperatures upon warming (Figure 9.3a): around T' $\approx$ 85 K and T" $\approx$ 180 K, also visible in the TCR plot (Figure 9.3c). These transitions were also observed by Siemons et al. [26]. They occur only on warming (no transitions in the cooling curve, Figure 9.3a), have a long time-constant (several hours) and are hysteretic with temperature, implying a structural origin. At lower temperatures (T $\approx$ 25 K), the structural hysteresis ceases to exist at the metal-insulator transition (T_{MIT}), which therefore must have a different origin, as discussed by Liao et al. [27], Lü et al. [28].

These transitions are completely absent in the low oxygen pressure grown sample, which is known to be more bulk-like [2–4] and they must be a signature of the two-dimensional confinement of the electrons at the LAO/STO interface and represent changes in the 2DEG conduction behaviour which are driven by changes in the structure of the STO surface or near-surface region. The interplay between structure and strain appears to impact the conductivity significantly, in agreement with other work [28–35].

Turning to the power law coefficients of the high oxygen pressure sample, there are some remarkable differences. The three regions (30-80 K, 100-170 K, 190-240 K) in the R–T curve have been fit separately in the analysis, resulting in the corresponding power law coefficients α_1, α_2 and α_3 as shown in Figure 9.3. In the temperature ranges of 30-80 K (α_1, between T_{MIT} and T') and above T" $\approx$ 180 K (α_3), a value of α significantly smaller than 2 is found (both in cooling[1] and warming). The limit of T^1 ($\alpha = 1$) dependence is observed in other complex oxide systems such as, e.g. $YBa_2Cu_3O_{7-\delta}$ (YBCO) and related high-T_c superconductors. This non-Fermi-liquid behaviour arises from charged-impurity scattering in 2D electron systems with low carrier density and large effective mass, as well as to some extent, with a phonon contribution [36, 37]. Indeed, the effective mass

[1]The cooling curve can be fitted within the same temperature ranges to allow comparison with the warming. However an excellent fit of the entire cooling curve can be obtained with $\alpha \approx 2.26$. This would imply a different scattering mechanism in cooling compared to warming.

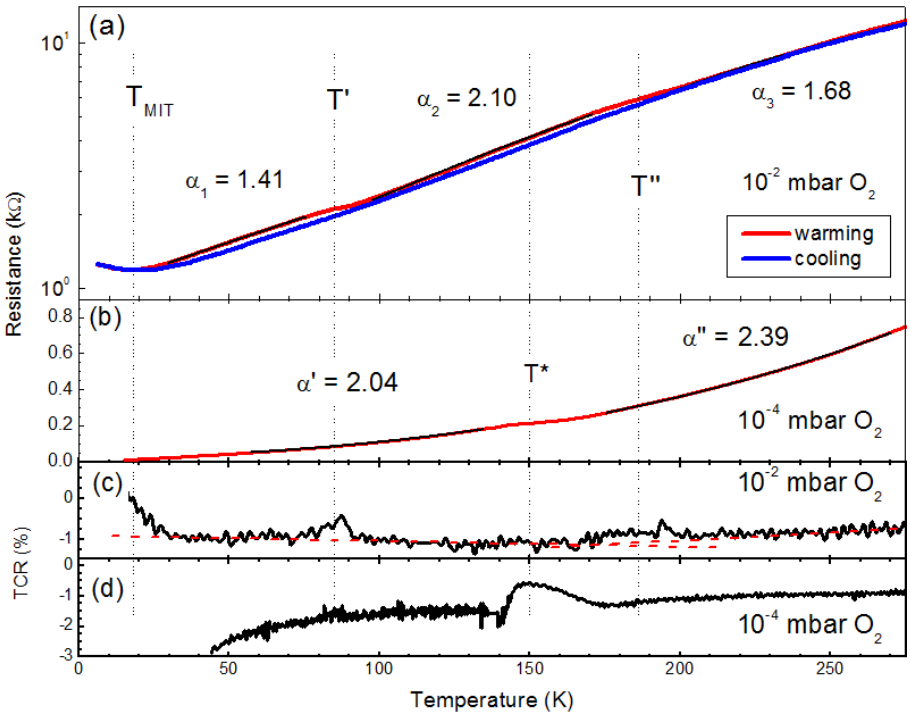

Figure 9.3: **(a)-(b)** Resistance versus temperature upon cooling & warming with power law fits for LAO/STO deposited at **(a)** pO_2 10^{-2} mbar **(b)** pO_2 10^{-4} mbar. The α values in both **(a)** and **(b)** indicate the power law exponent in that temperature range. **(c)-(d)** Temperature coefficient of resistance (TCR) versus temperature highlighting the transitions in the warming curves of the **(c)** 10^{-2} and **(d)** 10^{-4} mbar sample. The red dotted line in **(c)** is a guide to the eye of a linear background to the TCR curve.

in the LAO/STO system has been estimated as approximately 3 times the free electron mass [38, 39]. This deviation from bulk-like T^2 behaviour therefore marks a fundamental characteristic of the purely 2D confined LAO/STO 2DEG in this temperature range. Based on these observations, it can be concluded that structural phase transitions near the interface determine the temperature ranges with different modes of conduction, suggesting an intimate interplay between structure and transport.

Some theoretical models suggest that non-Fermi-liquid behaviour arises in the vicinity of a quantum critical point and that it is (partially) magnetic in origin [40]. Without confirming the validity of this hypothesis, it might be related to the occurrence of a negative magnetoresistance, as presented in section 9.2. In any case, this unique, $\alpha < 2$ T-dependence thus marks a fundamental characteristic of a confined LAO/STO 2DEG. This can be possibly interpreted in terms of the dual carrier model introduced in section 7.5: the type II, bulk-like carriers follow the electron-electron scattering mechanism, while the interface confined type I carriers are more inclined towards non-Fermi-liquid behaviour.

To further highlight the impact of the observed structural transitions, detailed transport measurements versus temperature were performed on the LAO/STO sample deposited in the relatively high pO_2 of 10^{-2} mbar (Figure 9.4). Clear changes in both carrier density and mobility are observed at T' and at T", though less pronounced (more smeared out) in the latter. Even the bulk STO transition temperature (labelled T_{bulk}) is visible. However nothing happens at the T* observed in the low oxygen pressure sample.

The bulk STO phase transition at 105 K, also called antiferrodistortive transition, is related to the rotation of oxygen octahedra around the *c*-axis, creating a tetragonal phase out of the high temperature cubic phase [1, 41, 42]. Doping either by adding atoms or creating oxygen vacancies, as well as strain, has been reported to influence the phase transition temperature [1, 23, 24, 41–43]. Dramatic changes in the transport properties of the LAO/STO 2DEG are observed, which are most likely related to structural transitions close to the interface, as the data suggests. Given that the bulk transitions in STO is related to oxygen octahedra rotations, it is plausible that similar rotations are involved in these surface or interface transitions. This implies that oxygen octahedral rotations must have a significant impact on the 2DEG, thereby confirming earlier hypotheses [28, 29, 31, 32, 35, 44].

In the discussion so far, the value of $\alpha_2 \approx 2$ has been ignored. It seems that in the intermediate temperature region, i.e. between T' and T", the dominant conduction path lies deeper in the STO substrate. No satisfying explanation could be found for this observation.

9.4 Conclusions

Photoluminescence experiments show an abundance of oxygen vacancies in LAO/STO heterointerfaces deposited at low (10^{-4} and 10^{-5} mbar) pO_2, as expected from the literature (section 7.3). An analysis of the R–T behaviour of these samples clearly reveals a bulk-like three-dimensional conduction mode with a T^2 dependence of the resistance. Heterostructures deposited at higher (10^{-2} mbar) pO_2 behave significantly different and exhibit distinct transition temperatures in their R–T curves. The boundaries appear to be associated with structural transitions in the surface of the STO and are possibly related to oxygen octahedra rotations. These samples tend towards a non-Fermi-liquid behaviour (T^1 dependence of the resistance) in the low (30-80 K) and high (190-240 K) temperature region, which indicates a higher degree of interface confinement of the electrons. These results already hint at the fact that an intimate interplay might exist between oxygen

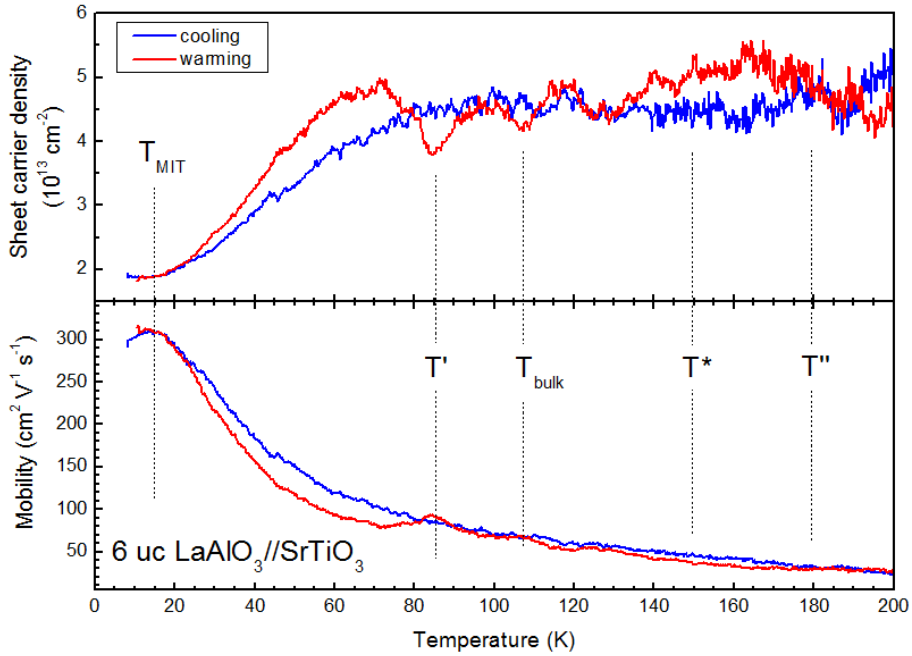

Figure 9.4: Sheet carrier density and electron mobility versus temperature for a 6 uc LAO/STO heterostructure. All transition temperatures, known or observed, are indicated.

octahedral rotations and transport at the LAO/STO heterointerfaces.

Bibliography

[1] D. Bäuerle and W. Rehwald. Structural phase transitions in semiconducting $SrTiO_3$. *Solid State Communications*, 27:1343–1346, 1978.

[2] Alexey S. Kalabukhov, Robert Gunnarsson, Johan Börjesson, Eva Olsson, Tord Claeson, and Dag Winkler. Effect of oxygen vacancies in the $SrTiO_3$ substrate on the electrical properties of the $LaAlO_3/SrTiO_3$ interface. *Physical Review B*, 75:121404, 2007.

[3] M. Basletic, J.-L. Maurice, C. Carrétéro, G. Herranz, O. Copie, M. Bibes, E. Jacquet, K. Bouzehouane, S. Fusil, and A. Barthélémy. Mapping the spatial distribution of charge carriers in $LaAlO_3/SrTiO_3$ heterostructures. *Nature Materials*, 7:621–625, 2008.

[4] G. Herranz, M. Basletic, O. Copie, M. Bibes, A. N. Khodan, C. Carrétéro, E. Tafra, E. Jacquet, K. Bouzehouane, A. Hamzic, and A. Barthélémy. Controlling high-mobility conduction in $SrTiO_3$ by oxide thin film deposition. *Applied Physics Letters*, 94:012113, 2009.

[5] C. W. Schneider, M. Esposito, I. Marozau, K. Conder, M. Doebeli, Yi Hu, M. Mallepell, A. Wokaun, and T. Lippert. The origin of oxygen in oxide thin films: role of the substrate. *Applied Physics Letters*, 97:192107, 2010.

[6] A. Koitzsch, J. Ocker, M. Knupfer, M. C. Dekker, K. Dörr, B. Büchner, and P. Hoffmann. In-gap electronic structure of $LaAlO_3$-$SrTiO_3$ heterointerfaces investigaged by soft x-ray spectroscopy. *Physical Review B*, 84:245121, 2011.

[7] X. Wang, J. Q. Chen, A. Roy Barman, S. Dhar, Q.-H. Xu, T. Venkatesan, and Ariando. Static and ultrafast dynamics of defects of $SrTiO_3$ in $LaAlO_3/SrTiO_3$ heterostructures. *Applied Physics Letters*, 98:081916, 2011.

[8] Y. Kozuka, M. Kim, C. Bell, B. G. Kim, Y. Hikita, and H. Y. Hwang. Two-dimensional normal-state quantum oscillations in a superconducting heterostructure. *Nature*, 462:487–490, 2009.

[9] Bharat Jalan, Susanne Stemmer, Shawn Mack, and S. James Allen. Two-dimensional electron gas in δ-doped $SrTiO_3$. *Physical Review B*, 82:081103, 2010.

[10] M. Ben Shalom, M. Sachs, D. Rakhmilevitch, A. Palevski, and Y. Dagan. Tuning spin-orbit coupling and superconductivity at the $SrTiO_3/LaAlO_3$ interface: a magnetotransport study. *Physical Review Letters*, 104:126802, 2010.

[11] A. D. Caviglia, M. Gabay, S. Gariglio, N. Reyren, C. Cancellieri, and Triscone J.-M. Tunable Rashba spin-orbit interaction at oxide interfaces. *Physical Review Letters*, 104:126803, 2010.

[12] M. Sachs, D. Rakhmilevitch, M. Ben Shalom, S. Shefler, A. Palevski, and Y. Dagan. Anomalous magneto-transport at the superconducting interface between $LaAlO_3$ and $SrTiO_3$. *Physica C: Superconductivity*, 470:S746, 2010.

[13] M. Ben Shalom, A. Ron, A. Palevski, and Y. Dagan. Shubnikov–De Haas oscillations in $SrTiO_3/LaAlO_3$ interface. *Physical Review Letters*, 105:206401, 2010.

[14] F. M. Hashimzade, Kh. A. Hasanov, and M. M. Babayev. Negative magnetoresistance of an electron gas in a quantem well with parabolic potential. *Physical Review B*, 73: 235349, 2006.

[15] Franklin J. Wong, Seung-Hyub Baek, Rajesh V. Chopdekar, Virat V. Mehta, Ho-Won Jang, Chang-Beom Eom, and Yuri Suzuki. Metallicity in $LaTiO_3$ thin films induced by lattice deformation. *Physical Review B*, 81:161101, 2010.

[16] X. Wang, W. M. Lü, A. Annadi, Z. Q. Liu, K. Gopinadhan, S. Dhar, T. Venkatesan, and Ariando. Magnetoresistance of two-dimensional and three-dimensional electron gas in $LaAlO_3/SrTiO_3$ heterostructures: influence of magnetic ordering, interface scattering and dimensionality. *Physical Review B*, 84:075312, 2011.

[17] A. Brinkman, M. Huijben, M. Van Zalk, J. Huijben, U. Zeitler, J. C. Maan, W. G. Van Der Wiel, G. Rijnders, D. H. A. Blank, and H. Hilgenkamp. Magnetic effects at the interface between non-magnetic oxides. *Nature Materials*, 6:493–496, 2007.

[18] S. A. Grigera, R. S. Perry, A. J. Schofield, M. Chiao, S. R. Julian, G. G. Lonzarich, S. I. Ikeda, Y. Maeno, A. J. Millis, and A. P. Mackenzie. Magnetic field-tuned quantum criticality in the metallic ruthenate $Sr_3Ru_2O_7$. *Science*, 294:329–332, 2001.

[19] M. Egilmez, M. M. Saber, I. Fan, K. H. Chow, and J. Jung. Correlation of structural phase transition and electrical transport properties of manganite films on $SrTiO_3$. *Physical Review B*, 78:172405, 2008.

[20] W. G. Baber. The contribution to the electrical resistance of metals from collisions between electrons. *Proceeings of the Royal Society A*, 158:383–396, 1937.

[21] M. Kaveh and N. Wiser. Theory of the sample dependence of the electron-electron scattering resistivity in metals. *Journal of Physics F: Metal Physics*, 12:935–950, 1982.

[22] Y. Tokura, Y. Taguchi, Y. Okada, Y. Fujishima, T. Arima, K Kumagai, and Y. Iye. Filling dependence of electronic properties on the verge of the metal–Mott-insulator transitions in $Sr_{1-x}La_xTiO_3$. *Physical Review Letters*, 70(14):2126–2129, 1993.

[23] D. van der Marel, J. L. M. van Mechelen, and I. I. Mazin. Common Fermi-liquid origin of T^2 resistivity and superconductivity in n-type $SrTiO_3$. *Physical Review B*, 84:205111, 2011.

[24] Z. Salman, R. F. Kiefl, K. H. Chow, M. D. Hossain, T. A. Keeler, S. R. Kreitzman, C. D. P. Levy, R. I. Miller, T. J. Parolin, M. R. Pearson, H. Saadaoui, J. D. Schultz, M. Smadella, D. Wang, and W. A. MacFarlane. Near-surface structural phase transition of $SrTiO_3$ studied with zero-field β-detected nuclear spin relaxation and resonance. *Physical Review Letters*, 96:147601, 2006.

[25] Z. Salman, M. Smadella, W. A. MacFarlane, B. D. Patterson, P. R. Willmott, K. H. Chow, M. D. Hossain, H. Saadaoui, D. Wang, and R. F. Kiefl. Depth dependence of the structural phase transition of $SrTiO_3$ studied with β-NMR and grazing incidence x-ray diffraction. *Physical Review B*, 83:224112, 2011.

[26] Wolter Siemons, Gertjan Koster, Hideki Yamamoto, Theodore H. Geballe, Dave H. A. Blank, and Malcolm R. Beasley. Experimental investigation of electronic properties of buried heterointerfaces of $LaAlO_3$ on $SrTiO_3$. *Physical Review B*, 76:155111, 2007.

[27] Y. C. Liao, T. Kopp, C. Richter, A. Rosch, and J. Mannhart. Metal-insulator transition of the $LaAlO_3$–$SrTiO_3$ interface electron system. *Physical Review B*, 83:075402, 2011.

[28] W. M. Lü, X. Wang, Z. Q. Liu, S. Dhar, A. Annadi, K. Gopinadhan, A. Roy Barman, H. B. Su, T. Venkatesan, and Ariando. Metal-insulator transition at a depleted $LaAlO_3/SrTiO_3$ interface: evidence for charge transfer induced by $SrTiO_3$ phase transitions. *Applied Physics Letters*, 99:172103, 2011.

[29] C. L. Jia, S. B. Mi, M. Faley, U. Poppe, J. Schubert, and K. Urban. Oxygen octahedron reconstruction in the $SrTiO_3/LaAlO_3$ heterointerfaces investigated using aberration-corrected ultrahigh-resolution transmission electron microscopy. *Physical Review B*, 79:081405(R), 2009.

[30] M. Salluzzo, J. C. Cezar, N. B. Brookes, V. Bisogni, G. M. De Luca, C. Richter, S. Thiel, J. Mannhart, M. Huijben, A. Brinkman, G. Rijnders, and G. Ghiringhelli. Orbital reconstruction and the two-dimensional electron gas at the $LaAlO_3/SrTiO_3$ interface. *Physical Review Letters*, 102:166804, 2009.

[31] H. W. Jang, D. A. Felker, C. W. Bark, Y. Wang, M. K. Niranjan, C. T. Nelson, Y. Zhang, D. Su, C. M. Folkman, S. H. Baek, S. Lee, K. Janicka, Y. Zhu, X. Q. Pan, D. D. Fong, E. Y. Tsymbal, M. S. Rzchowski, and C. B. Eom. Metallic and insulating oxide interfaces controlled by electronic correlations. *Science*, 331:886–889, 2011.

[32] Ke-Jin Zhou, Milan Radovic, Justine Schlappa, Vladimir Strocov, Ruggero Frison, Joel Mesot, Luc Patthey, and Thorsten Schmitt. Localized and delocalized Ti $3d$ carriers in $LaAlO_3/SrTiO_3$ superlattices revealed by resonant inelastic x-ray scattering. *Physical Review B*, 83:201402(R), 2011.

[33] C. W. Bark, D. A. Felker, Y. Wang, Y. Zhang, H. W. Jang, C. M. Folkman, J. W. Park, S. H. Baek, H. Zhou, D. D. Fong, X. Q. Pan, E. Y. Tsymbal, M. S. Rzchowski, and C. B. Eom. Tailoring a two-dimensional electron gas at the $LaAlO_3/SrTiO_3$ (001) interface by epitaxial strain. *Proceedings of the National Academy of Sciences of the United States of America*, 108(12):4720–4724, 2011.

[34] J. E. Boschker, C. Folkman, C. W. Bark, A. F. Monsen, E. Folven, J. K. Grepstad, E. Wahlström, C. B. Eom, and T. Tybell. Structural coupling across the $LaAlO_3/SrTiO_3$ interface: high-resolution x-ray diffraction study. *Physical Review B*, 84:205418, 2011.

[35] N. Lazarides, V. Paltoglou, P. Maniadis, G. P. Tsironis, and C. Panagopoulos. Strain-induced interface reconstruction in epitaxial heterostructures. *Physical Review B*, 84: 245428, 2011.

[36] S. W. Tozer, A. W. Kleinsasser, T. Penney, D. Kaiser, and F. Holtzberg. Measurement of anisotropic resistivity and Hall constant for single-crystal $YBa_2Cu_3O_{7-x}$. *Physical Review Letters*, 59(15):1768–1771, 1987.

[37] X. L. Lei. On the linear temperature dependence of resisitivity in $YBa_2Cu_3O_{7-x}$. *Journal of Physics C: Solid State Physics*, 21:L83–L88, 1988.

[38] A. Dubroka, M. Rössle, K. W. Kim, V. K. Malik, L. Schultz, S. Thiel, C. W. Schneider, J. Mannhart, G. Herranz, O. Copie, M. Bibes, A. Barthélémy, and C. Bernhard. Dynamical response and confinement of the electrons at the $LaAlO_3/SrTiO_3$ interface. *Physical Review Letters*, 104:156807, 2010.

[39] D. Rakhmilevitch, M. Ben Shalom, M. Eshkol, A. Tsukernik, A. Palevski, and Y. Dagan. Phase coherent transport in $SrTiO_3/LaAlO_3$ interfaces. *Physical Review B*, 82: 235119, 2010.

[40] G. R. Stewart. Non-Fermi-liquid behavior in d and f-electron metals. *Review of Modern Physics*, 73:797–85, 2001.

[41] Feizhou He, B. O. Wells, S. M. Shapiro, M. von Zimmerman, A. Clark, and X. X. Xi. Anomalous phase transition in strained $SrTiO_3$. *Applied Physics Letters*, 83(1): 123–125, 2003.

[42] Feizhou He, B. O. Wells, and S. M. Shapiro. Strain phase diagram and domain orientation in $SrTiO_3$ thin films. *Physical Review Letters*, 94:176101, 2005.

[43] A. Tkach, T. M. Correia, A. Almeida, J. Agostinho Moreira, M. R. Chaves, O. Okhay, P. M. Vilarinho, I. Gregora, and J. Petzelt. Role of trivalent Sr substituents and Sr vacancies in tetragonal and polar states of $SrTiO_3$. *Acta Materialia*, 59:5388–5397, 2011.

[44] Satoshi Okamoto, Andrew J. Millis, and Nicola A. Spaldin. Lattice relaxation in oxide heterostructures: $LaTiO_3/SrTiO_3$ superlattices. *Physical Review Letters*, 97: 056802, 2006.

Chapter 10

Effect of laser fluence variations on LAO/STO

After having discussed the distinct effects of oxygen vacancies on LAO/STO and excluded them as the dominant conduction mechanism in the high pressure deposited samples, this chapter focuses on the impact of varying the laser fluence during deposition of LAO/STO. Even though the initial motivation is to enhance interface intermixing, the outcome reveals that not only the structure but also the stoichiometry of both the LAO film and STO surface are of utmost importance for the transport properties of the 2DEG. Off-stoichiometry in the STO can influence the oxygen octahedra rotations which emerged as significant in the previous chapter.

10.1 Introduction

As indicated in section 7.4, one of the mechanisms by which the polar catastrophe in LAO/STO can be avoided, is by interdiffusion between the LAO and the STO, leading to the creation of an intermixed interface. Since La-doping can render STO conductive, this is a possible explanation for the transport properties of the 2DEG. Samples are fabricated by pulsed laser deposition, during which the sputtered species impact in the substrate surface with a certain kinetic energy ($\approx$ 100 eV). Intuitively, a higher fluence would be expected to increase the amount of intermixing or interface roughness. Changing the laser energy density at the target surface may also alter the stoichiometry of the plume due to an altered laser-material coupling for different chemical elements, resulting in a non-stoichiometric deposition [1–4]. By analysis of the structural (by XRD and MEIS - see chapter 2) and transport properties, an attempt is made to elucidate which mechanisms influence the conductivity at the interface and to determine their optimum balance.

10.2 Sample fabrication

The standard deposition procedure for LAO/STO samples was followed, as outlined in chapter 8. The laser fluence was measured behind all optics, in order to take variable viewport transmission into account. All LAO films grown for analysis had a thickness of approximately 6 nm ($\approx$ 15 unit cells). The growth was monitored by RHEED (with Fourier analysis of the signal) and verified by reflectometry. In both cases a nearly linear dependence of the growth rate on the laser fluence was observed (Figure 10.1). The slope is comparable for both techniques, confirming their reliability.

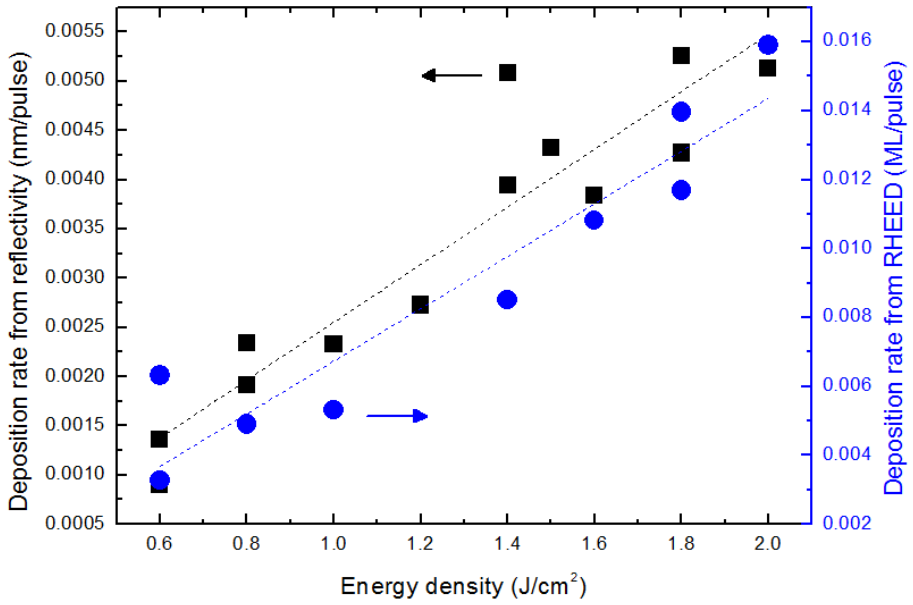

Figure 10.1: Deposition rate of LAO at different laser fluences as measured by x-ray reflectometry (■) and RHEED (•). Linear fits are indicated by dotted lines.

By fitting the experimental x-ray reflectivity data with simulated curves, the roughness of both the (air/)LAO and LAO/STO interface can be determined. These roughnesses are shown in Figure 10.2. There appears to be no clear correlation between roughness and laser fluence, or at least not on the scale accessibly by reflectometry.

10.3 Structural characterisation

10.3.1 XRD

Both the in-plane as well as out-of-plane lattice parameter of all samples was determined. A reciprocal space map of the $(\bar{1}\ 0\ 3)$ reflections of the LAO film and the STO substrate, as collected on diffractometer B2 (see section 2.2.2), is shown in Figure 10.3a for a 1 J/cm^2 sample. It is representative for all samples, irrespective of laser fluence: all LAO films are fully strained in plane. This is in agreement with the rocking curve measurements (on diffractometer B1) at the LAO (0 0 1) and STO (0 0 1) peaks: they exhibit a similar full width at half maximum value, implying a similar crystal quality of film and substrate.

Figure 10.3b shows the evolution of the out-of-plane lattice parameter with respect to the laser fluence. Its value clearly increases with the laser fluence, deviating from the elastic limit of perfect LAO on perfect STO. A similar increase in out-of-plane lattice parameter has been reported by [4]. The authors related this to an increase in the La/Al ratio of their LAO films.

10.3.2 MEIS

The MEIS technique was introduced before in section 2.5 and is used here to reveal more information on the stoichiometry and crystalline quality of the LAO overlayers. Random and aligned MEIS spectra are shown in Figures 10.4a and 10.4b respectively for a low (0.6 J/cm^2), intermediate (1 J/cm^2) and high (1.8 J/cm^2) fluence sample. In both cases, the He^+ ions probe the target up to a maximum depth of about 100 nm. Therefore the

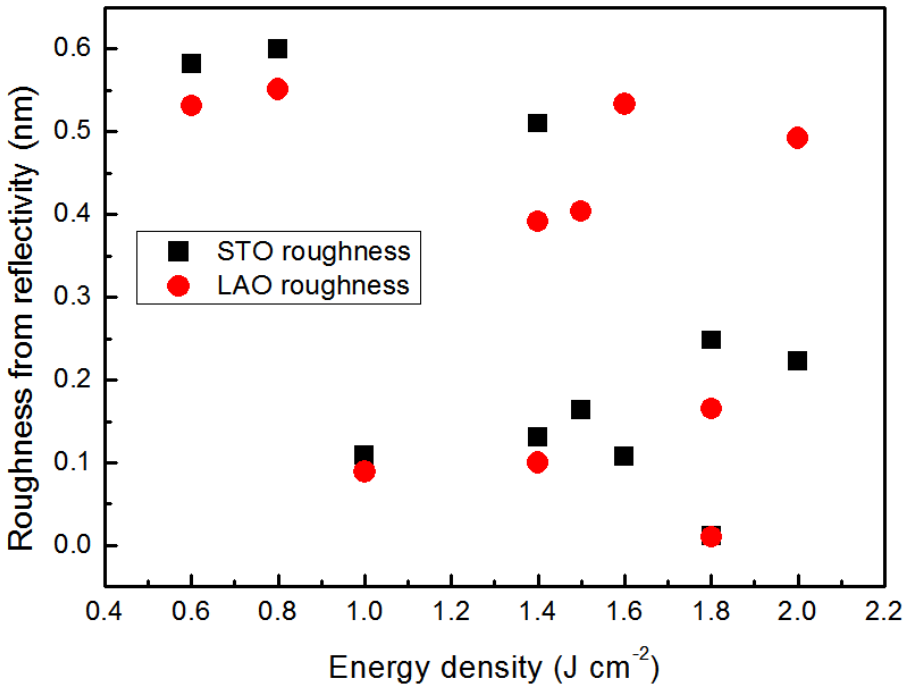

Figure 10.2: Roughness of (air/)LAO (•) and (LAO/)STO (■) (interfaces) at different laser fluences as determined by x-ray reflectometry.

obtained signals contain information from the heaviest elements in the film (La, Al) and the substrate (Sr, Ti). The sensitivity of the analysis is too low to detect oxygen atoms. Within the penetration depth, the area of each random signal corresponds to the amount of the probed element.

In the crystallographically 'aligned' mode, surface atoms in the sample effectively screen deeper lying atoms, meaning that peaks from the substrate elements (Sr, Ti) and buried film elements (La, Al) are not visible. Due to the effect of screening, aligned peaks are often called surface peaks. This screening depends on various parameters, the crystalline quality of the material being the most important factor. The presence of crystal defects strongly affects the behaviour of the surface peak.

In the random MEIS spectra (Figure 10.4a) the La signal appears at the highest backscattering energy as it is the heaviest element present in the sample. The Sr signal appears next to La, at a slightly lower energy. It assumes the shape of a large plateau instead of a sharp peak as the substrate thickness exceeds the probed depth. The signals from Al and Ti are rather weak and not well resolved: they largely disappear in the background. The similarity of the La spectra between the samples indicates that the LAO thickness, as well as the La content, is comparable for all samples.

In the aligned spectra (Figure 10.4b), the La surface peak height decreases significantly with increasing laser fluence. This can be caused by two factors, either by a widely different La content in the film or by a different sample crystalline quality. The former is however inconsistent with Figure 10.4a. Therefore, an increase in laser fluence must lead to a La sublattice quality improvement, which causes a better shadowing of the lower lying La-atoms and thus a lower peak intensity.

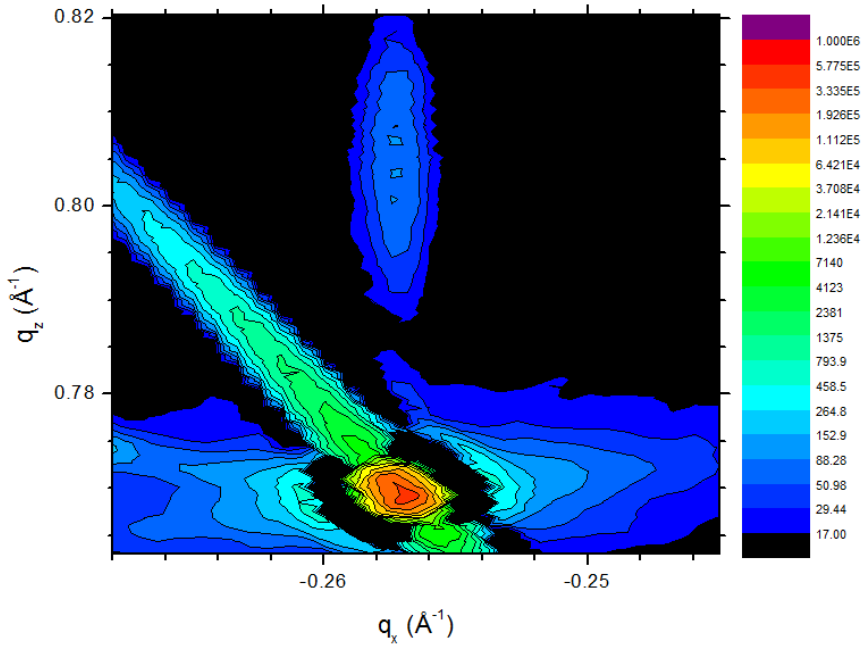

(a)

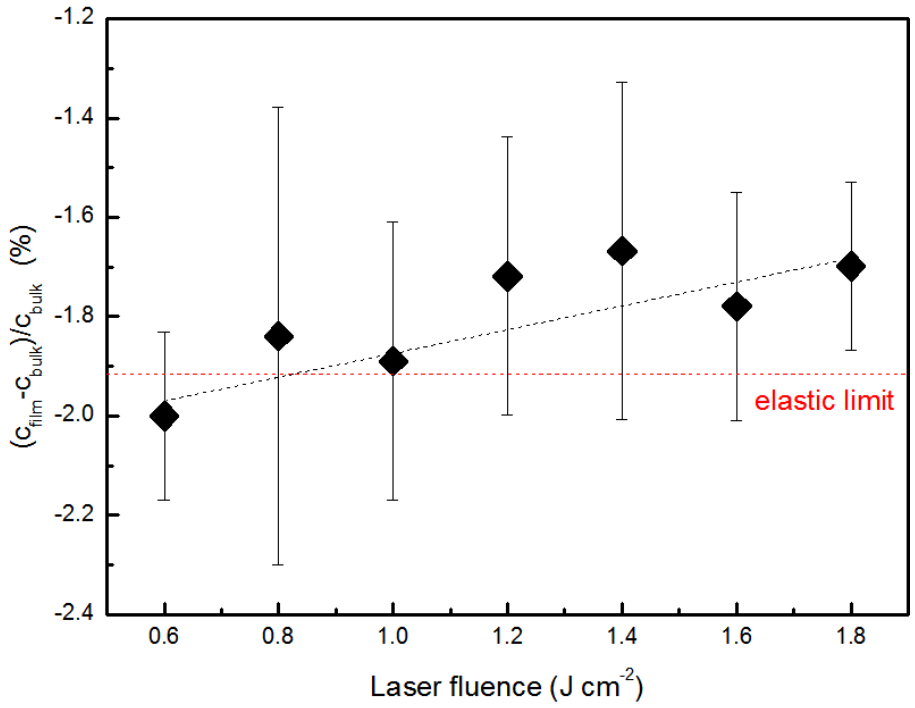

(b)

Figure 10.3: **(a)** Reciprocal space map of the $(\bar{1}03)$ reflections of the LAO film and the STO substrate for a 1 J/cm^2 sample.
(b) Change in the LAO out-of-plane lattice parameter versus laser fluence.

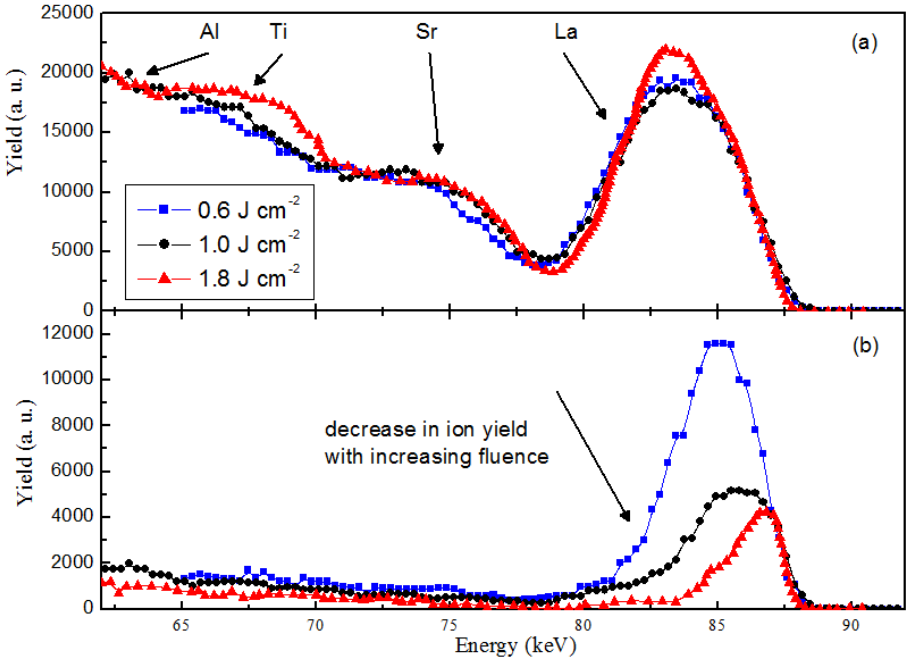

Figure 10.4: Random **(a)** and aligned **(b)** MEIS spectra (using $^4He^+$ ions at 100 keV) for LAO/STO deposited at low, intermediate and high laser fluence. All samples behave similar in **(a)**, indicating similar thickness and overall La-content. In **(b)** the ion yield clearly decreases with increasing fluence, indicating an improvement of the La sublattice quality.

10.4 Transport properties

The fluence-dependence of characteristic transport properties (sheet resistance, sheet carrier density and mobility) is shown in Figure 10.5 at a temperature of 200 K, which is above the metal-insulator transition for all 2DEG samples to allow proper comparison, similar to the case for transition metal doped LAO/STO interfaces [5]. The sheet resistance of the 1 J/cm^2 sample is the lowest, implying an optimum laser fluence value in terms of transport properties. The electron mobility at 200 K exhibits only a small variation, which indicates that the determining scattering mechanism remains the same for all films, except for the highest fluence sample.

10.5 Discussion

An improvement of the LAO crystal quality as the laser fluence increases, is observed from the MEIS analysis (Fig. 10.4). This can be interpreted largely as an improvement of stoichiometry with respect to the La/Al ratio. Theoretically the introduction of oxygen vacancies is also possible, as these tend to expand the lattice. It is however expected that the effect of plume stoichiometry dominates when varying the laser fluence [1, 2, 4, 6] at constant oxygen pressure (see section 4.2).

Paradoxically, Figure 10.3 shows that with increasing fluence the LAO unit cell distortion increasingly deviates from the predicted elastic strain for (perfect) LAO on (perfect) STO. The XRD data demonstrate that the in-plane lattice parameter of film and substrate match throughout the set of samples and it is only the out-of-plane lattice parameter that changes. The most reasonable explanation which covers these observations is that the

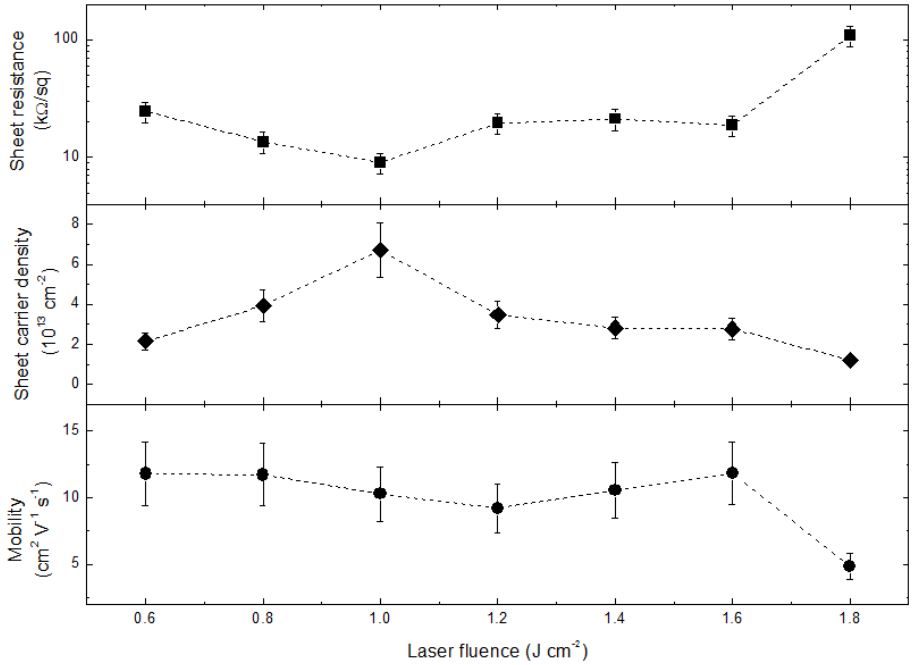

Figure 10.5: Sheet resistance, sheet carrier density and mobility at 200 K for heteroepitaxial LAO/STO samples deposited with varying laser fluence.

near-surface STO lattice is modified as the laser fluence increased. This is caused by the impacting species, creating crystallographic defects such as oxygen and/or cation vacancies [7]. In the light of reports which point to induced oxygen octahedra rotations as an important aspect to the conductivity [8–11, and chapter 9], the decrease in carrier density (from 1 J/cm^2 to 1.8 J/cm^2, see Figure 10.5) follows the deviations from stoichiometric interfaces.

A more speculative, yet not unrealistic, explanation could be an interpretation from the thermodynamic modelling of Fe:$SrTiO_3$ grain boundaries by De Souza [12]. In his work, De Souza [12] extends the scope towards thin films and perovskite interfaces. He predicts a migration of oxygen vacancies at the heterointerface from the material with a higher to the one with a lower thermodynamic formation energy. For the LAO/STO case, this would be to the STO, as was proven experimentally by tracer diffusion experiments [13]. This creates an electron-trapping space charge layer at the interface between the two perovskites. An increase in laser fluence during LAO deposition is likely to cause an increased defect concentration at the interface, more specifically a potentially higher oxygen vacancy concentration [7]. This creates an increasingly wider space charge layer as the laser energy density increases, which causes a further trapping of carriers from the interface and hence a lower observed sheet carrier density (Figure 10.5). The presence of an increasing number of oxygen vacancies at the STO surface also explains the deviation of the LAO lattice (Figure 10.3), as mentioned above, and will also influence the rotation of the oxygen octahedra [14].

10.6 Conclusions

At the lowest laser fluence values, the structural quality (stoichiometry) of the deposited LAO is insufficient to generate the optimum carrier density. A lower electrostatic build-up in the LAO reduces the driving force for the reconstruction at the interface and therefore

reduces the carrier density. At higher fluences, the defects created at the STO surface are the limiting factor, i.e. by distorting the oxygen octahedra rotations in the near-interface region. The interplay between these two structural phenomena gives rise to an optimum laser fluence with the lowest sheet resistance at an intermediate laser fluence, i.e. 1 J/cm^2 in our case.

Bibliography

[1] Tsuyoshi Ohnishi, Keisuke Shibuya, Takahisa Yamamoto, and Mikk Lippmaa. Defects and transport in complex oxide thin films. *Journal of Applied Physics*, 103:103703, 2008.

[2] D. J. Keeble, S. Wicklein, R. Dittmann, L. Ravelli, R. A. Mackie, and W. Egger. Identification of *A*- and *B*-site cation vacancy defects in perovskite oxide thin films. *Physical Review Letters*, 105:226102, 2010.

[3] T. C. Droubay, L. Qiao, T. C. Kaspar, M. H. Engelhard, V. Shutthanandan, and S. A. Chambers. Nonstoichiometric material transfer in the pulsed laser deposition of $LaAlO_3$. *Applied Physics Letters*, 97:124105, 2010.

[4] L. Qiao, T. C. Droubay, T. Varga, M. E. Bowden, V. Shutthanandan, Z. Zhu, T. C. Kaspar, and S. A. Chambers. Epitaxial growth, structure and intermixing at the $LaAlO_3/SrTiO_3$ interface as the film stoichiometry is varied. *Physical Review B*, 83: 085408, 2011.

[5] T. Fix, F. Schoofs, J. L. MacManus-Driscoll, and M. G. Blamire. Influence of doping at the nanoscale at $LaAlO_3/SrTiO_3$ interfaces. *Applied Physics Letters*, 97:072110, 2010.

[6] L. Qiao, T. C. Droubay, V. Shutthanandan, Z. Zhu, P. V. Sushko, and S. A. Chambers. Thermodynamic instability at the stoichiometric $LaAlO_3/SrTiO_3$ (001) interface. *Journal of Physics: Condensed Matter*, 22:312201, 2010.

[7] G. Herranz, M. Basletic, O. Copie, M. Bibes, A. N. Khodan, C. Carrétéro, E. Tafra, E. Jacquet, K. Bouzehouane, A. Hamzic, and A. Barthélémy. Controlling high-mobility conduction in $SrTiO_3$ by oxide thin film deposition. *Applied Physics Letters*, 94:012113, 2009.

[8] J. Verbeeck, S. Bals, A. N. Kravtsova, D. Lamoen, M. Luysberg, M. Huijben, G. Rijnders, A. Brinkman, H. Hilgenkamp, D. H. A. Blank, and G. Van Tendeloo. Electronic reconstruction at *n*-type $SrTiO_3/LaAlO_3$ interfaces. *Physical Review B*, 81:085113, 2010.

[9] C. L. Jia, S. B. Mi, M. Faley, U. Poppe, J. Schubert, and K. Urban. Oxygen octahedron reconstruction in the $SrTiO_3/LaAlO_3$ heterointerfaces investigated using aberration-corrected ultrahigh-resolution transmission electron microscopy. *Physical Review B*, 79:081405(R), 2009.

[10] H. W. Jang, D. A. Felker, C. W. Bark, Y. Wang, M. K. Niranjan, C. T. Nelson, Y. Zhang, D. Su, C. M. Folkman, S. H. Baek, S. Lee, K. Janicka, Y. Zhu, X. Q. Pan, D. D. Fong, E. Y. Tsymbal, M. S. Rzchowski, and C. B. Eom. Metallic and insulating oxide interfaces controlled by electronic correlations. *Science*, 331:886–889, 2011.

[11] J. E. Boschker, C. Folkman, C. W. Bark, A. F. Monsen, E. Folven, J. K. Grepstad, E. Wahlström, C. B. Eom, and T. Tybell. Structural coupling across the $LaAlO_3/SrTiO_3$ interface: high-resolution x-ray diffraction study. *Physical Review B*, 84:205418, 2011.

[12] Roger A. De Souza. The formation of equilibrium space-charge zones at grain boundaries in the perovskite oxide $SrTiO_3$. *Physical Chemistry Chemical Physics*, 11:9939–9969, 2009.

[13] C. W. Schneider, M. Esposito, I. Marozau, K. Conder, M. Doebeli, Yi Hu, M. Mallepell, A. Wokaun, and T. Lippert. The origin of oxygen in oxide thin films: role of the substrate. *Applied Physics Letters*, 97:192107, 2010.

[14] D. Bäuerle and W. Rehwald. Structural phase transitions in semiconducting $SrTiO_3$. *Solid State Communications*, 27:1343–1346, 1978.

Chapter 11

Rare-earth doping of LAO/STO interfaces

The previous chapter clearly demonstrated that defects in the LAO (cation off-stoichiometry) and at the STO surface (most likely oxygen vacancies) have a profound impact on the conduction of the LAO/STO heterostructure. In the first part of this chapter, an intermixed LAO/STO interface is artificially simulated by the insertion of (La,Sr)TiO_3 layers. A detailed transport study reveals similarities, but also fundamental differences between the undoped and artificially intermixed interfaces. In the second part of the chapter, several other rare earth dopants – same valence but different ion size – are introduced and their effect on transport and morphology are studied.

11.1 Introduction

As mentioned in section 7.4, several authors strongly believe that the interface conduction of LAO/STO heterostructures can be solely ascribed to interface intermixing (see e.g. [1, 2]). This is usually envisaged as being *A*-site cation doping of the STO, i.e. La diffusing into the STO substrate. The bulk properties of La-doped STO have been studied extensively: $La_xSr_{1-x}TiO_3$ is usually viewed in terms of La^{3+}-doping of the Sr-site of STO and is metallic with electron-like carriers for a wide range of x [3–9].

There are several motivations for artificially inserting LSTO layers at the LAO/STO interface (section 11.2). Firstly, to (partially) simulate intermixing conditions and compare the transport properties of undoped & doped systems. Secondly, if the interface is already intermixed, the thermodynamic driving force for further interdiffusion is lowered. And lastly, perhaps there is a possibility of inserting extra carriers from the La-doping.

The layers inserted here have the nominal composition of $(La_{0.5},Sr_{0.5})TiO_3$ – experiments with $(La_{0.02},Sr_{0.98})TiO_3$ did not reveal a strong dependence, most likely because this material on its own is not conductive under the deposition conditions employed. The location of the substrate in the heterostructures is indicated by a double dash, '//'.

After modulating the carrier density with La-doped interlayers, other rare earth dopants are inserted at the interface (section 11.3), namely Nd, Sm and Dy, all as $(RE_{0.5},Sr_{0.5})TiO_3$. These RE-ions are expected to have the same valence of RE^{3+} as opposed to the Sr^{2+}, but should exhibit an effect in the strain, relating to their different ion sizes ($r_{La} > r_{Nd} > r_{Sm} > r_{Dy}$).

In order to provide a comparison, thick 120 uc films of RE:STO are grown on STO (0 0 1) under the same conditions as the LAO/1 uc RE:STO//STO heterostructures. Lattice parameters are obtained from XRD, using the B1 diffractometer on RE:STO films

(with profile fitting and averaging over 3 (0 0 l) peaks) and using the B2 diffractometer to determine the LAO (1 0 3) reflection for an accurate measurement of the out-of-plane LAO lattice constant. Since only one unit cell of RE:STO is present, it is impossible to detect by XRD and so the LAO is used as a probe for this monolayer.

Electrical contacts were made with Al wires using a wire bonder. The Hall effect was measured in van der Pauw configuration (see section 2.3). The resistance versus temperature (R–T) curves were obtained during the warming up cycle in a 4-point contact measurement with a spacing of approximately 5 mm between the positive and negative terminals. All R–T curves are fitted with the power law of equation (9.1) (see section 9.3).

11.2 Interfaces with $(La_{0.5},Sr_{0.5})TiO_3$

A 120 uc (almost bulk) $La_{0.5}Sr_{0.5}TiO_3$ film grown epitaxially on an STO substrate was found to be highly conducting in line with the bulk properties of LSTO[1]. The R–T (Figure 11.1) is mostly T^2, indicative of electron-electron (Fermi-liquid) scattering, agreeing with the results on bulk LSTO samples [5], doped STO [10] and oxygen deficient LAO//STO heterostructures (section 9.3).

In 'standard' LAO//STO heterointerfaces, the onset of conduction occurs above a threshold LAO thickness of 3–4 uc [11, 12]. The existence of this threshold is normally advanced as the most convincing support for the electronic reconstruction model for conduction at this interface (see section 7.2 and e.g. [13]). To verify that a single LSTO layer at the interface does not support conduction in its own right, samples capped with STO or with LAO below the critical thickness were grown: 15 uc STO/1 uc LSTO//STO and 2 uc LAO/1 uc LSTO//STO. Both of these samples were insulating at room temperature. Samples with LAO overlayers thicker than this threshold were conductive, as expected. These results clearly indicate that even if an LSTO interlayer is introduced at the interface, this is not sufficient in itself to induce conduction.

A next set of experiments was aimed at determining the extent to which the presence of LSTO layers influences carrier density and mobility in a heterostructure with a sufficiently thick LAO capping layer. Hall measurements (Figure 11.2) were made on LAO/1 uc STO//STO, LAO/1 uc LSTO//STO and LAO/3 uc LSTO//STO samples (with 15 uc LAO in all cases). No non-linearity in the Hall voltage was observed within the magnetic field limits (inset of Figure 11.2), so the data are interpreted as a single carrier band (see section 7.5 and references therein for dual carrier model behaviour). The reference sample with 1 uc of homoepitaxial STO takes into account the fact that 2DEG properties seem to degrade with increasing thickness of pulsed laser deposited STO even under optimised conditions (chapter 10). The 1 uc LSTO sample follows the temperature-activated trend of the undoped interface, but its 200 K carrier density of over 10^{14} cm^{-2} clearly exceeds the value of the undoped LAO/1 uc STO//STO reference sample by almost an order of magnitude. The carrier density in the 3 uc LSTO sample is rather low and more or less constant over the temperature range, possibly reflecting extrinsic doping. The other two samples exhibit a degree of temperature-activation in the temperature dependence of their carrier density. The mobilities of all heterointerfaces are similar, indicating no significant change in scattering, despite the very different carrier densities in the LSTO-doped samples.

The carrier density values obtained for the 1 uc LSTO sample (over 10^{14} cm^{-2} at 200

[1]Remarkably, a 120 uc LSTO film grown under identical conditions on a $NdGaO_3$ (001) substrate was found to follow a semiconducting R–T behaviour. The film was fully strained to the substrate as evidenced from a reciprocal space map around the NGO (206)/LSTO (113) reflections.

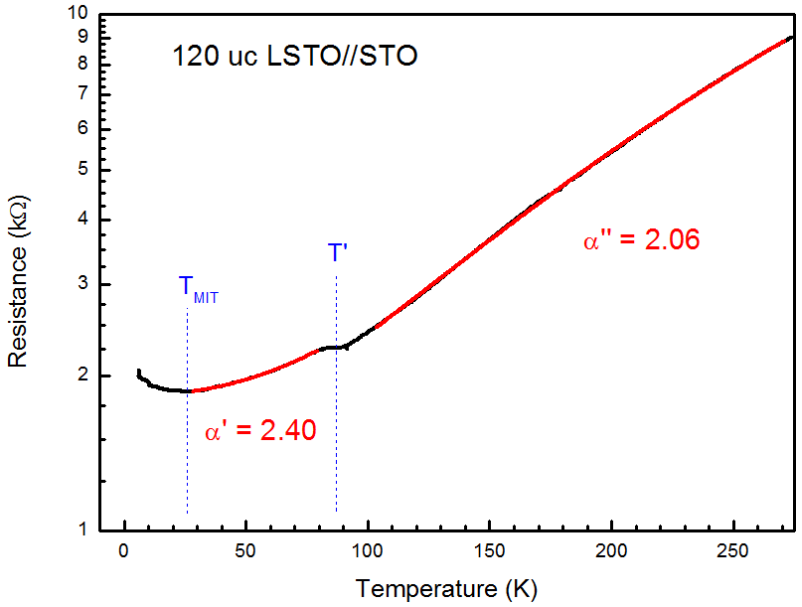

Figure 11.1: Resistance versus temperature of a 120 uc $La_{0.5}Sr_{0.5}TiO_3$ film grown epitaxially on STO, with power law fits in different temperature ranges.

K) are the highest reported for LAO//STO heterointerfaces produced by PLD at this oxygen pressure. Authors have reported higher carrier densities of LAO//STO samples, but these were always deposited in low oxygen pressures (see section 7.3). The 10^{-2} mbar oxygen partial pressure used here is sufficiently high to avoid significant influence of oxygen vacancies in the STO substrate on the conductive properties, as was demonstrated in chapter 9.

The R–T behaviour of La-doped heterointerfaces with up to 3 unit cells of LSTO on STO, capped with either 15 unit cells of STO or LAO is shown in Figure 11.3. The transition temperatures discussed in section 9.3 are also clearly present in these LSTO-interfaced samples and are therefore not associated with the incorporation of the LSTO layer. One transition (at T' $\approx$ 85 K) also appears in the LSTO//STO sample (Figure 11.1), which might indicate a relation to La or oxygen vacancy doping, known to lower the transition temperature [14]. The STO-capped 15 uc STO/3 uc LSTO//STO sample was studied in order to understand the nature of the conduction mechanism in the absence of LAO and also to determine whether the presence of LAO with LSTO interlayers is required at all. Similar to the case of $\approx$ 4uc of Nb:STO capped by STO [15], this sample shows a conductive behaviour, but only above $\approx$180 K. The power law dependence in this region is approximately T^2, with a comparable exponent appearing for the 15 uc LAO/3 uc LSTO//STO sample in the same temperature region, again pointing towards bulk-like Fermi-liquid behaviour (as for LSTO, see above). With LAO as the capping layer, the resistance is significantly lowered, as mentioned before. Upon reducing the thickness of the LSTO from 3 uc to 1 uc, the resistance is lowered further by an order of magnitude, indicating a different mechanism than purely extrinsic doping to generate the mobile carriers.

In discussing these results the starting focus is on the LAO/1 uc LSTO//STO sample which shows a much larger density of carriers at all temperatures compared to LAO/STO reference interfaces. These carriers must be induced by the La-doping of a single unit cell, but the results demonstrate that these are inactive unless a sufficient thickness of LAO caps the structure. Rather than having three times the number of carriers, a LAO/3

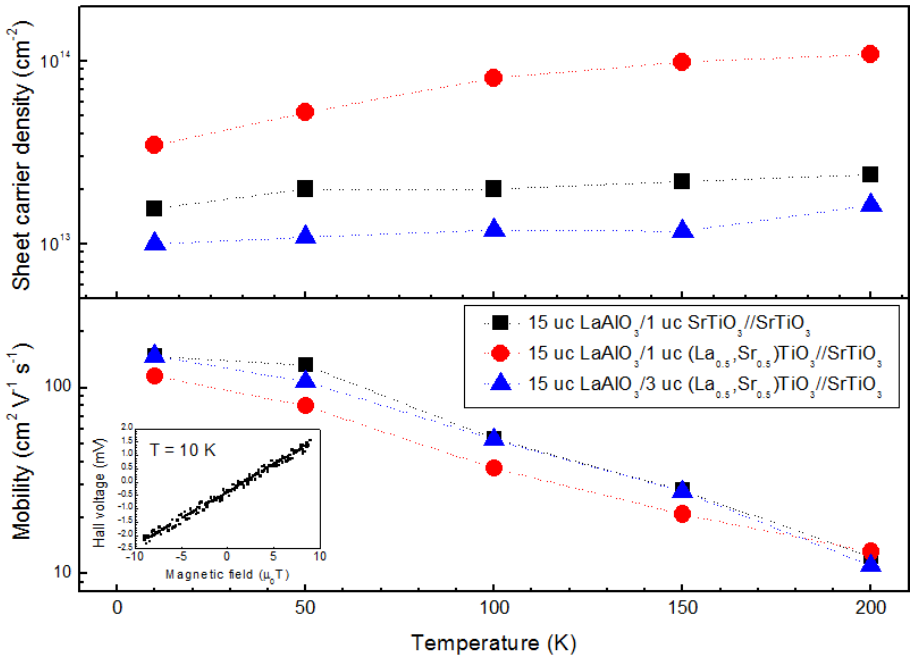

Figure 11.2: Sheet carrier density and mobility for LAO/1 uc STO//STO, LAO/1 uc LSTO//STO and LAO/3 uc LSTO//STO heterostructures. Inset: Hall voltage (corrected for magnetoresistance) at 10 K for the LAO/1 uc STO//STO sample.

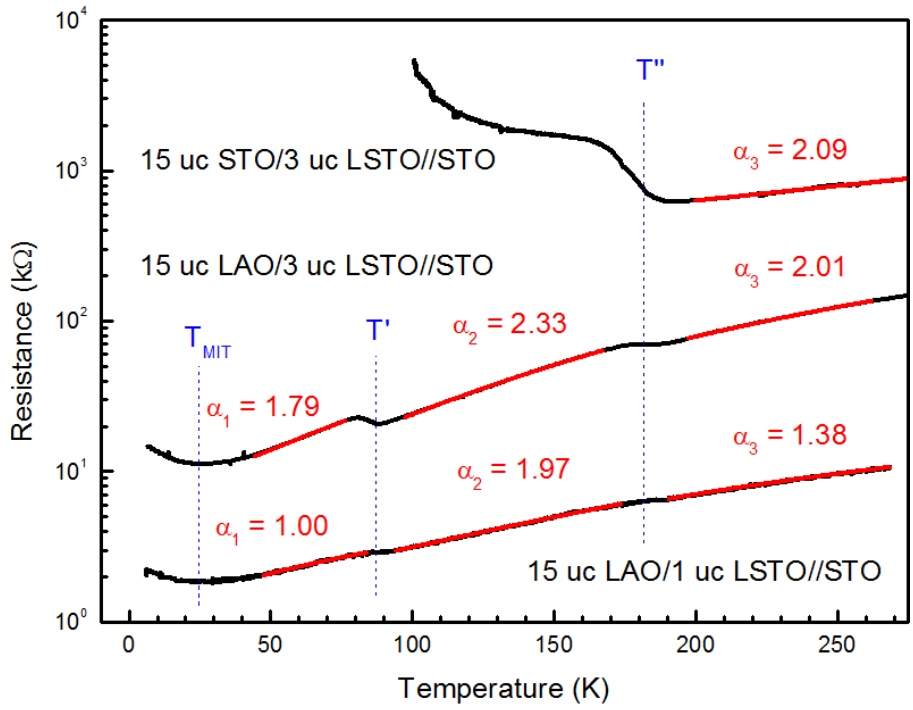

Figure 11.3: Resistance versus temperature with power law fits for STO/3 uc LSTO//STO, LAO/3 uc LSTO//STO and LAO/1 uc LSTO//STO heterostructures. Transition temperatures are marked by a dashed line.

uc LSTO//STO sample actually has significantly fewer mobile carriers. This potentially indicates a complex interaction between electronic or structural changes induced by the LAO capping layer and the presence of dopants. The latter can be either deliberately introduced as in these heterostructures or can arise from interface interdiffusion as observed for LAO//STO (section 7.4).

To verify the hypothesis that the carriers are related to and confined to the interface and not merely supplied by the LSTO, a heterostructure of 15 uc LAO/1 uc STO/1 uc LSTO//STO was grown. The carrier density was found to be reduced to $\approx 1.6 \cdot 10^{13}$ cm^{-2} (at 200 K), the value for LAO/1 uc STO//STO, i.e. as if the LSTO layer was not present. This confirms the interface confinement and excludes a pure intermixing mechanism, similar to earlier offset-doping experiments with transition metal doped STO [16].

In order to observe general trends in the α_i values, they are plotted against the number of LSTO unit cells for each temperature region (Figure 11.4). As the LSTO thickness increases, both α_1 and α_3 tend towards bulk doped-like behaviour, i.e. $\alpha \approx 2$. Put differently, as the LSTO thickness decreases, these values tend towards $\alpha \approx 1$, which implies a more two-dimensional confinement of the carriers (non-Fermi-liquid behaviour, i.e. $\alpha = 1$) as introduced in section 9.3. This nearly linear T-dependence (shaded blue region in Figure 11.4) thus marks a fundamental characteristic of a 2D confined LAO/1 uc LSTO//STO 2DEG, even more so than the unmodified interface. This interface confinement corroborates earlier results on interface doping [16]. The results above show that the LSTO interface thickness needs only to exceed a single unit cell, before the dominant conduction in the intermixed layer switches from non-Fermi-liquid-like scattering to bulk electron-electron scattering. Just as in YBCO in the higher temperature range, no phonon scattering contribution ($\alpha \rightarrow 3$) is observed [17]. An $\alpha \approx 2$ temperature dependence also occurs in the intermediate region (100-170 K) of all heterostructures (Figure 11.4), which might indicate that the carriers are lying deeper in the (L)STO in this temperature regime, most likely related to the structural phase changes occurring at the boundaries of the temperature range (T' and T").

11.3 Interfaces with other RE-ions

11.3.1 Transport measurements

There appears to be a great variation of carrier density depending on the RE-dopant atom, not only in the bulk RE:STO film, but also in the LAO/1 uc RE:STO//STO heterostructure (Figure 11.5). Only the data at 200 K are shown, since at this temperature all films are (more or less) conductive. The La:STO based structures have the highest carrier density, as discussed in detail in section 11.2. The trend of the LAO/STO heterostructures perfectly follows that of the RE:STO thin films. It appears that, despite all RE ions being electron donors (valence of 3+), only the La and Nd defect levels are efficient as electron donors, whereas the other smaller ions (Sm, Dy) act mostly as electron traps. Similar trends were observed by Jang et al. [18], although their structures did not contain any LAO and the effect has been solely ascribed to oxygen octahedra rotations.

The observed mobilities in for all LAO/1 uc RE:STO//STO samples are fairly similar (Figure 11.6), indicating no major change in the scattering mechanism, despite the differences in carrier density. All mobility values do seem to converge at 200 K however, with a value of ≈ 10 $cm^2/V/s$, which seems to be a fundamental value for (doped) STO at this temperature [7, 19, 20].

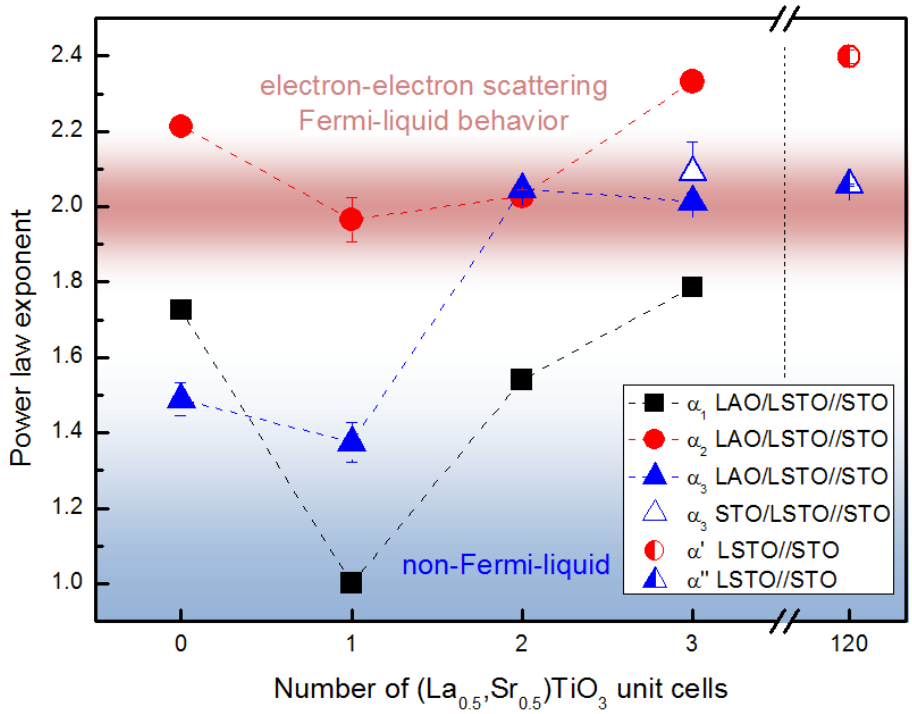

Figure 11.4: Overview of power law exponents from the resistance versus temperature fits for various samples containing LSTO as well as an undoped LAO//STO heterostructure

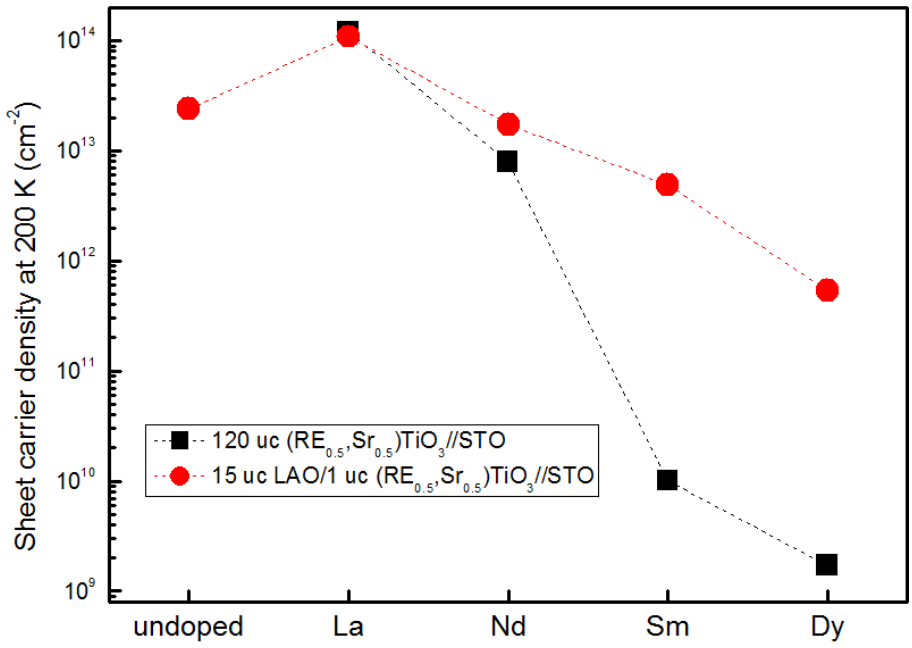

Figure 11.5: Sheet carrier density at 200 K as a function of the RE-dopant for 120 uc RE:STO (black) and 15 uc/1 uc RE:STO//STO (red) samples.

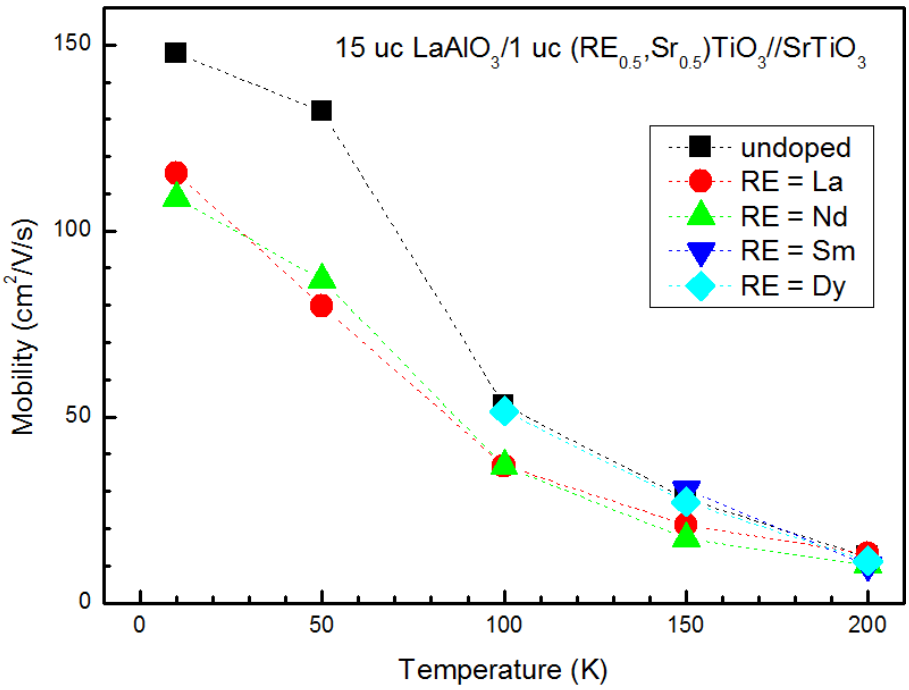

Figure 11.6: Evolution of the mobility versus temperature for LAO/1 uc RE:STO//STO heterostructures.

11.4 Strain analysis of RE-defects

X-ray spectra, around the STO (0 0 2) reflection, for the 120 uc RE:STO//STO films are shown in Figure 11.7, with a dashed line roughly indicating the position of the film peak. All these films were found to be fully strained in-plane, as the (1 0 3) reciprocal space map confirmed. The variation is more or less as expected, with a decreasing deviation from the STO lattice parameter value as the ion size decreases. Strangely however, the Nd:STO does not seem to follow that trend.

Comparing the relative change in c-parameter value of the RE:STO films with that of the LAO films (which are also fully strained in plane), reveals a stunning resemblance between the two data sets (Figure 11.8). The LAO c-parameter deviates by $\approx 1\%$ from the fully strained theoretical elastic value, which could arise from changes in the STO-surface during PLD (see section 10.5) as well as off-stoichiometry (section 10.5 and [21]). The smaller modulation of $\approx 0.25\%$ however follows the trend from RE:STO films.

Similar strain-imitation has been observed before in cuprate superconductor lattices and has been termed 'Madelung strain' by the authors [22]. Essentially the electrostatic repulsions induced by the bottom layer (i.e. RE:STO) is transferred to or affects the top layer (i.e. LAO). Although this may appear reasonable, it happens in the LAO/STO heterostructure when even only a single unit cell of RE:STO is introduced. This clearly shows the sensitivity of the LAO to electrostatic repulsions in this configuration – something that has been described (in the thin LAO limit) by Cancellieri et al. [23].

11.5 Conclusion

A significant (order of magnitude) enhancement of the carrier density to 10^{14} cm^{-2} has been observed in LAO/1 uc LSTO//STO heterostructures, as compared to undoped LAO//STO. A sufficient thickness of LAO is still required for 2DEG formation, excluding

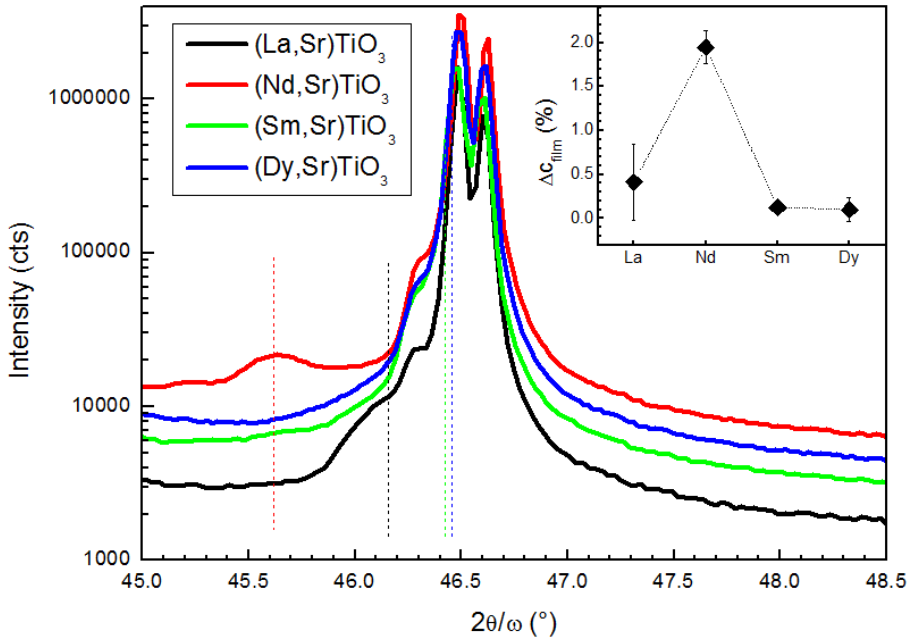

Figure 11.7: X-ray diffraction spectra for 120 uc RE:STO//STO films around the STO (0 0 2) peak. The film positions are indicated with a dashed line. The STO (0 0 2) peak exhibit clear splitting due to the Cu Kα_1 and Cu Kα_2 lines.
Inset: calculated relative change of the out-of-plane lattice parameter of the RE:STO films as a function of RE-dopant.

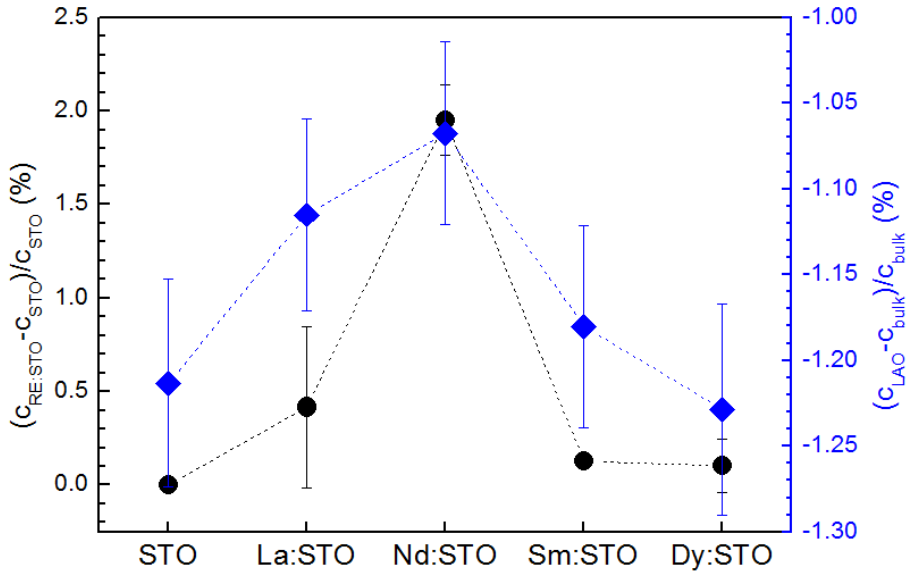

Figure 11.8: Evolution of relative change of the out-of-plane lattice parameter for RE:STO films (black •) and LAO (in LAO/1 uc RE:STO//STO films; blue ♢) versus RE dopant.

purely extrinsic effects. Detailed analysis of the R–T behaviour was performed on interface doped heterostructures (LAO/n uc LSTO//STO, where n = 1–3). Two-dimensionally conducting samples with a single (n = 1) LSTO uc at the interface tend towards non-Fermi-liquid behaviour in the low (30-80 K) and high (190-240 K) temperature region and appear to be even more interface-confined than undoped LAO//STO. Samples with more LSTO unit cells ($n > 1$) are increasingly dominated by electron-electron scattering as the LSTO thickness increases.

In order to further investigate the strain component on the conductivity of RE-doped LAO/STO heterointerfaces, an artificial defect layer of $(RE_{0.5},Sr_{0.5})TiO_3$ was introduced with RE-ions of decreasing size (La, Nd, Sm and Dy). It was found that, in terms of transport, the position of the RE defect level within the bandgap (and hence its efficiency as a donor) probably plays an important role in the trapping (Sm, Dy) or enhancement (La, Nd) of type I carriers. There appears to be no connection between the conductivity and the strain induced by the RE-defects, due to an apparent anomaly for Nd-doping. The variation in strain in RE:STO//STO films however is distinctively reflected in the strain of the 15 uc LAO overlayer in the heterostructures, despite the fact that the RE:STO layer is only a single unit cell thick.

All the LAO/RE:STO//STO results above point towards an LAO overlayer that is very sensitive to electrostatic and structural fluctuations, that have a significant influence, yet ambiguous connection with the conductivity at the interface.

Bibliography

[1] P. R. Willmott, S. A. Pauli, R. Herger, C. M. Schlepütz, D. Martoccia, B. D. Patterson, B. Delley, R. Clarke, D. Kumah, C. Cionca, and Y. Yacoby. Structural basis for the conducting interface between $LaAlO_3$ and $SrTiO_3$. *Physical Review Letters*, 99: 155502, 2007.

[2] S. A. Chambers, M. H. Engelhard, V. Shutthanandan, Z. Zhu, T. C. Droubay, L. Qiao, P. V. Sushko, T. Feng, H. D. Lee, T. Gustafsson, E. Garfunkel, A. B. Shah, J.-M. Zuo, and Q. M. Ramasse. Instability, intermixing and electronic structure at the epitaxial $LaAlO_3/SrTiO_3$ (001) heterojunction. *Surface Science Reports*, 65:317–352, 2010.

[3] N. G. Eror and U. Balachandran. Self-compensation in lanthanum-doped strontium titanate. *Journal of Solid State Chemistry*, 40:85–91, 1981.

[4] Joseph E. Sunstrom, Susan M. Kauzlarich, and Peter Klavins. Synthesis, structure and properties of $La_{1-x}Sr_xTiO_3$ ($0 \leq x \leq 1$). *Chemistry of Materials*, 4:346–353, 1992.

[5] Y. Tokura, Y. Taguchi, Y. Okada, Y. Fujishima, T. Arima, K Kumagai, and Y. Iye. Filling dependence of electronic properties on the verge of the metal–Mott-insulator transitions in $Sr_{1-x}La_xTiO_3$. *Physical Review Letters*, 70(14):2126–2129, 1993.

[6] A. Ohtomo, J. Nishimura, Y. Murakami, and M. Kawasaki. Electronic transport properties in $SrTiO_3$–$LaAlO_3$ solid-solution films. *Applied Physics Letters*, 88:232107, 2006.

[7] Junwoo Son, Pouya Moetakef, Bharat Jalan, Oliver Bierwagen, Nicholas J. Wright, Roman Engel-Herbert, and Susanne Stemmer. Epitaxial $SrTiO_3$ films with electron mobilities exceeding 30,000 $cm^2\ V^{-1}\ s^{-1}$. *Nature Materials*, 9:482–484, 2010.

[8] D. J. Keeble, B. Jalan, L. Ravelli, W. Egger, G. Kanda, and S. Stemmer. Suppression of vacancy defects in epitaxial La-doped $SrTiO_3$ films. *Applied Physics Letters*, 99: 232905, 2011.

[9] Meng Gu, Craig R. Dearden, Chengyu Song, Nigel D. Browning, and Yayoi Takamura. Structural variability in $La_{0.5}Sr_{0.5}TiO_{3\pm\delta}$ thin films. *Applied Physics Letters*, 99: 261907, 2011.

[10] D. van der Marel, J. L. M. van Mechelen, and I. I. Mazin. Common Fermi-liquid origin of T^2 resistivity and superconductivity in n-type $SrTiO_3$. *Physical Review B*, 84:205111, 2011.

[11] S. Thiel, G. Hammerl, A. Schmehl, C. W. Schneider, and J. Mannhart. Tunable quasi-two-dimensional electron gases in oxide heterostructures. *Science*, 313:1942–1945, 2006.

[12] Mark Huijben, Alexander Brinkman, Gertjan Koster, Guus Rijnders, Hans Hilgenkamp, and Dave H. A. Blank. Structure-property relation of $SrTiO_3/LaAlO_3$ interfaces. *Advanced Materials*, 21(17):1665–1677, 2009.

[13] Rossitza Pentcheva and Warren E. Pickett. Electronic phenomena at complex oxide interfaces: insights from first principles. *Journal of Physics: Condensed Matter*, 22: 043001, 2010.

[14] D. Bäuerle and W. Rehwald. Structural phase transitions in semiconducting $SrTiO_3$. *Solid State Communications*, 27:1343–1346, 1978.

[15] Y. Kozuka, M. Kim, H. Ohta, Y. Hikita, C. Bell, and H. Y. Hwang. Enhancing the electron mobility via delta-doping in $SrTiO_3$. *Applied Physics Letters*, 97:222115, 2010.

[16] T. Fix, F. Schoofs, J. L. MacManus-Driscoll, and M. G. Blamire. Charge confinement and doping at $LaAlO_3/SrTiO_3$ interfaces. *Physical Review Letters*, 103:166802, 2009.

[17] S. W. Tozer, A. W. Kleinsasser, T. Penney, D. Kaiser, and F. Holtzberg. Measurement of anisotropic resistivity and Hall constant for single-crystal $YBa_2Cu_3O_{7-x}$. *Physical Review Letters*, 59(15):1768–1771, 1987.

[18] H. W. Jang, D. A. Felker, C. W. Bark, Y. Wang, M. K. Niranjan, C. T. Nelson, Y. Zhang, D. Su, C. M. Folkman, S. H. Baek, S. Lee, K. Janicka, Y. Zhu, X. Q. Pan, D. D. Fong, E. Y. Tsymbal, M. S. Rzchowski, and C. B. Eom. Metallic and insulating oxide interfaces controlled by electronic correlations. *Science*, 331:886–889, 2011.

[19] A. Dubroka, M. Rössle, K. W. Kim, V. K. Malik, L. Schultz, S. Thiel, C. W. Schneider, J. Mannhart, G. Herranz, O. Copie, M. Bibes, A. Barthélémy, and C. Bernhard. Dynamical response and confinement of the electrons at the $LaAlO_3/SrTiO_3$ interface. *Physical Review Letters*, 104:156807, 2010.

[20] Pouya Moetakef, Tyler A. Cain, Daniel G. Ouellette, Jack Y. Zhang, Dmitri O. Klenov, Anderson Janotti, Chris G. Van de Walle, Siddharth Rajan, S. James Allen, and Susanne Stemmer. Electrostatic carrier doping of $GdTiO_3/SrTiO_3$ interfaces. *Applied Physics Letters*, 99:232116, 2011.

[21] L. Qiao, T. C. Droubay, T. Varga, M. E. Bowden, V. Shutthanandan, Z. Zhu, T. C. Kaspar, and S. A. Chambers. Epitaxial growth, structure and intermixing at the $LaAlO_3/SrTiO_3$ interface as the film stoichiometry is varied. *Physical Review B*, 83: 085408, 2011.

[22] Vladimir Y. Butko, Gennady Logvenov, Natasha Bozovic, Zoran Radovic, and Ivan Bozovic. Madelung strain in cuprate superconductors – a route to enhancement of the critical temperature. *Advanced Materials*, 21(36):3644–3648, 2009.

[23] C. Cancellieri, D. Fontaine, S. Gariglio, N. Reyren, A. D. Caviglia, A. Fete, S. J. Leake, S. A. Pauli, P. R. Willmott, M. Stengel, Ph. Ghosez, and J.-M. Triscone. Electrostriction at the $LaAlO_3/SrTiO_3$ interface. *Physical Review Letters*, 107:056102, 2011.

Chapter 12

ATiO$_3$ modified LAO/STO heterostructures

In the previous chapter rare earth doped STO interlayers were inserted at the LAO/STO interface. There appears to be an interplay between electrostatic doping and strain, which is hard to decouple. Therefore in this chapter, perovskite interlayers with A-site cations of the same valence as Sr are inserted: a purely structural effect on the conduction is to be expected.

12.1 Introduction

In order to focus on the effects of strain at the LAO/STO interface, other research groups have attempted to grow LAO/STO heterostructures on different substrates, such as $(LaAlO_3)_{0.3}(Sr_2AlTaO_3)_{0.7}$ (LSAT) [1–3], $NdGaO_3$ [1, 4] and $DyScO_3$ [1]. The ideal case would be to grow an LAO/STO heterostructure on a ferroelectric $BaTiO_3$ (BTO) substrate: the in-plane cell parameter can then be tuned by an electric field applied to the BTO. This has however been impossible to achieve, mostly because of the unknown BTO surface termination. The recipes for STO surface termination (e.g. [5, 6]) were unsuccessful, as did oxygen annealing treatments.

An alternative approach is to insert different titanate perovskites at the interface between LAO and STO while maintaining the same valence as Sr^{2+}. Candidates for this are $CaTiO_3$, $BaTiO_3$, $SnTiO_3$ and $PbTiO_3$. $CaTiO_3$ is usually indexed in an orthorhombic unit cell, but also a pseudo-cubic unit cell with $a \approx 0.3822$ nm is plausible [7, 8]. The crystal structure of $BaTiO_3$ is tetragonal at room temperature with $a = 0.3990$ nm and $c = 4.035$ nm. $SnTiO_3$ is predicted to be a ferroelectric perovskite (e.g. [9]), but this has not been verified experimentally so far. Thick films on STO do not seem to result in the correct perovskite phase, but rather an ilmenite phase [10]. $PbTiO_3$ is another ferroelectric, but is not used here because of its hazardous nature and contamination of the deposition chamber with the volatile Pb.

Targets are pressed & sintered following the usual procedure with the appropriate amounts of starting powders (see sections 2.1.2 and chapter 8). Depositions are carried out at 10 Hz and a substrate temperature of 850 ℃, with the optimised laser fluence of 1 J/cm^2 (chapter 10). Lattice parameters are determined from reciprocal space maps around the (1 0 3) reflection of STO and LAO. Ionic radii are obtained from references [11] and [12].

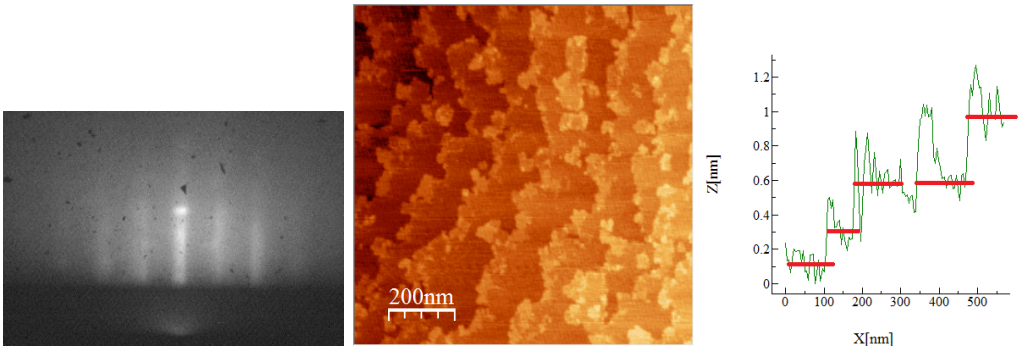

(a) (b) (c)

Figure 12.1: **(a)** RHEED diffraction pattern of a ≈ 7 nm $SnTiO_3$ film on STO along STO [1 0 0].
(b) AFM image of a ≈ 12 nm $SnTiO_3$ film on STO.
(c) Linear section across the steps in **(b)** showing a step height of ≈ 0.4 nm. A new layer has nucleated at the step edges.

12.2 Structural characterisation

Firstly it is important to verify that all materials grow in 2D mode on STO. This is especially relevant for $SnTiO_3$, which assumes an ilmenite like $SnTiO_x$ structure in thick films [10]. In the thin limit however, $SnTiO_3$ appears to grow layer-by-layer, as evidenced from RHEED and consecutive AFM (Figure 12.1). The steps on the AFM scan, with a height of ≈ 0.4 nm, suggest that up to ≈ 10–12 nm the $SnTiO_3$ grows in a perovskite-like structure on STO.

Also $BaTiO_3$ and $CaTiO_3$ were found to grow fully strained on STO up to a thickness of ≈ 5 nm. This means that all the aforementioned ATiO$_3$ materials can be assumed to be fully strained into a perovskite-like unit cell when a single layer of them is inserted at the LAO/STO interface.

Heterostructures of 15 uc LAO/1 uc ATO//STO were grown as previously described. Careful analysis of the RHEED intensity oscillations reveals that the growth of the LAO is influenced by the presence of the additional ATO layer (Figure 12.2). In all curves (LAO on STO, LAO on $CaTiO_3$ and LAO on $BaTiO_3$), the period of the first oscillation is different from all the following ones (which have the same period). This could be due to non-uniform surface termination, but that is not the case here: the first oscillation is well-defined and has the correct period with respect to the starting surface. Furthermore, the oscillation period is exactly the same and in phase, irrespective of the sample, after the first or second LAO layer. This points towards the so-called 'reconstruction induced phase shift' (RIPS) effect, which was briefly introduced in section 2.2.1. It indicates that the initial growth stage of the LAO is strongly influenced by the (strained) interface layer, but on the other hand this is compensated within 1-2 deposited layers.

The influence of the interfacial layer on the structure of the LAO becomes even more apparent in the strain in the layer. Just as in section 11.4, a single unit cell of a different (strained) material has a profound impact on the volume of the LAO unit cell . The LAO is fully strained in-plane, while the c-axis lattice parameter (and thus the unit cell volume) follows the trend of increasing A-site cation size, as anticipated (Figure 12.3).

This behaviour confirms the interface-induced straining of LAO found in section 11.4 for the RE:STO interlayers, which can be explained in terms of the so-called 'Madelung strain' [13]. From the results above it is clear that the structure of the 2DEG heterostruc-

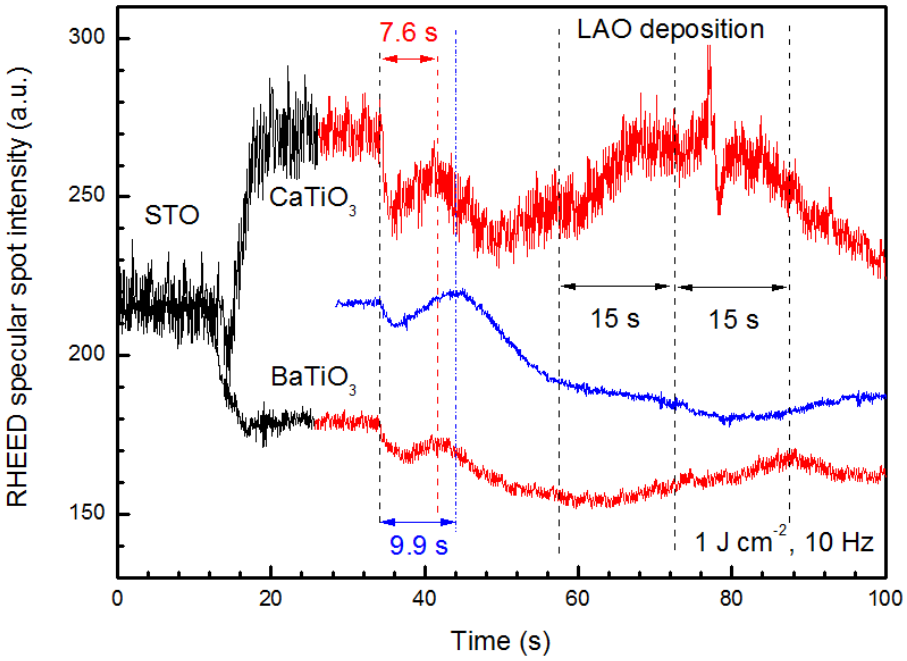

Figure 12.2: RHEED specular spot intensity profile for the deposition of LAO on $CaTiO_3$ (top, red), on $BaTiO_3$ (bottom, red) and on a bare STO substrate (middle, blue). The black trace follows the deposition of 1 uc of $CaTiO_3$ and $BaTiO_3$. Different peak-to-peak times are indicated in different phases of the deposition. All depositions are performed at 1 J/cm^2 and 10 Hz.

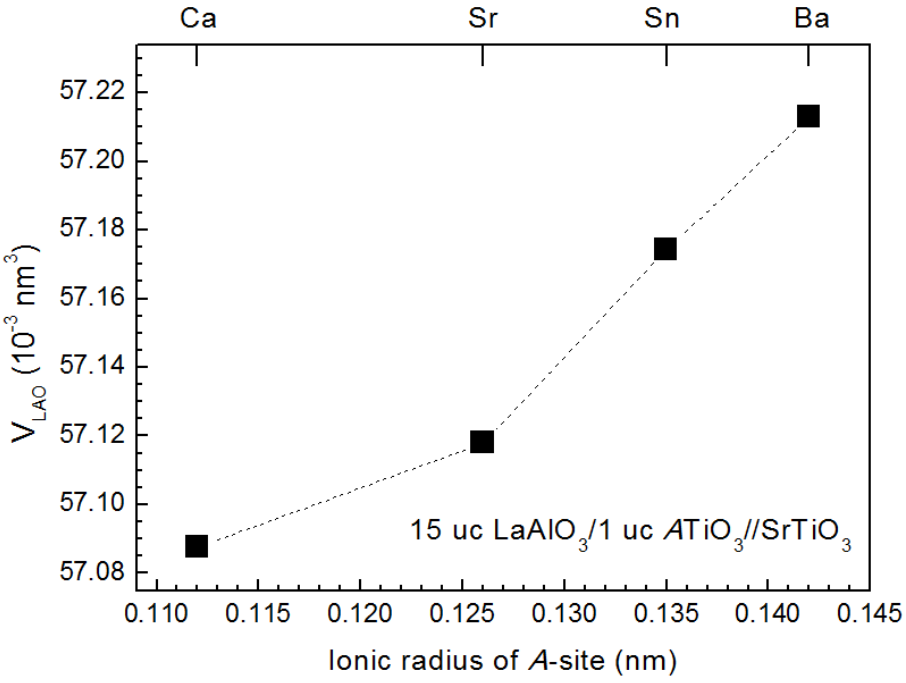

Figure 12.3: Variation of LAO unit cell volume versus ion size of the underlying $ATiO_3$ unit cell in the heterostructure.

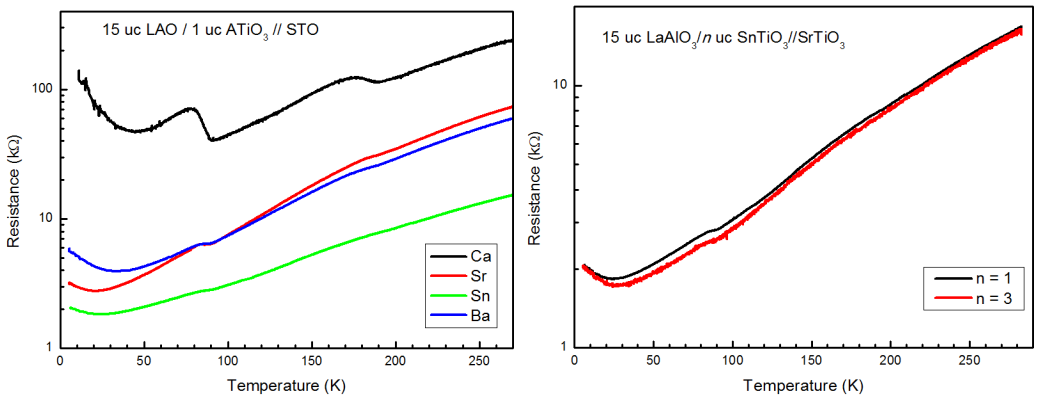

(a) (b)

Figure 12.4: Resistance versus temperature curves (in warming) (**a**) for LAO/1 uc $ATiO_3$//STO samples with A = Ca, Sr, Sn and Ba; (**b**) LAO/1 uc $SnTiO_3$//STO and LAO/3 uc $SnTiO_3$//STO.

ture is successfully modified by inserting perovskites with varying A-site cation sizes. The next step is to have a look at how these modifications affect the transport properties.

12.3 Transport measurements

A first direct and easy comparison is in the resistance versus temperatures curves of all samples (Figure 12.4a). The R–T is measured in the same way as in sections 9.3 and 11.2 and also here distinct transition temperatures (T' and T") at the same positions are observed. The resistance decreases as the A-site cation changes from Ca, to Sr and to Sn, but then increases again for Ba. The observed resistance for the $SnTiO_3$-interface is almost as low as for the 1 uc LSTO-interfaced samples in section 11.2. There is however one fundamental difference: three instead of just a single unit cell at the interface does not make a significant difference in terms of resistance (Figure 12.4b). This confirms that the effect is purely structural here, whereas there was a charge (compensation) component present in the LSTO series. The extent to which the transitions are clear in the graph, seems to depend on the resistance.

In different temperature ranges, these curves can be fitted with equation (9.1) as before. The resulting power coefficients are displayed versus A-site cation in Figure 12.5. The coefficient in the low temperature regime, α_1, has a clearly increasing trend, suggesting more influence of the lattice (and lower two-dimensionality) for bigger A-site cations. Aside from the Ca-case, this trend can be observed in the α_3 as well. The phonon contribution becomes more significant for all but the Sr-cation in the intermediate temperature regime. It is however difficult to fully interprete these data.

Despite what would be expected, the electron mobility is more or less the same for all heterostructures (Figure 12.6), except for the (highly resistive) $CaTiO_3$-interfaced sample. Clearly changing the A-site cation changes the sheet carrier density, in a way similar to a single unit cell of LSTO. The $SnTiO_3$ interface reaches a carrier density just below 10^{14} cm^{-2}, close to the maximum observed by LSTO-doping (section 11.2).

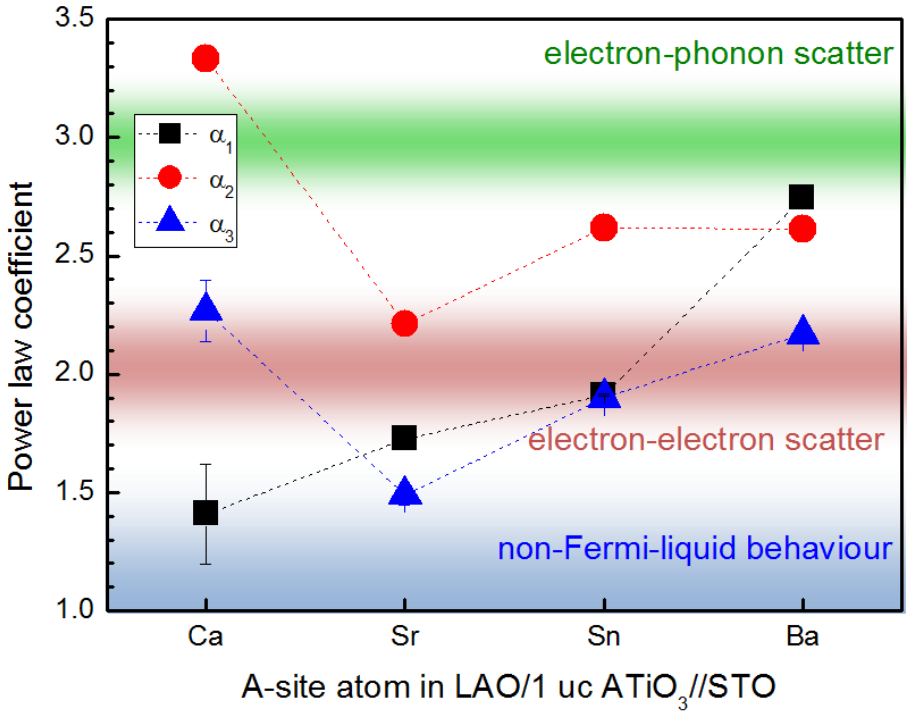

Figure 12.5: Power law coefficients from R–T curves of Figure 12.4 versus A-site cation.

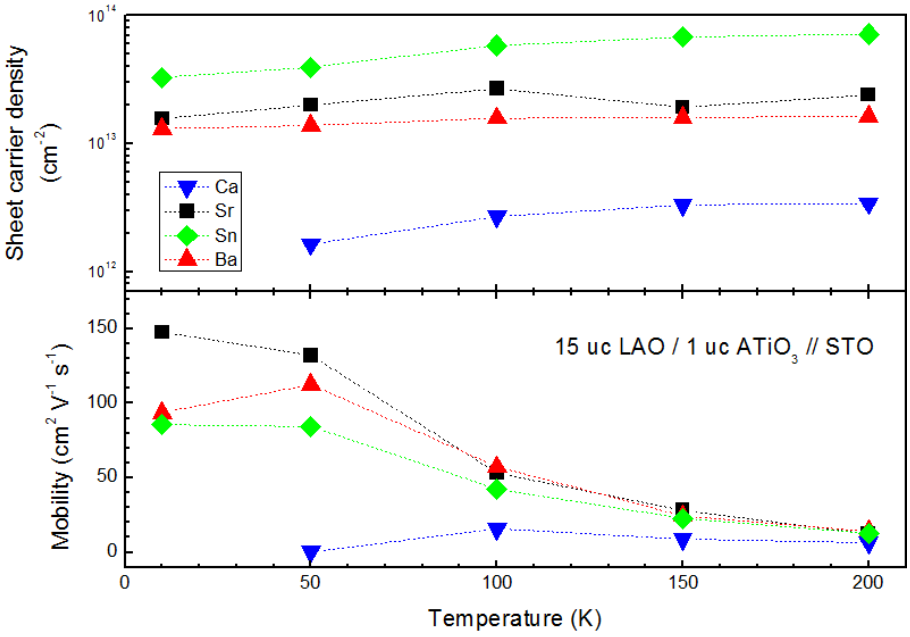

Figure 12.6: Sheet carrier density (top) and electron mobility (bottom) for LAO/1 uc ATiO$_3$//STO samples with A = Ca, Sr, Sn and Ba.

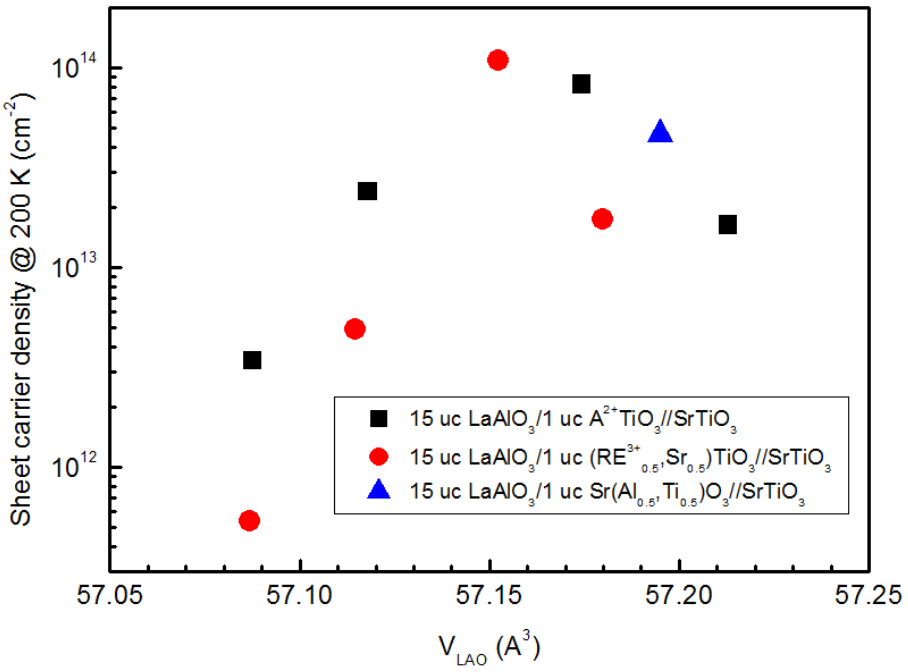

Figure 12.7: Sheet carrier density at 200 K versus unit cell volume of LAO for different sets of interface doped samples.

12.4 Discussion

From the structural measurements and electronic transport characterisation above, it is clear that there is a distinct interplay between interface strain and conductivity, with an optimum amount of strain with respect to carrier density. This is even more pronounced when the volume of the LAO unit cell V_{LAO}, which is related to the strain induced by the interface unit cell, is plotted together with the carrier density at 200 K (Figure 12.7). The use of V_{LAO} allows the comparison of and with other doped heterostructures, such as RE:STO (chapter 11) and Sr(Al$_{0.5}$,Ti$_{0.5}$)O$_3$[1]. Apparently there is an optimum LAO distortion that generates the highest carrier density in the interface-ATO (or STO).

From a structural perspective, LAO normally crystallises in a rhombohedral structure at room temperature [14, 15]. Due to the epitaxy on STO however, it is forced to be tetragonal, which causes large in-plane oxygen octahedra rotations, approximately 1.6°. For small rotations, this does not affect the c-lattice parameter, but in this case a pseudo-Jahn Teller distortion could occur, causing deformations along the out-of-plane direction, as suggested by Lee and Demkov [16]. From the measured deformation of the LAO, with its known elastic constants [17], it is possible to estimate the stresses in the thin film (Table 12.1). These large stresses need to be compensated by the interface layer and the substrate. Strain accommodation in perovskites happens within 2–4 uc [18]. This small penetration depth emphasises the importance of the interface ATiO$_3$ layer.

The size of the A-site cation will play an important role in this strain accommodation: it will determine how easily the TiO$_6$-octahedra can rotate. For example, this rotation is easy in CaTiO$_3$, which is not cubic at room temperature due to these rotations [7, 8, 19]. It can be expected that rotation in BaTiO$_3$ is the most difficult. Therefore, with respect to carrier density (Figure 12.7), there must be an optimum rotation in-plane.

[1]Since Al^{3+} is a p-type dopant in STO and accepts 0.5 electrons per unit cell (due to stoichiometry), this heterostructure should be insulating according to the electronic reconstruction hypothesis.

ATiO$_3$	ϵ_{ip} (%)	ϵ_{op} (%)	σ_{ip} (GPa)	σ_{op} (GPa)
Ca	3.03	-1.22	11.41	5.60
Sr	3.03	-1.13	11.56	5.88
Sn	3.03	-1.07	11.64	6.03
Ba	3.03	-0.75	12.13	6.96

Table 12.1: Experimental strains & calculated stresses in the LAO films of experimental LAO/ATiO$_3$//STO interfaces.

With such large stresses and potentially large induced oxygen octahedra rotations in the STO (as observed by TEM [20] and HRXRD [21]), other distortions could occur. In manganites for example, these rotations go along with Jahn-Teller distortions to determine their conductive properties (see e.g. [22, 23]). Such Jahn-Teller(-like) distortions, relating to deformations of TiO_6 octahedra in titanate perovskites, also affect the conduction in these materials. Electron transport is enabled in LSTO [24] and doped $BaTiO_3$ [25] through this phenomenon.

The deduction outlined above could form an alternative hypothesis to the true origin of conduction at LAO/STO interfaces. Due to the epitaxial stress of a thin film of LAO on STO, oxygen octahedra rotations and Jahn-Teller-like lattice distortions are introduced in the uppermost layer of the substrate. This changes the electronic configuration, which can mobilise carriers that are inherently present at the interface, such as from oxygen vacancies or from La-intermixing. From the ATiO$_3$-series, it is clear that there is an optimum distortion of the interface, that generates the maximum amount of carriers. The fact that lattice distortions are at the core of the conduction mechanism, explain the various strain-related effects that have been described by other authors (section 7.5).

12.5 Conclusions

A clear trend in the LAO strain with respect to the interface ATiO$_3$ unit cell is observed, with an increasing volume of the LAO unit cell as the A-site ion increases in size. This strain effect seems to have a significant influence on the conduction, with $SnTiO_3$ giving the best results in terms of sheet carrier density (just below 10^{14} cm^{-2} at 200 K). A strong lattice coupling of the carriers is observed, which can be related to a combination of oxygen octahedra rotations and Jahn-Teller-like distortions in the titanate perovskite interface. This might form an alternative explanation for conduction at LAO/STO interfaces.

Bibliography

[1] C. W. Bark, D. A. Felker, Y. Wang, Y. Zhang, H. W. Jang, C. M. Folkman, J. W. Park, S. H. Baek, H. Zhou, D. D. Fong, X. Q. Pan, E. Y. Tsymbal, M. S. Rzchowski, and C. B. Eom. Tailoring a two-dimensional electron gas at the $LaAlO_3/SrTiO_3$ (001) interface by epitaxial strain. *Proceedings of the National Academy of Sciences of the United States of America*, 108(12):4720–4724, 2011.

[2] P. Brinks, W. Siemons, J. E. Kleibeuker, G. Koster, G. Rijnders, and M. Huijben. Anisotropic electrical transport properties of a two-dimensional electron gas at $SrTiO_3$–$LaAlO_3$ interfaces. *Applied Physics Letters*, 98:242904, 2011.

[3] F. Gunkel, P. Brinks, S. Hoffmann-Eifert, R. Dittmann, M. Huijben, J. E. Kleibeuker, G. Koster, G. Rijnders, and R. Waser. Influence of charge compensation mechanisms on the sheet electron density at conducting $LaAlO_3/SrTiO_3$-interfaces. *Applied Physics Letters*, 100:052103, 2012.

[4] Hans Boschker. *Perovskite oxide heteroepitaxy – strain and interface engineering.* PhD thesis, Universiteit Twente, 2011.

[5] G. Koster, B. L. Kropman, G. J. H. M. Rijnders, D. H. A. Blank, and H. Rogalla. Quasi-ideal strontium titanate crystal surfaces through formation of strontium hydroxide. *Applied Physics Letters*, 73(20):2920–2922, 1998.

[6] R. Gunnarsson, A. S. Kalabukhov, and D. Winkler. Evaluation of recipes for obtaining single terminated perovskite oxide substrates. *Surface Science*, 603(1):151–157, 2009.

[7] M. A. Carpenter, C. J. Howard, K. S. Knight, and Z. Zhang. Structural relationships and a phase diagram for $(Ca,Sr)TiO_3$. *Journal of Physics: Condensed Matter*, 18: 10725–10749, 2006.

[8] Kevin S. Knight. Structural and thermoelastic properties of $CaTiO_3$ perovskite between 7 K and 400 K. *Journal of Alloys and Compounds*, 509:6337–6345, 2011.

[9] William D. Parker, James M. Rondinelli, and S. M. Nakhmanson. First-principles study of misfit strain-stabilized ferroelectric $SnTiO_3$. *Physical Review B*, 84:245126, 2011.

[10] Thomas Fix, S.-Lata Sahonta, Vincent Garcia, J. L. MacManus-Driscoll, and Mark G. Blamire. Structural and dielectric properties of $SnTiO_3$, a putative ferroelectric. *Crystal Growth and Design*, 11:1422–1426, 2011.

[11] R. D. Shannon. Revised effective ionic radii and systematic studies of interatomic distances in halides and chalcogenides. *Acta Crystallographica A*, 32(5):751–767, 1976.

[12] Joseph W. Bennett, Ilya Grinberg, Peter K. Davies, and Andrew M. Rappe. Pb-free ferroelectrics investigated with density functional theory: $SnAl_{1/2}Nb_{1/2}O_3$ perovskites. *Physical Review B*, 83:144112, 2011.

[13] Vladimir Y. Butko, Gennady Logvenov, Natasha Bozovic, Zoran Radovic, and Ivan Bozovic. Madelung strain in cuprate superconductors – a route to enhancement of the critical temperature. *Advanced Materials*, 21(36):3644–3648, 2009.

[14] S. A. Hayward, F. D. Morrison, S. A. T. Redfern, E. K. H. Salje, J. F. Scott, K. S. Knight, S. Tarantino, A. M. Glazer, V. Shuvaeva, P. Daniel, M. Zhang, and M. A. Carpenter. Transformation processes in $LaAlO_3$: neutron diffraction, dielectric, thermal, optical and Raman studies. *Physical Review B*, 72:054110, 2005.

[15] Ekhard K. H. Salje and Michael A. Carpenter. High frequency elastic losses in $LaAlO_3$ and its importance for $LaAlO_3/SrTiO_3$ heterojunctions. *Applied Physics Letters*, 9: 051907, 2011.

[16] Jaekwang Lee and Alexander A. Demkov. Charge origin and localization at the n-type $SrTiO_3/LaAlO_3$ interface. *Physical Review B*, 78:193104, 2008.

[17] M. A. Carpenter, S. V. Sinogeikin, J. D. Bass, D. L. Lakshtanov, and S. D. Jacobsen. Elastic relaxations associated with the $Pm\bar{3}m$-$R\bar{3}c$ transition in $LaAlO_3$: I. Single crystal elastic moduli at room temperature. *Journal of Physics: Condensed Matter*, 22:035403, 2010.

[18] Michael A. Carpenter, Ruth E. A. McKnight, J. Howard, Christopher, Qindi Zhou, Brendan J. Kennedy, and Kevin S. Knight. Characteristic length scale for strain fields around impurity cations in perovskites. *Physical Review B*, 80:214101, 2009.

[19] A. M. Glazer. The classification of tilted octahedra in perovskites. *Acta Crystallographica Section B*, 28(11):3384–3392, 1972.

[20] C. L. Jia, S. B. Mi, M. Faley, U. Poppe, J. Schubert, and K. Urban. Oxygen octahedron reconstruction in the $SrTiO_3/LaAlO_3$ heterointerfaces investigated using aberration-corrected ultrahigh-resolution transmission electron microscopy. *Physical Review B*, 79:081405(R), 2009.

[21] J. E. Boschker, C. Folkman, C. W. Bark, A. F. Monsen, E. Folven, J. K. Grepstad, E. Wahlström, C. B. Eom, and T. Tybell. Structural coupling across the $LaAlO_3/SrTiO_3$ interface: high-resolution x-ray diffraction study. *Physical Review B*, 84:205418, 2011.

[22] T. Egami and Despina Louca. Electron-lattice coupling in manganites and cuprates. *Journal of Superconductivity*, 12(1):23–26, 1999.

[23] B. R. K. Nanda and S. Satpathy. Polar catastrophe, electron leakage and magnetic ordering at the $LaMnO_3/SrMnO_3$ interface. *Physical Review B*, 81:224408, 2010.

[24] Joseph E. Sunstrom, Susan M. Kauzlarich, and Peter Klavins. Synthesis, structure and properties of $La_{1-x}Sr_xTiO_3$ ($0 \leq x \leq 1$). *Chemistry of Materials*, 4:346–353, 1992.

[25] S. Köhne, O. F. Schirmer, H. Hesse, T. W. Kool, and V. Vikhnin. Ti^{3+} Jahn-Teller polarons and bipolarons in $BaTiO_3$. *Journal of Superconductivity*, 12(1):193–195, 1999.

Chapter 13

Transition metal doping of LAO/STO interfaces

After having studied the fundamentals behind the LAO/STO conduction by deliberately introducing defects at the interface, the focus is shifted towards functionalising the 2DEG. This chapter briefly introduces the effect of transition metal doping of LAO/STO heterostructures, but mainly focuses on the analysis of some of these samples by x-ray circular magnetic dichroism (XMCD) in order to find out about their magnetic ordering.

13.1 Introduction

The motivation to introduce a small concentration of first row transition metals (abbreviated TM) at the LAO/STO interface is similar to such doping in bulk or thin film semiconducting oxides: if a beneficial *sp–d* hybridisation occurs, ferromagnetism might arise in the 2DEG (see part I of this work). Studies with Co and Mn [1] and the other transition metals [2] indicate a strong dependence of the transport properties of the 2DEG on the type of TM, even if the concentration is only 2 at%. All decrease the carrier density at the interface, presumably by a trapping mechanism, but the extent to which this happens, appears to be related to the TM's relevant ionisation energy [2]. This points towards an electrostatically governed induced conduction, as pointed out in section 7.2. It should be noted, the results of chapter 12 in mind, that the series also follows the TM^{3+} ion size, suggesting a possible structural explanation as well. By inserting an undoped STO layer on top of a Mn-doped layer, the transport properties of the 'undoped' 2DEG are once again achieved, which proves that the mobile electrons are situated within 1 unit cell at the interface [3].

Because of the nature of the supposed magnetism, i.e. confined to the interface or at least to the doped STO unit cells (up to 3), bulk magnetisation characterisation techniques are unable to provide any information. XAS and XMCD on the other hand can directly probe the nature & state of the Co-ions present.

13.2 Sample preparation

Several factors influence the sample preparation for the XAS measurements. The amount of material to probe, i.e. the transition metal, needs to be sufficiently present to be able to detect it. A high concentration ($>$ 2 at%) or large number of unit cells however strongly suppresses the conductive properties of the interface. The maximum feasible is therefore

3 unit cells of 2 at% doped STO. In order for the conductive properties of the LAO/STO to arise, at least 3-4 unit cells of LAO are required [4]. However, the limited escape depth of the electrons in TEY mode imposes a maximum on the LAO thickness. Therefore only 5 unit cells of LAO are deposited, to give a heterostructure of 5 uc LAO/3 uc 2 at% TM:STO//STO, as well as control samples of 3 uc 2 at% TM:STO//STO. This implies that the useful signal will be coming from approximately $2 \cdot 10^{13}$ atoms, if the whole sample would be inside the beam. Since the beam size is approximately 200 μm in diameter, the actual number of signal contributing TM atoms is $\approx 10^{10}$.

The transition metals used in this study are Co and Sc. The former is a common dopant in ZnO and other oxides (e.g. ITO [5]), in an attempt to induce ferromagnetic interactions. Specifically for STO, it was discovered that thin films of (La,Sr)(Co,Ti)$O_{3-\delta}$ are ferromagnetic, although its microscopic origin remains unclear [6, 7]. The La serves as an electron donor in this structure, which might activate the ferromagnetic coupling of the Co-impurities. In the 2DEG structures electrons are introduced through a different mechanism, but might have the same effect. The Sc-doped interface serves mostly as a control sample, since no magnetic *sp-d* interactions are expected in this system (Sc^{3+} has no *d*-electrons). It should be noted however that thin films of 2 at% Sc:STO were observed to be ferromagnetic, with a saturation magnetisation of 2.960 ± 0.631 emu/cm^3, with other parameters also similar to ferromagnetic ZnO (section 5).

In order to avoid charging of the (mostly insulating) samples under the incident photon beam, a 2-3 nm Au film is sputtered on top. A conductive path to the sample holder is then created by contacting this Au-pad either by a W-clip, a track of conductive silver epoxy or both. It appears that the contacting method does not influence the quality of the measurement, although the W-clip might block part of the fluorescence yield. The angle of incidence of the photon beam is 45^o in all cases.

13.3 Results

In all samples, the Ti signal is clearly visible and exhibits the distinct features of Ti^{4+}. The Ti^{3+} expected from the electronic reconstruction disappears in the background, since its concentration is so low: theoretically only half of one TiO_2 layer ($\approx 10^{11}$ atoms in the beam spot). It has however been observed by HAXPES [8]. No dichroism was observed over the Ti *L*-edge. The average XAS profile (in TEY and FY) is shown Figure 13.1, the multiplet structure (originating from ionisation) is clearly visible and similar to other Ti^{4+} data in literature [9, 10].

The average XAS spectrum of the LAO/Co:STO sample, recorded in TEY around the Co-edge, is shown in Figure 13.2. There are 4 features visible, large ones at 778 eV and 783 eV (L_3 edges) and corresponding L_2 edges at 793 eV and 798 eV respectively. The first peak displays a clear multiplet structure at the expected energy, indicative of Co^{2+}, while the second set is more smooth and metal-like. Remarkably the energy split between the L_3 and L_2 edge is the same as for Co, except the peaks occur approximately 5 eV higher. There is however no element known to exhibit a signal at these energies. The closest possible line would be a Ba *M*-edge, but also that would imply a shift by 3 eV. Furthermore, this line does not occur in the Sc-reference, which excludes a beamline impurity.

Reflecting back to the structure and unique properties of the LAO/STO interface, the presence of the LAO might be able to explain such a shift. In a purely electrostatic picture, each unit cell of LAO contributes a charge of approximately 0.9 eV [11], which would in this 5 uc case be $\approx$ 4.5 eV. An electrostatic shift can not explain the lack of multiplet

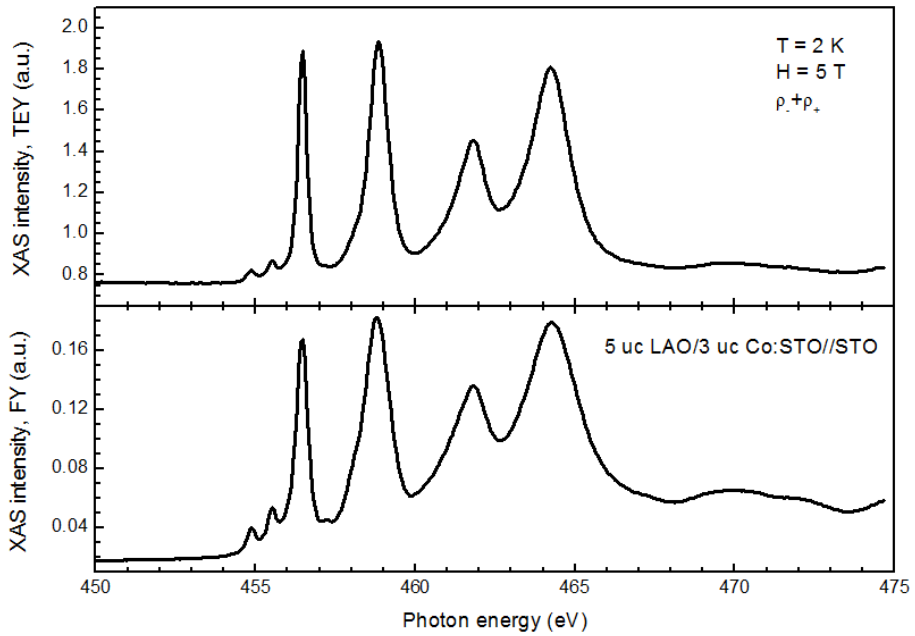

Figure 13.1: Average XAS in TEY (top) and FY (bottom) over the Ti L-edge at a temperature of 2 K and in a magnetic field of 5 T for the 5 uc LAO/3 uc Co:STO//STO sample.

structure on this peak, unless the Co-ions have trapped carriers from the interface to effectively nullify their formal charge. This 5 eV shift is however not observed in the Ti spectrum, whereas the Ti signal should be equally affected, since the electrons have to tunnel through the LAO to be detected. The absence of this shift for the Ti implies that this explanation is insufficient to describe the observation.

The dependence of the dichroic signal on the magnetic field is shown in Figure 13.3 for both peaks. The Co^{2+} (Fig. 13.3a) clearly exhibits paramagnetic behaviour. This is similar to results obtained for Mn:ZnO (see chapter 5) as well as Co:ITO thin films [5]. Surprisingly however, the Co-like peak (Fig. 13.3b) does not exhibit any XMCD at all: the XAS signal does not change with field (or polarisation, due to reversal symmetry). If this signal would indicate Co metal, ferromagnetic or superparamagnetic behaviour would be expected, depending on cluster size.

The field-dependent behaviour of the Co^{2+} is definitely paramagnetic rather than ferromagnetic. Just as for the Mn:ZnO (see chapter 5), this can be fitted with a Brillouin function:

$$M = M_0 \left\{ \left(\frac{2J+1}{2J} \right) \coth \left[\frac{(2J+1)y}{2J} \right] - \left(\frac{1}{2J} \right) \coth \left(\frac{y}{2J} \right) \right\} \tag{13.1}$$

where M_0 is the saturation magnetisation, $y = g\mu_B JH/k_B T$, g the spectroscopic splitting factor (2.0023 for free electrons), J the total angular momentum and μ_B the Bohr magneton and k_B the Boltzmann constants [12].

The effective magnetic moment p can be calculated from:

$$p = g\sqrt{J(J+1)} \tag{13.2}$$

After fitting, a total angular momentum J of 0.983 is obtained for the Co^{2+} in the LAO/Co:STO sample; the effective moment is then equal to 2.796 μ_B/Co. This value is lower, but in reasonable agreement with the theoretical value of 3.78 μ_B/Co for paramagnetic Co ions in the upper spin state [5]. Hakimi et al. [5] reported a comparable value of

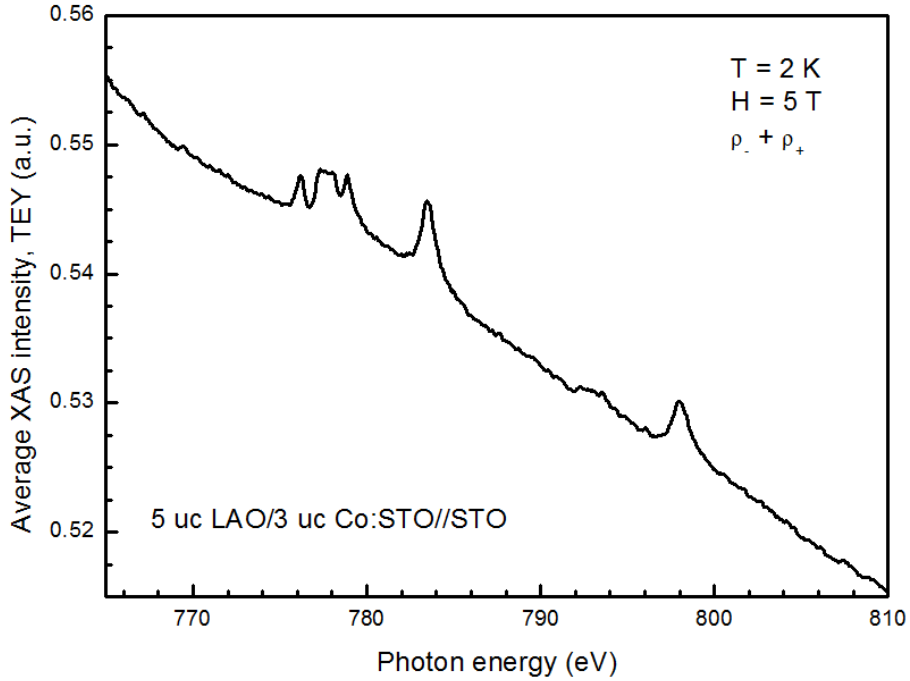

Figure 13.2: Average XAS spectrum, in TEY mode, of the LAO/Co:STO//STO sample at a temperature of 2 K and a field of 5 T.

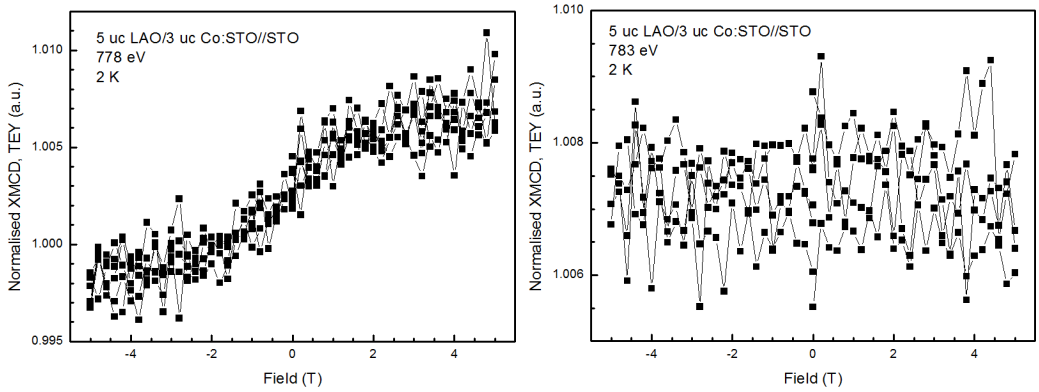

(a) (b)

Figure 13.3: Normalised XAS signal (in TEY) versus magnetic field at a temperature of 2 K for the LAO/Co:STO//STO sample at an energy of **(a)** 778 eV (Co^{2+}) and **(b)** 783 eV (Co-like).

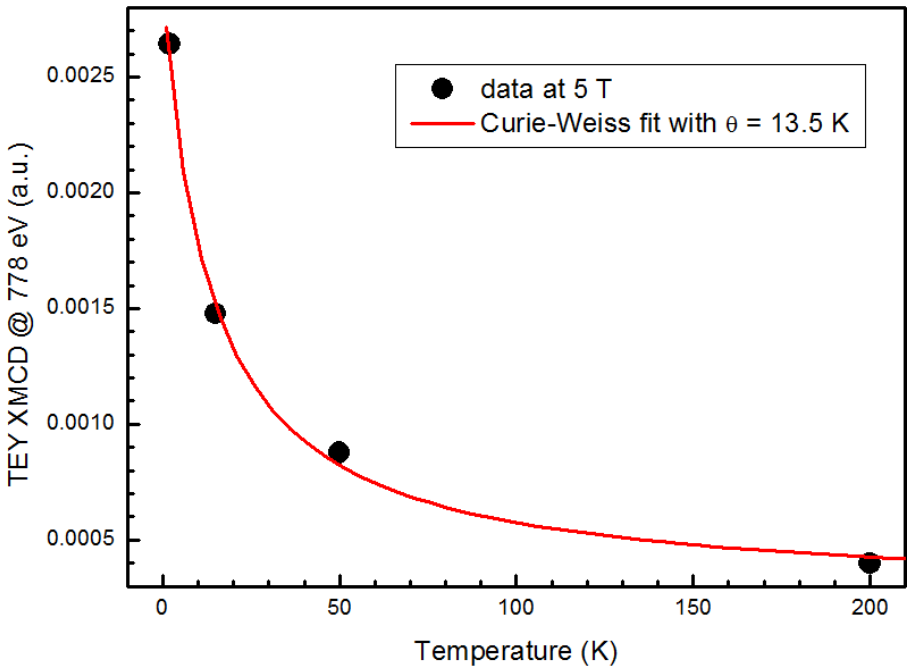

Figure 13.4: Normalised XAS signal (in TEY) of the Co^{2+} L_3 edge at 5 T versus temperature for the LAO/Co:STO//STO sample. The red line is a Curie-Weiss law fit through the data.

2.32 μ_B/Co in Co:ITO.

Similar paramagnetic field dependent behaviour was observed at higher temperatures on the Co^{2+} peak. The results are summarised in Figure 13.4, which also shows a fit of the data with a Curie-Weiss law (as in chapter 5 for Mn:ZnO). This emphasises once again the purely paramagnetic trend of the Co^{2+} – the fitted Curie-Weiss temperature is $\approx$ 14 K. This temperature is comparable to the one observed by Hakimi et al. [5] ($T_{CW} \approx 13 \pm 4$ K).

Comparing the XAS spectrum of the LAO/Co:STO sample to the control samples yields an interesting result (Figure 13.5). The two sets of peaks appear in both TEY and FY in the LAO/Co:STO sample, although the Co^{2+} signal appears more distinct in the TEY, indicating that it is closer to the (conductive) interface. This is already in contradiction with the hypothesis of trapped electrons stated above. Furthermore the Co:STO sample also exhibits both sets of peaks, whereas it should not contain the shifted metal-like one if the LAO-charge hypothesis is correct. It is therefore unclear what the nature of this peak is. The LAO/Sc:STO sample does not contain any Co-related peaks, which clearly demonstrates that both peaks are related to the Co-doping of STO and are unrelated to the presence of the LAO.

Fix et al. [2] suggested that the Co is initially present as Co^{3+} in the STO, but after electronic reconstruction under the influence of the LAO reverts to Co^{2+}. It seems that this is not the case, as Co^{2+} appears to dominate in both the LAO/Co:STO and Co:STO samples. Co^{3+} might be present, but a careful analysis and spectral simulation should be done, which is extremely difficult because of the sloped background and small signal. The valence of the Co in Co:STO might be influenced by its exposure to air and related absorption or compensating surface defects.

The Co^{2+} in the Co:STO sample also exhibits paramagnetic behaviour (Figure 13.6), with a total angular momentum of 0.994 and an effective magnetic moment of 2.818 μ_B/Co.

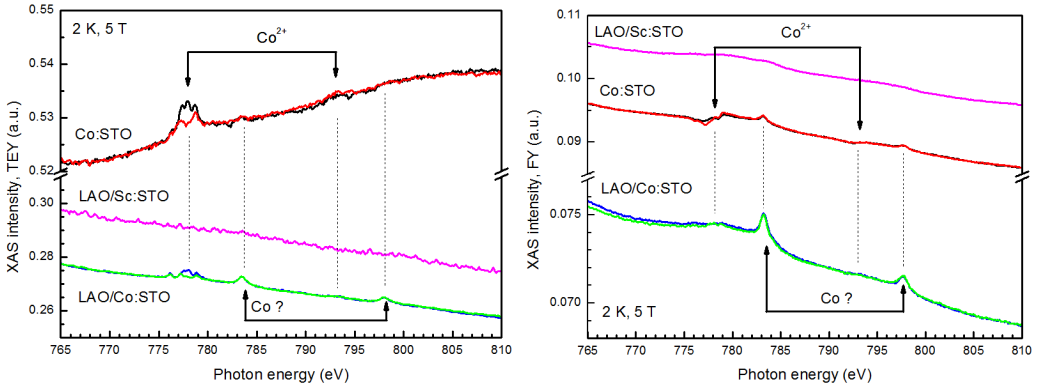

(a) (b)

Figure 13.5: Comparison of XAS data for all samples, data were collected in **(a)** TEY and **(b)** FY at a temperature of 2 K and a field of 5 T.

This is similar to the Co^{2+} in the LAO/Co:STO sample. Therefore the introduction of extra carriers into the Co:STO layer does not enhance the magnetic moment of the Co dopants.

13.4 Summary

Doped interfaces of LAO/Co:STO, LAO/Sc:STO and a Co:STO control sample have been studied by XAS and XMCD, with a focus on the behaviour of the Co. The dopant appears to be present as Co^{2+} mainly and exhibits a purely paramagnetic behaviour, rather than fulfilling the goal of achieving ferromagnetic coupling in the 2DEG. An extra set of peaks appears for all Co-doped samples, including the control Co:STO//STO. Their shape is metal-like (no multiplet structure) and $L_{3,2}$-splitting is Co-like, but they are displaced by approximately 5 eV from the expected Co-position (or 3 eV from the Ba energy). This peak also does not exhibit any dichroism. It is therefore unclear what the nature of this peak is. After the XMCD analysis of the Co:STO and comparison with other studied cases, the ferromagnetic nature of transition metal doped STO is deemed similar to defect-based behaviour of Mn:ZnO discussed in Chapter 5.

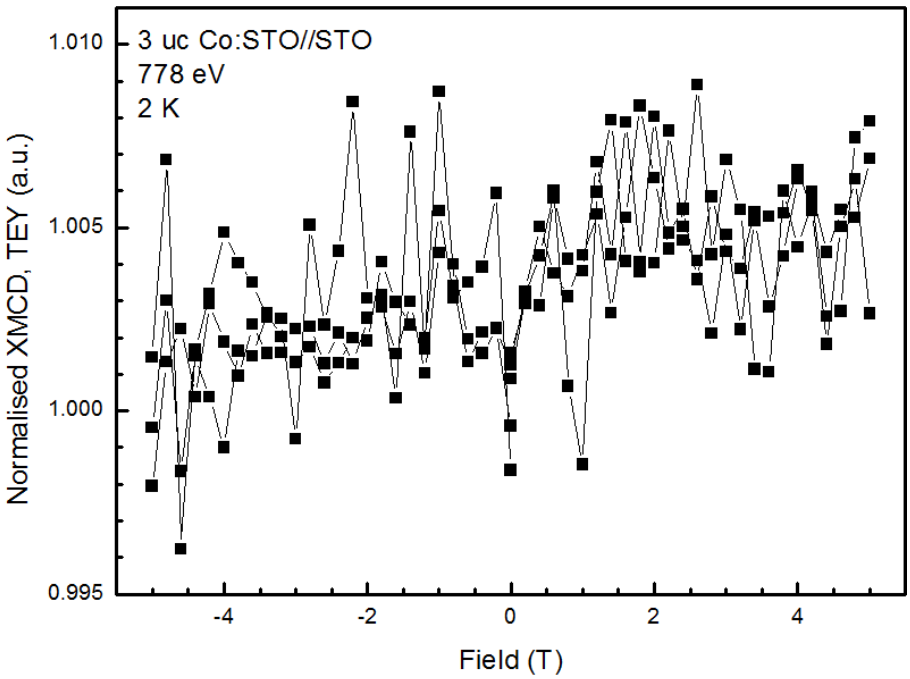

Figure 13.6: Normalised XAS signal (in TEY) versus magnetic field at a temperature of 2 K for the Co:STO//STO sample at an energy of 778 eV (i.e. Co^{2+}).

Bibliography

[1] T. Fix, J. L. MacManus-Driscoll, and M. G. Blamire. Delta-doped $LaAlO_3/SrTiO_3$ interfaces. *Applied Physics Letters*, 94:172101, 2009.

[2] T. Fix, F. Schoofs, J. L. MacManus-Driscoll, and M. G. Blamire. Influence of doping at the nanoscale at $LaAlO_3/SrTiO_3$ interfaces. *Applied Physics Letters*, 97:072110, 2010.

[3] T. Fix, F. Schoofs, J. L. MacManus-Driscoll, and M. G. Blamire. Charge confinement and doping at $LaAlO_3/SrTiO_3$ interfaces. *Physical Review Letters*, 103:166802, 2009.

[4] S. Thiel, G. Hammerl, A. Schmehl, C. W. Schneider, and J. Mannhart. Tunable quasi-two-dimensional electron gases in oxide heterostructures. *Science*, 313:1942–1945, 2006.

[5] A. M. H. R. Hakimi, F. Schoofs, R. Bali, N. A. Stelmashenko, and M. G. Blamire. Origin of magnetism in cobalt-doped indium tin oxide thin films. *Physical Review B*, 82:144429, 2010.

[6] T. Fix, M. Liberati, H. Aubriet, S.-L. Sahonta, R. Bali, C. Becker, D. Ruch, J. L. MacManus-Driscoll, E. Arenholz, and M. G. Blamire. Ferromagnetism in Co-doped $(La,Sr)TiO_3$. *New Journal of Physics*, 11:073042, 2009.

[7] O. Copie, K. Rode, R. Mattana, M. Bibes, V. Cros, G. Herranz, A. Anane, R. Ranchal, E. Jacquet, K. Bouzehouane, M.-A. Arrio, P. Bencok, N. B. Brookes, F. Petroff, and A. Barthélémy. Structural and magnetic properties of Co-doped $(La,Sr)TiO_3$ epitaxial thin films probed using x-ray magnetic circular dichroism. *Journal of Physics: Condensed Matter*, 21:406001, 2009.

[8] M. Sing, G. Berner, K. Goss, A. Müller, A. Ruff, A. Wetscherek, S. Thiel, J. Mannhart, S. A. Pauli, C. W. Schneider, P. R. Willmott, M. Gorgoi, F. Schäfers, and R. Claessen. Profiling the interface electron gas of $LaAlO_3/SrTiO_3$ heterostructures with hard x-ray photoelectron spectroscopy. *Physical Review Letters*, 102: 176805, 2009.

[9] Akane Agui, Masaichiro Mizumaki, Yuji Saitoh, Tomohiro Matsushita, Takashi Nakatani, Atsuko Fukaya, and Eiko Torikai. Soft x-ray absorption spectra of ilmenite family. *Journal of Synchrotron Radiation*, 8:907–909, 2001.

[10] M. Salluzzo, J. C. Cezar, N. B. Brookes, V. Bisogni, G. M. De Luca, C. Richter, S. Thiel, J. Mannhart, M. Huijben, A. Brinkman, G. Rijnders, and G. Ghiringhelli. Orbital reconstruction and the two-dimensional electron gas at the $LaAlO_3/SrTiO_3$ interface. *Physical Review Letters*, 102:166804, 2009.

[11] N. C. Bristowe, Emilio Artacho, and P. B. Littlewood. Oxide superlattices with alternating p and n interfaces. *Physical Review B*, 80:045425, 2009.

[12] K. M. Reddy, J. Hays, S. Kundu, L. K. Dua, P. K. Biswas, C. Wang, V. Shutthanandan, M. H. Engelhard, X. Mathew, and A. Punnoose. Effect of Mn doping on the structural, morphological, optical and mangetic properties of indium tin oxide films. *Journal of Materials Science: Materials in Electronics*, 18:1197–1201, 2007.

Chapter 14

Functionalising the LAO/STO interface

In the previous chapter it was shown that transition metal doping of the interface-STO does not induce any (more) ferromagnetism. Such doping however does have a significant (negative) impact on the transport properties, possibly by influencing oxygen octahedra rotations. This chapter focuses on artificially introducing layers of (anti)ferromagnetic perovskites at the LAO/STO interface, with the goal of inducing a 2DEG in this functionalised 'defect' layer.

14.1 Introduction

Most perovskites have similar (pseudo-)cubic lattice parameters, allowing for easy integration of several layers with different properties. $SrMnO_3$ (SMO; $a = 0.3805$ nm, $T_N = 260$ K) is a notable antiferromagnet [1], the spins of which can become uncompensated upon La-doping due to a Mn-multivalence (Mn^{3+}/Mn^{4+}) state. This multivalence state might also be introduced through the electronic reconstruction mechanism, intermixing or oxygen vacancies, which makes it a potentially interesting material for the LAO/STO interface.

Due to the profound negative impact of Ti-site doping on the conductive properties of the LAO/STO heterostructure (chapter 13 and [2, 3]), it could be wise to leave the Ti-layer intact and modify the *A*-site ion only, as in chapter 12. $CoTiO_3$ (CTO; $T_N = 38$ K [4]) does however crystallise in a hexagonal ilmenite structure ($a = 0.507$ nm, $c = 1.392$ nm), although the distortion from the cubic perovskite is relatively small.

Other materials that were attempted were $SrCoO_3$ ($a = 0.384$ nm; $T_C = 305$ K, [5, 6]) and $BaCrO_3$ ($a \approx 0.385$ nm), the latter predicted to be a half-metal [7]. Unfortunately neither of these two compounds could be deposited in the right phase within the window of LAO/STO depositions (700-850 ℃, $pO_2 \approx 10^{-2}$ mbar). The majority phases obtained on STO (001) were polycrystalline $Sr_2Co_2O_5$ and $BaCrO_4$ (with or without $BaTiO_3$ buffer) respectively, as determined by x-ray diffraction. An AFM topography image of a $BaCrO_x$ film is shown in Figure 14.1: islands with specific crystallographic orientations with respect to the STO substrate are clearly visible, with seemingly randomly oriented crystallites between the islands.

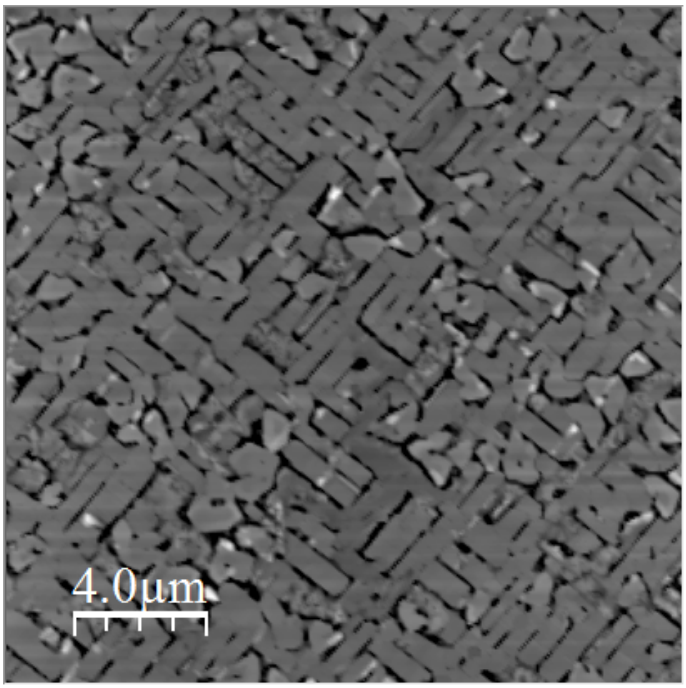

Figure 14.1: AFM topography scan of a $BaCrO_x$ film on an STO (001) substrate; 12000 pulses deposited at 850 °C in 10^{-2} mbar O_2 (1 J/cm^2, 10 Hz).

14.2 LAO/$SrMnO_3$//STO

Despite the small lattice mismatch and a similar multivalence state of the Mn-ion, heterostructures with 1 or 3 uc of $SrMnO_3$ at the interface are all insulating at room temperature. It is unclear why this is the case: its origin might be structural (i.e. relating to oxygen octahedra rotations) or electronic (i.e. relating to the Mn ionisation state and self-compensation). This trend was already observed upon increasing Mn-dopant concentration in LAO/Mn:STO//STO heterostructures [3]. It can be expected that $LaMnO_3$ (another perovskite antiferromagnet) will result in the same insulating character of the heterointerface.

14.3 LAO/$CoTiO_3$//STO

14.3.1 Pulsed laser deposition of $CoTiO_3$ on STO

$CoTiO_3$ (CTO) crystallises in an ilmenite structure and behaves as an antiferromagnetic insulator with a Néel temperature of approximately 38 K [4]. It has mostly been investigated as a potential high-k gate dielectric to replace SiO_2 in CMOS [8]. The fabrication procedure is commonly a direct oxidation of sputtered metal layers [8] or a sol-gel procedure for thicker films [9]. However so far, pulsed laser deposition (PLD), despite being a widespread technique for the deposition of oxides, has not been applied for the growth of CTO thin films.

CTO films were grown on single-crystal $SrTiO_3$ (001) substrates using the PLD system described in section 2.1.2. The repetition rate is set to 10 Hz and the laser fluence fixed at 1.5 J/cm^2. The substrate heater temperature was varied between 600 and 850 °C. The oxygen partial pressure during deposition and cooling down was kept constant at 10^{-2} mbar. The CTO target was prepared by solid state reaction from a stoichiometric

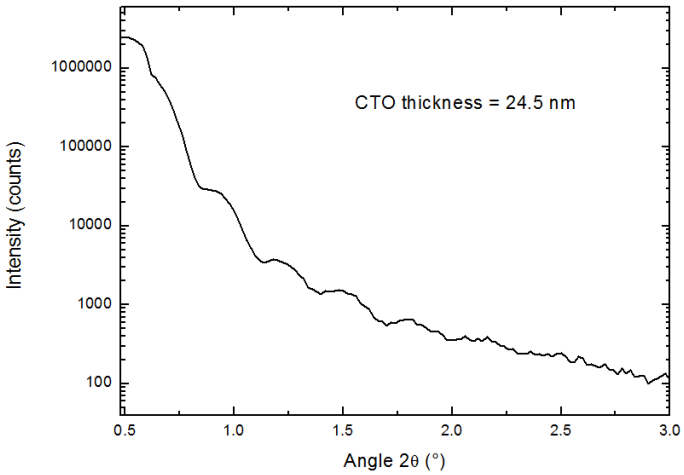

Figure 14.2: X-ray reflectivity measurement on a 24.5 nm $CoTiO_3$ film grown at 700 ℃.

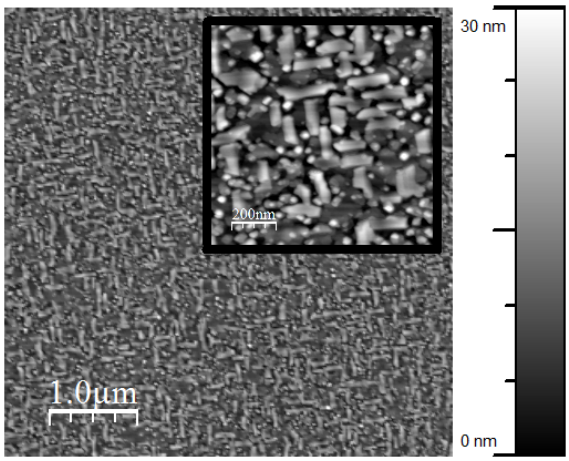

Figure 14.3: AFM image of a $CoTiO_3$ film on STO, grown at 850 ℃. The inset shows a detailed view.

mixture of Co_3O_4 and TiO_2 powders (see chapter 8 for details). The powders were milled, mixed, pressed and sintered at 1100 ℃ for 9 hours. The resulting phase of the target, as evidenced by XRD, was mainly $CoTiO_3$. Film thicknesses are determined by x-ray reflectivity (see section 2.2.2), which exhibits clear fringes (Figure 14.2).

Surface characterisation

To allow seamless CTO integration in the LAO/STO deposition sequence, the substrate heater temperature was initially set at 850 ℃. An AFM image of a film grown at this temperature is shown in Figure 14.3. The CTO exhibits a clear island growth whereby two perpendicular orientations appear to be favourable. The in-plane cubic directions of the STO are parallel to the edges of the image. The sides of the islands seem to be at an angle rather than parallel to the [1 0 0] or [0 1 0] directions.

Upon decreasing the deposition temperature to 700 ℃ or 600 ℃, the CTO initially grows in a layer-by-layer mode up to two unit cells (2.6 nm thickness), after which islands nucleate. Figure 14.4 shows an AFM image of a 2.6 nm film (with surface steps clearly visible) and a 5 nm film for comparison. The island size is equal to or smaller than the AFM tip (20-30 nm) so cannot be determined by this method. The RHEED specular spot

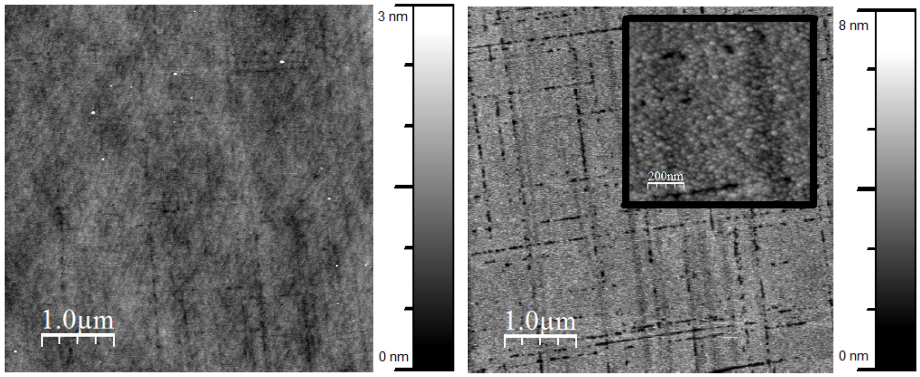

(a) (b)

Figure 14.4: AFM images of $CoTiO_3$ films grown at 600 ℃ with a thickness of **(a)** 2.6 nm (2D growth) and **(b)** 5 nm (3D after 2D).

intensity oscillation during the growth of 2 initial unit cells of CTO at 700 ℃ is displayed in Figure 14.5. The reflected electron diffraction pattern recorded along the STO [1 0 0] is also shown before and after the deposition. Streaks indicating a smooth surface are clearly visible. Post-heating a layer-by-layer grown CTO film to 850 ℃, results in a restructuring of the surface and the nucleation of islands, with a morphology similar to films grown at that temperature.

Crystallographic characterisation

CTO films grown at 700 ℃ were studied by x-ray diffraction to reveal the crystallographic relationship with the STO (Figure 14.6). For the 5 nm film, no diffraction peaks other than the substrate stand out from the background. The thicker films (9.2 and 24.5 nm) exhibit dominant peaks corresponding to the (0 0 3) and (0 0 6) planes, as well as weaker (0 0 9) and (0 0 12) reflections (not shown). The rocking curve full width at half maximum (FWHM), an indication of the degree of orientation of the film, equals 0.180° on the (0 0 3) and (0 0 6) reflections for the 24.5 nm film, on an STO substrate with a rocking curve FWHM of 0.107°. This implies a very good *c*-axis orientation of CTO with respect to the STO. Based on all 4 *c*-axis reflections, the out-of-plane lattice parameter of the 24.5 nm CTO film is extended by $0.23 \pm 0.10\%$.

The 9.2 nm film also has a minor peak corresponding to either the CTO (2 0 5) or (1 1 $\bar{6}$) direction, with the same rocking curve FWHM dependence. Since this peak is no longer visible in the 24.5 nm film, it could be related to the 2D to 3D transition because of the higher contribution of the interface for the thinner film. In the 24.5 nm however, a distinct peak at 37.8° emerges with a rocking curve FWHM of 0.583°, i.e. different from the CTO phase. This peak corresponds to anatase TiO_2 (0 0 4), implying that an excess Ti in the plume condenses as the film continues to grow beyond the 2D mode, hence acting as additional lattice mismatch alleviation mechanism above the critical thickness..

To further understand the epitaxial relationship, an x-ray ϕ-scan was performed on the CTO (1 0 4) reflection and the STO (1 1 1) as well as the STO (0 1 1) (Figure 14.7a). There is a clear correspondence between the CTO and the STO (1 1 1) direction, but the CTO film exhibits two-in plane orientations at 90° from each other. This means that the orthorhombic CTO [1 0 0] can be aligned either along the [1 1 0] or [$\bar{1}$ 1 0] of the underlying STO substrate, resulting in two non-equivalent CTO orientations (Figure 14.7b). The effect of this twinning is clearly visible in the films grown at 850 ℃: islands

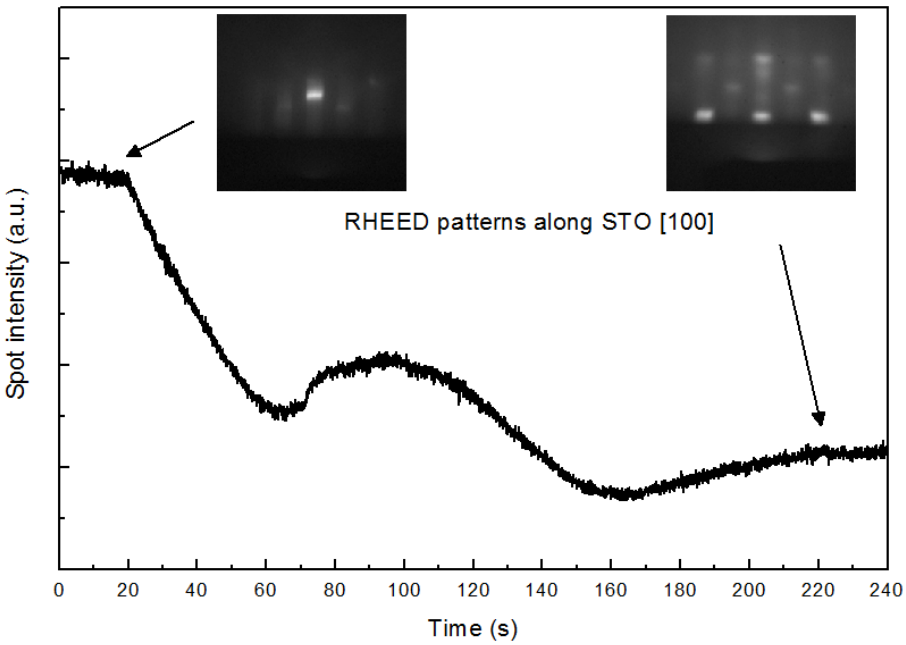

Figure 14.5: RHEED specular spot intensity versus time, with the diffraction pattern before and after the deposition of 2 unit cells of CTO on STO, recorded along the STO [1 0 0] at 700 °C.

are perpendicular to each other and the edges are along a <1 1 0> STO direction. During 2D growth, the CTO is most likely to be fully strained along the diagonals of the STO unit cell, resulting in a biaxial tensile strain of ≈0.68% (Figure 14.7b). This value is however too high to be maintained throughout the whole film, therefore a transition to 3D growth occurs.

Magnetic characterisation

Samples were cooled in the absence of a magnetic field ('zero field cooled') and subsequently measured by VSM in an applied magnetic field in order to pick up the antiferromagnetic transition. Measurement of the magnetic moment versus temperature of the thickest (24.5 nm) CTO film, reveals an anomaly around 50-60 K, which is related to the antiferromagnetic Néel temperature (Figure 14.8a–b). Powder from the target (mainly $CoTiO_3$ phase) measured under the same conditions (Figure 14.8c) revealed a peak around 38-40 K, i.e. the bulk transition temperature. This suggests that the tensile strain as a result of the heteroepitaxy with the STO increases the antiferromagnetic transition temperature by about 22 K. Such strain-driven enhancement is not unexpected and has been observed in systems such as NiF_2 [10], $YMnO_3$ [11] and Fe_2VSi [12]. The magnetic measurements suggest that the antiferromagnetic order in $CoTiO_3$ is strongly coupled to the lattice.

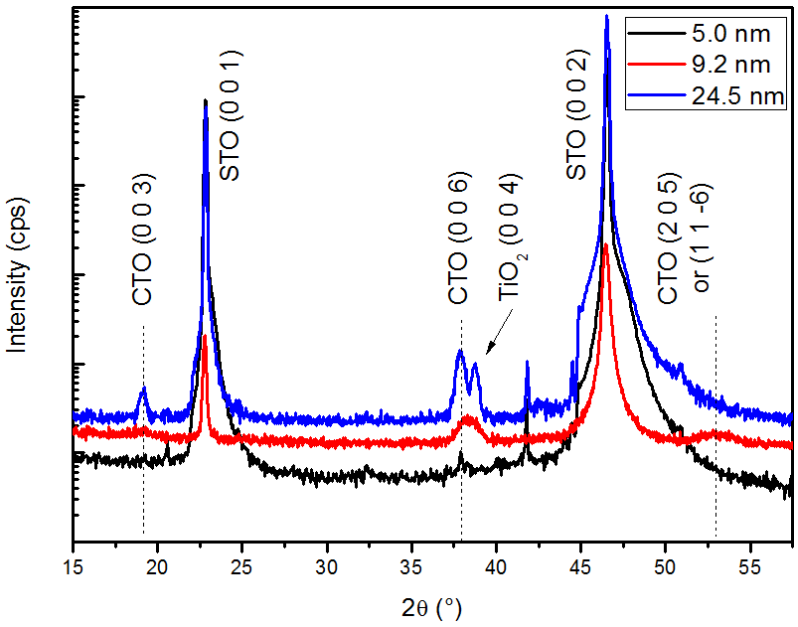

Figure 14.6: X-ray diffraction pattern of a 4.9, 9.2 and 24.5 nm CTO film grown at 700 ℃. STO substrate peaks are indicated & indexed. Peaks corresponding to CTO (0 0 3) (around 18°) and (0 0 6) (around 38.7°) are visible in the higher thicknesses. There is a spurious CTO orientation near 53° in the intermediate thickness, possible due to an interface contribution and a TiO_2 (0 0 4) peak at 37.8° in the 24.5 nm film.

14.3.2 Transport properties of heterostructures

Having characterised the CTO growth and properties, it can now be incorporated in the LAO/STO system. Heterostructures of 15 uc LAO/2 uc CTO//STO are deposited at 700 ℃ in 2D mode, as verified by RHEED. A resistance versus temperature curve of such a sample is shown in Figure 14.9. First of all it is remarkable that the interface is still conductive, even if more resistive: this means that the electronic or structural reconstruction of the LAO/STO can be induced in other thin perovskite layers with appropriate elements at the interface (i.e. Ti or V [13], not Mn [section 14.2]). Secondly a large anomaly and hysteresis is observed around 60 K, the temperature of the antiferromagnetic transition found for CTO films on STO (see Figure 14.8). The implication is twofold: two unit cells of CTO are already antiferromagnetic and the 2DEG appears to be affected by the spin ordering.

Unfortunately only 2 samples out of 20 grown were found to be conductive, despite the same nominal growth and correct 2 uc CTO termination (as additionally verified by the LAO RHEED oscillation period). More detailed measurements on patterned Hall bars did not reveal any conclusive results with respect to carrier density or mobility or influence of the antiferromagnetic transition. One possible explanation for the low reproducibility could be in the observed variation of CTO deposition (Figure 14.10). It appears that the number of pulses required for the deposition of 2 CTO uc varied greatly through the runs. This could be due to laser fluence fluctuations, changes in illuminated area (laser focus), state of the target, all leading to a variable plume composition, among other reasons. Re-polishing the target surface to a pristine condition did not yield any improvement.

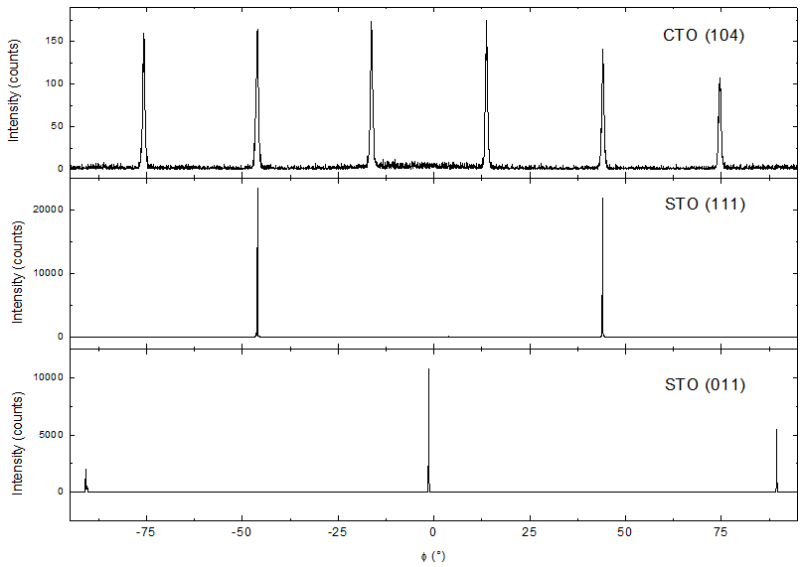

(a)

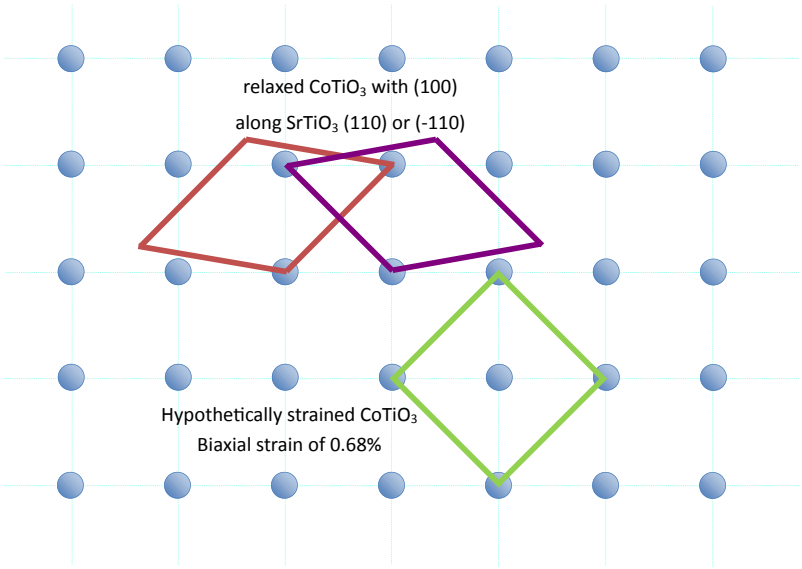

(b)

Figure 14.7: **(a)** Phi-scan on a 24.5 nm CTO film grown at 700 ℃. The CTO peaks clearly correspond to STO (111) reflections, but can also be rotated by 90° in-plane. **(a)** Schematic drawing of the possible orientations of relaxed and hypothetically strained CTO on STO (001) surfaces.

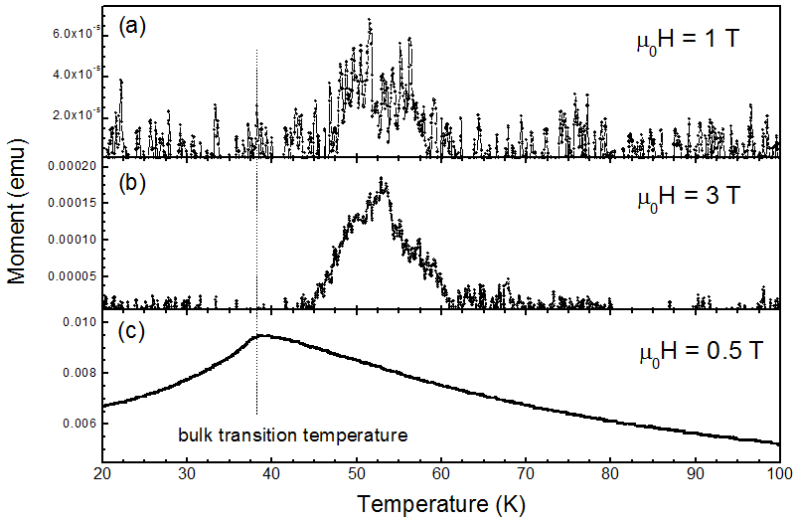

Figure 14.8: Magnetic moment versus temperature for **(a)-(b)** a 24.5 nm CTO film (grown at 700 ℃) with the diamagnetic background from the STO substrate subtracted, in a magnetic field of **(a)** 1 T and **(b)** 3 T; **(c)** bulk powder (from the target) warmed in a magnetic field of 0.5 T.

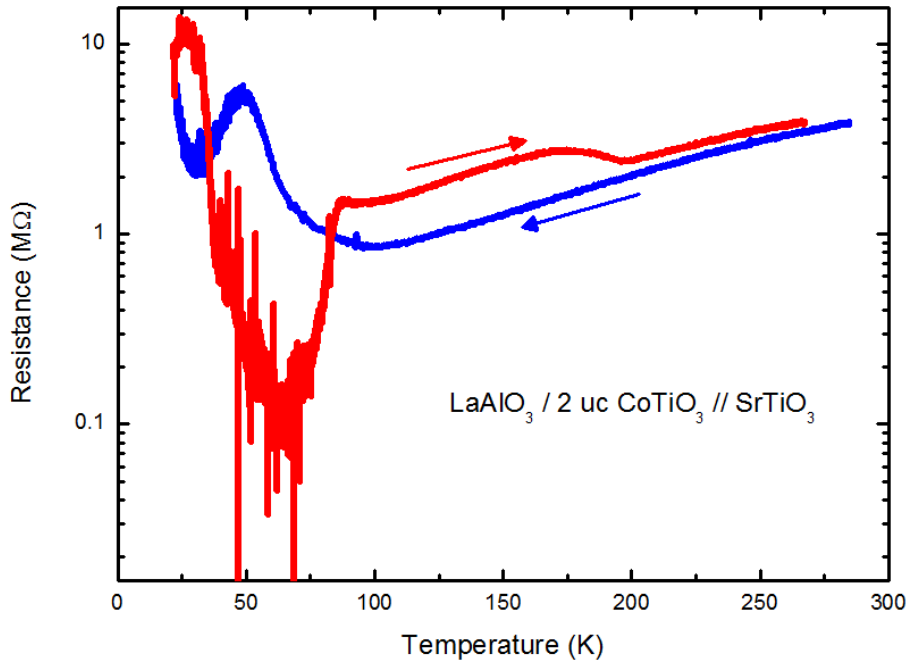

Figure 14.9: Resistance versus temperature curve for a 15 uc LAO/2 uc CTO//STO sample.

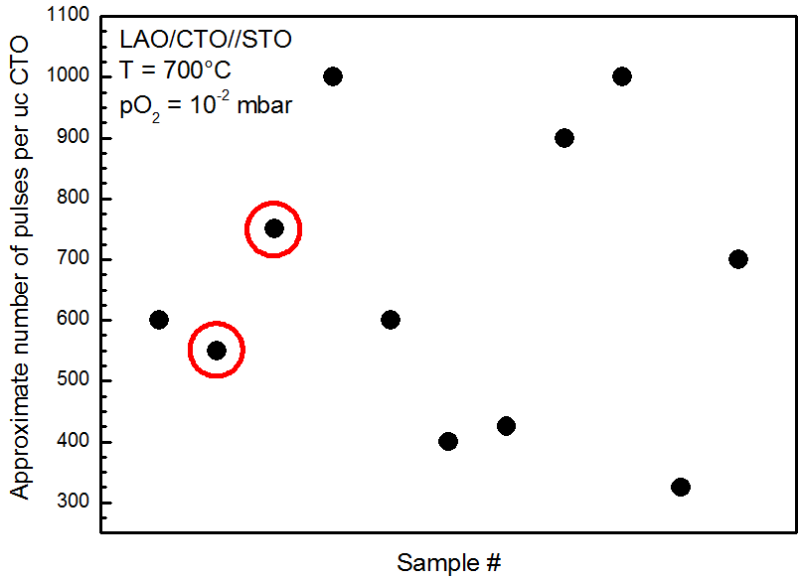

Figure 14.10: Variation in number of pulses required per uc of CTO during PLD of LAO/CTO//STO heterostructures at 700 °C. The red circles indicate the conductive samples.

14.4 Conclusion

Despite the low reproducibility observed here, $CoTiO_3$ seems a promising candidate to functionalise the LAO/STO interface. Perhaps with an improved growth control (e.g. by MBE), better results can be obtained. It might even be possible to create a two-dimensional hole gas: a single uc of $SrCoO_3$ (to switch the substrate termination), followed by 1-2 uc of $CoTiO_3$ would expose the $(CoO)^0$ layer at the interface with LAO. Since Co can have both the 2+ as well as 3+ valence state, hole doping could be supported through the electronic reconstruction model (section 7.2).

Overall it appears to be difficult to find suitable functional perovskite materials to insert at the LAO/STO interface, especially in terms of compatible growth parameters to obtain the right phase. However, electron transfer into this artificial functional defect construction seems possible.

Bibliography

[1] B. R. K. Nanda and S. Satpathy. Polar catastrophe, electron leakage and magnetic ordering at the $LaMnO_3/SrMnO_3$ interface. *Physical Review B*, 81:224408, 2010.

[2] T. Fix, J. L. MacManus-Driscoll, and M. G. Blamire. Delta-doped $LaAlO_3/SrTiO_3$ interfaces. *Applied Physics Letters*, 94:172101, 2009.

[3] T. Fix, F. Schoofs, J. L. MacManus-Driscoll, and M. G. Blamire. Influence of doping at the nanoscale at $LaAlO_3/SrTiO_3$ interfaces. *Applied Physics Letters*, 97:072110, 2010.

[4] R. E. Newnham, J. H. Fang, and R. P. Santoro. Crystal structure and magnetic properties of $CoTiO_3$. *Acta Crystallographica*, 17:240, 1964.

[5] Jun Hee Lee and Karin M. Rabe. Coupled magnetic-ferroelectric metal-insulator transition in epitaxially strained $SrCoO_3$ from first principles. *Physical Review Letters*, 107:067601, 2011.

[6] Youwen Long, Yoshio Kaneko, Shintaro Ishiwata, Yasujiro Taguchi, and Yoshinori Tokura. Synthesis of cubic $SrCoO_3$ single crystal and its anisotropic magnetic and transport properties. *Journal of Physics: Condensed Matter*, 23:245601, 2011.

[7] Z. H. Zhu and Yan H. Half-metallic properties of perovskite $BaCrO_3$ and $BaCr_{0.5}Ti_{0.5}O_3$ superlattice: LSDA+U calculations. *Journal of Applied Physics*, 106: 023713, 2009.

[8] Tung Ming Pan, Tan Fu Lei, and Tien Sheng Chao. Comparison of ultrathin $CoTiO_3$ and $NiTiO_3$ high-k gate dielectrics. *Journal of Applied Physics*, 89(6):3447–3452, 2001.

[9] Yi-Jing Lin, Yen-Hwei Chang, Wein-Duo Yang, and Bin-Siang Tsai. Synthesis and characterization of ilmenite $NiTiO_3$ and $CoTiO_3$ prepared by a modified Pechini method. *Journal of Non-Crystalline Solids*, 352:789, 2006.

[10] Hongtao Shi, D. Lederman, K. V. O'Donovan, and J. A. Borchers. Exchange bias and enhancement of the Néel temperature in thin NiF_2 films. *Physical Review B*, 69: 214416, 2004.

[11] K. H. Wu, H.-J. Chen, Y. T. Chen, C. C. Hsieh, C. W. Luo, T. M. Uen, J. Y. Juang, J.-Y. Lin, T. Kobayashi, and M. Gospodinov. Marked enhancement of Néel temperature in strained $YMnO_3$ thin films probed by femtosecond spectroscopy. *Europhysics Letters*, 94:27006, 2011.

[12] N. Fukatani, K. Ueda, and H. Asano. Epitaxial strain and antiferromagnetism in Heusler Fe_2VSi thin films. *Journal of Applied Physics*, 109:073911, 2011.

[13] A. David, R. Frésard, Ph. Boullay, W. Prellier, U. Lüders, and P.-E. Janolin. Structural transition in $LaVO_3/SrVO_3$ superlattices and its influence on transport properties. *Applied Physics Letters*, 98:212106, 2011.

Chapter 15

Conclusions & outlook for $LaAlO_3/SrTiO_3$

By deliberately introducing defects, either through varying deposition parameters or through the insertion of doped layers, the fundamental nature of the conduction at the LAO/STO interface has been determined. Variation of the oxygen pressure during deposition clearly distinguished two-dimensional from bulk-dominated conduction, as evidenced from the power law fitting of resistance versus temperature curves. This characteristic non-Fermi-liquid behaviour was also observed for a single unit cell of LSTO inserted at the LAO/STO interface, which enhanced the sheet carrier density by an order of magnitude to 10^{14} cm^{-2} at 200 K. By changing the laser fluence while depositing LAO on STO, the interplay between conduction and structural integrity was revealed: a balance between stoichiometry of the LAO as well as the STO surface is essential. This structural factor became even more clear when ion sizes in a single unit cell near the LAO/STO interface were varied, which resulted in a better fundamental understanding of the interface conduction.

The key to a conductive interface appears to be a favourable degree of oxygen octahedra rotation and out-of-plane distortion, induced by the epitaxial stress of the rhombohedral LAO, which is to some extent transferred to the interface unit cells of the underlying cubic STO. This point of view unifies parts of all existing and proposed theories for conduction at the interface: intermixing probably occurs, as well as oxygen vacancy creation as well as a structural distortion to compensate an internal electric field in the LAO film. The results of the preceding chapters can be fully explained, from oxygen vacancy dominant conduction, to off-stoichiometric lattice distortions due to laser fluence effects, to doping of the interface with various cation sizes in a perovskite host lattice, all of which modify the oxygen octahedra rotations in the STO and thus the conduction of the LAO/STO interface.

From a fundamental and theoretical perspective, it would be interesting to analyse the structural transitions that occur at the LAO/STO interface in more detail, for example by grazing incidence x-ray diffraction or β-NMR, similar to work by Salman et al. [1] on bare STO. Knowing the mechanism of each transition could potentially allow a suppression or enhancement in order to tune the carrier density to the desired value or influence the electron scattering mechanism.

Practically speaking, functionalising the interface with a(n anti)ferromagnetic layer with a reasonably high Curie temperature, preferably near room temperature, would be of great interest in order to create a spin-polarised conductive channel and subsequently

a field effect transistor. Several materials have been tried in this work, all of which were (probably) unsuccessful: the key is obtaining the right coupling of the lattice distortions across the interface. Manganites would be a prime candidate based on their Curie temperature, but are very sensitive to oxygen octahedra rotations themselves. Probably strain (e.g. from a different substrate) could help in achieving the correct distortion.

Bibliography

[1] Z. Salman, M. Smadella, W. A. MacFarlane, B. D. Patterson, P. R. Willmott, K. H. Chow, M. D. Hossain, H. Saadaoui, D. Wang and R. F. Kiefl. Depth dependence of the structural phase transition of $SrTiO_3$ studied with β-NMR and grazing incidence x-ray diffraction. *Physical Review B*, 83:224112, 2011.

Chapter 16

Conclusion

By exploiting their sensitivity to defect fluctuations, the functional properties of both the ZnO as well as the $LaAlO_3/SrTiO_3$ oxide system could be better understood. In the case of the ZnO, the ferromagnetic properties could be manipulated by changing the deposition conditions. This in turn is linked to strain inside the film and therefore to the intrinsic defect balance, which governs the localised ferromagnetism.

Controlled modification of the $LaAlO_3/SrTiO_3$ interface, including the introduction of artificial defect layers, allowed to determine the nature of the conduction mechanism. Despite earlier hypotheses in literature, the two-dimensional conduction is found to be fundamentally structural in origin and most likely related to $LaAlO_3$-induced oxygen octahedra rotations in the near-surface $SrTiO_3$. By controlling film stoichiometry, limiting interface defects and inserting layers with an optimum modification of these octahedra, sheet carrier density could be enhanced by an order of magnitude. Functionalisation remains a challenge due to the structural compatibility and its influence on the interface conduction.

Better understanding of the physical phenomena at the base of the functional properties of both studied oxide systems, should allow extrapolation to other and new systems or heterostructures in order to create improved functional oxides.

Additionally, both system case studies show that defect management in oxide thin films provides an important handle in order to control and tune functional behaviour in these versatile materials. This implies that growth and post-treatments should be well understood in terms of their structural impact on these materials, in order to integrate oxides into larger device configurations.